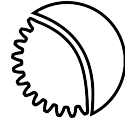UNIVERSITAT POLITÈCNICA DE VALÈNCIA

INSTITUTO DE INGENIERÍA MECÁNICA Y BIOMECÁNICA

UNIVERSITAT POLITÈCNICA DE VALÈNCIA

Department of Mechanical and Materials Engineering – DIMM

Institute of Mechanical and Biomechanical Engineering – I2MB

Ph.D. Thesis

Analysis of osteoporosis effect on the mechanical behaviour and morphometry of human cancellous bone

Presented by: Ms. Raquel Megías Díaz

Supervised by: Dr. Ana Vercher Martínez

Dr. Eugenio Giner Maravilla

Dr. Ricardo Belda González

Valencia, March, 2024

Acknowledgements

Agradecimientos

Una tesis doctoral requiere de un gran esfuerzo durante un largo periodo de tiempo. Y por eso, me gustaría agradecer en las próximas líneas a todas las personas que han estado a mi lado durante este camino. Gracias a todos vosotros por estar a mi lado durante estos años.

En primer lugar, quería agradecer a mis directores de tesis, Ana Vercher, Eugenio Giner y Ricardo Belda, por confiar en mí para embarcarme en este proyecto. Gracias por vuestro tiempo, vuestra ayuda, vuestros consejos, vuestra experiencia y vuestra guía, que han sido fundamentales para poder realizar esta tesis. He tenido los mejores referentes para aprender y crecer profesionalmente.

Han sido muchas las personas con las que he tenido la suerte de coincidir a lo largo de los años en la sala de becarios. Y aunque normalmente tengamos ocupación del 100 % con todo lo que ello implica, ha sido un verdadero placer compartir día a día con vosotros. A todos, muchas gracias. Sin embargo, me gustaría agradecer a aquellos compañeros que han soportado los días malos, han sido apoyo en los baches y con los que he compartido cada alegría: Ricardo Belda, Norberto Feito, Xavi García, Jose Vicente Calvo, Jorge Gómez, Antonio Quiñonero y Diego Infante. Gracias por todos esos cafés para recargar la batería, pero sobretodo por estar siempre ahí.

Otra persona a la que me gustaría reconocer su inestimable ayuda es a Federico Olmeda, "Fede" para nosotros. Eres un pilar fundamental para todos. Además de siempre estar disponible, lo hace con la mejor de las actitudes no importa la

Abstract

The main objective of this thesis is to analyse the effect of osteoporosis on the mechanical behaviour of cancellous bone. The mechanical behaviour of cancellous bone has been addressed through different approaches: experimental tests, finite element (FE) models and medical imaging obtained by micro-CT.

The impact of osteoporosis has been studied on different scales. Firstly, a study has been undertaken at the lamellar tissue level of trabecular bone to estimate the equations that define the elastic and strength properties as a function of bone mineral density (BMD) and tissue porosity. These equations are inferred from finite element (FE) models and allow us to characterise the behaviour of lamellar bone tissue covering a wide range of porosities and BMDs.

A study of the cancellous structure and lamellar tissue has been carried out using a stereomicroscope and field emission scanning electron microscope (FE-SEM). At lamellar tissue level, it was possible to observe the arrangement of lamellae in different locations, such as trabeculae and at their intersections. In addition, it has been possible to evaluate the natural tissue porosity and that produced by bone diseases, such as osteoporosis. All this information has been incorporated to the numerical models in order to define the properties of cancellous bone samples. The estimated elastic and strength equations consider an orthotropic behaviour and it is possible to quantify how BMD and porosity affect these properties.

On the other hand, the mechanical behaviour under compression of human trabecular bone samples from femoral heads has been studied. These samples

are classified into three study groups: healthy group (HG), osteoarthrosic group (OA) and osteoporotic group (OP). The samples have been studied using experimental tests, medical imaging obtained by micro-CT and finite element models, enabling to obtain a great deal of information regarding the mechanical behaviour of the bone. The trabecular microarchitecture strongly influences the mechanical response. The most important results obtained are the apparent modulus, the failure stress and the failure strain. After image segmentation, it was possible to generate finite element models and study the morphometry of the specimens. The numerical models have made it possible to estimate the properties at the tissue level: the Young's modulus at the tissue level and the yield and failure strains. The results revealed that at the tissue level, Young's modulus does not vary appreciably, even if the bone shows bone pathology. A similar yield behaviour is observed for all groups, with differences only in the final failure strain.

The morphometry study has enabled to analyse the morphometric parameters that differentiate between healthy and diseased specimens and even to differentiate between different pathologies. The morphometric parameters have been correlated with the mechanical response in order to analyse those that have the most significant influence on the mechanical response. The correlations obtained make it possible to estimate the mechanical response of trabecular bone using micro-CT images without the need for experimental tests. The parameters obtained from the mechanical response have also been related. These relationships permit to know the behaviour of each of the samples, which is different depending on the disease they suffer.

Finally, bioinspired samples and minimal surface area triple periodic structures (TPMS) obtained by additive manufacturing have been studied. These bioinspired samples are made of polylactic acid (PLA) as the printing material. The samples show a similar orthotropic behaviour to the trabecular samples. These simulants can be used for pre-studies when bone samples are not available. The treatment of large bone fractures requires unconventional techniques for bone fixation. Bone scaffolds with triple periodicity that result in equal orthotropic properties in all three orthogonal directions are often used. These systems must have bone-like stiffness in the vicinity of the defect to avoid implant loosening. To this end, a methodology has been proposed to design patient-specific bone scaffolds that allow the orthotropic mechanical properties in each direction to be calibrated according to a specific bone.

Resumen

En esta tesis, el principal objetivo es analizar el efecto de la osteoporosis en el comportamiento mecánico del hueso trabecular. El comportamiento mecánico del hueso trabecular se ha abordado desde diferentes enfoques, como son los ensayos experimentales, los modelos de elementos finitos (EF) y la imagen médica obtenida por micro-CT.

El impacto de la osteoporosis se ha estudiado en distintas escalas. En primer lugar, se ha abordado un estudio a nivel de tejido lamelar del hueso trabecular para estimar las ecuaciones que nos permitan definir las propiedades elásticas y resistentes en función de la densidad mineral ósea (DMO) y la porosidad del tejido. Estas ecuaciones inferidas en los modelos de elementos finitos permitirán estudiar el comportamiento del tejido óseo lamelar abarcando un amplio rango de porosidades y DMOs.

Se ha realizado un estudio de la estructura trabecular y del tejido lamelar utilizando un estereomicroscopio y el microscopio electrónico de barrido de emisión de campo (FESEM). Al nivel del tejido lamelar, se ha podido observar la disposición de las lamelas en distintas localizaciones, como en las trabéculas y sus intersecciones. Además, se ha podido evaluar la porosidad tisular natural y la producida por enfermedades óseas, como la osteoporosis. Toda esta información ha sido incorporada a los modelos numéricos para poder definir las propiedades en las muestras trabeculares. Las ecuaciones elásticas y resistentes estimadas consideran un comportamiento ortótropo y es posible cuantificar cómo afectan la DMO y la porosidad a estas propiedades.

Por otro lado, se ha estudiado el comportamiento mecánico a compresión de muestras humanas de hueso trabecular procedente de cabezas femorales. Estas muestras se han clasificado en tres grupos de estudio: grupo sano (HG), grupo artrósico (OA) y grupo osteoporótico (OP). Estas muestras se han estudiado mediante ensayos experimentales, imagen médica obtenida por micro-CT y modelos de elementos finitos, permitiendo obtener gran información sobre el comportamiento mecánico del hueso. La respuesta mecánica está fuertemente influenciada por la microarquitectura trabecular. Los resultados obtenidos más importantes son el módulo aparente, la tensión de fallo y la deformación de fallo. Tras la segmentación de imagen, se han podido generar modelos de elementos finitos y estudiar la morfometría de las muestras. Los modelos numéricos han permitido estimar las propiedades a nivel de tejido: el módulo de Young a nivel de tejido y las deformaciones de fluencia y de fallo. Los resultados han revelado que a nivel de tejido no se aprecian variaciones en el módulo de Young aunque el hueso presente una patología ósea. Un comportamiento de fluencia similar se ha observado para todos los grupos, con diferencias únicamente en la deformación de fallo.

El estudio de la morfometría ha permitido analizar los parámetros morfométricos que diferencian las muestras sanas de las enfermas, e incluso a diferenciar entre diferentes patologías. Se han correlacionado los parámetros morfométricos con la respuesta mecánica para analizar aquellos que tienen mayor influencia sobre la respuesta mecánica. Las correlaciones obtenidas permiten estimar la respuesta mecánica del hueso trabecular utilizando las imágenes micro-CT sin necesidad de realizar ensayos experimentales. Los parámetros obtenidos de la respuesta mecánica también se han relacionado entre sí. Estas relaciones permiten conocer el comportamiento de cada una de las muestras que es diferente según la enfermedad que padecen.

Finalmente, se han estudiado muestras bioinspiradas y estructuras triplemente periódicas de mínima superficie (TPMS) obtenidas mediante fabricación aditiva. Estas muestras bioinspiradas se han fabricado con ácido poliláctico (PLA) como material de impresión. Las muestras bioinspiradas muestran un comportamiento ortótropo igual que las muestras trabeculares. Estos simulantes pueden ser utilizados para hacer estudios previos cuando no se disponga de las muestras óseas. El tratamiento de fracturas óseas de gran tamaño requiere de técnicas no convencionales para la fijación del hueso. Suelen utilizarse andamios óseos con triple periodicidad que tienen como resultado propiedades ortótropas iguales en las tres direcciones ortogonales. Estos sistemas deben disponer de rigideces similares al hueso en la vecindad del defecto para evitar el aflojamiento del implante. Con este objetivo, se ha propuesto una metodología

que permite diseñar andamios óseos paciente-específicos que permiten ajustar las propiedades mecánicas ortótropas en cada dirección en función del hueso.

Resum

En esta tesi, el principal objectiu és analitzar l'efecte de l'osteoporosi en el comportament mecànic de l'os trabecular. El comportament mecànic de l'os trabecular s'ha abordat des de diferents plantejaments, com són els assajos experimentals, els models d'elements finits (EF) i la imatge mèdica obtinguda per micro-CT.

L'impacte de l'osteoporosi s'ha estudiat en diferents escales. En primer lloc, s'ha abordat un estudi a nivell de teixit lamellar de l'os trabecular per a estimar les equacions que ens permeten definir les propietats elàstiques i resistents en funció de la densitat mineral òssia (DMO) i la porositat del teixit. Estes equacions inferides en els models d'elements finits permetran estudiar el comportament del teixit ossi lamel·lar abastant un ampli rang de porositats i DMOs.

S'ha realitzat un estudi de l'estructura trabecular i del teixit lamel·lar utilitzant un estereomicroscopi i el microscopi electrònic de rastreig d'emissió de camp (FESEM). Al nivell del teixit lamel·lar, s'ha pogut observar la disposició de les lamel·les en diferents localitzacions, com en les trabècules i les seues interseccions. A més, s'ha pogut avaluar la porositat tissular natural i la produïda per malalties òssies, com l'osteoporosi. Tota esta informació ha sigut incorporada als models numèrics per a poder definir les propietats en les mostres trabeculars. Les equacions elàstiques i resistents estimades consideren un comportament ortòtrop i és possible quantificar com afecten la DMO i la porositat a estes propietats.

D'altra banda, s'ha estudiat el comportament mecànic a compressió de mostres humanes d'os trabecular procedent de caps femorals. Estes mostres s'han classificat en tres grups d'estudi: grup sa (HG), grup artròsic (OA) i grup osteoporòtic (OP). Estes mostres s'han estudiat mitjançant assajos experimentals, imatge mèdica obtinguda per micro-CT i models d'elements finits, permetent obtindre gran informació sobre el comportament mecànic de l'os. La resposta mecànica està fortament influenciada per la microarquitectura trabecular. Els resultats obtinguts més importants són el mòdul aparent, la tensió de fallada i la deformació de fallada. Després de la segmentació d'imatge, s'han pogut generar models d'elements finits i estudiar la morfometria de les mostres. Els models numèrics han permés estimar les propietats a nivell de teixit: el mòdul de Young a nivell de teixit i les deformacions de fluència i de fallada. Els resultats han revelat que a nivell de teixit no s'aprecien variacions en el mòdul de Young encara que l'os present una patologia òssia. Un comportament de fluència similar s'ha observat per a tots els grups, amb diferències únicament en la deformació de fallada.

L'estudi de la morfometria ha permés analitzar els paràmetres morfomètrics que diferencien les mostres sanes de les malaltes, i fins i tot a diferenciar entre diferents patologies. S'han correlacionat els paràmetres morfomètrics amb la resposta mecànica per a analitzar aquells que tenen major influència sobre la resposta mecànica. Les correlacions obtingudes permeten estimar la resposta mecànica de l'os trabecular utilitzant les imatges micro-CT sense necessitat de realitzar assajos experimentals. Els paràmetres obtinguts de la resposta mecànica també s'han relacionat entre si. Estes relacions permeten conéixer el comportament de cadascuna de les mostres que és diferent segons la malaltia que patixen.

Finalment, s'han estudiat mostres bioinspirades i estructures triplement periòdiques de mínima superfície (TPMS) obtingudes mitjançant fabricació additiva. Estes mostres bioinspirades s'han fabricat amb àcid polilàctic (PLA) com a material d'impressió. Les mostres bioinspirades mostren un comportament ortòtrop igual que les mostres trabeculars. Estos simulants poden ser utilitzats per a fer estudis previs quan no es dispose de les mostres òssies. El tractament de fractures òssies de gran grandària requerix de tècniques no convencionals per a la fixació de l'os. Solen utilitzar-se bastides òssies amb triple periodicitat que tenen com a resultat propietats ortòtropes iguals en les tres direccions ortogonals. Estos sistemes han de disposar de rigideses similars a l'os en el veïnatge del defecte per a evitar l'afluixament de l'implant. Amb este objectiu, s'ha proposat una metodologia que permet dissenyar bastides òssies

pacient-específics que permeten ajustar les propietats mecàniques ortòtropes en cada direcció en funció de l'os.

Contents

Chapter 1

Introduction

1.1 Motivation

Nowadays, life expectancy has increased significantly. As a result, we have an ageing population. For this reason, this part of society has to deal with age-related pathologies, such as bone diseases. Some of the most frequent bone diseases are rheumatoid arthritis [1], arthrosis [2], arthritis [3], and the most prevalent in society, osteoporosis [4–6]. Many of these illnesses cause different changes in bone integrity and structure, triggering a greater fragility and an increased likelihood of undergoing a bone fracture.

Osteoporosis is a public health concern because it affects more than 200 million people worldwide, and approximately 30 % to 50 % of the postmenopausal women suffer from this disease [7]. By 2025, an estimated 13.5 million fractures due to osteoporosis will occur worldwide, and 500 million people will be living with osteoporosis. One in two women and one in five men over the age of 50 will undergo an osteoporotic fracture in their lifetime, often leading to chronic pain, loss of mobility, reduced independence, and in the worst case, mortality. Even though only 20 % of people who have undergone an osteoporotic fracture are diagnosed with this pathology [8, 9]. All these reasons reinforce the need to study the mechanical behaviour of bone, which can detect bone diseases in early stages and treat patients before bone fractures account.

In addition, osteoporosis is characterised by loss of bone mass due to the negative balance of bone remodelling cycling, in which bone material is removed faster than new bone is deposited [10]. The imbalance produced in bone remodelling process results from metabolic changes. This bone mass loss implies weakening of bone structure by decreasing trabecular thickness, increasing bone porosity, and in rapid osteoporosis, excess bone tissue is removed, resulting in a so-called osteoclastic perforation [11, 12].

The main clinical procedure to predict osteoporosis is using dual-energy X-ray absorptiometry (DXA) scanning and measuring bone mineral density (BMD) to obtain the so-called T-score [13]. Three levels are defined for assessing bone state: normal bone density, low bone mass (usually diagnosed as osteopenia), and finally, osteoporosis. These stages are defined by a range of T-score values: from -2.5 to lower values it is established as osteoporotic bone, between -2.5 to -1.0 is the so-called osteopenia, and from -1.0 to higher values is the normal bone [14]. The usual body location for taking these measurements is the femoral neck and the lower back. However, this procedure has several problems, such as the points selected for measuring. The values measured may not represent the behaviour of the region [15, 16]. Due to the trabecular heterogeneity, the bone state estimation may be imprecise. Besides, some risk factors will promote the development of osteoporosis, such as low D vitamin, alcohol, smoking, some metabolic diseases, or some drugs [17]. Furthermore, the measured values are not able to detect if bone architecture has developed a degeneration which affects its stiffness. Thus, DXA and densitometry may need to improve their accuracy, including morphometry information, to better diagnose osteoporosis [18, 19]. Many osteoporosis patients do not have any symptoms, so until the bone fracture occurs, they do not know they suffer from this disease. For this reason, osteoporosis is the so-called "silent epidemic".

All this information has encouraged the study of bone morphometry to understand bone architecture changes and deeper into the diseased bone mechanic behaviour. Many researchers have focused their work on studying morphometric parameters of bone or the relationship between bone structure and stiffness, such as Ding and Overgaard [20, 21]. Furthermore, some others have gone further down to local morphometry, the decomposition of cancellous bone into rods and plates such as Müller, Stauber or Nazarian [22–24] and its influence on bone stiffness.

One essential tool to analyse bone mechanics is using numerical methods such as the finite element method (FEM). Numerical models allow the simulation of a wide range of situations, such as studying different load cases, characterizing the mechanical behavior of bone, reproducing bone remodelling in

a fracture [25, 26] or analyzing a treatment's evolution [27]. Thanks to this non-destructive methodology, it is possible to carry out studies with different casuistry without the need to perform several experimental tests or the lack of having a large number of samples. On the other side, as it is known, bone has a hierarchical structure [28]. Thus, for its study, it is necessary to analyse its behaviour at different scales [29–31]. Numerical models have enabled this research at different scale lengths of bone structure using homogenization methods. It is crucial to analyse the structure and definition of bone at lower scales, such as nanoscale or microscale, to understand fracture mechanisms and the mechanical response of bone.

In the last decades, owing to the upswing of additive manufacturing (AM) [32], the development of patient-specific implants has opened up a wide field of study. The broad range of techniques and materials offered by AM enables the manufacturing of complicated geometrical implants. Scaffolds are the preferred structure to fill the gap produced by a bone defect, usually a fracture, and promote bone remodelling of the tissue surrounding the implant, thus, healing the bone. However, in recent years, triply periodic minimal surface (TPMS) structures have gained prominence because of the advantages they offer over scaffolds, such as less stress concentrators, large surface area to volume ratio, the diffusion of oxygen, nutrients and metabolic waste, resulting in an adequate cellular growth and proliferation of new cells [33]. Furthermore, Computer Aided Design (CAD) and AM permit the design and manufacture of patient-specific implants with complex geometries that perfectly suit the bone defect, enhancing the healing process. Lastly, finite element models allow to carry out numerical analysis to obtain preliminary results and make possible changes to achieve the optimal implant for the patient before the manufacture. These numerical analyses avoid the waste of material and time that destructive test will trigger [34, 35].

Finally, for all those mentioned above, studying and characterising cancellous bone at its different scale length levels enhances the diagnosis, enables the treatment of patients, and improves the assessment of the mechanical behaviour of bone. In order to achieve this, it is essential to study collagen fibrils orientation, tissue organisation, cancellous bone architecture through imaging techniques and morphometric study, and bone response by carrying out experimental tests. Furthermore, studying different cancellous bone samples with several bone diseases will improve the knowledge of bone mechanical behaviour. Besides, future bone fractures due to this type of diseases, which affect a large part of the ageing society, can be prevented.

1.2 Aims

The main objective of this thesis is to study the mechanical behaviour of osteoporotic cancellous bone. Specifically, the aim is to evaluate changes in both morphometry and mechanical response due to bone's pathological state: healthy, osteoporotic, or osteoarthrosic. To this end, a multi-scale approach is addressed, starting at the lamellar tissue level by obtaining the elastic properties and strength limits as a function of bone mineral density (BMD) and microporosity. Three types of bone, osteoporotic, osteoarthrosic, and healthy, are evaluated to analyse the differences in both strength and mechanical properties. This study is addressed from different approaches: mechanical, morphometric and imaging.

First of all, the mechanical characterisation is reached through the following approaches: finite element modeling, experimental testing, and medical images. Furthermore, the morphometric study is achieved by analysing micro-CT images from osteoporotic, osteoarthrosic, and healthy cancellous bone from human femoral heads. Finally, image analysis is carried out in two different microscopes: the petrographic microscope and the field emission scanning electron microscope (FESEM). Cancellous bone architecture is evaluated, and the differences between study groups are quantified. Using FESEM, it is possible to see the mineral deposition at lamellar tissue. The information obtained from the images is of great relevance to understand the orientation of collagen fibers for considering tissue anisotropy at the numerical models and making them more realistic.

On the other hand, another objective emerged when combining additive manufacturing (AM) and bone fracture. Bone surrogates and triply periodic minimal surface (TPMS) structures have been generated by fused deposition modelling using polylactic acid (PLA) for the treatment of large bone defects.

From this research, the following secondary objectives arise, presented by topic:

- Mechanical characterisation

    - To assess elastic properties and strength limits as a function of bone mineral density (BMD) and microporosity for lamellar tissue.

    - To study and compare the mechanical behaviour of osteoporotic, osteoarthrosic and healthy cancellous bone samples extracted from human femoral heads.

– To assess the microarchitecture of cancellous bone and its changes due to pathology.

– To analyse failure models for different types of cancelous bone (osteoporotic, osteoarthrosic and healthy).

• Image analysis

– To study and compare morphometric parameters between healthy and diseased cancellous bone.

– To evaluate the influence of morphometric parameters in cancellous bone mechanical properties.

– To analyse cancellous bone microarchitecture and bone mineral deposition in order to know how to define the tissue mechanical properties in the finite element models.

– To obtain images from FESEM which show the different bone structure of the studied bone types and microporosity.

– To use micro-computed tomography (μ-CT) images to characterise osteoporotic, osteoarthrosic and healthy cancellous bone morphometry.

• Additive manufacturing (AM)

– To use fused modelling deposition (FDM) to obtain bone surrogates and TPMS samples to evaluate them as bone replacements.

– To study the behaviour of bone surrogates and TPMS and compare it with cancellous bone.

– To calibrate the mechanical properties of polylactic acid (PLA) and compare them with cancellous bone properties.

1.3   Thesis organisation

The content of this PhD thesis is organised as follows:

Chapter 1 contains the introduction of the thesis. This chapter includes the motivation behind the research that has led to this thesis. Furthermore, the objectives of this study are presented and finally, the organisation of the content of this thesis is detailed in this chapter.

Chapter 2 consists of a thorough review of the state of the art of the topics covered in this thesis. The content of this chapter is mainly about bone tissue, osteoporosis, numerical modelling of bone, experimental and morphometric characterisation of cancellous bone, and imaging techniques for bone characterisation.

Including bone tissue properties in the numerical models at the micro-scale is one of the main novelty of this thesis. For this reason, the hierarchical levels of bone structure, the orientation of the mineral collagen fibers, the porosity of bone tissue, and its elastic and strength properties are studied. In addition, this chapter presents the different methods used for studying and evaluating bone mechanics, such as finite element models, experimental tests, imaging techniques, and bone morphometry itself.

Chapter 3 deals with image analysis of the lamellar tissue. Two different microscopes have been employed for studying lamellar tissue: the petrographic microscope and the field emission scanning electron microscope (FESEM). Furthermore, the obtained images have been used to analyse the collagen fibrils' orientation, mainly in the struts of the lamellar tissue. The aim is to be able to define the lamellar tissue properties as realistic as possible in the finite element models, where information about the orientation of the collagen fibrils is essential.

Chapter 4 presents the explicit expressions for the estimation of the elastic constants of lamellar bone as a function of bone mineral density (BMD) and microporosity. Lamellar tissue has natural porosity, which is important to be considered to estimate both elastic and strength properties. Moreover, when bone has some diseases, such as osteoporosis with osteoclastic perforation, this porosity becomes more important because the holes it leaves in bone tissue are of larger dimensions.

Chapter 5 provides the strength limits of lamellar bone as a function of bone mineral density (BMD) and porosity. The cavities in the bone tissue will decrease the strength properties, so it is important to consider them.

Chapter 6 contains the experimental and numerical characterisation of the mechanical behaviour of osteoporotic, osteoarthrosic, and healthy cancellous bone samples. Experimental tests under quasi-static compressive loads have been carried out. Finite element models have been generated to estimate bone tissue elastic and failure properties as a function of the pathology.

Chapter 7 presents the surrogates of cancellous bone, which have been obtained by additive manufacturing. These surrogates have been produced by fused deposition modelling (FDM), which is the technology of 3D printers. Polylactic acid (PLA) has been chosen as a manufacturing material. Experimental tests under quasi-static compression loads have been performed, and numerical models have been generated to calibrate the elasticity and failure in the micro-scale numerical models. The aim of this study is to evaluate the potential use of these surrogates as prostheses for the treatment of large bone defects or fractures that cannot be fixed using conventional methods.

Chapter 8 states the thesis conclusions and the main contributions that have been achieved.

Finally, chapter 9 presents the future works that have arisen from the research of this thesis.

Chapter 2

State of the art

This chapter presents the review of the state of the art about cancellous bone mechanical and morphometric characterisation. Different approaches have been used to assess cancellous bone in this thesis, so their foundations are presented in this section. On the other hand, bone diseases such as osteoporosis and osteoarthrosis have been explained in detail in order to understand how they affect bone mechanical behaviour.

2.1 Hierarchical structure of bone

Bone is the primary component of the skeletal system. It plays a crucial role in the body, both in terms of biomechanics and metabolism. The main functions performed by the skeletal system are the following: to preserve the body shape, to protect soft tissues and vital organs, exercising as a reservoir for ions and calcium, and to transfer the strength of muscle contraction while motioning [28, 36]. Furthermore, bone exhibits persistent structural adaptation in response to external mechanical and chemical stimuli. It grows in the direction that endures significant stress levels, thereby adjusting its micro-architecture to accommodate the imposed loads. Moreover, it possesses regenerative and healing properties that facilitate repairing microcracks and fractures [30]. Bone is considered an optimized material due to the ability to

grow and remove or deposit bone exclusively where it is needed using as little material as possible.

2.1.1   Introduction to hierarchical levels of the bones structure

Bone is arranged in a hierarchical structure, which greatly provides high mechanical properties such as strength, toughness, stiffness, lightweight, and energy absorption [30]. With the purpose of comprehending bone mechanical properties, it is required to know and understand the behaviour, components, and properties at each different level and the relationship between them [37, 38]. Bone is organised in the following scales, usually ranging between 4 to 7 levels [39], starting from the highest level to the smallest, such as Figure 2.1 shows: macroscale, mesoscale, microscale, sub-microscale, and nanoscale.
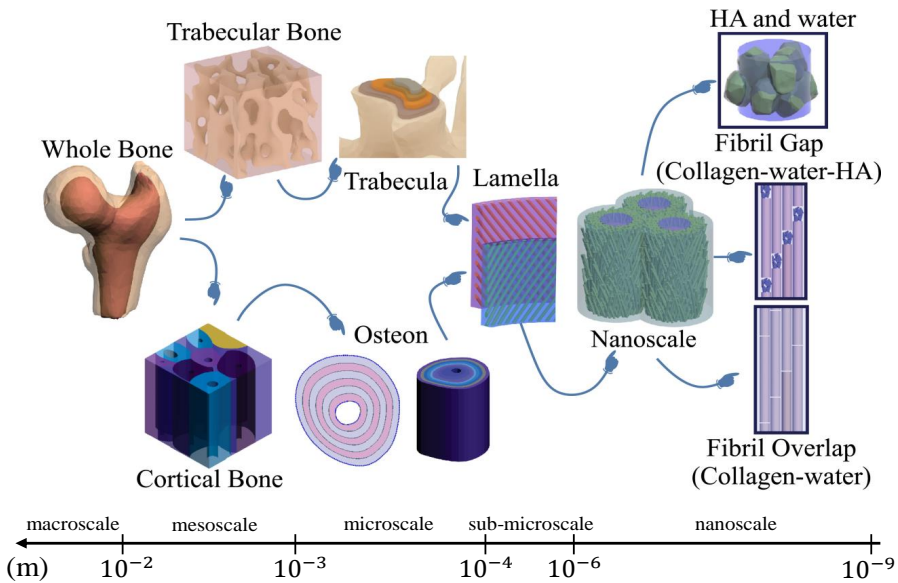
Figure 2.1: Hierarchical structure of bone. Image extracted from [40].

The upper scale level of bone is the macroscale, which corresponds to the whole bone, also known as the organ-scale level. Long bones, such as the tibia, humerus and femur, present the classical model of the macroscopic structure of bone. A typical long bone in adult anatomy is composed of a centrally located cylindrical shaft known as the diaphysis, accompanied by two wider

and rounded ends referred to as the epiphyses, as it is shown in Figure 2.2. In addition, the region that connects the epiphysis with the diaphysis in long bones is called the metaphysis. The diaphysis primarily consists of cortical bone, whereas the metaphysis and epiphysis are mainly composed of cancellous bone with a slim shell of cortical bone.
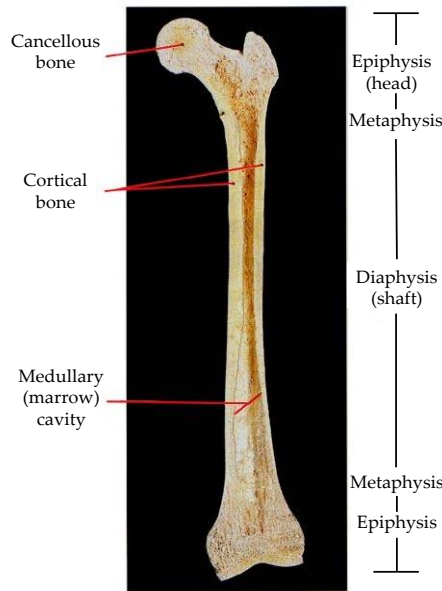
Figure 2.2: Macroscopic structure of long bones presented in a femur. Image extracted from [41].

At the following scale level, the mesoscale, the main components are cortical and cancellous bone. In a human adult skeleton, roughly 80 % of the skeletal mass is cortical bone. This type of bone is solid mass, dense, and it is present in the outer walls of bones. The most important roles that cortical bone performs are the protective and the supportive functions of the skeleton. Conversely, the amount of cancellous bone in the skeleton is only 20 %. This bone, also recognised as trabecular bone, is formed by a lattice of plates and rods known as trabeculae located within the internal regions of bones [36].

At the microscale, different structures are found depending on the type of bone. At this level, cortical bone is formed by secondary osteons embedded in an interstitial matrix consisting of highly mineralised older osteons. In secondary osteons, the lamellae are organised into concentric cylinders. The diameter of the osteons ranges between 200 - 300 μm and various millimeters long, aligned

with the long axis of the bone. The secondary osteon is primarily composed of the Haversian canal (Figure 2.3), through which the blood vessels pass. Regarding cancellous bone, the lamellae are arranged along the trabeculae principal direction, forming structures known as hemiosteons. Cancellous bone has no Harvesian canal; instead, the trabecular framework harbours marrow cavities. Furthermore, at the sub-microscale, the lamellae, which form osteons of trabeculae, are presented. These lamellae consist of mineralised collagen fibrils which are arranged into sheet structures with dimensions around 3-7 μm [28, 30]. At the lamellar tissue level, both cortical and cancellous bone present bone cells called osteocytes. These cells live in ellipsoidal cavities known as lacunae, and they will be empty when the cells die. All the osteocytes are interconnected through the canaliculi system, as it is illustrated in Figure 2.3. The structure of the lamellae is shared by both cortical and cancellous bone. Owing to this PhD thesis is developed around cancellous bone and lamellar tissue, both are widely explained in the next section.

Haversian canal

Osteocyte
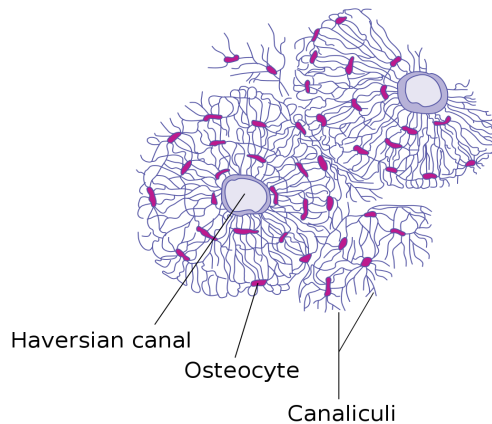
Canaliculi

Figure 2.3: Diagram of the canaliculi network which interconnect osteocytes in secondary osteons. Image extracted from [42].

Finally, at the nanoscale, bone is composed of three main components: water, calcium phosphate mineral in hydroxyapatite (HA) platelets form, and an organic matrix, predominantly collagen type I. The role of the inorganic components of bone is to provide compression strength and stiffness, while the organic components supply tension properties.

2.1.2 Cancellous bone and lamellar tissue structure, features and properties

Cancellous bone is a highly porous and heterogeneous material with varying material properties [24], mainly found at the epiphysis and metaphysis of long bones and in the vertebral bodies. Its microarchitecture mainly consists of a framework of struts and, in some cases, such as in vertebrae, also plates (Figure 2.4 a). Adult bone tissues, both cortical and cancellous, are laminated at the microscale [43]. The tissue arranged at these layers is the so-called lamellar bone tissue, being the mineralised collagen fibrils its main constituent. Consequently, strength and stiffness properties of lamellar tissue are essential to analyse the mechanical behavior of bone at the meso and macro-scale. In the lamellar tissue, mineralised fibre bundles, embedded in the extra-fibrilar matrix, confer a predominant orthotropic symmetry [44–46] leading to an anisotropic behavior under generic multi-axial loading.

On the other hand, the mineral content and the porosity at the lamellar tissue level (microporosity) are two essential parameters related to bone mechanics behavior. It is well known that an increase in the volumetric bone mineral density (BMD) has a direct implication on the rise of stiffness and, if it is excessive (i.e. due to the absence of bone resorption in the bone remodelling process) the tissue will become more brittle [47–50].

Regarding the microporosity, it also contributes to decrease the mechanical response of bone tissue. Porosity possesses a strong influence on the strength and stiffness of bone. These mechanical properties vary inversely with increasing porosity [48, 49]. Several agents contribute to the microporosity increase [51]: old age, estrogen deficiency in post-menopausal women, glucocorticoids and immobilization. In addition, when a rapid bone loss is prevalent (commonly after menopause), depth cavities may occur due to an excessive osteoclastic resorption leading to the trabecular bone perforation of structural elements, causing the loss of the structural continuity [52]. Osteoclastic perforation was also observed by Mosekilde [53] in a scanning electron microscope study of the remodelling process of vertebral trabecular bone. In Gentzsch *et al.* work [54], two types of resorption lacunae in trabecular bone were observed. Moreover, lacunar and tunnelling perforation are distinguished denoting microstructural changes related to disturbed bone remodelling. Advances in computer tomography techniques have shown that porosity is responsible for a substantial amount of bone loss and consequently, the resultant higher bone fragility and mechanical competence deterioration.

Concerning microporosity, Martínez-Reina *et al.* [44] studied the three main natural sources that contribute to the formation of tissue porosity in cortical bone (some sources are shown in Figure 2.4 b), which are presented in the following equation:

$$P_{tissue} = P_{lac} + P_{can} + P_{vas} \tag{2.1}$$

where P_{lac} is the porosity due to the lacunae, that are small ellipsoids with approximate diameters of $4 \times 9 \times 22$ μm [55] that contain bone cells (osteocytes). P_{can} represents the porosity due to the canaliculli, which are very fine channels radiating from the lacunae. They both constitute the lacunocanalicular system that produces a porosity of about 5 % [56]. P_{vas} denotes the vascular porosity that is mainly due to Havers' canals that run the length of osteons together with Volkmann canals and its evaluation depends on the bone remodelling activity. Following the work of Martínez-Reina *et al.* [44], vascular porosity could vary between 1 and 20 %. Consequently, the total porosity for lamellar tissue in cortical bone varies between 6 and 25 %. In Equation 2.1, the collagen-apatite porosity has been neglected.
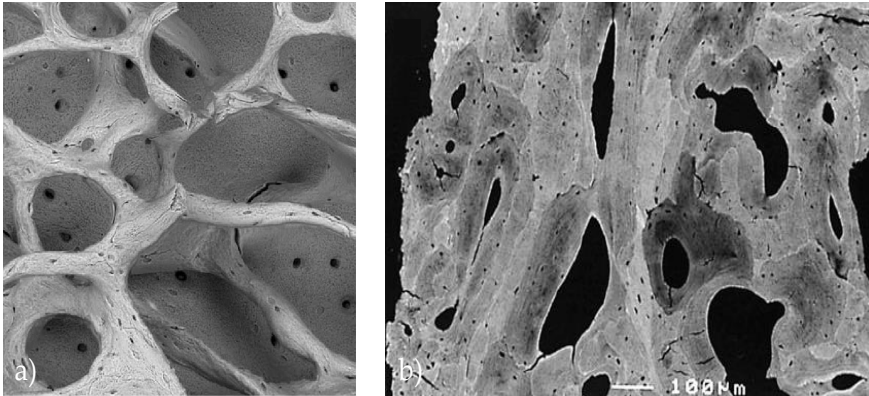
Figure 2.4: a) Trabecular bone architecture in the distal femur of 14-week old wild-type mouse evaluated with backscattered electrons in a scanning electron microscope (BSE SEM) (field width 584 microns), image extracted from [57], and b) backscattered electron imaging of a polished human cortice with various gray levels depending on their mineralisation degree, image extracted from [58].

Regarding the porosity of lamellar tissue in trabecular bone, lacunocanalicular system is also present in the trabecular packets or hemiosteons of cancellous bone. For this term, the same porosity value than in cortical bone is assumed (up to 5 %). With respect to the variable P_{vas}, the marrow cavity harbours the vascularization in trabecular bone, instead of Havers' canals, however, this term is also associated with bone turnover activity. For trabecular bone, no reference value has been found in the literature quantifying the microporosity due to the osteoclastic perforation.

By other side, the non-isotropic nature of lamellar tissue is also a relevant aspect to be included in the quantification of bone mechanical properties. In the review of biomechanics and mechanobiology of trabecular bone presented in Oftadeh *et al.* [59], it is stated that at the microstructural scale, trabeculae consist of groups of parallel lamellae bounded by cement lines primarily oriented also parallel to the trabecular surfaces. In addition, the three-dimensional ultrastructure bone arrangement in relation to the local trabecular direction is analyzed in Georgiadis *et al.* [60]. They state that bone ultrastructure is mostly aligned to trabecular microstructure near trabecular surface. However, when going towards trabecular core, the ultrastructure alignment decreases to around 40 %.

Cancellous tissue was characterised as a microstructure consisting of layers interspaced with transition zones where the proportions of collagen and mineral vary [61]. Hosaki-Takamiya *et al.* [62] observed that collagen bundles in trabecular bone run along the long axis of the trabecula. In Hammond *et al.* work [63], the filbril orientation is addressed in a numerical model of trabecular bone.

In the study presented by Haj-Ali *et al.* [64], a three-dimensional multiscale micromechanical model, where the lamellar tissue is modelled as a multilayered laminate, is suggested. The mineralised collagen fibrils follow a determined angular orientation pattern. That work deals with the linear anisotropic mechanical properties of the cancellous bone while no strength analysis is performed. Some other researchers, such as Hellmich, have developed multiscale approaches to study the hierarchical levels of bone. Fritsch and Hellmich [65] reinforced the importance of understanding the microstructural patterns in bone materials. They introduced a multiscale homogenisation scheme that quantifies the mechanical interaction of bone components, such as hydroxyapatite, collagen and water. They provided effective elastic properties of bone materials at different scales, from nanometers to millimetres. In further works, Colloca *et al.* [66] developed a multiscale analytical approach for bone remodelling simulations, connecting scales from collagen to trabeculae. The

main goal of this research was to predict changes in bone properties due to remodelling activities.

In the literature several references are found that reveal the importance of considering the tissue properties in the trabecular bone numerical models, when the mechanical competence of bone is under study. Hammond *et al.* [67] state that, only when the tissue anisotropy is considered in their numerical models, the shape and distributed microcracking typically observed in trabecular bone are reproduced. In Hammond and collegues work [63], the effect of tissue properties on the predicted stresses and strains is observed. This improves the correlation between the solution from numerical models with experimental data. For example, material heterogeneity seems to play an important role in resisting bone damage under cyclic loads with long service lives [68]. In addition, in Renders *et al.* [69], the authors demonstrate that the no consideration of the mineralisation heterogeneity overestimates the apparent Young's moduli.

2.1.3   Mechanical behaviour of bone

As aforementioned, bone tissue is an anisotropic, inhomogeneous and composite material, whose properties are strongly influenced by its hierarchical structure. Furthermore, morphological parameters and the proportion of bone components can vary from each person, from each anatomical site, and sometimes even though within the same bone. All these features make a challenging assessment of bone's elastic and failure properties. At the elastic range, bone behaves as a viscoelastic material, whose viscous response is due to the fluids in the bone matrix [70].

The analyses are usually carried out under quasi-static loads, which hypothesize a perfect elastic behaviour until reaching the yield point [71,72]. Throughout the elastic range, the deformations are reversible until the yield point; hereafter, permanent damage occurs, and deformations remain at the specimen. The characteristic response obtained from the bone analyses is the force-displacement curve, whose slope at the elastic domain corresponds to the stiffness or rigidity of the specimen. These results are analogous to the stress-strain response, whose slope is known as the Young's modulus. It is essential to distinguish between the apparent Young's modulus, which is influenced by the microarchitecture of the sample, density, and elastic properties, and Young's modulus of the material, which is an inherent property of the bone tissue.

After the yield point, some microcracks appear in the elastic-continuum damage mechanics domain, which is the post-yielding behaviour. If the load is still applied, fractures would be developed mainly on the bone surface [73]. Bone has different behaviour when subjected to tensile or compression loads. On the one hand, under tensile conditions behaves more brittle, and the yield point and fracture are achieved at a lower stress level [74]. On the other hand, when bone is subjected to compression loads, its behaviour is more ductile, and the tendency of the fracture sections is to densify, then it is able to continue bearing more load level. Moreover, the strain rate influences cancellous bone stiffness and strength properties. Increased strain rates due to cancellous bone viscoelasticity lead to higher stiffness, yielding, and ultimate stresses. However, no significant correlation has been reported regarding yielding and ultimate strains [75].

Furthermore, anisotropy in cancellous bone arises from a combination of its architectural features and ultrastructural organisation. Numerous studies have focused on investigating anisotropy, which exhibits spatial variability as it is influenced by bone's adaptation to external loads [36]. In their study, Keaveny *et al.* [76] introduced the concept of the strength-to-anisotropy ratio (SAR) and found that the strength of the bone varied based on the direction of loading, specifically in axial and shearing loading modes. Furthermore, the study reported an asymmetry in the strength properties under tension-compression conditions, with higher values observed for the latter loading mode.

Cyclic loading of cancellous bone leads to a decrease in stiffness, which can be attributed to the development of microcracks at various length scales [70]. For instance, the occurrence of non-traumatic vertebral failure is believed to be influenced by the progressive accumulation of damage caused by cyclic loading. The fatigue behavior of cancellous bone can be divided into three distinct regions. In the first region, there is a rapid decline in stiffness accompanied by the formation of localized microcracks, typically occurring within a low number of loading cycles. The second region involves toughening mechanisms such as bridging, crack deflection, or plasticity, which contribute to an increase in fatigue life while microcracks continue to grow without a significant loss of stiffness. Lastly, the third region is characterised by the coalescence of microcracks, leading to a sudden decrease in stiffness and ultimately resulting in bone fracture. Additionally, it has been documented that fatigue failure mechanisms primarily take place at the ultrastructural level rather than at larger scales, resulting in comparable accumulation of fatigue strain across different locations. Considering the continuous process of bone remodeling, it can be

inferred that the fatigue life determined through cyclic testing represents a conservative estimate of its true value [76].

Cancellous bone exhibits time-dependent failure behavior, where creep deformation leads to permanent deformation caused by sustained loads [76]. This creep deformation varies based on the type of loading and local mechanical properties. The creep deformation process can be characterised by three stages, starting when the creep rate decreases and then some relaxation occurs. Then, a consistent and constant creep rate is observed during the secondary creep stage. The final stage is associated with an increasing creep rate and the accumulation of damage, which can result in failure if the load is still applied [77]. Lastly, it is acknowledged that creep contributes to the accumulation of damage during fatigue loading [78].

Finally, it is important to consider the significant impact that has the hydration on the mechanical properties of bone. Dry samples exhibit greater modulus and strength compared to wet samples, but their toughness is reduced. Consequently, dry bones absorb less strain energy and exhibit a higher degree of brittleness compared to wet bones [70]. In addition, other essential point is the conservation methods of the bone samples because they also have a significant influence on the mechanical properties. Szebényi *et al.* [79], found that the Young modulus and compressive strength of the vertebrae were influenced less by frozen storage, making it the recommended method for the conservation of vertebrae. This literature review also suggests that strength characteristics are affected by different storage methods, but substantial discrepancies can only be observed in the case of long-term storage.

2.1.4 Elastic properties of bone

Determining the elastic properties of cancellous bone is crucial in assessing its mechanical competence and conducting thorough mechanical evaluations related to bone healing and bone-implant interactions. Two important elastic properties are the apparent Young's modulus, E_{app}, and the Young's modulus at the tissue level, E. The first parameter is associated with the stiffness of cancellous bone at a macroscale, while the second parameter represents the elastic modulus at the microscale, specifically at the lamellar bone level. These two parameters are interconnected because the tissue-level Young's modulus, combined with the lattice architecture, influences the overall stiffness observed.

Several studies have documented the elastic properties of cancellous bone in different species. These studies have explored diverse locations and method-

ologies to obtain these properties. Table 2.1 summarizes the apparent elastic properties of human cancellous bone from different locations, as reported in the literature.

Table 2.1: Elastic apparent modulus (E_{app}) values reported in the literature for cancellous bone from different testing methods, loading modes, species and anatomical sites. Mean and standard deviation values are presented when reported. Table taken from Belda PhD thesis [80].

E_{app} [MPa]	Test method	Specie	Site	Conditions	Ref.
1538 ± 674	Compression	Human*	Femoral head	Wet	[81]
3230 ± 936 2700 ± 772	Compression Tension	Human	Femoral neck	Wet	[82]
356 310 247	Compression	Human** Human*** Human*	Femoral head	Wet	[83]
1359.6 ± 1135.7 1493.7 ± 1226.4	Compression Nanoindentation - FE	Human	Femur	Dry	[84]
622 ± 302 597 ± 330	Compression Tension	Human	Trochanter	Wet	[82]
344 ± 148 349 ± 133	Compression Tension	Human	Vertebra	Wet	[82]
99 ± 38.5	Compression	Human	Vertebra	Wet	[85]
276 231	Tension Compression	Human	Vertebra	Wet	[86]
1091 ± 634 1068 ± 840	Compression Tension	Human	Tibia	Wet	[82]
428 ± 227.8	Compression	Human	Tibia	Dry	[87]
689 ± 438 871 ± 581	Compression Optical extensometer	Human	Tibia	Wet	[88]

* Osteoporotic
** Osteoarthritis
*** Normal

The measurements are typically conducted along the primary direction of trabecular orientation, and the apparent properties are commonly evaluated through axial testing conducted under quasi-static conditions. In certain instances, experiments involving optical extensometers, finite elements, or nanoindentation are employed. For instance, Odgaard and Linde's work [88] has conducted a comparison between compression testing and the use of an optical extensometer. They discovered that the latter method yielded higher estimations due to lower displacement measurements. Conversely, Chevalier *et al.* [84] compared the effectiveness of compression tests with a combination of finite element models based on micro-CT, where the properties were defined

through nanoindentation. The authors obtained similar estimations, but the finite element models tended to overestimate the elastic modulus.

The literature presents a wide range of apparent modulus values for cancellous bone, which can be attributed to specimen conditions and location variations, as indicated in Table 2.1. Most measurements listed in Table 2.1 pertain to experiments conducted under wet conditions, and no clear distinction is observed when compared to measurements conducted under dry conditions. Theoretically, it would be expected higher modulus values from measurements performed under dry conditions [70].

In Li and Aspden's study [83], they observed differences in metrics among normal, osteoarthritic, and osteoporotic cancellous bone. Consistent with expectations, the osteoarthritic samples exhibited the highest values, followed by the normal and osteoporotic specimens. Regarding the elastic modulus, the femoral specimens exhibited the highest values, while the vertebral samples had the lowest values. Considering the influence of volume fraction or apparent density on the apparent properties, it is crucial to reference the results accordingly [36, 76]. The low value reported in Ladd *et al.* work [85] can be attributed to the low bone volume fraction observed in the analyzed samples, ranging between 6.8 % and 10.4 %. This trend is consistent with the findings of Morgan and Keaveny [82], who also reported similar patterns across different locations. Specifically, the vertebral specimens exhibited the lowest apparent density, which correlates with the apparent modulus, while the femoral neck showed the highest apparent density and corresponding higher modulus values.

In a recent review conducted by Wu and colleagues [89], Young's modulus of cancellous bone at the tissue level was examined. The review discusses various methods employed for this purpose and presents a summary of estimations categorized by the methods. The methods considered included ultrasonic testing, nanoindentation, micro-mechanical testing of single trabeculae, and a combination of macro-level mechanical testing and numerical models based on micro-CT images. In their comprehensive review, Wu *et al.* [89] documented a range of tissue elastic modulus values between 1.2 and 22.3 GPa. However, it is worth noting that only a few of the cited references approached the lower boundary of this range.

Table 2.2 exhibits the reported Young's modulus at the tissue level from various sources, encompassing different locations, conditions, and methods. In this review, the average values range from 2 to 20.95 GPa, indicating a significant dispersion of data. The reported values are derived from diverse

Table 2.2: Elastic modulus at the tissue level (E) reported in the literature for cancellous bone from different testing methods, loading modes, species and sites. Mean and standard deviation values are presented. Table taken from Belda PhD thesis [80].

Tissue level Young's modulus (E) [GPa]	Test method	Specie	Site	Conditions	Ref.
14.22 ± 1.07 12.25 ± 1.01	Nanoindentation	Human	Femur (inner trabeculae) Femur (outer trabeculae)	Dry	[90]
11.4 ± 5.6	Nanoindentation	Human	Femoral neck	Wet	[91]
13.5 ± 2.0	Nanoindentation	Human	Vertebra	Dry	[92]
20.95 ± 2.1	Nanoindentation	Human	Femur	Dry	[84]
11.31-15.80	Microindentation	Human	Vertebra	Dry	[93]
12.18 ± 0.8	Attenuation coefficient SR-μCT	Human	Femoral neck	Wet	[94]
18.8 ± 5.2	Compression - FE	Human*	Femoral head	Wet	[81]
18.0 ± 2.8	Compression - FE	Human	Femoral neck	Wet	[95]
6.6 ± 1.07	Compression - FE	Human	Vertebra	Wet	[85]
5.6 ± 0.2	Compression - FE	Whale	Vertebra	Wet	[96]
12.59 ± 2.13	Compression - FE	Human	Femur	-	[97]
18.7 ± 3.4	Axial - FE	Bovine	Tibia	-	[98]
16.24 ± 2.47 16.85 ± 2.1	Tension	Human** Human*	Femur	Dry	[99]
10.4 ± 3.5 14.8 ± 1.4	Microtensile Ultrasound	Human	Tibia	Dry	[100]
2.0 ± 1.0	3-point bending	Bovine	Femur	Wet	[101]
10.09 ± 2.42 11.38 ± 1.42	3-point bending	Human** Human*	Femur	Dry	[99]

* Osteoporotic
** Normal

techniques such as nanoindentation, microindentation, density-based measurements, a combination of compression testing and finite element modeling, tension tesing, ultrasound, and bending testing.

Nanoindentation testing reveals a range of elastic modulus values between 11 and 21 GPa, with lower metrics observed under wet conditions for the same location, resulting in 11.4 GPa compared to 14 or 21 GPa. Conversely, when employing a combination of compression testing and image-based finite element analysis, elastic modulus values ranging from 5.6 to 19 GPa are obtained. Some researchers argue that this methodology underestimates the values due to potential side artifacts associated with compression testing. However, many efforts have been made in certain studies to address this issue and minimize its effects [102–104]. This combination of high-resolution imaging and testing allows the estimation of the elastic properties at the tissue level and enables the analysis of stresses and strains at a local level.

Studying local effects is possible through testing single trabeculae; however, it presents challenges such as compliance effects during testing, avoiding damage caused by gripping in tension tests, and accurately estimating the cross-sectional area [70]. On the other hand, ultrasonic tests yield a reported value of approximately 15 GPa indicated in Rho *et al.* work [100], which falls within the higher range of values obtained through nanoindentation and compression-FE methodologies. Nonetheless, the presence of voids tends to attenuate ultrasonic waves, adding complexity to the application of this technique [89].

2.1.5 Strength properties of bone

The clinical importance of determining cancellous bone strength properties lies in their ability to indicate bone quality and their crucial role in developing numerical models. These models allow for the simulation of various scenarios, including multiaxial loading, implant design and validation, and evaluation of disease treatments. Simulations offer notable advantages over experiments, such as the ability to simulate destructive situations, lower costs, and the capacity to model complex loading configurations impractical to carry out experimentally. Owing to failure modeling, it is crucial to establish suitable properties based on the specific failure mode. Strength is the key property to define static failure, while fracture toughness is essential for studying crack growth. In the case of fatigue failure, fatigue strength plays a significant role.

Usually, strength properties have been evaluated primarily through experiments [36]. These experiments aim to estimate either the apparent strength properties [74,82] or the properties at the microscale by testing individual trabeculae [71, 99, 101]. The most commonly employed method for determining the yield point in experiments is the 0.2 % offset method, while the fracture point is defined as the maximum stress value observed within the stress-strain curve. Conversely, some authors have integrated experiments with digital image correlation to estimate yield properties at the level of trabecular tissue [71,99,105]. Numerous studies have sought to establish regression models based on experimental findings to estimate strength values.

Within advanced imaging techniques, image-based finite element models have emerged as a valuable tool for estimating strength properties at various length scales [95,99,101,105]. These finely discretized models consider the microstructure of specimens, enabling the estimation of local stresses and strains. This capability allows for replicating trabecular failure at the microscale and simulating apparent-level yielding and post-yielding phenomena in specimens [98]. Several finite element models have incorporated asymmetric strength proper-

ties and non-linear behavior to determine tissue yield properties [95,98]. Additionally, these finite element models validate reported failure parameter values from existing literature or obtained through independent experiments [71]. Typically, an inverse analysis criterion is employed to determine the failure properties for finite element models. This involves calibrating the model parameters to achieve a match with experimental data [99, 101]. Sometimes, the calibration process relies on a single parameter, often the yield strain or stress [97]. However, certain constitutive models may require the calibration of multiple parameters [99].

Carretta *et al.* [99] made a notable contribution by investigating tissue-level failure properties of healthy and osteoporotic human femoral cancellous bone. They achieved this by conducting single trabeculae testing under both tensile and bending conditions and employing sample imaging and finite element analysis. The authors highlighted the challenges associated with determining tissue failure properties through testing complete specimens, particularly when compared to single trabeculae testing. They emphasized the significance of having microscale properties available for use in simulations. In their study, Bevill *et al.* [106] employed a combination of testing and finite element modeling to investigate the impact of incorporating large deformations on estimating apparent yield values. Their findings indicated that the influence of including large deformations is notably significant for samples with low volume fractions. However, as the apparent densities increase, this effect diminishes.

Table 2.3 exhibits measurements of failure strains and stresses at the apparent level sourced from the literature, whereas Table 2.4 provides estimations of failure strains and stresses at the tissue level. Both tables present values for yield strains (ϵ_y) and stresses (σ_y), as well as ultimate strains (ϵ_u) and stresses (σ_u) for cancellous bone. The reported data includes information of the species, location, calculation method, loading direction, loading mode, and reference sources.

The yield values at the apparent level, as shown in Table 2.3, were determined using the 0.2 % offset method. In some instances, FE analysis was employed to validate the metrics. Yield stress values vary significantly depending on the apparent density and elastic modulus. On the other hand, the yield strains tend to remain relatively constant for a given location, loading mode, and direction. In addition, it is worth noting that higher yield strain values have been observed in compression compared to tension. In most studies, limited focus has been given to ultimate strain values. However, for human vertebral tissues, the reported values range from 1.29 % to 2.5 % in compression, while they are approximately 1.58 % in tension.

Conversely, the tissue-level yield values presented in Table 2.4 were determined through an inverse calibration process, where numerical models were adjusted to reproduce tests. These estimations were obtained using various methods, such as single trabeculae testing or a combination of stress whitening and digital image correlation. Remarkably, the latter method yielded the highest values, although it may be less accurate than other approaches. It is essential to highlight that the estimated yield strain values at the tissue level tend to be lower than those at the apparent level. The combination of high discretization and testing methods has proven effective in accurately estimating failure properties at the microscale.

Table 2.3: Failure strains and stresses measurements at the macro (apparent) level reported in the literature, resuming the estimation method, loading mode, species and anatomical site. Table taken from Belda PhD thesis [80].

ε_y [%]	σ_y [MPa]	ε_u [%]	σ_u [MPa]	Method	Loading mode	Species and site	Ref.
0.73	1.48	-	-	0.2 %	Tension	Human -	[86]
0.75	1.19	-	-		Compression	vertebra	
0.81	-	2.5	-	0.2 %	Compression	Human -	[107]
0.72	-	1.57	-		Tension	vertebra	
0.81	-	-	-	0.2 % -	Compression	Human -	[106]
0.33	-	-	-	FE	Tension	[1]*	
0.77	2.02	-	-		Compression	Human -	
0.70	1.72	-	-		Tension	Vertebra	
0.73	5.83	-	-		Compression	Human -	
0.65	4.50	-	-	0.2 %	Tension	Tibia	[82]
0.70	3.21	-	-		Compression	Human -	
0.61	2.44	-	-		Tension	Trochanter	
0.85	17.45	-	-		Compression	Human -	
0.61	10.93	-	-		Tension	Femur Neck	
0.88	14.37	-	-	0.2 %	Tension	Bovine -	[108]
1.17	21.09	-	-		Compression	Tibia	
0.62	84.9	-	-	0.2 %	Tension	Human -	[95]
1.04	135.3	-	-		Compression	Femur	
0.78	1.75	1.59	2.23	0.2 %	Tension	Human -	[74]
0.84	1.92	1.45	2.23		Compression	Vertebrae	
0.78	14.36	-	-	0.2 % -	Tension	Bovine -	[98]
1.08	20.62	-	-	FE	Compression	Tibia	
0.69	1.1	1.29	1.29	0.2 %	Compression	Human - Vertebrae	[109]
3.01	14.957	3.695	16.113	0.2 %	Compression	Whale - Vertebrae	[110]

1* The study was carried out on different locations: femur, tibia and vertebra.

Table 2.4: Failure strains and stresses measurements at the micro or tissue level reported in the literature, including the estimation method, loading mode, specie and anatomical site. Table taken from Belda PhD thesis [80].

ε_y [%]	σ_y [MPa]	ε_u [%]	σ_u [MPa]	Method	Loading mode	Specie and Site	Ref.
0.46-0.63	88-121	-	-	FE	Compression	Bovine -	[105]
0.18-0.24	35-43	-	-		Tension	Tibia	
1.6	-	12	-	σ whitening & DIC	3-point bending[2*]	Bovine - Femur	[101]
0.72	115.43	5.14	166.89	Single trabeculae testing	Tension	Human[3*] - Femur	[99]
1.45	138.67	8.2	204.98		3-p bending		
0.77	130.28	2.4	164.71		Tension	Human[4*] - Femur	
1.21	135.98	6.01	208.62		3-p bending		
0.6	-	-	-	FE - testing	Tension	Bovine - Tibia	[98]
1.01	-	-	-		Compression		
0.41	82.8	-	-	FE - testing	Tension	Human - Femur	[95]
0.83	133.6	-	-		Compression		

2* Yielding estimation in tension area
3* Healthy donors
4* Osteoporotic donors

2.1.6   Bone failure at different scales

Bones experience loads during everyday activities, and they can fail if the loads exceed a certain threshold. The imbalance between the accumulation of damage and the remodelling process is believed to contribute to bone fragility [105]. Failure can happen at various levels within the hierarchical bone structure, and it is suggested that the initial inelastic deformation of bones occurs primarily at the nanoscale.

The strength properties of trabecular bone exhibit heterogeneity, anisotropy, and asymmetry, resulting in variations depending on factors such as location, age, and the direction and loading mode, including tension, compression, and shearing [76]. Regarding loading modes, compression generally yields higher strength values, followed by tension and shearing [74, 76]. In the late 1980s, Gibson [111] employed simplified configurations of trabecular bone to elucidate the modes of compression failure in cancellous bone, which are elastic buckling or plastic hinges. Gibson established a connection between the failure mechanism and either the bone structure's slenderness or apparent density. Buckling transpired at low apparent densities, whereas plastic hinges were observed at higher density values.

Zioupos [112] carried out an analysis of the distinct stages of bone's mechanical response to compression, including the elastic phase, damage mechanics phase, and fracture mechanics phase. The author also reviewed several approaches for determining the parameters effectively describing each phase. Following the initial elastic response, Zioupos identified the damage mechanics phase, where a decrease in stiffness was attributed to the formation of microcracks. Besides, the author emphasized the significance of toughening mechanisms at different scales within a biological material. Also, Zioupos recognized the phase of fracture mechanics and examined approaches documented in the literature for estimating fracture parameters. Lastly, the author identified crack deflection and bridging as mechanisms to withstand fracture during this phase.

In a more recent study, Launey *et al.* [113] conducted a comprehensive review of the mechanisms that enhance the toughness of bone across various scales. This work provides valuable insights into the fracture behavior of bone, shedding light on how it either fractures or withstands fractures. The authors describe the fracture process as a delicate equilibrium between the loads that amplify fracture surfaces, the intrinsic mechanisms of damage occurring ahead of the crack tip, and the extrinsic shielding mechanisms occurring behind the crack tip. The extrinsic mechanisms, such as crack deflection and bridging, impact scales larger than 1 μm, whereas the intrinsic mechanisms, such as plasticity, influence scales smaller than 1 μm.

On the molecular scale, collagen undergoes deformation primarily through molecular uncoiling, which occurs due to the breaking of hydrogen bonds. This phenomenon also takes place within collagen fibrils, where the extent of cross-linking determines the capacity to dissipate energy. Higher cross-link density renders collagen more brittle, contributing to the heightened risk of fractures in the elderly population. Moving to the subsequent level, the failure mechanism involves the sliding of mineralised collagen fibrils, wherein the mineral phase enhances stiffness and energy dissipation. At the microscopic level, microcracking serves as a connection between intrinsic and extrinsic toughening mechanisms. It acts as a form of inelastic deformation and functions as a mechanism for crack bridging and deflection. The toughening mechanisms encompass crack deflection and bridging from the microscale to the macroscale. However, research on these effects has predominantly focused on osteonal systems rather than cancellous bone.

Notwithstanding the complexity involved, the mechanism of bone failure can be considered relatively simple. Failure strains exhibit minimal dependence on specimen density and remain relatively consistent for a given location, age, direction, and mode [76]. More specifically, the failure strain demonstrates a low

yet gradually increasing linear relationship with apparent density under compression, although this correlation disappears under tension [74]. On the other hand, Bayraktar *et al.* [95] found no correlation between the apparent density and apparent modulus with both compressive and tensile yield strains. However, they observe a significant linear relationship between the elastic modulus and yield stress [76, 95, 98, 102]. The fact that strain represents the ratio of stress to modulus for an elastic material under uniaxial loading implies that failure strains remain relatively constant. Additionally, it has been observed that yield strain in cancellous bone is isotropic, meaning it does not depend on the loading direction [76]. This yield strain behavior strongly suggests that strains influence and control bone failure.

In cancellous bone, failure tends to occur in localized fracture bands rather than spreading uniformly throughout the material [113, 114]. The characteristic failure behavior of bone, which concentrates damage or complete fractures in specific areas when subjected to increasing loads, adds to its fascinating nature as a material. This localized damage concentration enables optimized remodeling processes in those controlled regions. Consequently, remodelling has been theorized to be triggered by damage mechanisms resulting from alterations in the bone's ultrastructure [36, 74, 76]. Most studies on failure in cancellous bone have focused on uniaxial loading conditions, primarily because they are simpler to analyze than the more complex multiaxial loading scenarios. Damage in cancellous bone significantly impacts its apparent elastic properties, causing a decrease in these properties. If the bone is overloaded, the damage can propagate, thereby increasing the risk of fractures [115]. Damage to bone has a notable impact on its ultrastructure, and there is a hypothesis that disturbances in the canaliculi network could serve as a stimulus for bone remodeling. It has been observed that the extent of damage exhibits a strong correlation with the applied strain, indicating that higher applied strains result in more significant damage [116]. Moreover, while there is a lower but still significant association, the loading mode and direction also influence the level of damage. Nevertheless, it must be noted that damage cannot be detected through clinical radiography [107].

In order to validate the failure models put forth in existing literature, it is crucial to employ failure detection methods. Typically, the damage has been identified through the analysis of histological sections that have been previously stained [86, 105, 116]. Nevertheless, this approach is time-consuming and destructive, prompting researchers to explore alternative methodologies. Scanning electron microscopy (SEM) is frequently utilized to visualize failure at high magnification [36, 111, 114]. It enables the identification of microc-

racks and various toughening mechanisms, but its scope is limited to surface analysis and very localized areas. Alternative techniques allow failure analysis over larger areas or even entire specimens, although they generally offer lower resolution than SEM. For instance, Nagaraja [105] investigated microdamage during uniaxial testing using micro-CT, image-based finite element analysis (FEM), and histological damage labeling. These approaches provided insights into microdamage patterns and characteristics in a non-destructive manner.

Several years ago, Nazarian and Müller [110] established an imaging system that enabled simultaneous testing and scanning of specimens. This innovative approach proved valuable in uncovering the initiation and progression of fractures. The authors conducted uniaxial compression tests on vertebral whale specimens, employing micro-CT imaging at each incremental load stage. This method provided valuable insights into the behavior of the specimens during the testing process, shedding light on fracture mechanisms. Their time-lapse imaging demonstrated that failure was localized within shear bands while the surrounding structure remained unaffected. Within the failure region, the trabeculae exhibited failure through bending before undergoing complete fracture [110].

In contrast, Wang *et al.* [115] presented a technique for detecting microdamage using micro-CT. Their method involved labeling the specimens with barium sulfate (BaSO4), which exhibits higher X-ray attenuation than bone tissue. This differential attenuation allowed for the identification and visualization of microdamage within the specimens. Subsequently, the acquired images were segmented, enabling accurate microdamage detection. It should be noted, however, that the technique cannot detect individual cracks, as these become visible only at higher resolutions [115].

The stress whitening effect in cancellous bone, associated with damage, has been investigated in other studies [71, 101, 114]. Thurner *et al.* [114] demonstrated that whitening was observed when examining yielded trabeculae using high-speed photography at high magnification, and its intensity increased with the applied load. Furthermore, they successfully established a correlation between the whitening effect and microdamage, which was observed well before reaching the apparent yielding point [114]. Subsequently, Jungmann and colleagues [101] integrated the stress whitening effect identified by Thurner *et al.* [114] with Digital Image Correlation (DIC) to assess local strains, the initiation of failure and fracture strains in individual trabeculae subjected to three-point bending tests. The mean yield strain recorded was approximately 1 ± 0.5 %, whereas the average strain leading to complete failure was approximately 8 ± 5 %. The yield values obtained using DIC were at the higher end of

the range reported in previous studies, possibly due to DIC's lower resolution than the Finite Element Method (FEM) analysis.

In summary, bone failure is characterised by a reduction in stiffness during the damage mechanics phase, followed by the development of fracture surfaces in the fracture mechanics phase. The behavior of bone under failure is influenced by its hierarchical microstructure, which incorporates toughening mechanisms at various length scales. These mechanisms range from the inelastic deformation resulting from uncoiling collagen molecules or the sliding of mineralised collagen fibrils at smaller scales to crack deflection and bridging from the micro to macroscales. These deformation mechanisms occur before reaching the apparent yield point and tend to localize failure within shear bands. Moreover, the strength properties of bone exhibit heterogeneity, anisotropy, and asymmetry. Despite this intricate nature, the yield strains of bone remain relatively constant and can be considered isotropic, at microscale.

2.2 Experimental characterisation of cancellous bone

Experimental tests are a powerful approach to characterise bone behaviour. These tests offer valuable insights into its mechanical properties and can be carried out under various loading conditions across different length scales. Experimental characterisation of bone can be performed under the elastic range, allowing for several more tests with the same sample. Some other tests, such as for fracture assessment, are destructive and only can be performed once. In addition, the characterisation of these mechanical properties is essential in assessing bone integrity concerning factors such as age, disease, or pharmacological treatment.

First of all, an important aspect is the sample preparation, which is crucial in obtaining accurate measurements. During whole bone testing, the typical procedure involves removing non-bone tissues and, based on the specific testing conditions, maintaining the sample's moisture or allowing it to dry. Several studies in the literature have addressed the preparation of cancellous bone samples [91, 117, 118]. In certain instances, cylindrical-shaped specimens are prepared by using a trephine extraction technique. These specimens are then tested along their principal axis [81, 87, 97]. In some other cases, parallelepiped-shaped samples are prepared through the use of precision band saws. This allows for testing the samples along their three principal directions [96, 119, 120]. To prepare these samples, bone marrow is often removed using an ultrasonic bath and/or water jet, and the samples are subsequently

either dried or kept moist using a saline solution. Several studies have reported the evaluation of bone volume fraction using Archimedes' principle as a criterion parameter for segmenting subsequent micro-CT images [84, 95].

After preparation, it is essential to consider for performing experimental tests the suitable storage of the samples since the samples are obtained until the tests are carried out. The storage conditions have an impact on the measured mechanical properties [117, 118]. Linde and Sorensen [118] analysed the effect of different storage methods: freezing at -20°C or ethanol. Even after being stored for a period of 100 days, the elastic properties of the samples showed no significant changes regardless the storage method. Moreover, thawing and refreezing the samples did not result in notable changes in their elastic properties [117]. Nevertheless, the viscoelastic properties exhibited slight yet significant variations after being stored for 100 days in either ethanol or frozen conditions [118].

Before starting with the experimental tests, it is important to emphasize the significance of the length scale in analysis and explore the commonly employed techniques specific to each scale. The mechanical properties of bone tissue are influenced by its structural organisation, composition, microstructure, and nanostructure [91]. Consequently, bone's highly hierarchical nature determines the testing type and outcomes depending on the length scale being investigated [121]. Testing can be categorized into macroscale (organ-level), mesoscale, microscale, or nanoscale.

At the macroscale and mesoscale, the most commonly used experimental tests include axial, bending, or torsion loading, which can be applied in monotonic or cyclic loads. Additionally, fracture toughness tests are employed to assess the fracture resistance of bone specimens by introducing a sharp notch [121]. The sample's geometry and composition influence the experimental tests in organ-level testing. Each type of bone is typically tested under loading conditions that mimic its *in vivo* behavior. For instance, vertebral bodies are subjected to compression, while long bones are tested under bending or axial loading conditions. At the mesoscale, which includes cortical and cancellous bone, testing involves considering factors such as microarchitecture, density, and bone volume fraction [121]. In the literature, quasi-static tests are the most commonly employed, and they assess properties such as the apparent modulus, yield and ultimate stresses and strains, as well as the work of fracture. Fatigue testing, on the other hand, utilizes stress amplitude to cycles to failure (S-N) or crack growth resistance (R) curves to define the fatigue strength.

Following the hierarchical bone structure, researchers have reported conducting tests on single trabeculae [122, 123] or employing micro-indentation techniques at the microscale. A single trabeculae test enables the acquisition of localized failure information [101], which can be challenging to assess at other scales of analysis. On the other hand, micro-indentation allows for the determination of tissue hardness and elastic modulus. This is achieved by measuring the contact area following indentation and calculating the slope of the indentation curve, respectively [121]. At the smallest level of the bone structure, the nanoscale, the commonly employed techniques include nanoindentation, atomic force microscopy, and scratch testing. Nanoindentation provides valuable insights into the lamellar and interlamellar regions' hardness and elastic modulus. On the other hand, scratch testing is utilized to measure in situ toughness [121].

The elastic response of cancellous bone under compression was a subject of debate in the past. Certain studies observed a toe region in the initial response, which they initially attributed to genuine nonlinear behavior. However, further investigation revealed that this phenomenon was an experimental artifact. Instead, a fully linear behavior was observed, with the apparent modulus being equal in both tensile and compressive loading conditions [72]. The term "side-artifacts" was coined to describe experimental artifacts resulting from specimen damage during the machining process, leading to trabecular connectivity disruption [72, 87, 88]. The impact of these side-artifacts on the underestimation of Young's modulus was quantified to be over 50 %, with a mean value of 27 %, through a comparison of parametric simulations, considering varying volume of analysis sizes, and compression testing results [124]. Notably, these side-artifacts are more pronounced in samples with low bone volume fraction and also affect the estimation of yield strength, resulting in underestimations ranging from 20 % to 32 % [125].

Owing to mitigate these artifacts, several procedures have been suggested. These include increasing the aspect ratio of the samples, embedding the sample ends in PMMA (polymethyl methacrylate), conducting preconditioning cycles and lubricating the platens to minimize friction at the sample-platens interface [72, 103, 104]. It has been found that preconditioning cycles up to an apparent strain of 0.5 % do not result in modulus degradation [103, 104]. There are additional experimental artifacts associated to the parallelism of opposing faces of the sample. If this condition is not appropriately satisfied, the contact between the compression platen and specimen may give rise to highly stressed regions, potentially causing the fracture of the sample in that particular area.

A proposed solution to address this issue involves the implementation of a pivoting compression platen [70].

To characterise the anisotropic and asymmetric behavior of cancellous bone, axial testing has been employed under compression or tension conditions [36]. Tensile tests involve gripping the specimens, which can potentially induce damage. However, embedding the sample end-caps can minimize this undesirable effect [74]. Among the experimental procedures, compression testing is the most commonly used method for estimating bone mechanical properties due to its simplicity compared to other techniques [70]. While properties obtained from overall sample behavior provide valuable insights, they do not capture the local inhomogeneities present in cancellous bone. These inhomogeneities serve as strain concentrators and play a crucial role in failure onset.

Indentation involves applying a known force to a semi-infinite half-space using a hard tip and directly or indirectly measuring the resulting contact area. Zysset reviewed the indentation techniques to assess the mechanical properties of human bone within these intermediate levels of organisation [126]. He determined that the anisotropic tissue hardness in individual bone structural units is influenced by both mineralisation and collagen orientation. Besides, he stated that the average tissue hardness remains unchanged both with aging and in the presence of osteoporosis.

Regarding indentation in bone tissue levels, microindentation has been carried out to evaluate the elastic properties of cancellous bone in various locations, age groups, genders, and orientations. This approach has yielded valuable insights, revealing that the core of a trabecula exhibits a higher modulus (approximately 5 % to 12 %) compared to the cortex. Furthermore, the axial direction exhibited significantly higher values, surpassing the transversal direction by approximately 18 % to 27 %. It is noteworthy to mention that no statistically significant differences were observed in relation to age or gender. This emphasizes that the decrease in macroscopic mechanical properties with age is influenced by changes in the microarchitecture rather than reducing material properties [93].

Nanoindentation is a methodology that enables the determination of the elastic modulus and hardness within surface layers, utilizing a depth indentation reduced to the submicron range. The estimation of hardness involves measuring the contact area when the maximum applied load is exerted, whereas the elastic modulus is determined by analyzing the unloading region of the load-displacement curve and utilizing the relationship between contact stiffness and elastic modulus.

In their study, Zysset *et al.* [91] revealed a correlation between hardness and the elastic modulus in the femur bone of humans, in both cancellous and cortical bone. The researchers observed that the cancellous bone exhibited lower values than cortical bone. This finding contradicted the previously held belief that both types of bone are composed of identical tissue. The authors attributed these results to variations in canalicular porosity, mineralisation, and the orientation of collagen distribution between the different bone types [91].

Additionally, several testing methods previously mentioned can be effectively combined with imaging techniques, such as micro-computed tomography (micro-CT) or capturing photographs during the experiment. This integration provides meaningful information about localized conditions that would otherwise remain unmeasurable. Moreover, this approach can be employed to experimentally validate fracture models, an issue that has yet to address in existing literature adequately. For instance, using photography or conducting micro-CT scans alongside implementing the digital volume correlation technique (DVC) offers insights into bone's localized deformation and fracture behavior. However, relying solely on visual inspections of these images must have the necessary precision. In addition, micro-CT entails substantial financial and time investments, making it suitable only for quasi-static conditions. Nonetheless, employing digital image correlation (DIC) on test-acquired images presents a speedy and cost-effective approach, enabling the estimation of strains and deformation mechanisms at smaller scales compared to the actual testing scale.

For measuring displacements in biological materials, various techniques are commonly employed, including displacement gauges for measuring displacements between compression platens, loading platen transducers, extensometers attached to specimens, strain gauges, and optical systems [70]. Among these options, digital image correlation (DIC), as an optical technique, offers several advantages. Firstly, this non-contact technique eliminates the risk of damaging specimens caused by the attachment of measurement systems. Furthermore, DIC measures local displacements directly on the specimen's surface, thereby avoiding compliance effects that may be associated with other measurement techniques.

Since DIC was implemented in the 80s decade, the accuracy of digital image correlation has undergone significant enhancements [127]. As a result, DIC has gained widespread adoption in various fields, serving as a reliable method for measuring displacements in diverse materials. A comprehensive review of DIC's applications, potential, and limitations in the field of biome-

chanics was conducted by Palanca *et al.* [128]. Several studies have employed digital image correlation to enhance the characterisation of organ-level fractures [129, 130]. Nevertheless, limited research has been conducted regarding the utilization of DIC in investigating the initiation and progression of failure in cancellous bone. Even so, a drawback of the DIC method is its limitation in providing measurements only at the surface level. As a result, if failure occurs beneath the visible surface, the method may not adequately characterise it. Although an averaging of subsurface behavior throughout the specimen thickness is conducted, it does not allow for clear identification of fractured areas at those subsurfaces. This limitation motivated the adoption of digital volume correlation (DVC), which enables sample scanning through micro-CT during quasi-static testing. However, it should be noted that DVC is applicable only under quasi-static conditions [131].

Finally, ultrasonic testing allows for estimating the elastic modulus by measuring the velocity of sound waves passing through a specimen with a known density [70]. Depending on the orientation of the transducer's vibrations concerning the propagation of ultrasound waves, either longitudinal or shear waves can be generated. This enables the calculation of both the longitudinal modulus (E) and the shear modulus (G). In addition, ultrasonic testing offers the advantage of multiple non-destructive measurements and is relatively affordable, making it a reliable tool for estimating elastic properties. Despite that, it is important to note that strength cannot be directly measured through ultrasonic tests and must be inferred by employing regression models based on the elastic properties [70].

2.3 Bone tissue characterisation using imaging techniques

Nowadays, many imaging techniques are available for studying the different levels of bone structure. Nevertheless, previous to the advancements in imaging techniques, the conventional approach to analyzing its structure involved studying sections through histomorphometry [132, 133]. When analyzing cancellous bone using imaging techniques, several considerations need to be taken into account. These include the imaging system itself, the resolution of the images, and the process of segmentation. The imaging system employed and its underlying physical principles directly impact the quality and characteristics of the resulting images, along with the scanning parameters utilized. Additionally, the resolution plays a crucial role in accurately detecting and defining structures at smaller length scales. Lastly, segmentation is of critical

importance as it affects both the estimation of microstructural characteristics and the development of numerical models based on the segmented masks.

2.3.1 Conventional imaging techniques for bone

The exceptional ability of calcified tissues to absorb radiation enables X-ray systems such as computed tomography (CT) or micro-computed tomography (micro-CT) to effectively visualize bone tissue with heightened sensitivity [134]. When using other techniques, such as magnetic resonance imaging (MRI), bone appears as background intensities due to the fundamental principles of the imaging method. MRI involves measuring relaxation times by applying a magnetic field that alters the spin orientation of the imaged material. However, when it comes to calcium, which has an even number of protons and neutrons, it fails to generate a magnetic resonance signal due to its lack of spin-angular momentum [135].

Bone imaging systems can be categorized based on the radiation dose they administer to the specimen, depending on their suitability for clinical applications. In particular, magnetic resonance imaging (MRI) does not subject the specimen to radiation exposure. On the other hand, systems such as computed tomography (CT), quantitative computed tomography (QCT), high-resolution peripheral quantitative tomography (HR-pQCT), or multi-row-detector computed tomography (MDCT) utilize low radiation doses. In contrast, micro-computed tomography (micro-CT) employs high radiation doses, making it unsuitable for clinical practice due to safety concerns.

To develop this research, X-ray micro computed tomography (micro-CT or μCT) has been used for scanning the trabecular bone samples. In order to capture the microarchitecture of trabecular bone, the specimens were scanned with high accuracy, specifically at 13.5 μm isotropic resolution. The selection of a high radiation imaging system, such as micro-CT, is justified due to its exceptional performance in achieving remarkable resolution and contrast for bone imaging. The operating principle of micro-CT relies on the measurement of X-ray attenuation throughout the scanned sample, as depicted in Figure 2.5.

X-rays are generated by the tube, and as they pass through the material, they undergo attenuation before being captured by the detector. Equation 2.2 presents the attenuation of an X-ray beam at a certain distance x, where μ is the attenuation coefficient and I_0 is the incident intensity. The sample is subjected to rotation, subsequently, the collected projections are used to compute and reconstruct the scanned 3D structure. Furthermore, it is usual to
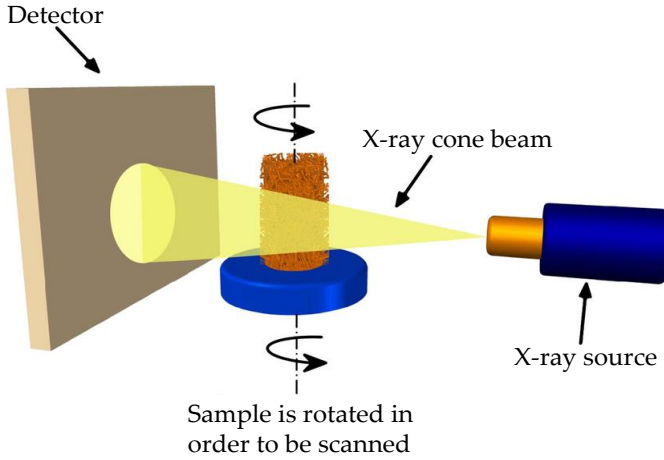
Figure 2.5: Principle of the micro-computed tomography system. Image taken from [136].

employ calibration phantoms that enable the correlation between the attenuation coefficient of micro-CT images and material density. These phantoms are scanned using identical imaging parameters since, as mentioned earlier, the image intensity values are dependent on these parameters. The utilization of calibration phantoms is highly functional because it allows the determination of material properties in numerical models based on their density.

$$I_x = I_0 e^{-\mu x} \tag{2.2}$$

Feldkamp and colleagues [137] conducted the first application of micro-CT to investigate cancellous bone. The imaging system utilized was initially designed for detecting defects in ceramic materials. In their study [137], they outlined the process of scanning and reconstructing images using micro-CT, emphasizing the significance of implementing image corrections for precise 3D reconstruction and accurate measurement of the attenuation coefficient (μ). Furthermore, they cautioned against the occurrence of beam hardening artifacts in the images and proposed corrective measures to address this effect. By enhancing the detector system and reducing the distance between the specimen and the X-ray source, they could to attain a spatial resolution of 70 μm. They asserted that further improvements could lead to even higher resolutions. Their subsequent goal involved examining bone's three-dimensional

(3D) architecture, a task typically accomplished using two-dimensional histological sections. They specifically concentrated on analyzing connectivity and anisotropy, which are genuine 3D properties.

Since then, micro-CT has emerged as a widely adopted tool for analyzing the microstructure of cancellous bone, monitoring disease progression and healing, and creating preclinical models. In Boerckel *et al.* [138] work, the authors provide a comprehensive overview of micro-CT's applications in bioengineering, mainly focusing on its utilization in bone tissue, cartilage, and cardiovascular structures. Additionally, the article introduces novel approaches, such as phase-contrast micro-CT, which hold significant potential for advancing micro-CT imaging in the foreseeable future.

Although it is widely used, conventional CT still has several shortcomings related to image quality, spatial resolution for particular applications or tissue contrast. Most of them are due to the current design of the energy-integrating detectors (EIDs), exhibited in Figure 2.6 a. In EIDs, low-energy photons play a crucial role in creating image contrast. However, their contribution to the final image is relatively limited due to integration, leading to reduced contrast-to-noise ratios in conventional CT images. On the other hand, photon-counting CT (PCCT) represents an innovative approach with the capability to address the constraints associated with EIDs, employing photon-counting detectors (PCDs) as depicted in Figure 2.6 b. PCDs are constructed from semiconductors, obviating the necessity for septa to isolate individual detector elements [139]. These PCD detector elements are smaller in size while maintaining their geometric efficiency [140]

Energy-integrating detectors transform incoming photons into visible light, which is subsequently converted into an electrical signal by photo-diodes. All detected photons are combined through integration to create the signal for a given projection. These detectors' spatial resolution relies on reflective septa to prevent interference between neighboring elements. On the other hand, photon-counting detectors generate an electron-hole pair when a photon interacts with the semiconductor material of the detector. The anode then attracts the electrons from this electron-hole pair, producing an electric pulse proportional to the incident photon's energy.

The resolution achieved with the EDIs is around 0.5 x 0.5 mm^2, whereas with PCCT range from 0.11 x 0.11 mm^2 to 0.5 x 0.5 mm^2 when combined with the magnification factor, these factors collectively determine the spatial resolution limit of the image of 0.07 x 0.07 mm^2 to 0.28 x 0.28 mm^2 [141]. Photon-counting CT detectors tally incoming photon numbers and assess their
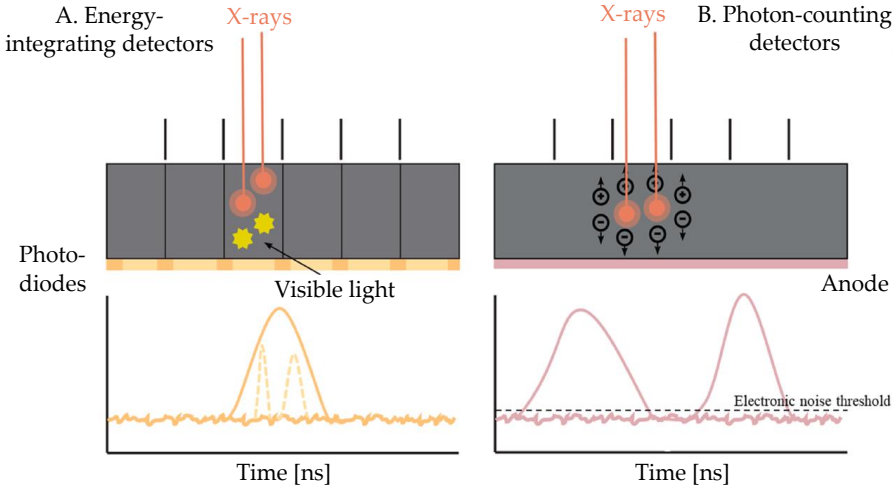
Figure 2.6: Scheme overview of CT. A: energy-integrating detectors and B: photon-counting detectors. Image extracted from [140].

energy levels. This method enhances contrast-to-noise ratios, superior spatial resolution, and refined spectral imaging. Photon-counting CT has the potential to diminish radiation exposure, reconstruct images with heightened detail, rectify beam-hardening distortions, maximize the utilization of contrast agents, and open doors for quantitative imaging, surpassing current CT technology [140, 141].

2.3.2 Techniques to evaluate bone hierarchical levels

Bone is a hierarchical structure where the arrangement and properties from a lower level directly influence the upper-scale behaviour. Consequently, numerous studies conducted across various structural scales have demonstrated that the orientation and arrangement of bone ultrastructure play a significant role in predicting mechanical properties such as bone strength or elastic modulus [142–144]. Over the years, several approaches have been suggested to explore the three-dimensional orientation of at least one of the four structural components of bone ultrastructure mentioned earlier. These methods encompass visible light, X-rays, electrons, or magnetic fields, with some exhibiting highly encouraging outcomes. Regarding the study of the hierarchical structure of bone, several imaging techniques with different resolutions are needed

and are exhibited in Figure 2.7. Then, knowing the resolution needed, it is possible to choose the best imaging technique for bone structure evaluation directly.
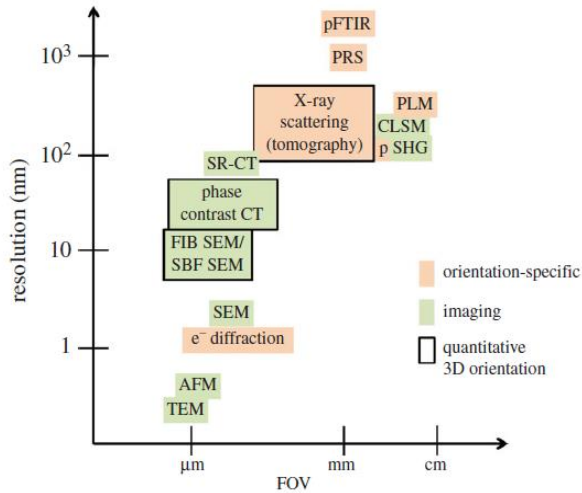
Figure 2.7: Orientation-specific techniques and imaging for the evaluation of bone ultrastructure organisation, based on their capabilities in terms of their spatial resolution and the field of view they cover, and their ability to derive the 3D orientation and arrangement of mineralised collagen fibrils. FOV=field of view. Image taken from Georgeadis *et al.* work [145].

Georgiadis *et al.* [145] work reviews of several techniques to assess bone ultrastructure organisation. They collect multiple studies where diverse imaging techniques have been use according to the level of the hierarchical structure of bone that is being studying, which are shown in Figure 2.8.

The first level is the macroscale, where the organ is assessed from the major to the minor scale. In Figure 2.8 a, the proximal femur is evaluated using scanning electron microscopy (SEM). Scanning electron microscopy (SEM) is the electron microscopy technique that is most commonly employed. It offers a nanometer-level resolution of the sample's surface, eliminating the need for extensive sample thinning as required in transmission electron microscopy
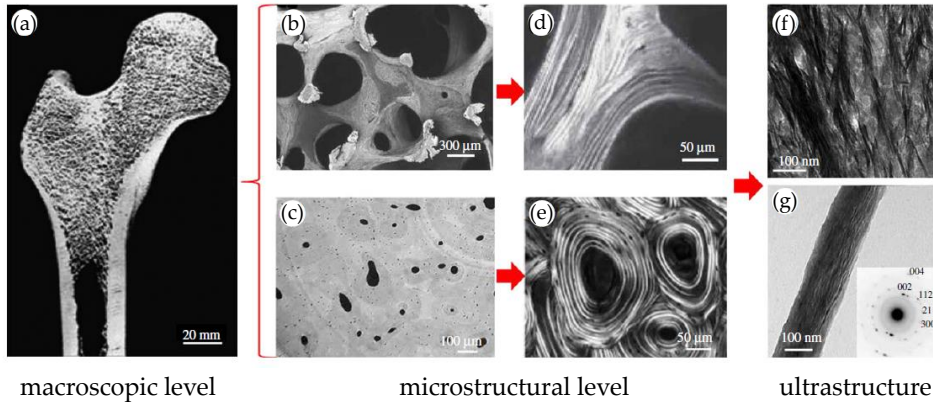
Figure 2.8: Different hierarchical levels of bone assessment using different imaging techniques. (a) Human femur cut in half and imaged using scanning electron microscopy (SEM). (b) Trabecular network imaged using SEM in backscattered electron mode. (c) Haversian system imaged using synchrotron radiation-based computed tomography (SR-CT). (d) Lamellar structure of trabecular bone imaged using polarized second harmonic generation (pSHG) imaging. (e) Lamellar structure of cortical bone imaged using circularly polarized light microscopy. (f) Mineralised collagen fibril bundles imaged using transmission electron microscopy (TEM). (g) Single mineralised collagen fibril and diffraction pattern (inset) showing the orientation of unit crystalcells imaged using TEM and electron diffraction, respectively. Figure taken from Georgeadis *et al.* work [145].

(TEM). Nevertheless, the equipment involved is expensive, and the procedures for preparing bone samples are time-consuming [146, 147]. By utilizing secondary electrons, SEM enables the analysis of sample texture and topography. In SEM, secondary electrons have been utilized to investigate the orientation of collagen fibrils in various tissues such as ligaments, menisci, tendons, cartilage, and bone [148, 149]. In addition, optical microscopy techniques like polarized second harmonic generation (pSHG) and polarized light microscopy (PLM) also have limitations regarding their spatial resolution, typically around 200 nm. However, they compensate for this limitation by offering a broader field of view, which enables the study of macroscopic samples.

Regarding the microstructural level, it is possible to distinguish between the mesoscale, where the cancellous and cortical bone is evidenced, and the microscale, where it is possible to see the trabeculae deposition and orientation (see Figure 2.8). The petrographic microscope or SEM can capture the trabecular network, whereas, for cortical bone, it is possible to use synchrotron

radiation-based computed tomography. Continuing downwards, at the microscale, it is possible to assess the lamellae disposition, which is highly different in cortical bone than in cancellous bone. For the lamellae disposition assessment, the best option is polarized light, pSHG imaging for the lamellar structure of trabecular bone, and circularly polarized light microscopy for lamellar structure of cortical bone. Other techniques also used for this study are staining the samples and their subsequent observation under the light microscope. The most relevant structure at the lowest bone level, the nanoscale, is the mineralised collagen fibrils bundles. The equipment needs a resolution of up to 100 μm, so TEM or electron diffraction is usually used in this level of bone.

On the other hand, the ability to evaluate the organisation of the ultrastructure, in conjunction with *in situ* mechanical testing, is a crucial aspect in comprehending the relationship between structure and function in bone tissue. However, it should be noted that not all of the techniques mentioned can be combined with mechanical testing. For instance, techniques that require sample sectioning such as PLM, FTIR, SHG in transmission mode, TEM (including electron transmission diffraction), or volume electron microscopic techniques are not compatible. Electron-based techniques implemented in an SEM setup are also unsuitable for *in situ* experiments, primarily due to the imaging process occurring under high vacuum conditions and the extensive sample preparation that alters the mechanical properties of the tissue.

The introduction of environmental scanning electron microscopy (ESEM) has addressed both the need to image samples in their natural "wet" state and the ability to conduct experiments on biological samples under moderate pressures. This advancement has facilitated *in situ* experiments on various biological samples. However, the application of *in situ* SEM experiments for bone tissue has been severely limited thus far. This is primarily due to the current inability of environmental SEM to provide the necessary spatial resolution required for assessing the organisation of bone's ultrastructure.

In recent years, X-ray-based techniques like small angle X-ray scattering (SAXS) and wide angle X-ray scattering (WAXS) have been employed for *in situ* experiments [150, 151]. However, these studies have been limited to a small number of specific points within the sample, thus lacking quantitative results regarding the three-dimensional orientation of the ultrastructure. To address this limitation, the orientation reconstruction technique known as 3D sSAXS [152] could be implemented for whole sample measurements, enabling the acquisition of comprehensive 3D information.

In contrast, light-based techniques do not cause damage to the specimen, although prolonged laser exposure can have detrimental effects on the sample [153]. Performing polarization-resolved spectroscopy (PRS) would require acquisition times of tens of seconds per spot, allowing for the observation of bone's viscoelastic behavior [154]. Reflection mode second harmonic generation (SHG), both polarized and unpolarized, has been utilized in conjunction with *in situ* experiments involving bone [155] and other tissues [156]. However, as mentioned earlier, reflection mode SHG only provides qualitative information about the orientation, originating from the sample surface or nearby regions.

Furthermore, due to the necessary sample preparation procedures and imaging conditions, electron microscopic techniques cannot be utilized *in vivo*, especially with living mammalian cells [157]. Moreover, when conducting *in vivo* measurements, it is essential to employ techniques capable of reaching bone tissue located a few millimeters below the skin surface. X-rays possess the inherent capability to penetrate deep into tissues; X-ray imaging techniques employed for investigating the organisation of bone ultrastructure operate at high resolutions. This necessitates using tiny samples and involves substantial X-ray doses, which is detrimental for *in vivo* applications. Local tomography [158] offers a potential solution to reduce the required dose by limiting the reconstructed region of interest to a smaller area than the entire sample. Nevertheless, this approach comes with the trade-off of potential reconstruction errors [159], such as cupping (a radial increase in the grey values towards the edge of the reconstructed circle) or other non-uniform errors across the field of view (FOV).

The use of SAXS and WAXS techniques *in vivo* is highly challenging primarily because of the substantial X-ray dose needed for signal detection. This is attributed to the fact that the primary X-ray beam is obstructed, and the signal is solely generated from the scattered X-ray photons, which are several orders of magnitude weaker than the transmitted photons. Nevertheless, X-ray phase-contrast techniques utilizing grating-based dark-field imaging offer a more feasible option for *in vivo* applications in animals [160], and potentially in humans [161, 162]. These methods can also be seamlessly integrated with standard X-ray absorption techniques [163]. Their ability to provide valuable insights into ultrastructure organisation, by leveraging signal modulations dependent on ultrastructure orientation, is anticipated to increase in the future. It is worth noting that these methods have not been extensively explored thus far. Moreover, two relatively new non-destructive X-ray scattering tomographic techniques [164] hold promise for potential *in vivo* ap-

plications. However, significant technological advancements, particularly in detector technology, would be required to minimize the dose deposited in the sample.

Visible light, being less harmful to biological tissues, presents an opportunity for in vivo investigations into the organisation of ultrastructure. However, the depth of penetration of light in hard tissues like bone is limited, restricting the assessment to superficial areas. For example, studies have demonstrated the transcutaneous application of Raman spectroscopy on bone [165, 166]. Moreover, *in vivo* application of SHG in tissues beneath the skin is feasible through the use of endomicroscopes [167]. These endomicroscopes not only allow the preservation of laser polarization but also enable pSHG imaging [168]. Therefore, the future utilization of PRS and (p)SHG holds potential for the *in vivo* evaluation of bone ultrastructural organisation.

2.3.3   Artifacts introduced in bone images

It is worth noting that a fundamental constraint inherent in all studies is the presence of artifacts introduced during sample preparation steps, such as sample sectioning, decalcification, dehydration or embedding [169]. Depending on the specific protocol employed, these procedures can potentially modify the tissue structure to varying degrees, thereby restricting the quantitative interpretation of results. However, a lack of quantitative investigations concerning the impact of these factors on ultrastructure orientation and arrangement is evident.

Image artifacts are defined as deviations between the reconstructed imaging and the expected density and geometry of the material [170]. These artifacts have the potential to deteriorate image quality, leading to implications for diagnosis and measurements. Typically, they manifest as patterns of bright or dark shadows, rings or distortions, and can be classified based on their source: physics-based, patient-based, scanner-based and image reconstruction artifacts [171, 172].

First of all, patient-based artifacts mainly have three types: metallic materials, patient motion and imcomplete projections. The existence of metallic objects within the scanning area can result in significant streaking artifacts. These artifacts emerge due to the metal's density exceeding the typical range manageable by the computer, leading to incomplete attenuation profiles. Moreover, when scanning highly dense objects, the problem is further exacerbated by additional artifacts stemming from beam hardening, partial volume, and aliasing.

This problem can be solved by the patients, who must remove any metal objects, and also it can be solved by specific software which can substantially decrease. Owing to patient motion, it can give rise to misregistration artifacts, which typically manifest as shading or streaking in the reconstructed image. Measures can be implemented to prevent voluntary motion, but involuntary motion may be unavoidable during body scanning. Nevertheless, specific scanners incorporate special features intended to minimize the artifacts that result from such motion. Lastly, suppose any part of the patient extends beyond the scan field of view. In that case, the computer will possess incomplete information regarding that specific area, potentially generating streaking or shading artifacts. For this reason, it is essential to position the patient correctly and check that everything is inside the scan field [172].

The physics-based artifacts involve partial volume, photon starvation, and undersampling, whereas beam hardening is the prevailing and most commonly encountered one. An X-ray beam consists of photons with a range of energies. When the beam passes through a material, the lower-energy photons are absorbed, resulting in an overall increase in the mean energy of the beam. This phenomenon can impact density measurements and the estimation of morphometric parameters. The effects of beam hardening manifest as cupping artifacts (wherein areas of higher thickness experience more significant hardening than areas of lower thickness in a homogeneous material with a non-uniform shape) and as streaks and dark bands (which occur in heterogeneous materials with varying densities). To mitigate beam hardening artifacts, filters can be employed to attenuate the lower-energy components of the beam or calibration corrections can be applied using phantoms.

Depending on the imaging technique, it is possible to have some different imaging artifacts. Regarding computed tomography, several problems affect the resulting images, such as the presence of stranger objects, noise, spiral or swirl errors, and several aforementioned, like patient motion or partial volume effects [171]. The following image (Figure 2.3.3) exhibits the presence of a stranger object artifact, called "sunbeams".

These images are obtained at the micro-CT for cancellous bone samples (Figure 2.9 a and b) and cortical bone specimen (Figure 2.9 c). Yellow arrows point to the artifacts, and it is possible to appreciate that the pointed-out areas are brighter than the rest of the image. The explanation is that the samples have been contaminated with saw metallic remains during the cutting process. In this case, owing to the artifacts being on the bone surface, it is possible to crop the image and, thus, remove these imaging artifacts. Nevertheless, avoiding

this problem with a stringent cleaning process is possible before scanning the samples.
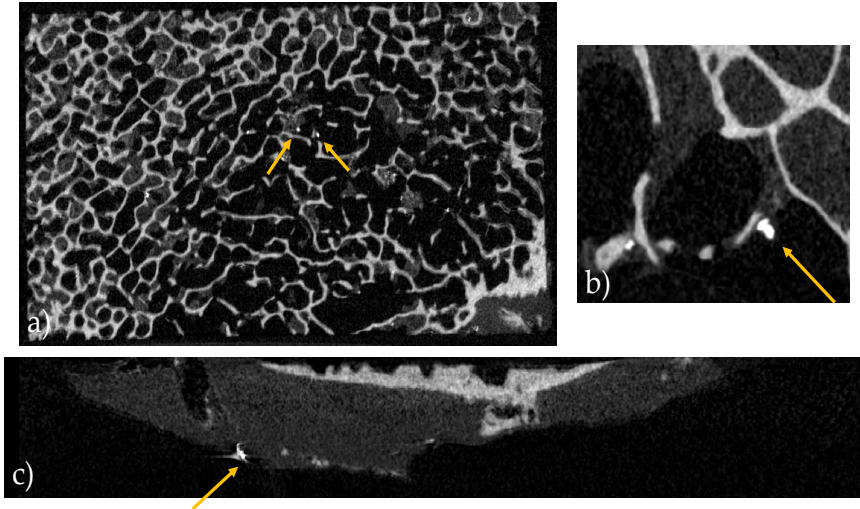
Figure 2.9: Imaging artifacts from micro-computed tomography (micro-CT). Yellow arrows point to the bright spots that originated due to metallic debris left behind by the saw when cutting. Original contribution.

A flawed cleaning procedure can lead to other image problems, such as dirt on the sample's surface. Figure 2.10 presents several images of human femoral head cancellous bone taken at the Field Emission Scanning Electron Microscopy (FESEM) at the Microscopy Service at the Polytechnic University of Valencia (UPV).

In Figure 2.10 a) and b), it is appreciated that there are dark bubbles and areas. These spots appear mainly for two reasons: traces of dirt on the surface of the bone and droplets of liquids used in the cleaning process. Moreover, Figure 2.10 c) exhibits rests of tissues and dirt on the trabecular structure. At last, Figure 2.10 d) presents several droplets and blurred areas. The cause remains unchanged: the presence of dirt on the surface of the bone. In conclusion, the cleaning process is essential to consider when preparing samples for image analysis.
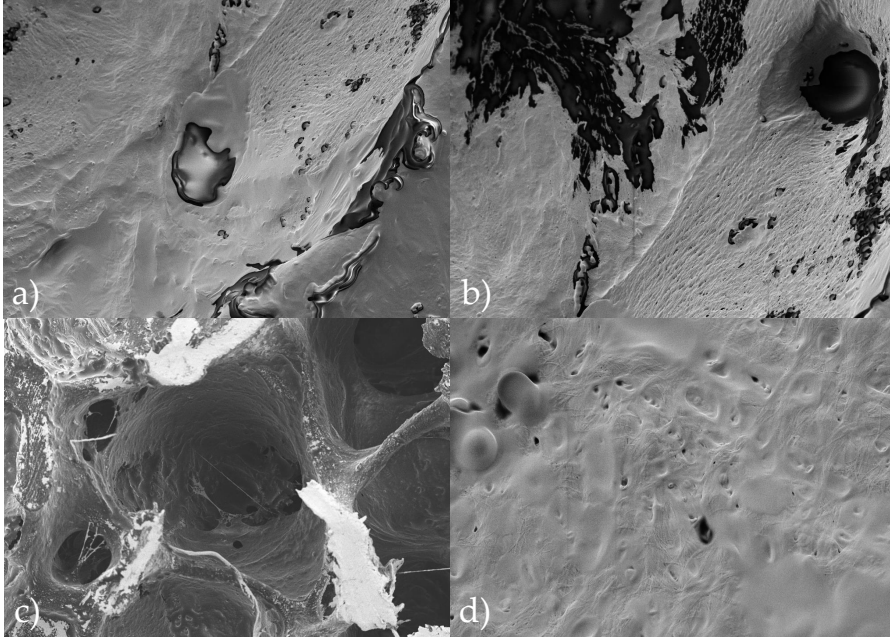
Figure 2.10: Inaccurate cleaning process lead to obtain useless images due to the dirty bone surface. Images obtained at the FESEM at the Microscopy Service at the Polytechnic University of Valencia (UPV). Original contribution.

2.3.4   Image segmentation methods

Image segmentation involves dividing an image or a collection of images into distinct parts. In the context of cancellous bone segmentation, it refers to the differentiation between bone and the background. The segmentation process is highly influenced by the features present in the image and the imaging system used. In the case of micro-CT, the significant disparity in absorption coefficients between bone and surrounding tissues makes segmentation relatively uncomplicated. In the existing literature, various segmentation methods have been utilized either individually or in combination, such as thresholding, active contours, or region growing.

Among these methods, thresholding is commonly employed to solve the problem of cancellous bone segmentation. This technique selects a specific gray level intensity or a range of intensities corresponding to bone tissue. Often, preprocessing steps involving the application of a smoothing filter are also included in the methodologies. The differentiating factor between various

thresholding segmentation techniques lies in how the threshold is determined: manually, based on density measurements, or automatically. Manual procedures rely on visual image inspection, while density-based approaches utilize calibration phantoms during the sample imaging process. On the other hand, automatic segmentation methods rely on analyzing image features to determine the appropriate threshold.

The global thresholding method is widely employed for cancellous bone segmentation due to its simplicity and effectiveness [170, 173]. This technique selects a gray level that distinguishes bone tissue from other tissues. However, using a fixed-global threshold can lead to certain drawbacks, such as the loss of thin trabeculae and an overestimation of the size of thick trabeculae. On the other side, adaptive thresholding demands distinct thresholds for individual images or neighborhoods. This approach entails manual intervention and typically involves more parameters than global thresholding, making it relatively slower. The selection of the local threshold varies across different methodologies, with options including intensity gradients or the local intensity distribution [174]. In the realm of automatic thresholding, a non-parametric method for automatically selecting the optimal threshold was introduced by Otsu [175]. This technique considers multiple classes within the image's grayscale and calculates the threshold that minimizes the variance within each class.

In addition, alternative approaches such as active contours or region growing have also been utilized to segment cancellous bone. Active contours, also known as snakes, are iterative techniques that rely on an initial contour. This contour evolves over iterations by minimizing a functional that combines internal and external energies. Various parameters that determine the contour's evolution and interaction with image features influence the method's effectiveness. However, this technique has certain drawbacks, such as needing the specification of multiple parameters, and the presence of local functional minima can potentially impact the solution.

Another iterative method used for cancellous bone segmentation is the region-growing technique. This method starts with a seed point and iteratively adds pixels to the segmented region if they meet a chosen criterion. Typically, this criterion is based on the distance from the seed point and the difference between the pixel intensity and a threshold value. However, compared to the previously mentioned methods, region growing tends to be slower due to its iterative nature. Additionally, the technique's effectiveness is influenced by the selection of the initial seed point, which can impact the final segmentation result.

Eventually, several studies in the literature have compared segmentation methods for cancellous bone. Gómez and colleagues [176] review segmentation methodologies found in the literature. They compared various automatic global thresholding approaches and finally proposed a method to adapt them locally. Some other studies developed more recently, such as Tassani *et al.* work [177], compared three commonly employed segmentation methods (global thresholding, Otsu's method, and active contours) for bone micro-CT images. They stated that global thresholding and active contours achieved higher accuracy. Due to the relatively low number of parameters involved in global thresholding, they concluded that global thresholding is a more suitable method to be used as a standard.

2.4 Morphometric characterisation of cancellous bone

The concept of morphometry encompasses various interpretations, but regarding biomechanics and bone tissue analysis context, it refers specifically to the study of the shape and dimensions of bones and their structural organisation. Bone morphometry is an area of study in medical research and diagnostics for evaluating bones' shape, size, and structure. It includes measurements such as length, diameter, cortical thickness, volume, and bone density, among others. In the past, the term commonly used for analyzing bone tissue was bone histomorphometry, which involved the preparation of histological sections that were examined under a microscope.

The beginnings of bone morphometry research date back to the early 20th century. During this time, scientists began to use measurement and analysis techniques to examine the characteristics and properties of human and animal bones. Measurements of bone tissue parameters were acquired through techniques like X-rays, computed tomography (CT) scans, or magnetic resonance imaging (MRI), which only allowed 2D analyses. In the following years, the progress in bone imaging has enabled researchers to obtain three-dimensional images that accurately measure bone shape and size, and permit to identify bone diseases, assess the risk of fractures, and monitor the effectiveness of treatments. When studying cancellous bone, it is widely recognized that both density and architecture play crucial roles [24, 76, 133]. Researchers have devoted much effort to studying and defining the parameters that define the architecture of trabecular bone. These efforts aim to establish connections between these changes and conditions, such as osteoporosis, or to understand better their impact on the mechanical strength of a structure resembling cancellous bone.

The parameters most frequently utilized for characterising cancellous microarchitecture are bone volume fraction (BV/TV), mean trabecular thickness (Tb.Th), mean trabecular separation (Tb. Sp), bone surface area to volume ratio (BS/BV), connectivity (Conn.), fractal dimension (D) and degree of anisotropy (DA). The mechanical properties of bone undergo changes that are not caused by the bone mineral density (BMD), but are due to changes in the microstructure of the bone. Some researchers, such as Odgaard or Ulrich, try to explain the variations in bone mechanical properties. Odgaard [133] argued that connectivity and architectural anisotropy are particularly interesting in mechanics-architecture relations. Moreover, Ulrich and collegues [134] and colleagues calculated the 3D indices and elastic constants of human cancellous bone from different skeletal sites. They found that the definition of mechanical properties of bone and the diagnosis of osteoporosis can be improved if, in addition to BMD, the 3D bone microarchitecture parameters, such as Tb.Th, Tb.Sp, Tb.N, DA, BV/TV and BS/BV are included. They stated that the correlation coefficient was improved from 53 % to about 90 %. Lastly, they concluded that the obtained regressions did not work for other different locations.

The characterisation of heterogeneous materials heavily relies on the degree of orientation, also referred to as the material degree of anisotropy. Regarding bone adaptation to external loads, the presence of preferred orientations in terms of microarchitecture anisotropy becomes crucial. In the field of bone histomorphometry, the initial study conducted by Whitehouse [132] introduced the concept of mean intercept length (MIL) on histological sections. This method involves counting the intersections between a grid of lines and the bone interface based on the orientation of the grid lines. When represented as a polar plot, the MIL generates an ellipse in 2D and an ellipsoid in 3D for materials with three symmetry planes. Building upon the MIL principle, other measurements such as volume orientation (VO) and star length distribution (SLD) have been derived.

Regarding fractal dimension (D), it is employed to quantify the structural complexity of a structure, specifically examining how the relationship between the number of measured characteristics alters as the length scale is modified. A fractal can be defined as an object that possesses a fractional dimension. In the context of cancer research, some authors have proposed using fractal dimensions to assess the presence and progression of cancerous cells [178]. In addition, other investigations propose the fractal dimension for assessing bone diseases. Chen *et al.* [179] suggested introducing fractal dimension as a complementary indicator to BMD to diagnose osteoporosis. The reason is because

the fractal dimension captures variations in bone microstructure, while BMD reflects changes in bone mineralisation. Therefore, by considering both indicators, the screening of osteoporosis can be enhanced in terms of accuracy. For instance, by analyzing 2D X-ray images of control and osteoporotic groups, it was reported that the fractal dimension outperformed BMD as a discriminatory measure [180, 181].

The box-counting method has been widely employed as a computational approach for determining the fractal dimension, both in two and three dimensions. This method involves dividing the region of interest into boxes of a specific side length ε and counting the number of boxes required to cover the entire perimeter of the structure. The boxes that cover the region of interest are defined as N. The process is then repeated with decreasing box sizes, resulting in a logarithmic relationship. The box-counting dimension is the ratio of log(N) divides log($1/\varepsilon$) when ε is trending to 0 [182], presented in Eq. 2.3. The slope of this relationship represents the fractal dimension. The box-counting method is relatively simple to implement and can be easily extended to three-dimensional settings.

$$D_{box} = \lim_{\varepsilon \to 0} \frac{logN}{log(1/\varepsilon)} \qquad (2.3)$$

An additional morphological parameter examined in this study is connectivity (Conn). This parameter has garnered attention due to the hypothesis that it is associated with architectural changes in osteoporosis. Connectivity, which is a three-dimensional (3D) feature, was predominantly assessed using histological sections before the work conducted by Odgaard and Gundersen [183]. These researchers introduced an authentically 3D methodology based on the Euler characteristic topological invariant to evaluate connectivity. Despite investigating the interrelation between connectivity and other morphometric parameters, the authors found no significant correlations. Consequently, they proposed that connectivity should be regarded as an autonomous parameter.

A novel technique to estimate the average trabecular thickness (Tb.Th) and separation (Tb.Sp) in three-dimensional (3D) images was introduced by Hildebrand and Rüegsegger [184]. Their methodology was motivated by the limitations of 2D measurements, which often relied on assumptions about the structure type. The approach proposed in their work involves fitting spheres to each point in the bone structure, enabling the calculation of local thickness maps. The estimation of Tb.Sp is performed similarly to Tb.Th, but by working with the negative of the 3D bone segmented mask. Several decades

after, Doube and colleagues developed an open-source software application for analyzing 3D bone morphometry called BoneJ [185]. This application is freely available for download and use by anyone.

All the investigations mentioned above have studied cancellous bone architecture; even so, some researchers focus on the so-called local morphometry, which refers to individual plates and rods. Stauber and Müller [23] presented a new method for the spatial decomposition of trabecular bone into its basic components: plates and rods, such as it is shown in Figure 2.11. Their approach enables the extraction of these elements from the bone sample through a series of consecutive algorithms. Subsequently, the extracted elements can be subjected to analysis using standard morphometric algorithms, allowing for the examination of their size, shape, and distribution. Previous studies have described spatial decomposition methods based on line skeletons [186–188]. However, these methods lack the capability to incorporate shape information, making it impossible to differentiate between plates and rods. Hence, the primary focus of these authors was on the topological analysis of line skeletons, utilizing the newly derived parameters in conjunction with global morphometry [188]. Their findings indicated that when combined local and global morphometry, the prediction of mechanical properties of bones could enhance.

In addition, further works focus on the relationship between individual rods and plates local morphometry with the contribution to bone stiffness, such as Stauber *et al.* [22] highlight in their study. They related the elastic properties of human trabecular bone samples to local and global morphometry. The study found that separate analysis of individual rods and plates may help to better predict age and disease-related fractures as well as to shed new light on the effect of pharmaceutical intervention in the prevention of such fractures beyond BMD. Moreover, the study found that the mean trabecular thickness of the rods was significantly related to bone stiffness, whereas the mean trabecular thickness of plates had no correlation to bone stiffness.

Once the mechanical properties were studied and related to the morphometric parameters, it aroused interest in evaluating diseased bone morphometry. Blain *et al.* [189] studied the cortical and trabecular bone distribution in the femoral neck in osteoarthritis and osteoporosis. They found that postmenopausal women presented a cortical thinning in the femoral neck and a loss of the trabecular bone mass and connectivity compared to osteoarthritis women. In addition, they established that the spatial distribution of the trabecula differs between osteoporosis and osteoarthritis, whereas cortical thinning is homogeneous. Furthermore, Montoya and colleagues [190] analysed
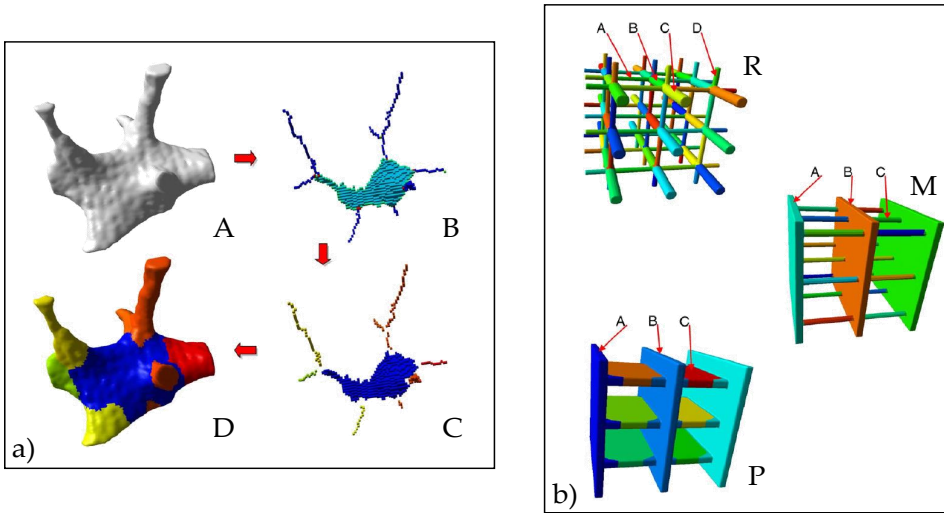
Figure 2.11: a) Spatial decomposition of trabecular bone. (A) The initial binary image that served as input for our algorithm is shown in panel. (B) A skeletonization and optimization algorithm is applied to get a homotopic shape preserving skeleton. (C) This point-classified skeleton is then spatially decomposed by removing the intersection points. (D) A two-way multicolor dilation algorithm was applied to find the volumetric extend of each element, yielding in the final spatially decomposed structure. b) The three computer-generated models used for the validation of the algorithm. To represent a wide variety of structures, a (R) rod, a (M) mixed, and a (P) plate model were produced. Images extracted from [23].

the bone turnover markers (BTM), bone mineral density (BMD), and the structural and mechanical properties of trabecular bone in patients with osteoporosis and osteoarthritis. Their work explored the relationship between BTM, BMD, microstructure, and biomechanical parameters in patients with osteoporosis and osteoarthritis. They provided evidence that the histomorphometric and biomechanical changes in bone microstructure in osteoporosis are opposite to those of osteoarthritis. They justified that osteoporosis patients have a less resistant bone with a higher risk of fragility fractures due to their decreased volume of trabecular bone, less trabecular number, and worse connectivity than osteoarthritis patients.

Ding and Overgaard studied cancellous bone morphometry from human femoral heads in patients with rheumatoid arthritis, osteoarthritis and osteoporosis [20, 21] using specimens such as the presented in Figure 2.12.
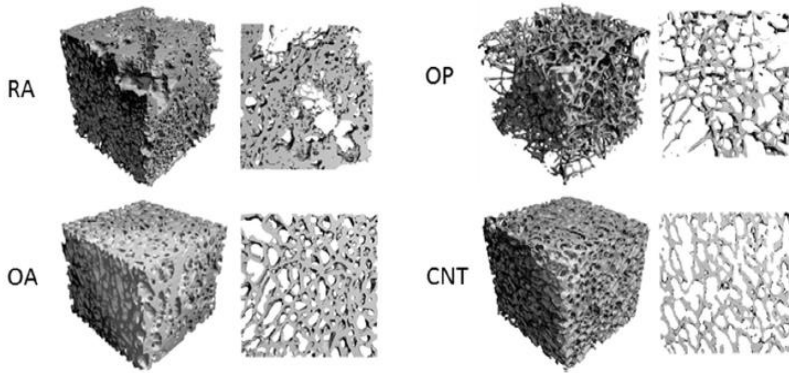
Figure 2.12: Differences in trabecular bone architecture due to different diseases. 3D reconstructions of micro-CT images for four groups of study which are rheumatoid arthritis (RA), osteoarthritis (OA), osteoporosis (OP) and control (CNT). Image extracted from Ding and Overgaard work [20].

Furthermore, they established significant differences in 3-D microarchitectural properties and rod-and plate-like trabecular morphometric properties among patients with rheumatoid arthritis (RA), osteoarthritis (OA), or osteoporosis (OP). The cancellous bone specimens from RA and OA groups displayed similar microarchitectural degeneration patterns and pronounced different OP microarchitectures. Besides, the OP group had the weakest cancellous bone strength, while the RA and OA groups exhibited a compensatory effect that maintains bone tissues, and hence mechanical properties. The single best determinant for mechanical properties was bone volume fraction. Their results enhanced the understanding of microarchitectural degeneration of diseased cancellous bone and are particularly important for the design and survival of joint prostheses [20]. Furthermore, in Ding and Overgaard [21] work, they suggested that some local morphometric parameters, along with other factors, such as abnormal collagen, mineralisation, erosion, and microdamage, may contribute to further compromising mechanical properties.

In this section, it has been highlighted the importance of studying bone morphometry because it has a direct relationship with mechanical properties. In addition, some morphometric parameters, such as fractal dimension, can be used for improving the diagnosis of bone diseases like osteoporosis. Moreover, the importance of local morphometry, consisting of rods and plates, has

been stated because the predictions are much more accurate with both local and global morphometry. Finally, the morphometric differences between bone diseases and how they affect bone mechanical properties have been exhibited.

2.5   Numerical modelling of cancellous bone

Numerical modeling of cancellous bone holds significant importance in various areas. These models are an essential tool for estimating mechanical properties specific to individual patients, in combination with medical image processing, to assess the effectiveness of disease treatments, designing implants, understanding damage and failure mechanisms at different levels, and analyzing how the microarchitecture influences the mechanical strength of the tissue. Conversely to experimental testing, numerical modeling offers several advantages. It enables multiple destructive or non-destructive simulations, considering complex loading and boundary conditions. It also facilitates the evaluation of parametric influences and analysis of local effects. Moreover, numerical modeling avoids the challenges associated with testing biological materials, which can degrade over time and can only be tested destructively once.

2.5.1   Parametric numerical models of bone

The intricate and diverse microstructure of cancellous bone has sparked interest in exploring simplified parametric models. These models aim to capture trabecular tissue's elastic and failure properties by reducing its structure to a few essential parameters. Discovering a foundational model that can serve as a representative structure and accurately replicate the mechanical behavior, either in part or in its entirety, is of significant research significance. This is particularly important because it allows for the isolation of the influence of parameter variations from other heterogeneous microstructural characteristics.

The initial numerical models of cancellous bone depicted its structure as a regularly recurring pattern, drawing from simplified interpretations of histological and SEM images. Gibson [111] identified four distinct structures of cancellous bone, comprising combinations of plate and rod formations, and put forth four simplified models: cubic or hexagonal with rod-like or plate-like characteristics, respectively. Additionally, he stated that examining the mechanical characteristics of cancellous bone can be inferred by studying how the wall cell undergoes deformation, which is influenced by its relative density and material properties. The suggested models demonstrated satisfactory perfor-

mance across various densities and configurations, when compared to stiffness and strength measurements documented in existing literature [111].

Kim and Al-Hassani [191] introduced a conceptualization of vertebral cancellous bone by examining microscope images [192]. Their proposal involved an analytical model that portrayed the bone as a hexagonal columnar structure with doubly tapered struts, see Figure 2.13. Using the simplified hexagonal model, they conducted a study to investigate the impact of age and gender on the effective modulus and collapse stress. The relationships established by Mosekilde [192] were employed for this purpose. The results were then compared with those obtained from a uniform (non-tapered) model, emphasizing the significance of tapered struts in enhancing the mechanical performance of the models. Despite that, their comparison lacks experimental data.
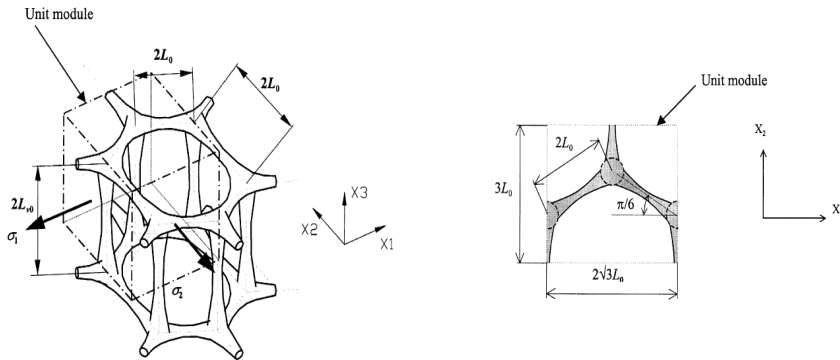
Figure 2.13: Hexagonal columnar structure model of vertebral trabecular bone. Image taken from Kim and Al-Hassani work [191].

On the other hand, Dagan *et al.* [193] devised a fundamental unit of a solitary trabecula that can be adjusted in terms of thickness and length to match the characteristics of trabecular bone. The model demonstrated a strong correlation with the apparent moduli findings obtained from osteoporotic bone samples taken from the human proximal femur. Subsequent studies applied the buiding block established by Dagan *et al.* [193] in their own investigations. In one of these studies [194], the parametric finite element (FE) model introduced in [193] was modified to incorporate crucial details regarding trabecular thickness, separation, and bone mineral density (BMD) obtained from quantitative computed tomography (CT) scans. This modified model was then employed to assess the stiffness of cancellous bone samples extracted from the

C7 vertebrae of large dogs. Additionally, the researchers performed multi-variable regressions based on the trabecular thickness, separation, and BMD. Moreover, the authors expanded their model to include the calculation of sample strength by incorporating an analytical linear relationship obtained from previous research [195].

In conclusion, the initial models aimed to depict cancellous bone as a periodic structure using microscope or SEM observations and incorporating parameters derived from those images. These investigations into simplified parametric models of cancellous bone played a crucial role in advancing our understanding of the various deformation mechanisms within cancellous bone structures. They served as the foundation for developing more precise models in subsequent research.

2.5.2   Image-based models

The progress in imaging technologies, such as micro-CT, has enabled the visualization of the complex and non-periodic microstructure of cancellous bone, along with the estimation of its tissue density. In a study conducted by van Rietbergen *et al.* [119], a finite element analysis was implemented, explicitly considering the cancellous bone microstructure using high-resolution micro-CT images. A novel approach was introduced to directly convert voxels into finite elements, facilitating the determination of elastic properties of the bone under various loading conditions. In their research, van Rietbergen *et al.* [119] acknowledged the limitation of assuming homogeneous material properties at that time. Furthermore, they examined the impact of voxel resolution and found that matching the models' volume fraction to that of the sample was more crucial than precisely matching the voxel size, within the range of 20 to 120 μm. This approach has since inspired numerous studies aimed at constructing finite element models based on bone imaging.

Nevertheless, micro-CT imaging requires a high radiation dose to attain enhanced contrast and image resolution. In contrast, in vivo imaging systems like HR-pQCT or MDCT offer the advantage of operating at lower resolutions, typically ranging from 80 to 168 μm [196]. Consequently, investigations have focused on assessing the capability of in vivo imaging systems to accurately characterise cancellous bone microstructure and evaluating the performance of subsequent finite element models in replicating its mechanical behavior. These evaluations are often carried out by comparing the results with models derived from micro-CT, which are considered as the reference standard [108, 196, 197].

Typically, the highest image resolution feasible is employed for Finite Element Method (FEM) analyses. However, challenges can emerge in terms of computational expenses when dealing with large specimens. Bevill and Keaveny [198] investigated a range of element sizes spanning from 20 to 120 μm, using specimens from several locations and bone volume fractions. The accuracy of yield stress prediction at different resolutions is influenced by the bone volume fraction. Coarser masks with lower bone volume fractions exhibit relatively higher errors compared to samples with higher volume fractions [108, 198]. In specimens with lower density, the size of the elements played a more significant role, resulting in a reduction in the apparent modulus of up to 41 %. On the other hand, for specimens with higher volume fractions, a reduction of 10 % was observed [108]. However, when it comes to model resolution, the clinical resolution of 80 μm demonstrated comparable capability to detect bone quality as higher resolution models with a resolution of 20 μm [198].

Ulrich and colleagues [196] conducted a comprehensive investigation on various image resolutions, ranging from 28 μm to 168 μm resolution. In addition, they delved deeper into the impact of different meshing techniques on estimating elastic modulus and von Mises stress. Their study compared direct conversion to finite elements with compensated hexahedron and tetrahedron meshes. The influence of the meshing technique varied depending on the analyzed microstructure. Samples with larger trabecular thickness demonstrated a minor impact, around 3 %, whereas samples with lower BV/TV experienced a significantly higher influence, reaching up to 40 %. Generally, the coarse meshes resulted in lower estimates of elastic and von Mises stresses than the reference model.

Regarding failure prediction, Bauer and colleagues [197] examined artificially coarsened models using the Pistoia criterion [199], a linear criterion that considers high strained volumes. The authors emphasized the significance of predicting the failure load and analyzing the distribution of micro-strains. They found that maintaining the lattice connectivity is more crucial than preserving the bone volume fraction, which tends to increase when the resolution is reduced for the same segmentation threshold.

Alternative methods for modeling cancellous bone based on images incorporate a representation of its structure as a combination of plates and rods [200]. This approach poses a challenge in segmenting individual trabeculae and explicitly defining the plates and rods that make up the structure. However, the plates and rods model demonstrates accurate predictions of elastic and strength properties compared to voxel-based models. Moreover, it offers significant advantages regarding memory usage, requiring less memory concern-

ing model size, and significantly reduces computational resources in nonlinear simulations [200].

2.5.3   Definition of material properties in numerical models

Conventionally, tissue material properties are determined using various methods. Several authors rely on attenuation coefficient values and their correlations with density and elastic properties [81, 201]. Experimental approaches include nanoindentation measurements [84] or applying inverse analysis calculations, which involve combining experimental data with three-dimensional imaging and finite element modeling [71, 76, 96]. Lastly, some studies adopt predefined values from existing literature [201].

Density-based continuum models are often employed when dealing with lower-resolution images, such as those obtained from CT or MDCT scans. These models establish the characteristics of the material within each finite element by averaging its properties based on the intensity of the gray level, which corresponds to tissue density [197]. A power law assigns the appropriate elastic modulus to each element, which considers the anatomical location and the apparent density determined through experimental means [202, 203]. Clearly, continuous models do not explicitly incorporate the microstructure of cancellous bone. However, they can serve as an initial approximation of its mechanical behaviour or as a computationally efficient method for prediction, particularly when resources are limited. Pahr and Zysset conducted a noteworthy study [204] that compared CT-based continuum finite element models with micro-CT-based models. Their findings revealed that CT-based continuum models, incorporating patient-specific cortex and density-fabric-based orthotropic cancellous bone material properties, yielded equivalent predictions to micro-FE models while requiring fewer computational resources.

On the other hand, for high-resolution finite element models, it is common to consider equivalent effective isotropic elastic properties, which are determined through inverse analysis using experimental data [96]. This calibration method has been shown to account for up to 95 % of the variation in Young's modulus when compared to experimental testing. Other researchers have investigated the use of inhomogeneous material properties in micro-finite element models [81, 201]. For instance, Berot *et al.* [81] examined a randomly distributed elastic modulus and observed differences of less than 2 % in estimating strain remodeling thresholds compared to assuming homogeneous tissue mechanical properties. In the computational models of Bourne and van der Meulen work [201], they introduced the inhomogeneities derived from micro-CT at-

tenuation coefficients in order to predict the apparent mechanical properties. Their findings demonstrated that assuming a homogeneous elastic modulus based on literature values overestimated the apparent properties. Furthermore, including an inhomogeneous distribution had a more pronounced effect on specimens with higher variability in tissue modulus, while its impact diminished for more homogeneous specimens.

Conversely, in a study by Gross *et al.* [94], it was found that accounting for mineral heterogeneity had minimal impact on estimating the apparent properties of human cancellous bone. They reported a 2 % overestimation for the homogeneous model. An alternative approach for determining the material properties can be achieved through nanoindentation. In their study, Chevalier *et al.* [84] compared the impact of assigning material properties to finite element (FE) models through nanoindentation and those obtained through back calculation from experiments. According to Chevalier work [84], the use of nanoindentation resulted in a significant overestimation of the apparent modulus by 24 %. The authors postulated that these variations were attributed to side-artifacts that occurred during the testing process, leading to a reduction in the estimation of the tissue's Young's modulus. Remarkably, this underestimation of the apparent modulus was consistent with previous research that examined experimental artifacts [124].

2.5.4 Estimation of bone elastic properties

Evaluating the structural integrity of cancellous bone and understanding its relationship with specimen-specific microarchitecture relies on accurately determining the elastic constants that describe its apparent behavior. Numerical simulations offer an advantageous alternative to experimental testing, as they help circumvent associated issues. Previous studies have reported that cancellous bone exhibits either orthotropic or transversely isotropic apparent behavior when analyzed in an on-axis manner [76, 96].

Van Rietbergen and colleagues [120] introduced a methodology for calculating the elastic constants of cancellous bone, building upon the work of Hollister and Kikuchi [205]. Their approach involved applying six unitary strain cases, consisting of three pure axial strains and three pure shear strains, directly on the micro-CT reconstructions of two specimens. This procedure eliminated the need for any prior assumptions regarding the elastic symmetries of the samples and effectively circumvented artifacts that may arise during experimental testing. The applied boundary conditions influence the estimation of homogenized elastic properties. Determining effective elastic properties in-

volves satisfying three main conditions: the structure must exhibit periodicity, the analyzed volume should contain a large number of microscale elements, and periodic boundary conditions must be applied [206]. Consequently, when employing the six unitary strain cases on cancellous bone, the resulting properties are considered apparent properties since they do not meet the periodicity requirement necessary for calculating the effective properties. These apparent properties serve as an upper bound for the effective elastic properties [207]. This technique was subsequently designated as kinematic uniform boundary conditions and has been employed to compute uniform properties across diverse species and locations [96, 120, 208], as well as to assess their associations with bone volume fraction [208].

Several studies have stated a significant impact of model size and boundary conditions on predicting elastic properties [206, 207]. Since cancellous bone is a non-periodic structure, its effective elastic properties cannot be directly calculated; however, its apparent properties can be determined. Pahr and Zysset [206] examined the influence of various boundary conditions on estimating the elasticity matrix. They evaluated uniform traction or uniform displacement-traction (orthogonal mixed uniform boundary conditions PMUBCs) and uniform displacement (kinematic boundary conditions, KUBCs) as opposed to periodic boundary conditions (PBC). PBC enables the computation of effective elastic properties. However, for non-periodic structures such as cancellous bone, an initial step of mirroring the structure is required to apply them. The researchers demonstrated that PMUBCs yield identical properties to PBCs, while KUBCs offer an upper limit for the effective elastic properties [206, 207]. Another approach, presented by Daszkiewicz *et al.* [207], introduced the concept of utilizing an embedded configuration to evaluate the effective elastic properties. This embedded configuration entails measuring the elastic properties at a specific distance from the cortex where the boundary conditions are applied, referred to as the in situ value. Additionally, the researchers examined the impact of sample size and observed a convergent trend with increasing volume.

2.5.5 Modeling failure in numerical models

The response of bone under axial loading until fracture can be classified into three stages: an elastic region (a linear phase characterised by reversible deformation), an elastic-continuum damage mechanics region (where diffuse microcracks emerge irreversibly), and a fracture mechanics region [73]. In the past few decades, there has been an increase in numerical resources, although not to the extent required by clinical practice for fracture risk assessment us-

ing μ-FE modeling. Specifically, incorporating cancellous bone microstructure necessitates millions of finite elements for a specimen of approximately 1 cm^3. Hence, achieving a balance between precision and computational efficiency becomes crucial when employing failure models. Numerous researchers have put forth nonlinear micro-finite element models in the literature to simulate both pre- and post-yielding behavior [71, 97, 105, 119, 209, 210]. Nevertheless, most of the proposed models focus solely on exploring the initial stages of failure, neglecting its propagation. Alternatively, some models that consider failure propagation tend to be overly intricate and involve challenging parameters to measure accurately. Moreover, it is needed to continue investigation into experimentally validating the damage models.

Failure models are valuable tools for estimating properties that are challenging to measure directly through experiments. For instance, numerical approaches have been employed to estimate yielding and fracture strains [98]. By using a tissue modulus and incorporating asymmetric failure strains, it becomes possible to predict the failure of cancellous bone. Additionally, this approach can retroactively calculate tissue failure properties by integrating simulations and experimental data [98]. Moreover, this approach has been used to evaluate the local strain threshold that triggers the initiation of bone remodeling in osteoporotic cancellous bone [81].

In contrast, in the literature, various approaches have examined post-yielding behavior. For instance, Schwiedrzik et al. [211] introduced a cohesive-frictional plasticity model based on the Drucker-Prager yield criterion. Through thorough validation against experimental data, the model demonstrated remarkable accuracy correlating to the stiffness and yield point observed in the experiments. Conversely, García et al. [209] expanded a two-dimensional version of elastic-plastic damage constitutive law to three dimensions, encompassing both cortical and cancellous bone. The model comprehensively describes the evolution modes of elastic, pure plastic, and damaged plastic. In addition, it distinguishes between tensile and compressive damage stresses. However, despite its complexity, the model lacks experimental validation.

One compelling approach for simulating failure using a straightforward model lies within continuum damage mechanics. These approaches employ a smeared crack method to simulate the initiation and propagation of cracks within the material [97, 210, 212, 213]. According to Nagaraja work [105], isotropic damage laws effectively replicate the nonlinear behavior of cancellous bone. Building upon this idea, Hambli [97] introduced and experimentally confirmed an isotropic damage law for simulating damage at the microscale within the trabecular lattice. The model incorporates an element deletion technique to

simulate complete fracture. Harrison *et al.* [214] conducted a study that examined the combination of an asymmetric damage approach and complete fracture using an element deletion technique. This approach also incorporated a cohesive parameter to calibrate brittle-ductile behavior accurately. Notably, their investigation enabled the estimation of yielding and failure strains while effectively modeling post-yielding behavior.

The methodology applied in Hambli's work [97] was also utilized to replicate bending failure in a single trabeculae, offering valuable insights into the failure mechanisms. In this context, regions experiencing tensile stresses contribute to the accumulation of damage and local rupture, resulting in modulus degradation. Conversely, areas experiencing compression enhance fracture toughness due to the closure of microcracks [71]. A more sophisticated constitutive exponential law was employed to model axial and bending failure in individual trabeculae, and its outcomes were experimentally validated [99]. Analysis was conducted on osteoporotic and healthy donors, revealing minimal variability in the yield strain, ranging between 10 % to 20 %. However, in contrast, the ultimate strain exhibited a wider range of variation, from 30 % to 40 %. Nevertheless, these intricate models need many parameters that are challenging to measure accurately. Moreover, they often demand higher computational resources for conducting the simulations.

2.6   Osteoporotic bone tissue characterisation

Osteoporosis is one of the most common bone diseases strongly rooted in our society which harms million people in the whole world. This bone disorder tends to affect mainly older people and postmenopausal women, who suffer the most severe consequences. This illness triggers the degradation of bone structure leading to an increased weakness and fragility of bone. For this reason, osteoporotic patients have a high risk of fracture. Owing to all these arguments, it is really important to study the osteoporotic bone and how it behaves for being able to diagnose at early stages of the disease, to prevent fractures and to treat patients.

2.6.1 Age-related bone diseases

Nowadays, life expectancy has increased, so as a result, we have an ageing population. This is the reason why every day we have to deal with more age-related diseases. Some of these pathologies are related to bone, and trigger pain, fractures, loss of life quality even death. The so called rheumatic diseases are a group of health disorders which affect the locomotor system (bones, muscles and joints), and which are not due to a traumatic cause. The most common diseases of this group in the elderly population are arthritis, osteoarthritis and osteoporosis.

Regarding the two first pathologies, they mainly affect the joint of bone, although in a different manner. First of all, arthritis is the swelling of the joint from non-degenerative causes. The main symptoms of arthritis are joint pain and tightness, which often worsen with age. The most common type of arthritis is the rheumatoid arthritis, which is a chronic inflammatory disorder that can affect more than just the joints. This disease is an autoimmune disorder that occurs when the immune system mistakenly attacks the body's tissues. In some people, the condition can damage different body systems, including skin, eyes, lungs, heart and blood vessels. In Figure 2.14 c) it is presented how rheumatoid arthritis affects to joint, which induces bone erosion and inflammation of synovial membrane (produces the synovial fluid that acts as a lubricant). Furthermore, it is possible to compare it with the normal state of the joint which is shown in Figure 2.14 a).
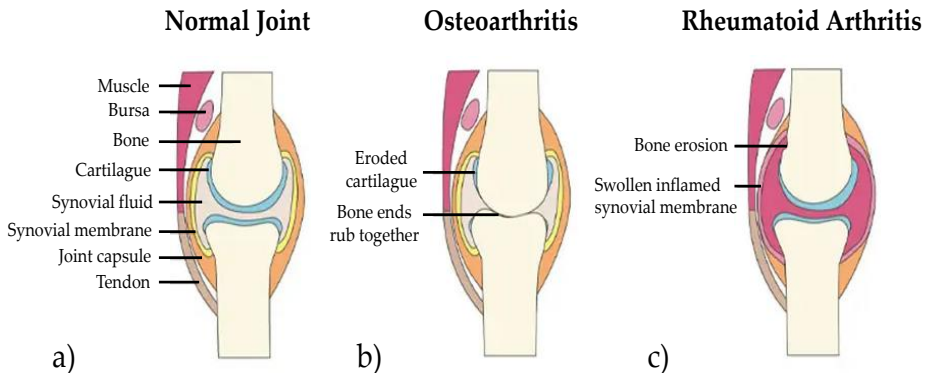
Figure 2.14: Knee joint scheme of a) normal joint, b) osteoarthritis and c) rheumatoid arthritis. Picture extracted from [215].

By other side, osteoarthritis is a chronic, degenerative and rheumatic disease with a progressive course which occurs when the cartilage (the tissue that covers the bone and acts as a shock absorber) inside the joints to protect them wears away. It should be highlighted that, although the suffix -itis in medicine is used for denoting inflammation or inflammatory pathologies, it does not work for the above mentioned disease. Some researchers have studied this issue in order to clarify it.

As early as 1983, Gardner [2] defined in his work the term of osteoarthrosis as the condition which may succeed damage to the avascular, aneural hyaline cartilage of synovial joints. Gardner also contemplated that some other researchers continue to use the alternative older term osteoarthritis, which implies inflammation rather than degeneration. Furthermore, the tendency in subsequent decades of study has been to use them as a synonym. In 2008, Mercuri [216] said that the term of osteoarthrosis is a synonym for osteoarthritis in some fields of research such as in medical orthopaedic literature.

On the contrary, Faustino [217] presented in his work other approach to define the differences between osteoarthritis and osteoarthrosis. In [217] is stated that osteoarthrosis must be understood as an evolving disease which has a variable pathogenic and clinical expressions throughout its evolution. In Figure 2.15 it is shown the development of the disease proposed in [217].

Figure 2.15: Osteoarthritis presented as an evolutive disease. Information extracted from Faustino work [217].

By one side, the inflammatory OA, true osteoarthritis, is when the synovial inflammation and microscopic changes at bone and cartilage level are predominant. On the other hand, mechanical OA, true osteoarthrosis, is the mechanical degenerative joint disease that represents more advanced stages of the disease, involving destructive changes of all joint structures, leading to disability and pain.

Alternatively, some researchers choose to explain the term of the disease for the avoidance of doubt, such as Ding and Overgaard in their studies [20, 21]. From now on in the present work, the term osteoarthritis shall refer to the degenerative disease which wears away the cartilage, as shown Figure 2.14 b).

Osteoporosis appears when the bone remodelling cycle does not work in the correct balance. This problem leads to a loss of bone mass and a high fragility of bone which implies a high risk of fracture. Owing to osteoporosis is the main bone disease to be studied in this work, an in-depth description of this disease will be carried out in the following sections.

2.6.2 Epidemiology and impact of osteoporosis

Osteoporosis is the most common bone diseases affecting people worldwide. This skeletal disorder is characterised by a compromised bone strength and predisposes the person to an increased risk of fracture, mainly in hip and spine [218]. As a result, osteoporosis has physical, financial and psychosocial consequences, which meaningfully affect the family, the individual and the community [219].

At the Unite States, the 2013 - 2014 National Health and Nutrition Examination Survey revealed that 16.5 % of American women aged 50 years or older had osteoporosis. In neighbouring countries such as Mexico and Canada it has been observed similar prevalence of osteoporosis. As the age arises the prevalence of osteoporsis by low bone mineral density (BMD) also does it. The rates go from 6.8 % in women aged 50 to 59 years to 34.9 % in women aged 80 years and older [218]. In Europe, osteoporsis is one of the most serious, debilitating and costly diseases and one of the least recognised. One in three women has osteoporsis in Europe and one in eight men aged 50 and older [220].

Eight new fractures occur every minute in the European Union. With this statistics, it is estimated than more than 23 million women and men are at high risk of undergoing an osteoporotic fracture in Europe. This pathology causes 4.3 million fragility fractures which excess the 56 billion euros each year

based on data for 2019 [221]. In the Unite States, there are registered more than 2 million fractures related to osteoporosis per year. Most of these fractures affected to postmenopausal women [218]. In Spain, 285000 new fragility fractures were estimated to be in 2019, which means 782 fractures per day or 33 per hour. In 2019 in Spain 1813 million euros were spent in the direct costs of incident fractures. The total costs generated of the osteoporosis, considering direct cost of incident fracture, long-term disability and intervention cost, make an amount of 4.3 billion euros [5].

In addition, a problem associated with this disease is the costs related to it. The population suffering from this disease has a high probability of undergoing a fracture. Apart from the pain of the patient, the surgery, the hospital stay and the rehabilitation are some of the costs associated with this fracture, so it means a high budget dedicated to cover these costs. Figure 2.16 shows the number of fractures occur per year due to osteoporosis in the Unite States, in the European Union and in Spain.
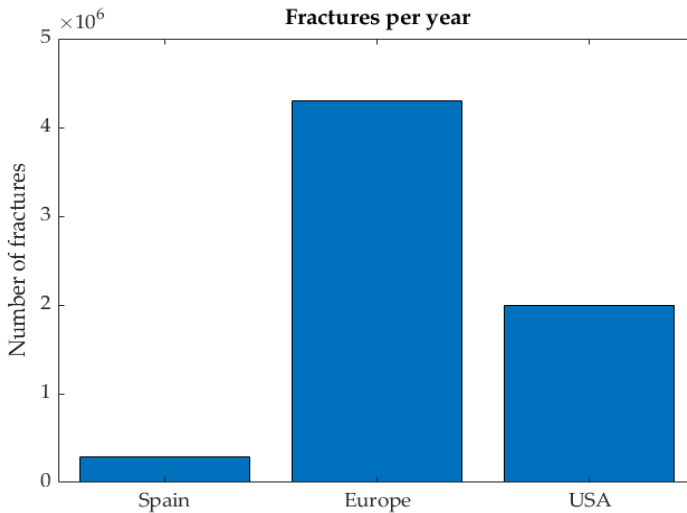
Figure 2.16: Fracture number related to osteoporosis in one year in the Unite States, in European Union and in Spain.

Owing to the huge presence that osteoporosis has in the society, it is really important to study how it behaves and the consequences that causes in bone

architecture and in bone mechanics. In this way, it would be possible to detect the disease at an early stage, which could mean the prevention of future fractures.

2.6.3 Pathogenesis of osteoporosis

The World Health Organisation (WHO) defines the osteoporosis as "a progressive systemic skeletal disease characterised by low bone mass and micro architectural deterioration of bone tissue with consequent increase in bone fragility and susceptibility to fracture".

The loss of bone mass is related to bone remodeling, which plays a major role in the emergence of osteoporosis. In this process, bone tissue is subjected to a constant change which is essential for bone strength. In Figure 2.17 it is shown a scheme of the bone remodeling cycle.
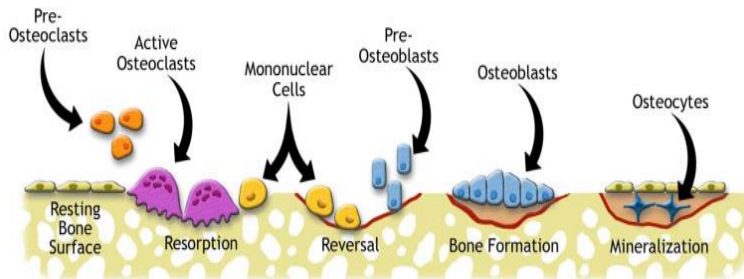
Figure 2.17: Scheme of the procedure followed in the process of bone remodeling. Image taken from [222].

First of all, old bone material, whose main components are the mineral and the protein matrix, is resorbed (removed) by osteoclasts action. Then, the osteoblasts take over the replacement with new healthy bone. Osteocytes interconnect in the solid matrix of bone via an extensive canalicular network that senses both mechanical loading and focal bone damage. The molecules that the osteocytes secrete regulate the rate of bone remodeling and the location where it is carried out. The mechanical loading and the circulating hormones, such as parathyroid hormone (PTH) and estrogen, are the ones which regulate the osteocyte activity [218].

Osteoporosis is a consequence of the imbalance of the two biological processes: the uncoupling of oteoblasts and osteoclasts, with an increase in osteoclast activity, leading to overall bone loss [14]. In the trabecular network formed by plates, the bone resorption produces a trabecular thinning and perforation. As a result, the trabecular area decreases [223]. Sometimes, an improper performance of osteoclasts in bone remodeling produces holes in the trabecular tissue, because they remove more material than the osteoblasts renew. In Figure 2.18, it is shown a comparison between healthy tissue (Figure 2.18 a)) and osteoporotic cancellous tissue (Figure 2.18 b)) perforated because of the osteoclasts high activity.

a) Healthy bone   b) Osteoporotic bone
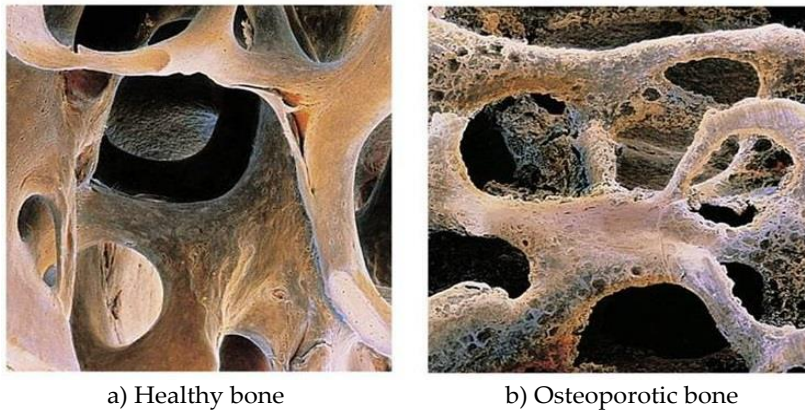
Figure 2.18: Comparison between a) healthy cancellous bone and b) osteoporotic cancellous bone with perforations consequence of a negative bone remodeling due to the high activity of osteoclasts (extracted from [224]).

Moreover, it is important to highlight that there are different types of osteoporosis which can affect different groups of the population. Figure 2.19 presents the classification of the different types of osteoporosis, where it is possible to clearly identify two main groups which are primary and secondary osteoporosis. Besides, other types of osteoporosis exist, but they are less frequent and are called "rare". One example of this type of osteoporosis is pregnancy and lactation associated osteoporosis (PLaOs), which is a rare and infrequent form of primary osteoporosis. It is characterised by the appearance of fragile fractures at the end of pregnancy or during the postpartum period, between 6-8 weeks after delivery, and most of these fractures occur in the spine. This osteoporosis occur in women over 30 years of age or first-time women. Although it is under research, there is no treatment for PlaOs, except

avoidance of heavy lifting, rest and means of support for the spine, such as corset [225].
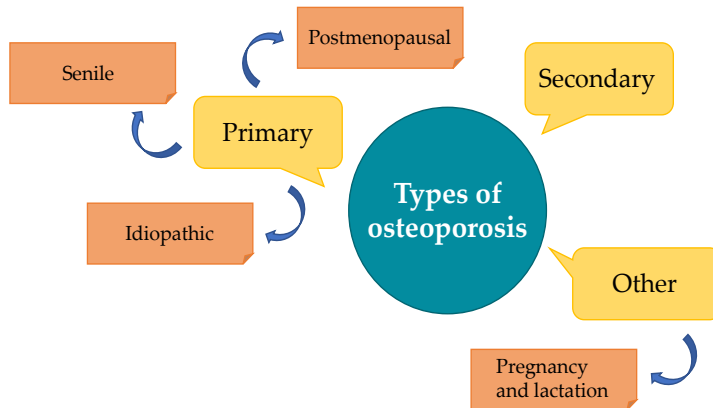
Figure 2.19: Classification of different types of osteoporosis.

Regarding the two main ones, the most common osteoporosis is the so-called primary osteoporosis which is gender and age-related. Roughly 95 % of all cases are due to primary osteoporosis, which can be divide into three groups as follows [226]:

- **Type I or postmenopausal:** one of the main causes of osteoporosis is the lack of estrogen. Besides, estrogen deficiency concerns the normal operation of bone remodeling cycle, which results in the increase of bone resorption and fast bone loss (high bone remodelling). What really happens is that osteoclastic resorption increases, whereas osteoblasts activity decreases. Consequently, the quantity of reabsorbed bone during the remodelling process is higher than the deposited, which leads to a bone loss. The increase of the overall bone resorption is because the weakened inhibition effect due to the reduction of available estrogen on both osteoclastogenesis and osteoclast activity. In women, two phases of bone loss can be defined as follows [227]:

  ◦ First phase: this phase mainly affects to cancellous bone and begins in the menopause. Owing to estrogen deficiency, a non-balanced increase in bone resorption as compared with formation has occurred. This stage can be defined as menopause related bone loss. This pronounced decrease of BMD is shown in Figure 2.20 in the first years of the left graph.

○ Second phase: after 4-8 years starts the second stage, which consists of a slow loss of cortical and cancellous bone and is primarily attributed to reduced bone formation. This is the only phase that suffer men, which is a bone loss related to age.

Men do not have an equivalent of menopause, therefore they usually do not suffer the rapid phase of bone loss. Nevertheless, they experiment a very similar pattern of the slow age-related bone loss as is presented in women [228]. All the trends for men bone loss are presented in Figure 2.20 in the right graph. Most of the affected population by this pathology are postmenopausal women who suffer the most severe fractures, such as spine or forearm fractures. Young postmenopausal women suffer less serious fractures, such as wrist fractures, which are important signs of osteoporosis.

- **Type II or senile:** it is characterised by a slow phase of trabecular and cortical bone loss (low bone remodelling) related to ageing in both men and women (usually over 65-70 years old) [226, 229]. The most typical fractures owing to type II osteoporosis include hip or femoral neck fractures, proximal humerus or shoulder, tibia and pelvis. The pathological mechanism of senile osteoporosis has not been fully clarified, however, secondary hyperthyroidism, nutrient deficiency or the decrease of osteoblasts activity.

- **Idiopathic:** in medical terms, idiopathic means that the origin of the disease is unknown [230]. This type of osteoporosis is infrequent and it is associated with the emergence in young adults and children with normal levels of hormones and vitamin D, without an evidence which can explain the weakness of bone. Idiopathic juvenile osteoporosis (IJO) affects both sexes equally and is a rare condition of primary bone demineralisation, which has a prepubertal onset and continues through puberty leading to a low bone formation and a huge decrease of trabecular bone. The main symptoms are back and limb pain, gait difficulties, multiple fractures to minimal trauma and radiological evidence of osteoporosis.

By the other side, secondary osteoporosis is due to certain diseases, side-effects of some medicines and risk factors and can be developed at any age [231]. There is a wide range of diseases and drugs that can affect bone quality and lead to osteoporosis such as anti-inflammatory medicines to treat asthma or rheumatism (cortisone), coumarin derivatives, high doses of thyroid hormones, chronic eating disorders like pancreatic, intestinal, hepatic or renal conditions, metabolic diseases, certain hormonal disorders as hyperthyroidism or diabetes
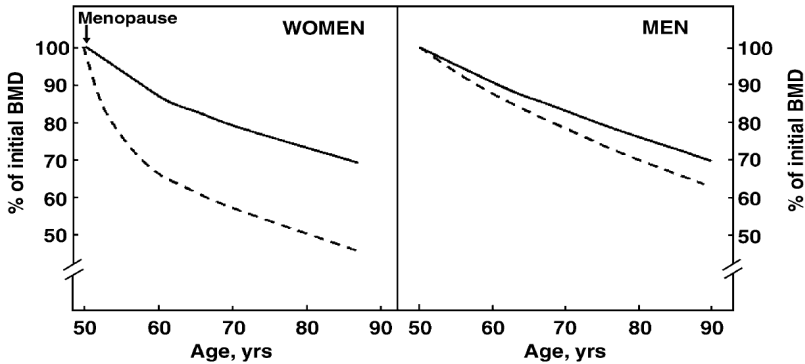
Figure 2.20: Bone loss age-related patterns in men and in women. Solid lines represent cortical bone loss and dashed lines represent trabecular bone loss. This image is based on multiple longitudinal and cross-sectional studies using DXA. Image extracted from [228].

mellitus, and malignant tumors. In addition, there are some risk factors which will develop osteoporosis such as genetic factors, cigarette smoking, alcohol consumption, physical inactivity, nutritional factors or prolonged immobilisation after a fracture [17]. Finally, glucocorticoid-induced osteoporosis proceeds through two phases starting with a rapid decrease in BMD due to increased bone resorption, during the remodelling process. This is followed by a slower phase in which a progressive decrease in BMD occurs as a result of the formation of deteriorated bone [232].

2.6.4   Diagnosis of osteoporosis

The World Health Organisation (WHO) classifies the bone mineral density (BMD) using a "T-score"(standard deviation's [SD] away from young adult mean bone mass value). Osteoporosis is defined as BMD with T-score equal to or less than -2.5 and osteopoenia with T-score between -2.5 and -1 SD. Figure 2.21 presents the T-score levels established by the WHO for defining the status of bone.

Some health professionals do not already use the term of osteopenia, but is defined as the stage of abnormal bone mineral density, but not as low as for diagnosing osteoporosis (BMD with T-score between -1 and -2.5). If osteopenia is not treated according to medical recommendations, osteoporosis will be

T-scores   Bone status
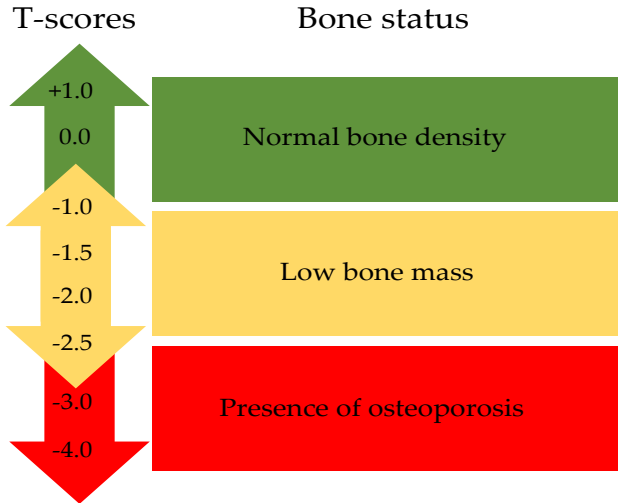
Figure 2.21: Definition of T-score levels established by the World Health Organisation (WHO) to define bone status (healthy, osteopenia or osteoporosis).

developed. It is important to emphasise the point that women are more likely to develop osteopenia after the age of 30 years old than men.

For the diagnosis of osteoporosis, it is recommended to use dual-energy X-ray absorptiometry (DXA) scanning for measuring the bone mineral density (BMD) and then calculating the T-score. In these cases, the femoral neck is the preferred body location for analysed the T-score. The reason why is because its highest predictive value for fracture risk unlike other parts of the skeleton. Other site where the impact of the osteoporosis is commonly studied is the spine. However, when the patient has any abnormality, the measurements can falsely elevate the bone mineral density, such as in post-menopausal women or elderly patients with degenerative changes. In such cases, the spine is not the chosen body location for measurements. Despite these particular cases, the preferred site for taking the measurements of the BMD for assessing the response of treatment is the spine [14].

In some other cases, exist some anatomic factors, such as hip replacement or arthritis, which prevent make measurements in the common anatomical sites like spine or hip and make them invalid. Hence, bone mineral density is measured in the distal one-third site of the radius, but also the assessment

of fracture risk and some other methods of diagnosing osteoporosis should be considered [218]. In addition, there are some other problems which can lead to high values of DXA-BMD such as micro-callus formations inside the vertebrae, bone islands and deformed or fractured vertebrae. T-score values obtained in these specific situations are neglected for a DXA evaluation [233].

The dual-energy X-ray absorptiometry (DXA) technique transforms the three-dimensional architecture of bone into two-dimensional reproductions which evidence the mass of calcium crystals per volume by the X-ray absorption in the unit of area (g/cm^2). For this reason, bone mineralisation effects on bone quality or the degree of bone structure are not distinguishable by DXA [233]. In Figure 2.22 it is presented a scheme of the steps followed in a densitometry assessment by DXA.

Region	DMO (g/cm²)	Adult – Young (%)		Adjust. Age (%)	
Neck	0.842	86	-1.1	88	-1.0
Wards	0.824	91	-0.7	103	0.2
Trochanter	0.988	125	1.8	120	1.5
Diaphysis	1.149	-	-	-	-
Total	1.030	103	0.2	102	0.1
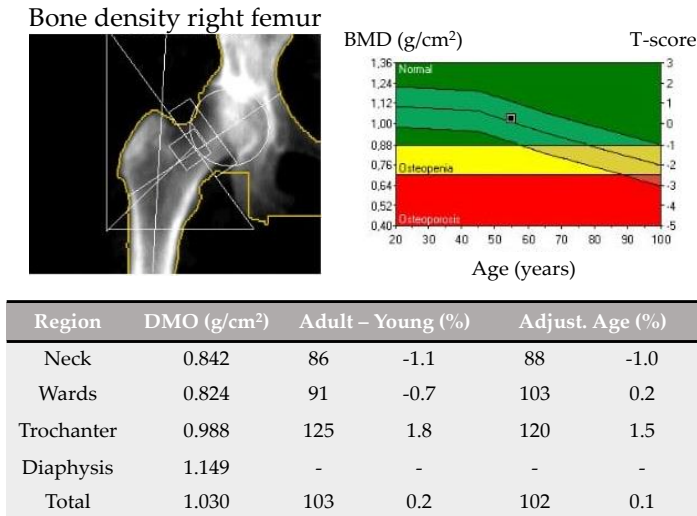
Figure 2.22: Densitometry evaluation by dual-energy X-ray absorptiometry (DXA) in the right femur (image taken from [234]).

Furthermore, there are more problems related to DXA evaluation such as the quantification of bone loss. Owing to the fact that the measurements of the bone mineral density (BMD) by DXA are at specific locations, it is possible to measure high values of BMD, and perhaps, at nearby locations will exist a loss of bone mass which will be unrecognized. The same effect will happen in the contrary situation.

Finally, due to all the aforementioned, it is stated that the DXA technique used for the diagnosis of the osteoporosis presents some drawbacks which will lead to inconsistent values of the BMD measures, and consequently, the T-score values. Therefore, the need arises to add some other parameters of study, such as the architecture of bone by a morphometric study, for making a better diagnose of osteoporosis.

2.6.5 Osteoporotic tissue

Osteoporosis is a chronic disease featured with great changes in bone architecture across bone length scales and a low mineral fraction [40]. Bone undergoes some variations such as low remodelling activity, thinning of the strut thickness or bone loss mass which entails an increased of both fragility and risk fracture. All these changes have a direct effect on bone mechanics, so it is quite important to study it.

Figure 2.23 a) shows the trabecular network of a healthy bone, whereas Figure 2.23 b) presents the degraded architecture of an osteoporotic cancellous bone. At first glance, major differences can be seen such as less number of struts, the ones that remain are thinner, less connection of the trabecular network or bigger spaces between rods. All these changes in bone structure are directly related to the mechanical properties, which will also be degraded.
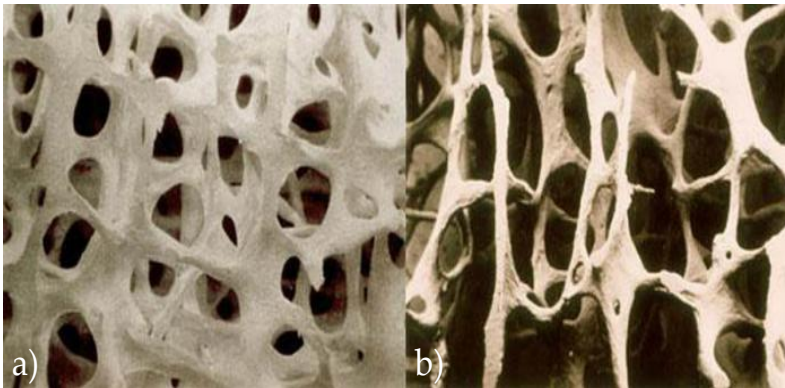
Figure 2.23: a) Bone tissue in healthy conditions and b) diseased bone tissue. Comparing both images it is possible to see the degradation of the trabecular network due to the illness. Image taken from [235].

One relevant point to note is that in an osteoporotic sample, it is really important to clearly distinguish among the possible sources of porosity, which can be identified as follows:

- Structural changes: several alterations in the microarchitecture of bone such as thinner rods thickness or lower number of struts in the cancellous network (Figure 2.23).

- Tissue perforations: deep cavities in bone tissue due to the negative balance of bone remodelling activity (Figure 2.18 b), usually known as osteoclastic perforations.

- Natural porosity: it is refered to small pores in the tissue, the lacunae left by the death of osteocytes and the gaps left by the canaliculi network presented in Figure 2.24.
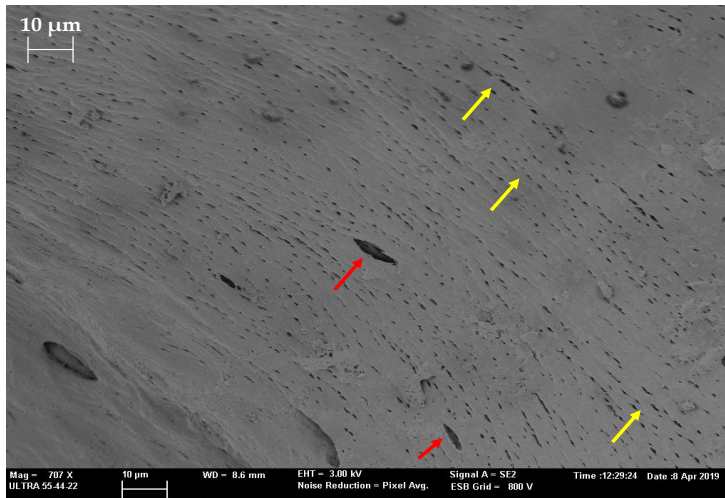
Figure 2.24: Natural porosity of bone tissue. Red arrows point porosity due to lacunae after osteocytes death. Yellow arrows point the pores left by the canaliculi network.

All these changes in bone tissue and trabecular network, will lead to a weakness of the bone. Müller *et al.* [236] studied the microscopic bone properties in different cases of osteoporosis in sheep. They reported that the maximum force until failure and the morphometric parameters of trabecular bone can change by up to 50 % due to osteoporosis.

Furthermore, there are some other factors that can be affected bone tissue such as matrix composition, microarchitecture, bone mineralisation and microdamage. In addition, it is known that age-related factors also affect the quality and integrity of bone tissue. These type of factors are not possible to be measured in the clinical practice. In postmenopausal osteoporosis, when all these changes are combined in structure, bone mass and quality, the result is the reduction of bone strength and the increased of fracture risk [218].

For all the above-mentioned reasons, the structure of bone should be included in the study of bone quality and to improve the diagnosis of some diseases such as osteoporosis. Therefore, several researchers focused their studies in the analysis of bone microarchitecture and its relevance to the mechanical response of bone.

Morphometric studies analyse the structure of bone, such as thickness of the rods, the quantity of struts and the connection between the ones that remain in the structure. Owing to each bone disease causes some different effects in bone architecture it is really important to analyse and study the morphometry of these types of sick bones. Moreover, it is possible to relate the morphometric parameters with some bone properties such as its stiffness.

In 2006, Müller *et al.* [22] studied the importance of the trabecular network structure in the evaluation of bone quality and stiffness. They found that some morphometric parameters of the microarchitecture of bone, such as bone volume (BV/TV) or surface ratio (BS/BV), have more influence in bone stiffness than the rest. They established that the greater bone volume, higher Young's modulus.

Over the years, many works have been analysed bone morphometry to study the behaviour of diseased bones. Blain *et al.* [189] studied osteoporotic and osteoarthritic femoral neck bones and found that the trabecular width, the trabecular number and the percentage of cancellous bone area was lower for the osteporotic bone. In line with this, they found the inverse tend for the trabecular separation which was greater for the osteoporotic bone. Finally, they stated that in postmenopausal women there was a loss of trabecular bone mass and connectivity in comparison with osteoarthritic women, and also, the cortical bone was thinner. Some other researchers continue studying the morphometry of bone such as Montoya *et al.* [190] or Ding and Overgaard in 2021 and 2022 [20, 21] due to the importance of considering microarchitecture in the study of bone mechanics.

In conclusion, osteoporosis is a bone disease which triggers many changes in bone structure and tissue. This degradation of bone leads to a high risk of fracture and devalued mechanical properties. Although osteoporosis is clinically diagnosed by the T-score value of BMD measured by DXA, this technique do not give information about bone architecture. For this reason, it is quite important to consider the morphometry of bone for an accurate diagnose. In osteoporotic bone, it is essential to include the sources of porosity which cause changes in bone structure and tissue, and take them into account in the study of bone mechanics.

2.7 Additive manufacturing in biomechanics

Over the years, traditional manufacturing has been used in the industry involving processes such as casting, injection moulding, forging, extruding, forming process, folding, laminating and machining manufacturing process such as turning, milling and drilling. All these manufacturing processes require formative and substractive approaches which entail expensive infrastructures and multiple steps. Furthermore, traditional manufacturing processes have some drawbacks such as they do not enable generations of complex geometries which are usually required for specific applications like patient-specific implants in biomedical engineering [237]. Moreover, some of these manufacturing processes involve a waste of material such as in turning or milling, which results in an expenditure of resources and money. For all these reasons, manufacturing technology has had to reinvent itself to adapt to new needs and has become more challenge and competitive.

In the recent decades, additive manufacturing has become increasingly important owing to the wide range of possibilities it offers in terms of available materials, geometries and technologies. Additive manufacturing (AM) may be defined the process of joining materials for the production of objects. The fabrication with AM technology is reached by adding successive layers of materials on those already deposited using direct data from 3D Computer Aided Design (CAD) models [238]. By contrast to substractive manufacturing methodologies, additive manufacturing is applicable to a wide range of materials, including metals, polymers, composites and biomedical products [239].

Additive manufacturing has become a strong tool for producing complex geometries in much cheaper and less time consuming mode [237]. At the beginning, the first important application was the production of rapid prototyping, but with the pass of the years and the improvement of this technique a grow-

ing number of applications used AM for manufacture products such as medical implants, hearing-aid shells, moulds for clear braces for teeth, aircraft engines (i.e. the GE fuel nozzle) and other aerospace parts [240]. In the last years, the interest in additive manufacturing processes has increased and it is estimated that accounts for more than 5 % of the total global market. Even so, AM technologies have several problems related to poor quality, low productivity and uncertainty of the mechanical properties of the final produced parts [239].

Finally, it is important to highlight that additive manufacturing involves several processes, but probably the most popularly known is 3D printing. In fact, the process for 3D printing is called Fused Deposition Modeling (FDM) which has some other techniques of production. In the following section, all the AM processes will be defined for being able to identify which process could be suitable for each specific case.

2.7.1 Definition of additive manufacturing processes

Additive manufacturing (AM) presents diverse processes, presented in Figure 2.25, which are material jetting, vat photo polymerization, binder jetting, material extrusion, directed energy deposition, sheet lamination and powder bed fusion.

Figure 2.25: The seven main types of additive manufacturing processes [241].

The seven main processes of additive manufacturing are the following:

- **Material jetting:** molten material or usually a binder (adhesive) is sprayed in a monitored manner using thin nozzles in order to bind the powder in a solid object. Every completed layer is cured by UV radiation. This process is similar to all laser-melting processes, although there is no change in the phases. In contrast, powder particles remain together due to the binder [32].

  One important point is the possible problems of this process. Firstly, the most important factors are droplet size and velocity, which have a main role in the deposition characteristics. Besides, a problem related to the quality of the finished part is that there are satellite droplets, which detach from the main droplet during flight, so the result is that the boundaries of the design part are not well defined [239].

- **Vat photo polymerization:** the object is created in a vat of a liquid resin photopolymer. Photopolymerisation cures or hardens each layer of micro-thin resin using ultraviolet (UV) light directed by monitored mirrors creating the object from below. Owing to this process uses liquid to form objects, there is no structural support of the material during the construction phase. The three primary subcategories are stereo lithography, continuous digital light processing and digital light processing.

  It is important to highlight that the parts manufactured through this technique usually have high surface finish and dimensional accuracy in comparison with other AM processes. However, this process has its drawbacks such as impact strength and durability of photopolymers is worst of those of good quality injection molded thermoplastics [242].

- **Binder jetting:** in this process a binding agent is deposited, usually in liquid state, selectively onto powdered material. The print head places layer by layer a bonding agent and construction material, and a powder spreader to generate the three-dimensional part. The main difference between binder jetting and material jetting is that in the first one the head printer only works in x and y, whereas in the other process it works in the three directions and has to cure by UV each layer once finished. One disadvantage is that the parts created by this process, using water based binder process and plaster based powder, tend to have low stiffness and strength [239].

- **Material extrusion:** this is a thermal process which uses heat extrusion nozzle for softening or melting the material. Generally, the most widely used material is plastic which is provided in the form of wire wound on

a spool. When the material is melted goes through the extrusion nozzle which places the material in a warm bed layer by layer. After that, the material cools off to solidify and generate the final 3D geometry [32].

There are several methods of this process such as fused deposition modelling (FDM), inkjet printing (IJP), contour crafting (CC), shaped deposition manufacture (SDM), extrusion free forming (EFF), robocasting, among others, but the most well-known is the first one because is the 3D printing technology. Nowadays, it is quite common to have a 3D printer at home because they are affordable and owe to create a wide range of products. For this reason, it is easy that people confuse the terms 3D printing, fused deposition modelling and additive manufacturing which are completely different, since one embraces the others.

- **Powder bed fusion:** this process consists of melting the powdered material and fusing it by a laser or an electron beam to produce the 3D object solid. The most common methods are electron beam melting (EBM), selective laser sintering (SLS), multi-jet fusion, direct metal laser sintering (DMSL), selective heat sintering (SHS) and selective laser melting. This AM process was one of the first to be commercialised. At first were developed to manufacture plastic prototypes, but this approach was extended to metal and ceramic powders [243].

- **Sheet lamination:** in this process a special type of paper is used, which has heat-sensitive adhesive applied in one of its faces. A roll provides the paper and is bonded to the previous layer using a heated roller which enables the adhesive of the paper. The contour of each layer is made by cutting with a CO_2 laser that is configured to cut only one layer of thickness [32]. Once the object is finished, the excess material is removed for obtaining the 3D part. Two methods of this process are laminated object manufacturing (LOM) and selective deposition lamination.

- **Directed energy deposition:** this method is quite similar to welding process, but it is much more complex. This process permits the generation of 3D objects by melting material while depositing. This approach can work with ceramics, polymers and metal matrix composites, although it usually used for metal powders. These machines deposit the melted material on specific surface, where it solidifies. With this technique, the nozzle can move in multiple directions, unlike the extrusion of the material.

Subsequently, we will focus on fused deposition modelling (FDM), a technology included in the material extrusion concept, since it will be employed in this PhD thesis.

2.7.2 Fused Deposition Modelling (FDM) Technology

Fused deposition modelling (FDM) is one of the technologies of material extrusion. FDM process is one of the most commonly used of the whole AM processes because it requires low technology, cost and maintenance [244]. Some other strong points of this technology are the wide range of materials available, compact design, easy to operate, low temperature operation, affordable cost and it usually do not need post-processing.

The scheme of FDM technology is presented in Figure 2.26. The main components are filament, the print cores, the extrusion nozzles and the heat platform. The material is stored in a spool in form of a wire, the so-called filament, which passes through the feeder and then goes upward the bowden pipe until reaches the print core entrance. The feeder has two gears to push upwards the filament, and it is important to keep clean. Once the filament is in the print core, it is liquefied by heating it few degrees above its melting point, so it solidifies just after being deposited. The melted material is extruded by pushing continuously the filament upwards for feeding the nozzles [238]. The material is deposited by the nozzles in the heat platform layer by layer. When one layer is finished, the platform moves one space down to let the nozzle deposit the next layer. Depending on the 3D printer, the platform is fixed in height with only a 2D movement in the plane. In this case, the printer cores move down to deposit the fused material on the platform and then go up to enable the starting of the following layer.

3D printers usually have two print cores which enable the printing either with two colors of the same material or with two different materials. This last option is quite interesting due to it permits building supports for a better generation of the final part (i.e. purple material shown in Figure 2.26 is the one used for generating the 3D object, whereas yellow material is the one used for printing the supports). After the printing is finished, the support material should be removed away from the 3D object. The material used for building supports should be easy to removed or soluble, such as polyvinyl alcohol (PVA) which is water soluble.

Furthermore, it is important to consider that there are several parameters to setup for defining the printing. Some of these parameters are layer thickness,
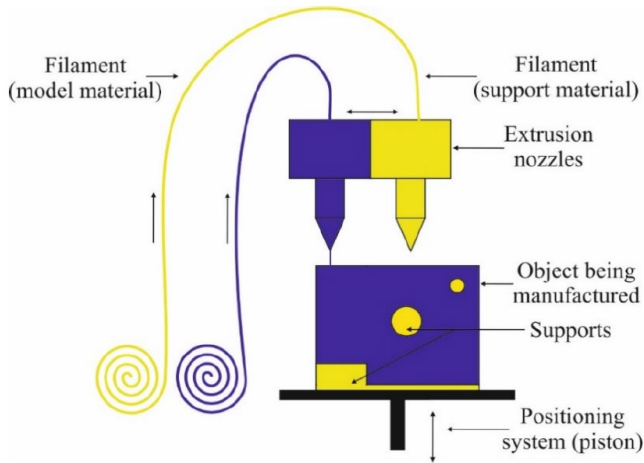
Figure 2.26: Fused deposition modelling (FDM) scheme. Picture extracted from [245].

filling quantity and pattern, wall thickness, adhesion to the heat platform or extrusion rate. The geometry of the final 3D object plays an important paper in the setup of the print parameters, for example, a more complex geometry requires a slower extrusion rate. The quality and the mechanical properties of the resulting part depends on the above mentioned parameters. In addition, temperature is other critical parameter because it is really important to setup all of them properly for having excellent results, such as the temperatures of the print cores, heat platform or chamber. A wrong configuration should lead to various issues such as air gaps between layers, distortions, material warping, dimensional accuracy or lower mechanical properties.

At the beginning, this technology was used mainly to produce rapid proto-types, but with the implemented improvements FDM has expanded the action fields to aerospace, implants, biomaterials, building or replacement parts. The simplicity of FDM, its affordable equipment, the wide range of materials and the recent improvements, permit to employ this technology in extra spaces such as laboratories, libraries, houses and schools [246]. Even though the ad-vantages, there are several drawbacks to solve such as poor surface texture, post-processing, mechanical weakness or void formation in comparison with other AM process like powder-based plastic which has better accuracy and surface quality [32].

2.7.3 Polylactic acid (PLA)

One strong point of fused deposition modelling (FDM) technology is that it allows the use of a widespread range of materials. In 3D printers it is possible to used different kind of filaments, such as metals or composite materials, but the most widely used are polymers. Polylactic acid (PLA) and acrylonitrile butadiene styrene (ABS) are the most popular ones. However, depending on the application, it is possible to choose from many more, such as polyethylene terephthalate (PET) and polyethylene terephthalate glycol (PETG) plastic used for food and drink packaging. In addition, it is possible to use thermoplastic elastomers (TPE), thermoplastic polyurethane (TPU) and thermoplastic co-polyester (TPC), which are used in automotive parts, household appliances and medical equipment due to their durability and extreme flexibility. On the other hand, polycarbonate (PC) is used in bulletproof glass, diving masks and electronic devices because it is transparent and resistant to impact and heat. Lastly, nylon has the best flexibility, durability and toughness, whereas polyvinyl alcohol (PVA) is utilised as a support material because it is soluble in water.

The material used in the present thesis is PLA because it is biodegradable, biocompatible and it has excellent properties for biomedical applications. Polylactic acid (PLA) is a thermoplastic aliphatic polyester which can be produced from lactic acid using renewable materials such as corn starch, sugarcane, maize, sugar beet and cassava [247, 248]. Moreover, PLA is compostable and its degradation produces water (H_2O) and CO_2 which can be used and reabsorbed by plants. Seawater, compost and soil are the most significant environments for PLA degradation [249, 250]. The whole process since the production of PLA, the manufacturing into a product and biodegradation, constitutes the life cycle of PLA, which is presented in Figure 2.27.

PLA has replaced common plastics often employed as materials for packaging such as polypropylene (PP), polyethylene terephthalate (PET), polyethylene (PE) and polystyrene (PS), because generally are not biodegradable or nonrecyclable. Furthermore, PLA presents a long list of advantages like thermal stability, desirable mechanical properties, low environmental impact, good biocompatibility, UV resistance, gas barrier and thermoplasticity. In addition, it has a high elastic modulus, transparency and strength in comparison to petroleum-based plastics. However, PLA has several drawbacks such as poor toughness, low melt strength or excessive brittleness which restricts its applications and promotion in some fields [247, 249, 252].

Figure 2.27: Diagram of polylactic acid (PLA) life cycle. Picture taken from Peng and Sun work [251].

Furthermore, it is possible to mix PLA with some other materials in order to improve its properties. There are various procedures such as the inclusion of inorganic fillers into PLA matrix, like carbon nanotubes, nanoclay, zinc oxide or titania (TiO_2), that are effective to enhance PLA properties [252]. Besides, one strong point of PLA is that it can be used as medical material because it has a great biocompatibility. PLA metabolism inside the human body produces lactic acid (LA), which can be metabolized and is non-hazardous and non-toxic. For this reason, PLA is used in medical applications such as implants, vascular stents, surgical growns, masks, medical sutures, heart valves and some other [249]. This point will be further developed in next section.

2.7.4   Implementation of additive manufacturing in biomedical field

Some strong points of AM technology, such as reduced waste of material, short production time, creation of innovative complex geometries or demanding materials, encourages the biomedical sector to use this kind of manufacturing processes. Additionally, this technology features an array of new applications
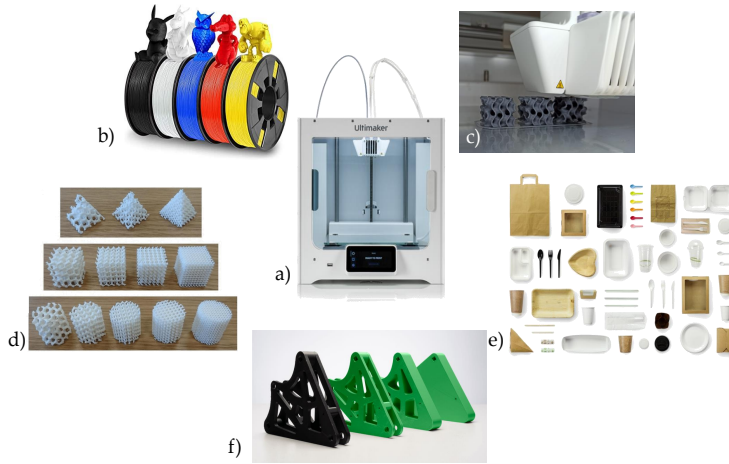
Figure 2.28: PLA used in 3D printers along with fused deposition modelling (FDM) technology. a) 3D printer, b) PLA filaments, c) 3D printer manufacturing, d) PLA scaffolds for bioengineering, e) PLA as a substitute for plastic in disposable packaging and f) prototypes.

which involve a large amount of medical purposes using additive manufacturing (AM) [237]. Several of the main applications of AM in the biomedical sector are orthopedics, drug deliver, organoids, surgical instruments, tissue regeneration, prosthesis, implants/scaffolds and tissue engineering (some of them are shown in Figure 2.29).

In the past decades, bioprinting has enabled the manufacturing of highly complex and intricate organoids. Nowadays, there is a large number of laboratories which have used this technique for producing biologically operative models such as kidney [253], skeletal muscle [254], liver [255], mammary epithelium [256], neurons [257] or myocardium [258]. All these complex 3D constructions of functional parts and organoids allow the study of some diseases and several treatment reactions. As usually, there are some drawbacks, such as replicating cell growth environment or the fact that some elastic biomaterials could not permit the generation of complex prototypes which can support their profile and also, restrict movements and cellular interactions [259].

One of the most popular applications of additive manufacturing (AM) in the biomechanical field is bone implants, which require specific features for avoiding problems such as stress shielding and encouraging osteointegration and bone growth [260]. Materials used for these applications play an essential role,
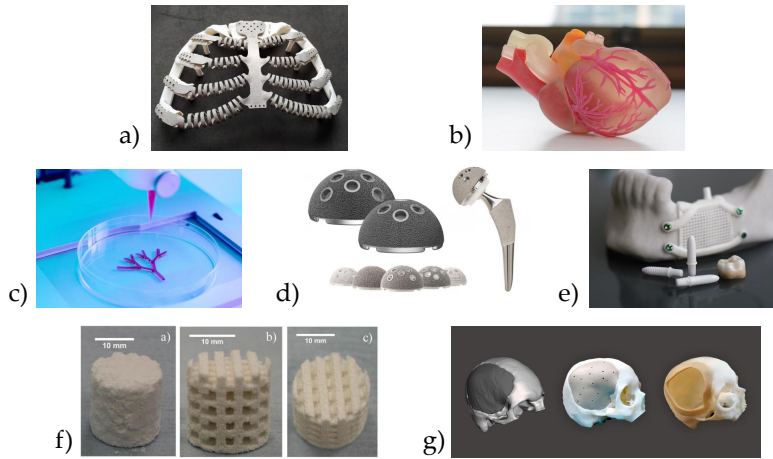
Figure 2.29: Several medical parts produced by additive manufacturing (AM): a) rib prosthesis, b) organs, c) blood vessels, d) femoral head prosthesis, e) dental implants, f) bone scaffolds and g) plate for skull prosthesis.

so they must have good mechanical properties and biocompatibility. Choosing the material for the implants is of great importance because not matching its elastic modulus with the human bones will produce a stress shielding phenomenon. This problem results in loose or broken implants. For this reason, researchers started introducing porous structures to mimic bone due to the ability of pore size and porosity to adjust the strength, density, and elasticity modulus of the resulting structure. In such a way, stress shielding can be eliminated o alleviated [261]. Moreover, these porous structures are auspicious for the adhesion and proliferation of osteocytes, all promoting the growth of new osteocytes into the pores [262]. Also, it allows the body fluids to circulate and permits a suitable waste and nutrient exchange with the surrounding tissue, promoting tissue reconstruction and regeneration [263, 264].

In the beginning, the most typical structures for bone implants were reticulated. These structures are composed of intertwined vertical and horizontal rods, resulting in a porous structure (Figure 2.30 a and b). The wide range of possibilities which AM offers, allows to generate scaffolds employing different manufacturing techniques, such as fused deposition modeling [265] or laser melting deposition, and several materials like polylactic acid (PLA) [266–269] or Ti6Al4V [270]. In addition, mixed materials such as Polylactic acid/Hydroxyapatite (PLA/HA) composite have been studied in some works because

of its good processability, bioactivity, and mechanical properties [271,272]. Hydroxyapatite (HA) is an inorganic mineral present in human bone and teeth. It plays a role in the structural strength of bone and in bone regeneration. For this reason, HA is sometimes mixed with PLA for improving implants' mechanical properties. Besides, other combinations have been studied in order to improve different features of materials, such as biocompatibility or mechanical properties [273–276].
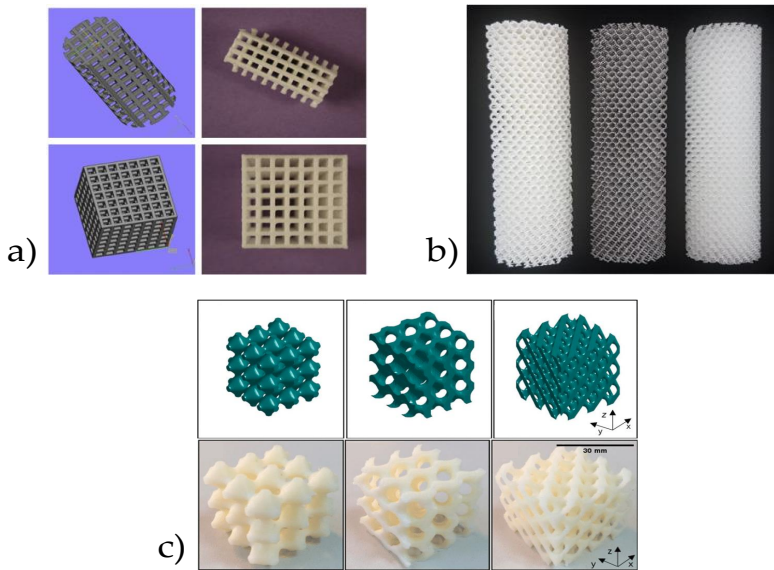
Figure 2.30: a) Designed 3D models of scaffold structures (left) and SLS-printed scaffold (right) [277], b) additive manufactured periodic open cellular structures (POCS) made of ABS, Ti6Al/4V and resin (from left to right) [278] and c) triply periodic minimal surface (TPMS) structures CAD (top) and FDM manufactured structures using ABS (bottom) [279].

Finally, triply periodic minimal surface (TPMS) structures (Figure 2.30 c) have become very popular in recent years because of their outstanding properties such as high strength-to-weight ratio, smooth surface, high energy absorption or interconnectivity, being used in several applications including robotics, acoustic attenuation, energy absorption or medical implants. These structures are periodic geometries with a continuously curved surface, implying a lower level of stress concentrators than other structures, such as scaffolds, and a smooth stress distribution at the surrounding surfaces. Moreover, TPMS structures have a lattice architecture more similar to trabecular network than scaffold structures. In addition, at every point on the surface, they have zero-

mean curvature, which improves the mechanical properties and load-bearing capacity [260, 280, 281].

In tissue engineering, a compromise between permeability and mechanical properties is required. Increasing the porosity of the structure leads to a reduction of Young's modulus of the implant. Furthermore, this interconnected porous structure enhanced the migration, adsorption, and proliferation of the cells, blood vessels, the transport of oxygen and nutrients, and the growth of bone tissue. All these characteristics are conducive to stable bone binding of the implant [282].

Additive manufacturing (AM) has enabled the manufacturing of all these types of porous structures due to the capability to generate complex geometries. The main problem of AM technologies for generating porous structures is accuracy. For this reason, implants obtained by these techniques usually need a postprocessing process to improve the surface finish owing to geometrical deviations that can affect the osseointegration process and the mechanical properties of these porous structures [280].

Chapter 3

Image analysis of cancellous bone

3.1 Introduction

In this chapter, we aim at studying the cancellous bone structure with imaging techniques. The main objective is to understand the arrangement of the trabecular network architecture through the analysis of images taken at different length scales. More specifically, we seek for characterising the orientation of the collagen fibrils that belong to the trabecular network struts.

This study focuses on lamellar tissue, which consists of a collection of struts and plates. As it is well known, bone adapts its growth conditioned by the stresses that it has to withstand, so these struts and plates grow according to them. Without taking into account the bone cells, lamellar tissue is formed by mineralised fibrils assembly and the extra-fibrilar matrix. These fibrils are made of molecules of tropocollagen type I, crystals of mineral and water, and have the same role as the fibers in a composite material, providing stiffness. On the other side, the extra-fibrilar matrix consists mainly of non-collageneous proteins, water and amorphous mineral.

Before the image analysis, bone samples were prepared. First, the samples were cleaned to remove all the organic remains, and then the lamellar tissue surface was ready for applying both imaging techniques, the field emission scanning electron microscope (FESEM) and the stereomicroscope. Through the use of the FESEM, it is possible to distinguish the mineralised skeleton of bone lamellar tissue and to infer the location of the collagen fibrils and their orientation at the struts. The knowledge of fibril orientation extracted from the images is essential for defining the elastic and stiffness properties of lamellar tissue in highly detailed numerical models.

In summary, in this chapter, we study the cancellous bone architecture and the lamellar tissue using μCT, the stereomicroscope, and the FESEM. The specimens studied in this section came from swine lumbar vertebral trabecular bone and human femoral heads.

3.2   Cancellous bone samples description

In this thesis, two types of cancellous bone samples have been analysed. On the one hand, swine lumbar vertebral cancellous samples have been studied by imaging techniques, such as FESEM and the stereomicroscope. Besides, the numerical models used for validating the elastic properties equations developed for lamellar tissue in Chapter 4 were generated from the vertebral specimens. Furthermore, bone surrogates manufactured by additive manufacturing (AM) studied in Chapter 7 were vertebral trabecular samples from the swine specimens.

On the other hand, cancellous bone samples from human femoral heads have been assessed by several approaches, such as imaging techniques, experimental tests, and numerical models. We have three types of femoral specimens, depending on whether they have or not a pathology, such as osteoporosis and osteoarthrosis, which are the bone diseases studied in this PhD thesis. These specimens have been studied and analysed in Chapter 6.

In the following sections, swine and human cancellous bone specimens will be described.

3.2.1 Swine cancellous bone samples from lumbar vertebrae

The vertebral column forms the central axis of the body skeletal structure. Together with the sternum and twelve pairs of ribs, it constitutes the trunk skeleton. The vertebral column provides strength and flexibility as a sturdy and flexible midline support [283]. The spine is composed of vertebrae, which are divided into seven cervical (C1-C7), twelve thoracic (T1-T12) and five lumbar (L1-L5). The sacrum and the coccyx are at the lower end of the spine. Figure 3.1 shows the anatomical parts of a standard vertebra.
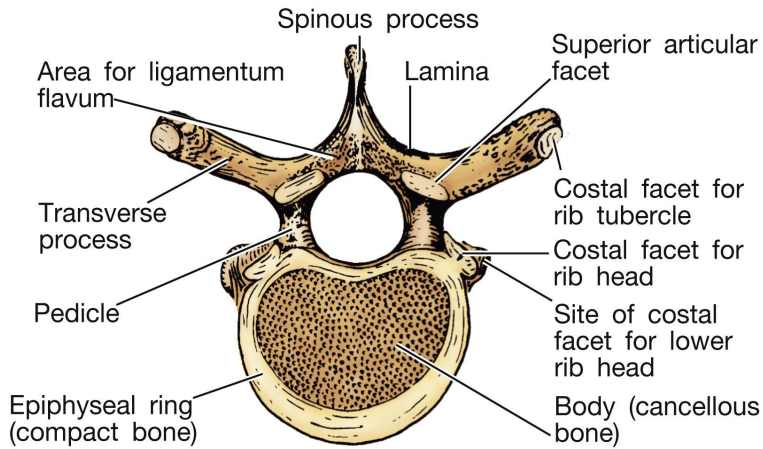
Figure 3.1: Anatomical regions of a standard vertebra [283].

Porcine spines are a common substitute for human specimens in both *in vivo* and *in vitro* experiments related to spinal fusion and instrumentation methods. The choice of experimental specimens is influenced by several factors, including the experiment nature, the animal characteristics, such as anatomical and functional similarities to human models, the composition of the bones and considerations of cost and availability [284]. McLain and colleagues [285] compared the morphometry of the fourth lumbar vertebrae in human, porcine, dog, and ovine specimens. The results revealed that porcine specimens displayed several distinct advantages compared to the other models investigated. Consequently, porcine samples are a viable substitute for human specimens *in vitro* analyses.

The vertebral bodies play a vital role in providing essential support to the spine weight-bearing system. Primarily composed of cancellous bone, the central

part of the vertebral body is specifically designed to withstand the typical forces exerted on it. By examining the orientations of trabeculae within the bone, we can infer the customary forces that the vertebra experiences [286].

The vertically oriented trabeculae within the vertebral body play a crucial role in supporting compressive loads. Additionally, at the upper and lower surfaces of the body, oblique trabeculae extend upward or downward to further assist in this compression-bearing function. These oblique trabeculae converge at the pedicles, providing resistance against tensile forces in that area. Moreover, they extend towards the superior and inferior facets and outward to the spinous process. The trabeculae oriented towards the facets are specifically aligned to support both compressive and shear forces acting on them. In contrast, the trabeculae directed towards the spinous process are designed to withstand the tensile and bending forces applied to this region. Altogether, this intricate arrangement of trabeculae within the vertebral body enables it to effectively manage various types of loads and stresses, maintaining the spine stability and functionality [286].

During compressive loading, the center of the end plate supports elevated pressure, making it a usual site for failure. This failure often arises from the nucleus of the disc rupturing the endplate. This can become a significant issue for patients with reduced bone strength, as seen in osteoporosis. Osteoporosis is characterised by decreased bone volume, leading to an increased risk of fractures even with smaller external loads. The vertebrae, filled with blood, may exhibit behavior akin to hydraulically enhanced shock absorbers when subjected to suddenly applied loads. This hydraulic-like effect could help dissipate and distribute forces, potentially reducing the impact on the end plates and lowering the risk of failure.

In Figure 3.2, from Mosekilde's work [287], it can be seen the trabecular architecture of the body of a vertebra with a prominent structure orientation in the vertical direction, formed by plates, and a trabecular lattice in the other two orthogonal directions, called rods or struts. This structure is directly related to the loads that the vertebrae withstand. Owing to the location of the vertebrae in the skeleton, the predominant applied loads are in the vertical direction. Therefore, plates grow and develop in such a direction, resulting in the stiffest direction of the vertebral body. Whereas in the other two orthogonal directions, the dominant structure is the strut which creates a trabecular lattice.

Moreover, age effects can be observed. Figure 3.2 (a) corresponds to a vertebral body from a young individual with a dense central trabecular network,
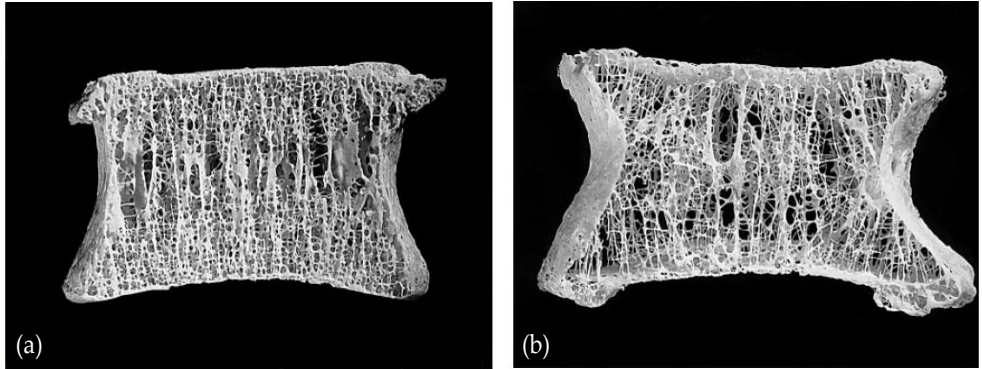
Figure 3.2: Human vertebral body from a young (a) and elderly (b) donor. Figure taken from [287].

whereas Figure 3.2 (b) corresponds to a vertebral body from an elderly individual whose trabecular bone density has decreased causing greater porosity. The degradation of bone architecture has a strong impact on the mechanical properties; thus, the vertebra shown in Figure 3.2 (b) can withstand less level of stress, being more likely to undergo a fracture.
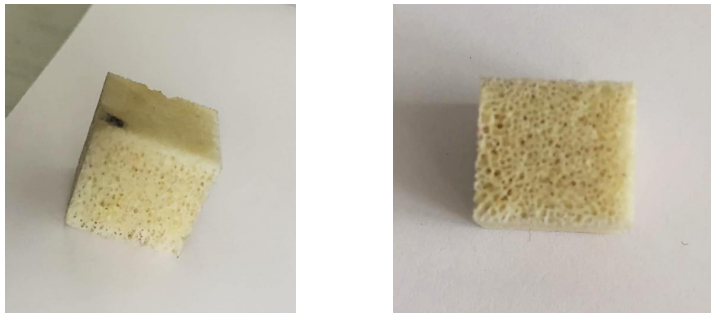
Figure 3.3: Swine cancellous bone samples from lumbar vertebrae analysed in this thesis.

Figure 3.3 presents the vertebral cancellous specimens used in this thesis. The studied cancellous bone samples were taken from the bodies of lumbar vertebrae of a skeletally mature swine, which does not have any pathology or disease that can affect the mechanical properties of bone. For its preparation, the specimens were cut using a saw, resulting in cubic samples with minimum

dimensions of 10 mm per side. The sample dimensions are crucial to ensure they are representative of the bone they originated from. In this chapter, cancellous bone structure and orientation of lamellar tissue are evaluated. The lumbar cancellous samples are used in this thesis to validate the elastic equations developed in Chapter 4 and to obtain bone surrogates manufactured by additive manufacturing in polylactic acid (PLA) in Chapter 7.

3.2.2 Human cancellous bone samples from femoral heads

The femur is the heaviest, longest and strongest bone in the human body whose principal function is gaiting stability and withstand the body weight [288]. The upper third of the limb is call proximal femur which is divided in four main sections (Figure 3.4): femoral head, femoral neck, intertrochanteric area and subtrochanteric area. There are two prominent bony protusions alongside the intertrochanteric area called greater trochanter and lesser trochanter. The upper end of the femur, which is the femoral head, fits into the hip cavity, called acetabulum, forming the hip joint. On the other hand, the lower end of the limb is joined to the tibia by the knee joint [289].
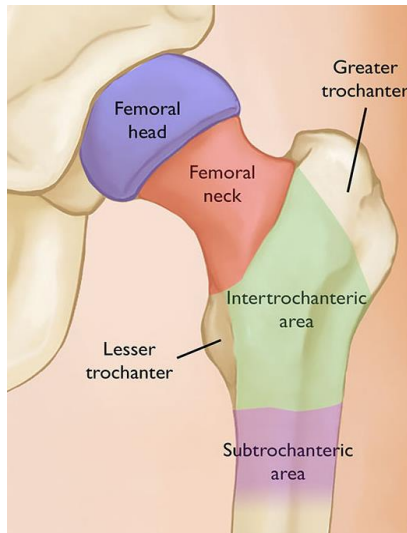
Figure 3.4: Anatomic regions of the proximal femur. Figure taken from [290].

The femoral head-neck junction is situated within the joint capsule and constitutes the subcapital area of the femoral neck. In contrast, the femoral neck-

intertrochanteric junction, known as the basicervical region, is located outside the joint capsule. The space between the greater and lesser trochanter of the femur defines the intertrochanteric region. Additionally, the area extending approximately 5 cm below the lesser trochanter is called the subtrochanteric region [291]. The proportion of the femoral neck to the femoral head strikes a balance between fracture resistance and the range of motion in the hip joint [292].

The hip joint consists of a spherical ball, the femoral head, that fits on the hip hole called the acetabulum. The hip joint plays a vital role in generating and transmitting forces during everyday activities, with an essential biomechanical function [292, 293]. While bearing approximately two-thirds of the total body weight, the hip joint must also facilitate the seamless movement of the lower limbs to enable bipedal gait. Throughout regular daily activities, forces equivalent to about 5.5 times the body weight are transmitted between the femur and pelvis [294–296]. The lower limb has evolved primarily for bearing weight and facilitating movement and demands greater strength and stability than the upper limb. The bones are larger and more robust, as their form and structure have adapted to provide support and withstand mechanical stresses [293]. Understanding the biomechanics of the hip is essential in comprehending structural hip abnormalities and injury mechanisms, with significant implications for treating trauma-related injuries and reconstructive surgeries [292].

Regarding the internal geometry of the femoral neck, in 1838, Ward [298] detailed the trabeculae orientation of the upper third of the femur. He depicted a trabecular network where he identified tensile trabeculae laterally along the femoral neck (blue line in Figure 3.5 (c) located in the lateral system of lamellae - L in Figure 3.5 (b)) and compression trabeculae medially along the femoral neck (red line in Figure 3.5 (c) located in the medial system of lamellae - M in Figure 3.5 (b)). In addition, the secondary trabeculae are oriented across the rest of the proximal femur (green line in Figure 3.5 (c) located in the intertrochanteric arch - I in Figure 3.5 (b)). Finally, the central part of the femoral neck is called Ward's triangle (red triangle in 3.5 (c) located in the middle hole pointed out with a W in Figure 3.5 (b)) which is surrounded by the compressive and tensile trabeculae and the secondary compression trabeculae. It should be noted that in the middle of the femoral neck, in Ward's triangle, there is an absence of trabeculae resulting from bone adaptation. All this trabeculae network system can be observed in the laminar structure too, depicted in Figure 3.6 where the compression, tension trabeculae and the secondary trabeculae are shown.
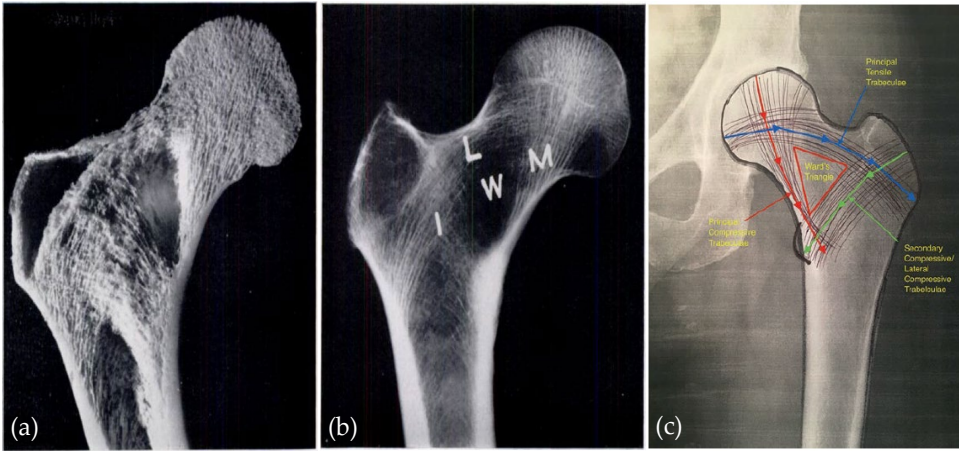
Figure 3.5: (a) Trabeculae orientation of cancellous bone in the frontal section of the upper third of the femur. (b) Internal weight-bearing system in the femoral neck. M - medial system of lamellae, L - lateral system of lamellae, W - Ward's triangle and I - intertrochanteric arch. (Images (a) and (b) extracted from Garden 1961 [297]). (c) Plain AP radiograph of the left hip demonstrating the principal compression (red line) and tension trabeculae (blue line) of the proximal femur as well as the secondary compressive trabeculae (green line) and the Ward's triangle (red triangle), extracted from [291].

As presented in both Figure 3.5 and Figure 3.6, the trabeculae main orientation changes according to bone adaptation, in contrast to the lumbar vertebrae presented in Section 3.2.1, which have a more homogeneous main orientation. Therefore, femoral cancellous specimens may not have such a predominant direction because it is challenging to cut the femoral heads in the saw and obtain the trabeculae aligned in one of the three orthogonal directions of the sample. Owing to the diversity of loads the femur withstands, the predominant structure observed in such samples is a strut and rod framework oriented in several directions to support the applied loads.

The bone resistance to fracture is influenced by its material composition, including the quantity and properties of the materials constituting it and the spatial distribution of bone mass [299]. Additionally, it is widely recognized that multiple factors influence fracture risk, and numerous independent risk factors have been identified to improve the accuracy and sensitivity of predictive fracture risk models [300].

Understanding the forces acting on the human femur is essential for healthcare professionals. Determining these forces during walking and other daily activ-
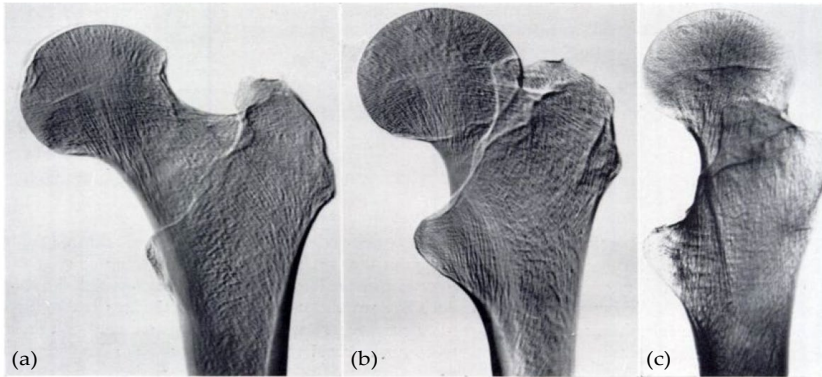
Figure 3.6: Serial radiographs of the calcar femorale showing its laminar structure. (a) Antero-posterior view. (b) Oblique view. (c) Lateral view. Figure taken from Garden 1961 [297].

ities makes it possible to calculate the stresses exerted on the femur, thereby identifying the areas prone to frequent femur fractures. Moreover, these forces are of significant interest in cases involving total hip prostheses and femoral neck and shaft fractures [301].

Proximal femoral fractures can be classified into two main groups based on their location relative to the hip joint capsule: intracapsular and extracapsular (see Figure 3.7). The hip joint capsule is a fibrous structure that surrounds and stabilizes the hip joint. Understanding the differences between these types of fractures is essential because it impacts their treatment and potential complications. Their principal features and classification are the following [302]:

- **Intracapsular Fractures:** femoral neck fractures that occur within the joint capsule of the hip. These fractures are associated with a higher risk of complications such as avascular necrosis (AVN), the death of bone tissue due to inadequate blood supply, and nonunion due to the tenuous blood supply to the femoral head. Furthermore, these fractures may have a higher risk of displacement and are generally less stable due to the limited blood supply and the absence of significant muscular attachments in the femoral neck region, so they may require more delicate surgical intervention to restore blood supply and stabilize the fracture. Intracapsular femoral fractures are presented in Figure 3.7 top, and are classified as follows:
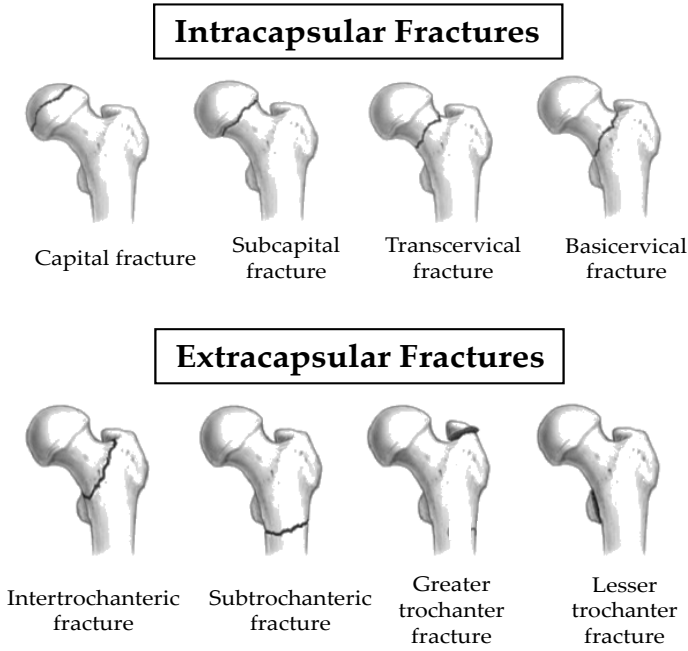
Figure 3.7: Main fractures of the upper third proximal femur. Images extracted from [303].

– Capital fracture: a fracture that occurs in the femoral head, also known as the capital region. Capital femur fractures are relatively rare because the robust structures of the hip joint protect the femoral head. However, this is usually the result of high-energy trauma and is often accompanied by hip joint dislocation. They can also occur in individuals with weakened bones, such as osteoporosis, or due to underlying diseases that affect the bone integrity. Capital femur fractures pose a significant risk of complications due to the potential disruption of the blood supply to the femoral head.

– Subcapital fracture: a fracture that occurs just below the femoral head at the so-called subcapital region. The fracture line is located below the femoral head and may extend horizontally or obliquely across the femoral neck. Subcapital fractures are prevalent in older individuals who undergo a fall, and due to osteoporosis, which is more common in old people, particularly in postmenopausal women.

These fractures in the young population occur as a result of high-energy injuries. Subcapital femur fractures, especially when displaced, can lead to several complications, including avascular necrosis of the femoral head, nonunion (failure of the fracture to heal properly), and post-traumatic arthritis in the hip joint.

– Transcervical fracture: a fracture that occurs in the femoral neck where the fracture line is typically horizontal or slightly oblique, crossing the femoral neck in a medial-to-lateral direction. Transcervical fractures can disrupt the blood supply to the femoral head, potentially leading to avascular necrosis.

– Basicervical fracture: a fracture that occurs at the junction of the femoral neck base and the intertrochanteric region. The fracture line is more oblique, extending from the base of the femoral neck into the femoral shaft. Basicervical fractures have a higher risk of displacement and may behave more like extracapsular fractures regarding healing and treatment options. The incidence of avascular necrosis is considered to be low compared to subcapital and transcervical fractures. Basicervical fractures have a high risk of displacement and may behave more like extracapsular fractures in terms of healing and treatment options.

- **Extracapsular Fractures:** occur outside the joint capsule and are associated with a more robust blood supply to the femoral head. These fractures are less likely to result in chronic complications such as avascular necrosis (AVN) or nonunion. Extracapsular fractures are generally more stable than intracapsular fractures due to the presence of robust muscular attachments and a better blood supply to the fractured area, and they can often be managed with more straightforward surgical fixation methods. Extracapsular femoral fractures are presented in Figure 3.7 bottom, and are classified as follows:

  – Intertrochanteric fracture: a fracture that occurs between the greater trochanter and the lesser trochanter of the femur, whose fracture line joins the greater and lesser trochanter through the intertrochanteric line. It is the most common type of hip fracture, and the prognosis for bone healing is generally good if the patient is healthy. Complications from intertrochanteric femur fractures include nonunion malunion, infection, and blood clots. Early mobilization and re-

habilitation are essential to reduce the risk of complications and promote functional recovery.

– Subtrochanteric fracture: a fracture that occurs below the lesser trochanter of the femur extending into the shaft (diaphysis) of the femur. In the elderly population, the most common trauma is due to low-energy, such as falls, whereas in the youth population, the injuries are because of high-energy traumatism, such as traffic accidents. Rehabilitation and physical therapy are crucial for regaining strength and function after surgery.

– Greater trochanter fracture: a fracture that occurs in the greater trochanter, in which the fracture line separates the greater trochanter from the rest of the femur.

– Lesser trochanter fracture: a fracture that occurs in the lesser trochanter, in which the fracture line separates the lesser trochanter from the rest of the femur.

Femur fractures can be classified as displaced or nondisplaced based on the alignment of the broken bone fragments. On the one hand, in a displaced femur fracture, the broken ends of the bone are no longer in their normal anatomical position. The bone fragments have moved, resulting in a visible gap or misalignment between the broken pieces (see Figure 3.8 c and d). Displaced fractures can be shifted laterally, angulated, or rotated. This fracture type often requires more aggressive treatment, such as surgery, to realign and stabilize the bone for proper healing. In addition, in displaced fractures, the broken bone ends may shift or misalign, potentially compressing the blood vessels that supply the fractured segment. This compression can reduce or completely obstruct blood flow to the affected area. Furthermore, AVN is a severe complication that can occur if the blood supply to the fractured segment is significantly compromised or wholly cut off.

On the other hand, nondisplaced femur fracture occurs when the broken ends of the bone remain relatively aligned and in their proper anatomical position (see Figure 3.8 a and b). The bone may have a crack or break, but the overall alignment is maintained. Nondisplaced fractures can often be treated effectively with conservative methods like immobilization using casts or splints. While a nondisplaced femur fracture can still be painful, the pain may be less severe than a displaced fracture. Additionally, there may be minimal to no visible deformity or swelling. Moreover, nondisplaced femur fractures can often be managed without surgery and have a shorter healing time than displaced
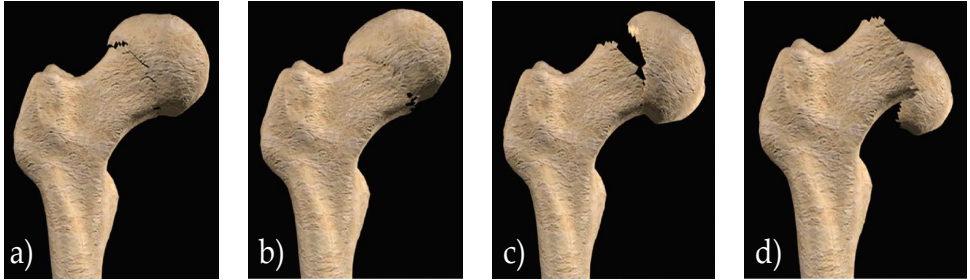
Figure 3.8: Classification of subcapital femoral neck fractures. a) Stage 1: can be incomplete or valgus impacted. b) Stage 2: complete but nondisplaced subacapital fractures. c) Stage 3: complete subcapital fractures which are partially displaced. d) Stage 4: complete subcapital fractures which are fully displaced. Image extracted from Sheehan *et al.* work [302].

fractures. Treatment usually involves immobilizing using a cast or brace to keep the bone fragments in place while healing. Weight-bearing restrictions are often enforced during the healing process. Lastly, in nondisplaced fractures, the bone ends remain relatively aligned, reducing the risk of direct compression or obstruction of blood vessels. As a result, the risk of blood supply problems is generally lower than displaced fractures. Regarding AVN, the risk may be lower and can still cause minor disruptions to the blood supply, especially if there is extensive bruising or swelling around the fracture site.

3.2.2.1 Classification of the human femoral cancellous bone specimens

In this thesis, human cancellous bone samples have been studied. These specimens come from human femoral heads extracted during total hip arthroplasty surgery in the Hospital Universitario Infanta Leonor of Madrid. The extracted femoral heads belong to different clinic groups, divided according to the doctors' criterion based on the type of fracture the patients present. The doctors classified the femoral heads into three groups: the healthy group (HG), the osteoarthrosic group (OA), and the osteoporotic group (OP). The definition of each group is the following:

- Healthy Group (HG): specimens obtained during total hip replacement surgery in the assistance process of mechanical pathology in patients under 65 years of age.

- Osteoarthrosic Group (OA): specimens obtained during total hip replacement surgery in the assistance process of degenerative pathology (arthrosis) in patients over 65 years of age.

- Osteoporotic group (OP): specimens obtained during total or partial hip replacement surgery in the assistance process of displaced subcapital fracture in patients over 65 years of age (see Figure 3.8 c and d).

The cancellous bone specimens studied in this thesis (see Figure 3.9 b) were prepared after rough cuts performed in the femoral head. In Chapter 6, the workflow followed to develop this research will be explained in detail.
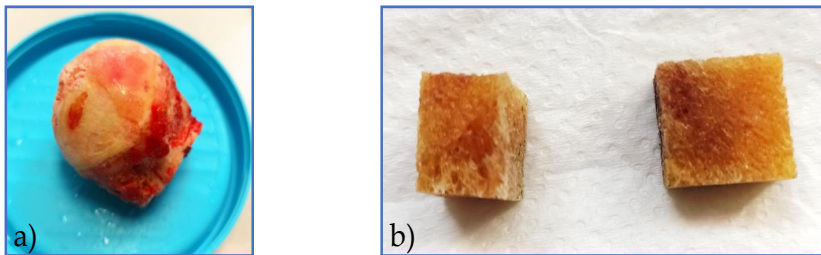
Figure 3.9: a) Femoral head extracted at the total hip arthroplasty surgery and b) cancellous bone samples studied in this thesis, prepared from the femoral head. Original contribution.

3.3   Cancellous architecture assessment at the stereomicroscope

In this section, we will focus the study on the trabecular architecture of bone. Some researchers, such as Stauber *et al.* [22], reveal the importance of considering these cancellous bone structures because they influence bone quality and stiffness. For this reason, it is essential for our work to study this architecture to improve our numerical models and our approaches to defining the cancellous bone properties.

Furthermore, rods and plates play an essential role when bone degenerates because, depending on the disease, these structures degrade differently, as Ding and Overgaard have shown in some recent studies [20, 21]. When bone is young and healthy, there is a greater density of rods and plates with higher thickness. In contrast, in an elderly or diseased bone, this trabecular network has a low quality and density. Some crucial parameters like ultimate stress, ultimate strain, or Young's modulus change as the trabecular architecture does.

For these reasons, both swine and human samples have been examined at the stereomicroscope to analyse our specimens trabecular architecture. A stereomicroscope or stereo microscope is a type of microscope used to provide a three-dimensional (3D) view of a specimen. Also known as a stereo zoom microscope, this microscope is fitted with separate objective lenses and two separate eyepieces, providing a different optical path to each eye. The result is a three-dimensional image because each eye sees at a slightly different angle. The magnification range of a stereomicroscope can vary, but it generally starts around 5x and can go up to around 100x, sometimes higher, depending on the model. These magnifiers view live or dead, opaque or translucent specimens of relatively large size.

The images exhibited in this section have been obtained at the stereomicroscope in the Department of Mechanical and Materials Engineering (DIMM) at the Polytechnic University of Valencia (UPV), which is shown in Figure 3.10. One essential part is the microscope objective, composed of a set of lenses that generate a first magnified image of the sample. Besides, there are two screws to focus the sample and zoom in and out. At the microscope base, there is a hole for the plate where the specimen is placed. On one side, this plate is white, and on the other is black, which is useful for having different backgrounds depending on the colour of the evaluated sample and having contrast for getting high-quality images. On the top of the column, there is a camera that allows to see the specimen on the computer screen. This camera has a software with several functions, such as controlling and modifying image parameters like brightness or contrast. In addition, it is possible to measure the image, which is highly helpful for taking measurements of the specimens. A light source can be switched on if brightness is needed. Additionally, it has a dimmer to regulate the light intensity in the field of view. Finally, the stereomicroscope has two light bulbs at the end of the tubes, which are flexible to adapt them to the necessity of exposition, height, and location of the light beam relative to the sample.
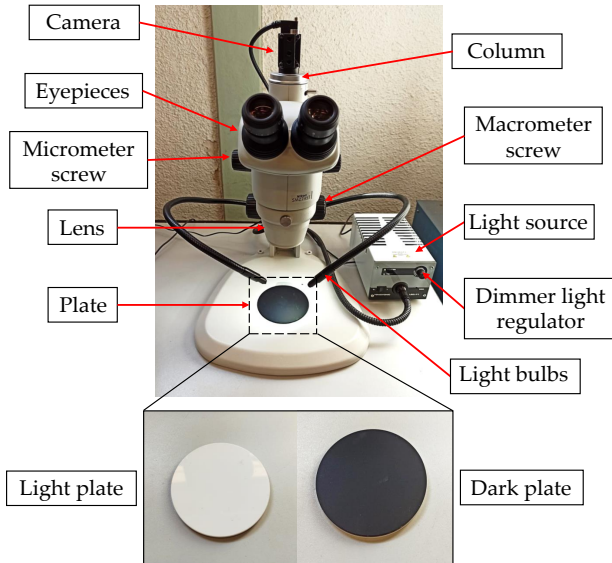
Figure 3.10: The stereomicroscope available at the Department of Mechanical and Materials Engineering (DIMM) used for the assessment of cancellous bone samples architecture. Original contribution.

The studied specimens do not need any specific treatment before using the stereomicroscope. It is recommended to take the samples out of the freezer around 24 hours before and let them in the fridge for defrosting. Even so, ice can be seen in the cancellous architecture in some images. As a final point, it is recommended to dry the samples so that no droplets are visible on the surface of the bone.

Figure 3.11 reveals the cancellous bone architecture of a vertebra from a lumbar vertebra of a skeletally mature swine. It is possible to identify the rod- and plate-like structures in each image, respectively. In Figure 3.11 b) it is shown the plate-like structure which is oriented along the vertical direction of the vertebra, as Mosekilde established in her work [287]. This preferred orientation is the stiffest direction of the vertebra because it is the one where most of the loads remain. Plates are the scaffolds of this type of bone. Owing to the function that plates develop, compared with the struts, they are thicker and longer. Lastly, it can be noted that for generating the plate architecture, little struts are also needed to join them, as seen in the image. On the other side, in the other two orthogonal directions of the vertebra, the prominent

architecture is the rod-like structure as evidenced in Figure 3.11 a). As can be seen, these struts constitute the trabecular network.
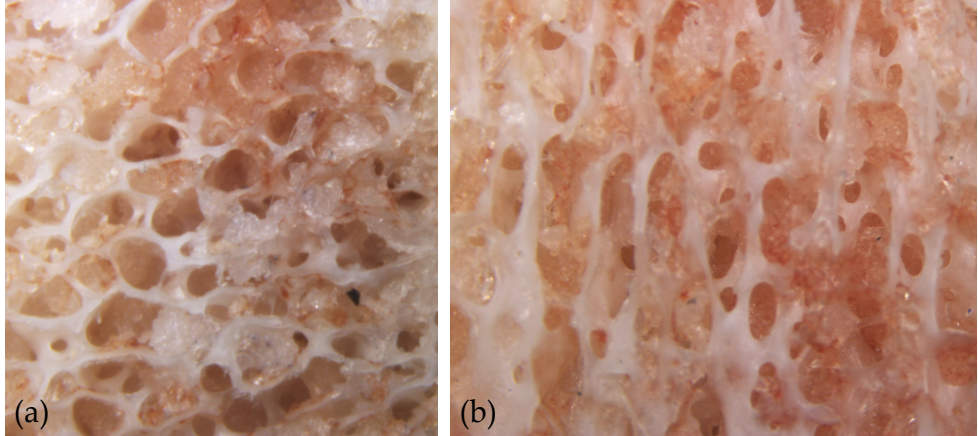
Figure 3.11: Cancellous bone architecture acquired at the stereomicroscope (swine vertebral cancellous bone). a) Rod-like structure and b) plate-like structure.

Several thickness measures have been taken on some struts and plates, presented in Figure 3.12. The lowest value collected is 106 μm for a transverse strut, whereas the highest is 223 μm for a vertical plate. It is important to consider that these results are merely a few values from the whole structure, which means it is possible to find higher or lower values in other architectural regions. Various works conduct a local morphometry analysis to evaluate bone microarchitecture separately for plates and rod structures. They also found slight differences in trabecular thickness between rods and plates, such as Stauber and Müller [22, 23]. Some researchers have defined the trabecula diameter around 100 μm; however, it is crucial to contemplate the body location because the trabecula thickness can barely change between different regions.

Table 3.1 collects the trabecular thickness (Tb.Th) obtained in the measurements made in our lumbar vertebral samples together with various results from the literature for vertebrae. These results are presented in microns (μm) with the mean value and the standard deviation. Our results are in agreement with the findings of Poillot *et al.* [304], Nazarian *et al.* [24] and Stauber and colleagues [22]. The lowest values are reported in Li *et al.* work [305]. It is essential to bear in mind that numerous other factors can vary the trabecular thickness, such as age or gender. Therefore, the minor differences between results can be related to these factors. Moreover, bone diseases are also a huge
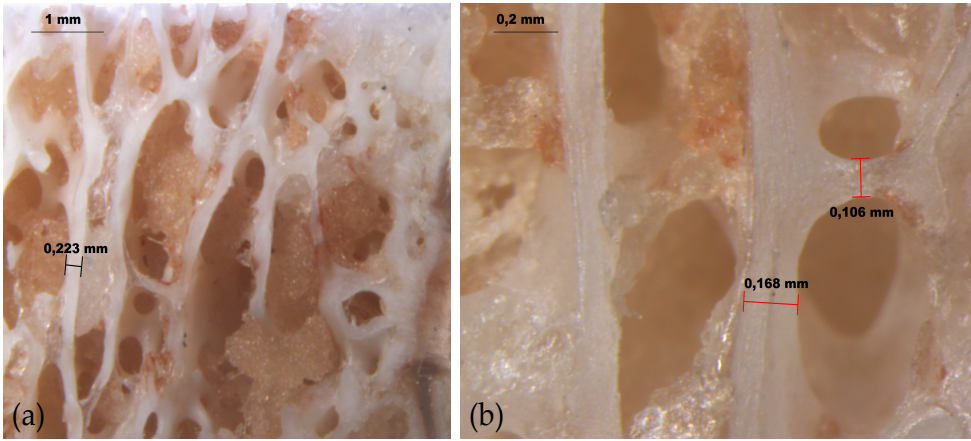
Figure 3.12: Trabecular thickness (Tb.Th) measured at the stereomicroscope.

problem, as many degrade the trabecular structure. However, all the results presented in Table 3.1 are for healthy vertebral specimens.

Table 3.1: Trabecular thickness (Tb.Th) from healthy vertebral cancellous bone.

Trabecular thickness (Tb.Th) (μm)	
This work	Literature
	146 ± 10 [24]
165.67 ± 58.53	136 ± 19 [22]
	113.3 ± 15.9 [305]
	160 ± 20 [304]

Conversely, the trabeculae from femoral head specimens do not have a clear predominant direction. Unlike the vertebrae, the femur has to withstand different loads during daily activities; then, the trabeculae are distributed to support such loads, as shown in Figure 3.5. Depending on the cutting plane, in some samples it is possible to see a more oriented trabecular structure, such as in Figure 3.13 (a) and (b), than in other samples or cutting planes, such as in Figure 3.13 (c) and (d).

The trabecular thickness has been measured for each studied group of human specimens in Figure 3.14, Figure 3.15 and Figure 3.16. The measurements
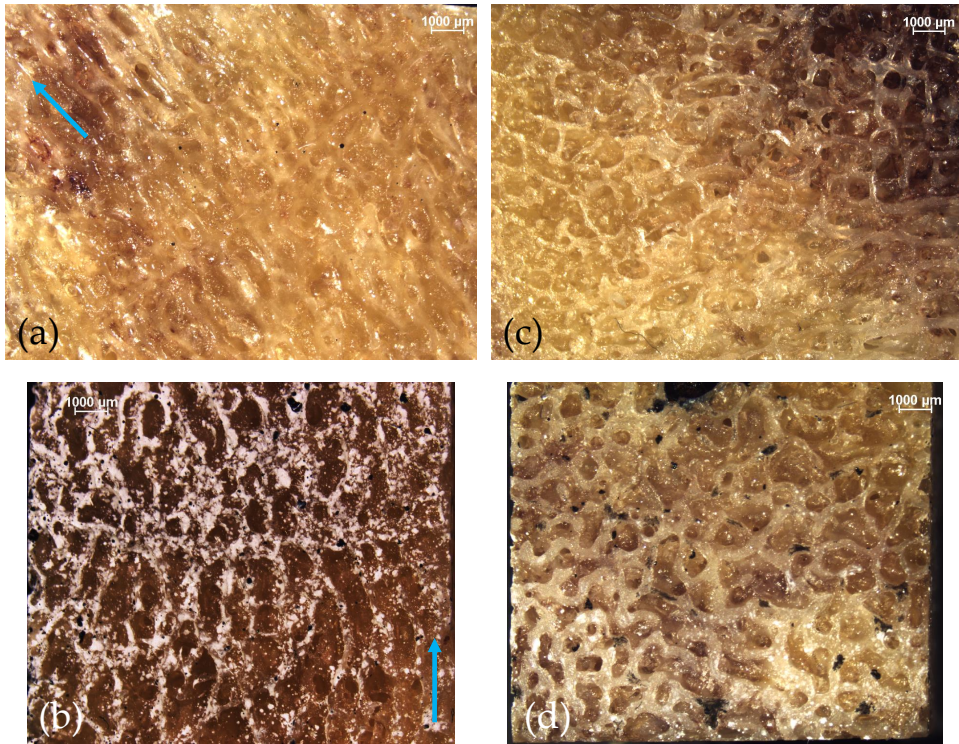
Figure 3.13: Trabeculae direction in the cancellous bone femoral head specimens. Blue arrows point out the main direction of the trabeculae, a) and b) cutting plane with the trabeculae oriented in the blue arrows direction, c) and d) cutting plane with rod-like structure.

obtained for the studied human femoral specimens have been presented with the mean value and the standard deviation in Table 3.2.

Before analysing the trabecular thickness (Tb.Th) results, it is possible to appreciate several differences between groups by examining the Figures 3.14 - 3.16. First of all, the trabeculae are thicker in the images of the HG samples compared to the groups that present a pathology, both OA and OP, being greater than the difference between HG and OP. The trabecular thickness (Tb.Th) is directly related to another morphometric parameter, the trabecular separation (Tb.Sp). Generally, when the trabecular thickness is large, the specimen is healthy or without pathologies that affect its architecture. Therefore, the trabecular separation is lower than in specimens with a degraded structure.
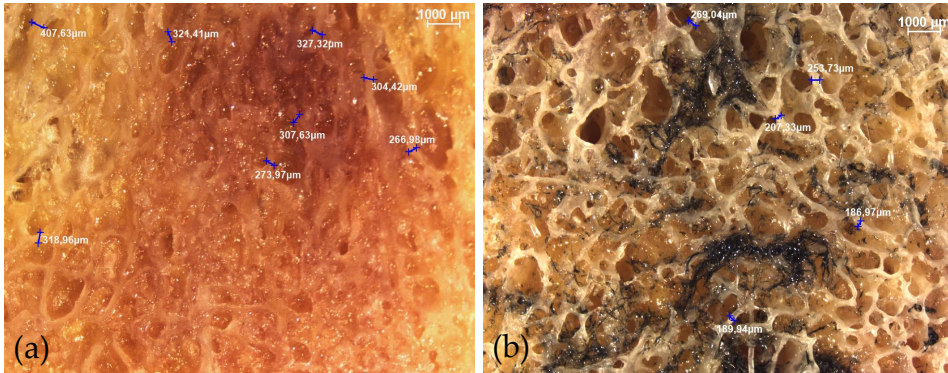
Figure 3.14: Trabecular thickness (Tb.Th) measured in cancellous bone specimens from the healthy group (HG) femoral heads.

The high diversity between specimens from the same group and between regions within a sample makes it necessary to take a large number of measurements to represent the group under study. This will be accomplished through the analysis of micro-CT images reducing time costs. Moreover, it is important to analyse the results to check possible further points which are extreme points out of the range of the studied group. When a high number of specimens is examined, it is possible to find a few exceptions that are not in the trend of the rest of the results. In these cases, it is crucial to neglect these results.

Regarding the results for the thickness of our human cancellous femoral specimens, the healthy group (HG) presents the highest values, 279.64 ± 62.04 μm. The groups presenting pathology, osteoarthrosic (OA) and osteoporotic (OP) groups, show lower values for the trabecular thickness than HG. Between diseased specimens, the osteoporotic samples show the lowest values for the trabecular thickness, 149.54 ± 52.70 μm, whereas the OA specimens present a thickness of 203.83 ± 36.05 μm. As a consequence, in the morphometric analysis we would expect that the trabecular separation presents an inverse trend than the trabecular thickness.

Trabecular thickness is a morphometric parameter that substantially influences the bone mechanical properties. A large thickness usually is presented in healthy individuals; hence, they are expected to withstand higher load levels. Specimens with a degraded structure due to bone disease are expected to support lower load levels, such as OA and OP specimens. Morphometric analysis has been carried out for the cancellous femoral specimens of the three
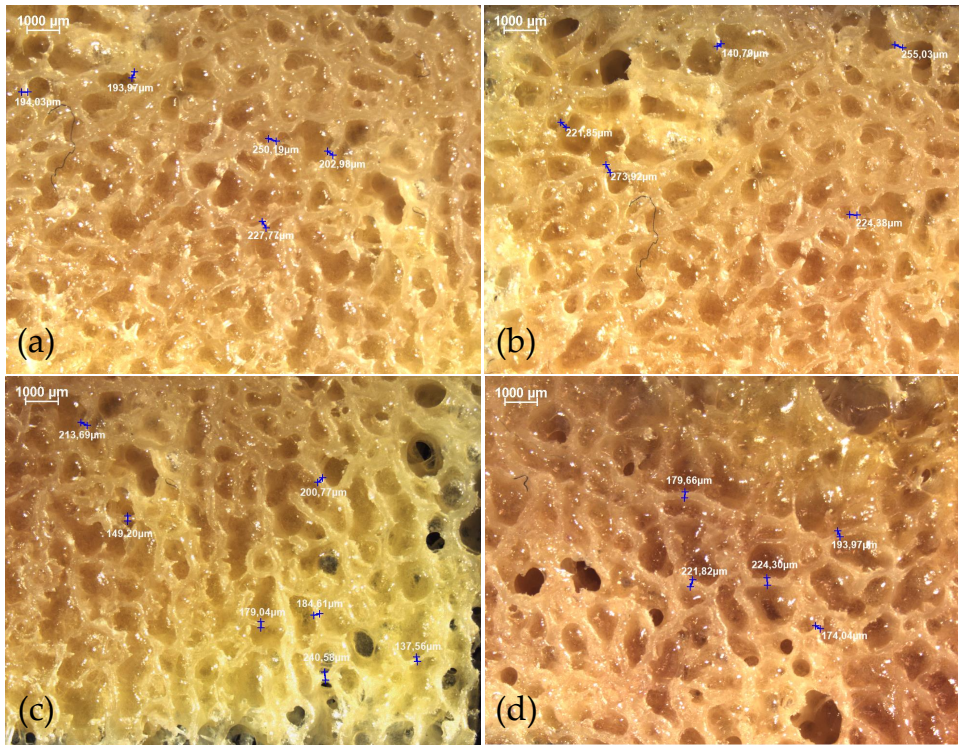
Figure 3.15: Trabecular thickness (Tb.Th) measured in cancellous bone specimens from osteoarthrosic (OA) femoral heads.

groups and the stress level that each group can resist, and both are presented in Chapter 6.

Apart from obtaining our results, it is essential to confront them to results in the literature. Table 3.2 presents the trabecular thickness (Tb.Th) for our human femoral cancellous specimens with the mean and standard deviation in microns (μm). Several results from the literature are collected from human femoral head cancellous specimens in the same conditions to compare the measurements.

First of all, it is important to keep in mind that many factors, such as body location, sex, gender, or bone disease, modify the trabecular thickness. In our samples, we have made different measures in the same specimen for the thickness variability. Depending on the literature work, there is a wide range
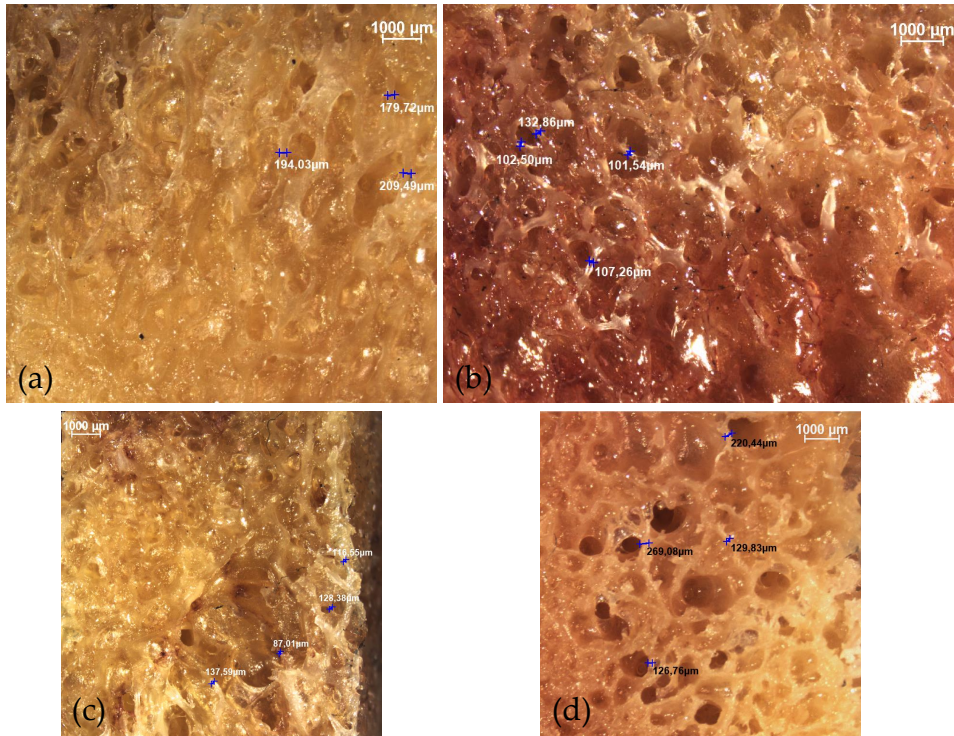
Figure 3.16: Trabecular thickness (Tb.Th) measured in cancellous bone specimens from osteoporotic (OP) femoral heads.

Table 3.2: Trabecular thickness (Tb.Th) from human femoral head cancellous samples classified into three groups: healthy group (HG), osteoarthrosis group (OA), and osteoporotic group (OP).

Trabecular thickness (Tb.Th) (μm)					
This work			Literature		
HG	OA	OP	HG	OA	OP
279.64 ± 62.04	203.83 ± 36.05	149.54 ± 52.70	193 ± 25 [21]	205 ± 28 [21]	187 ± 14 [21]
			150 - 240 [20]	160 - 330 [20]	110 - 210 [20]
			294.6 ± 48 [95]	95.1 ± 2.5 [189]	80.9 ± 4.1 [189]
			144.7 ± 11.9 [305]	200 ± 30 [306]	180 ± 30 [306]
			190 ± 30 [307]	238 ± 5 [190]	190 ± 10 [190]
			206.14 ± 34.11 [308]	170 ± 30 [307]	190 ± 30 [307]

of values for each studied group. Regarding HG, the lowest values have been found in Ding and Overgaard work [20] and in Li *et al.* [305]. In the pathological groups, both OA and OP, the lowest trabecular thickness is presented in Blain and colleagues' work [189]. Nonetheless, our results for the trabecular thickness are in agreement with those found in the literature.

In general terms, the lowest values are presented in the osteoporotic specimens. These findings are supported by the fact that osteoporosis degrades the trabecular network. Owing to the unbalanced activity of the remodelling cycle, many voids and holes arise in the lamellar tissue removing more mineral than it is deposited. Regarding the other two groups, although OA has pathology and HG does not, the trabecular thickness in certain works are similar or even overlap. Osteoarthrosis (OA) is considered inversely to osteoporosis, and both cannot coexist in the same patient. In OA, apart from the degeneration and degradation of the cartilage, the bone remodelling process has greater activity than in a healthy bone. For this reason, depending on the grade or stage of OA, in the most severe cases, the individual can have more bone material quantity in the anatomical location affected by this disease than a healthy individual. Hence, in some works, such as in Ding and Overgaard [20], the range for the OA group is slightly higher than for HG.

3.4   μ-CT images analysis of cancellous bone specimens

Two groups of cancellous bone samples are analysed in this thesis: (1) human femoral heads extracted from donors during total hip arthroplasty surgery and (2) lumbar vertebra from mature swine. From scanning all the cancellous bone samples by the micro-CT, we assess the microarchitecture of the specimens with high resolution for optimal morphometric analysis presented in Chapter 6.

The specimens were cut in a minitom saw (Struers ApS, Bellerup, Denmark). As an example, for human femoral head, Figure 3.17 depicts one sample of each group highlighting their dimensions. The sample dimensions are at least 10x10x10 mm to be representative of the whole specimen. Although the specimens are several centimeters long, at least in some directions, it is rather challenging to observe the bone microarchitecture due to the dense network of trabecular lattice, as shown in Figure 3.17. Most severe architecture problems, such as big holes, can be appreciated primarily in the diseased specimens usually belonging to OP (see Figure 3.17 osteoporotic group specimen).

Healthy Group (HG)   **Osteoarthrosic Group (OA)**   **Osteoporotic Group (OP)**

14.43x24.84x13.18 mm   13.76x13.49x12.06 mm   18.80x9.50x24.45 mm
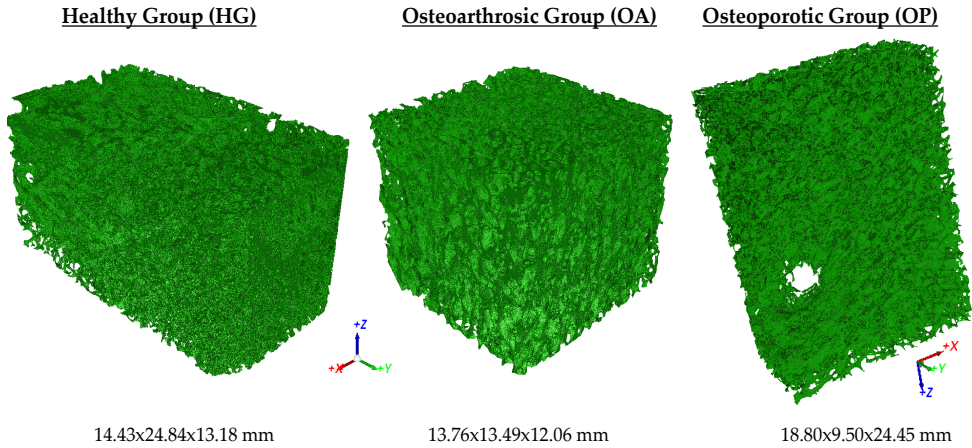
Figure 3.17: 3D reconstruction of femoral cancellous bone specimens of each group: healthy (HG), osteoarthrosic (OA) and osteoporotic (OP).

Nevertheless, it is possible to visually examine the specimens microarchitecture in the DICOM (Digital Imaging and Communication in Medicine) images from the micro-CT scan. Certain features of the sample structure, such as trabecular thickness, primary orientation, holes or interconnected regions are exhibited in these images. In most cases, this visual information is enough to distinguish between the three studied groups. Figure 3.18 presents one DICOM image representing each group.

At first sight, it is possible to distinguish several differences between the three images of Figure 3.18. When comparing the HG image with the other two images, the trabeculae are more homogeneous and thicker overall than in the other two specimens. Moving to the right, the middle DICOM image belongs to an OA specimen. The main feature of the OA group is the mineral concentration, the white localized regions. Moreover, the rest of the trabeculae are slightly thinner than in the HG specimen. Finally, the OP specimens are characterised by very separated thin trabeculae, such as the one shown in Figure 3.18. Therefore, as has been demonstrated, with the structure information provided by the DICOM images, it is possible to qualitatively discern between healthy (HG), osteoarthrosic (OA), and osteoporotic (OP) specimens in most cases.
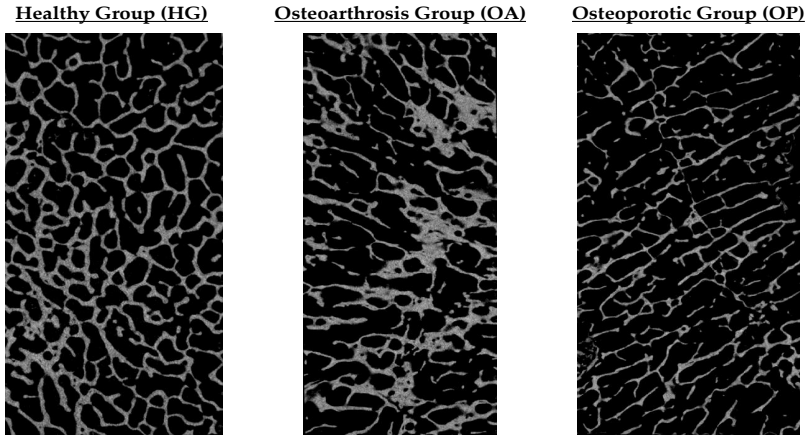
Figure 3.18: Differences between the three groups of human femoral cancellous bone specimens using DICOM images obtained with the micro-CT scanner.

On the other hand, some other significant structure features are found in some of the studied specimens, as shown in Figure 3.19. First of all, some structural defects are observed in most of the samples (probably due to the advanced age of the donors), such as big holes within the sample, as presented in Figure 3.19 a. This specimen belongs to the OP group, that besides of having these defects, shows other characteristics of this group, such as thin trabeculae. In addition, in both Figure 3.19 b and c images, the so-called epiphysis or growth line can be appreciated, which is the line of bone growth where most of the mineral is concentrated. This line is found at the ends of long bones, such as the femur, humerus, and tibia, and is responsible for bone length growth during childhood and adolescence. Regarding the femoral head being part of the epiphysis of the femur, it is possible to see this bone growth line in several cancellous samples. During this growth process, a large quantity of minerals, such as calcium and phosphorus are deposited in this area, making it denser and more visible on X-rays. When bone growth is complete, the growth plate closes and becomes solid bone, indicating that longitudinal growth is no longer possible.

Furthermore, in Figure 3.19 a and c, the orientation of the trabeculae can be recognised. As mentioned in Section 3.3, the trabeculae orientation can vary depending on how the cut was made in the microtom saw (see Figure 3.13) and depending on the cut region of the femoral head, such as shown in Figure 3.5 in Section 3.2.2.
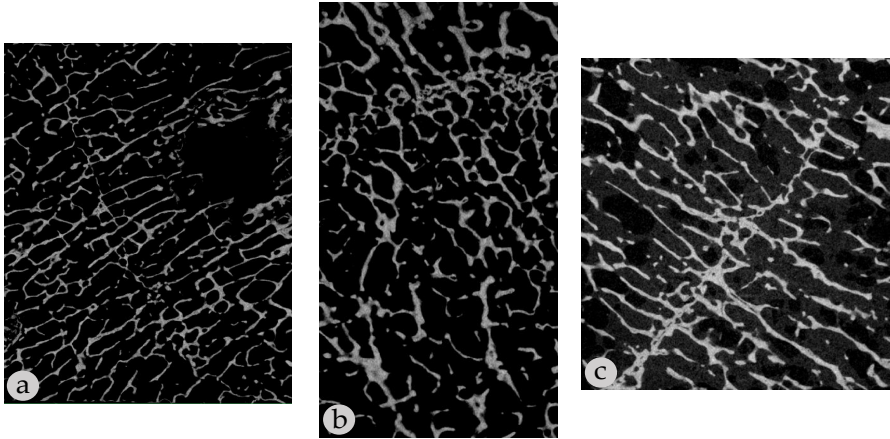
Figure 3.19: a) Hole within the specimen, b) epiphysis or growth line, and c) defects on the DICOM images due to insufficient cleaning.

Finally, it is essential to clean the specimens exhaustively; otherwise, the dirt remaining in the sample will show up in the micro-CT, as exhibited in Figure 3.19. The greyish area around the bone appears because the specimen is not cleaned enough, so some rests remain. Owing to these organic rests having a different density of bone, the intensity is that greyish colour in the DICOM images. If we compare Figure 3.19 c with Figure 3.19 a and b, it is recognised that both are well-cleaned because only the background in black and the cancellous bone in white are shown. Besides, cleaning is also crucial because the metallic rests of the saw disc can remain on the specimen. The metallic rests will reflect the rays more than bone, which are considered image artifacts, as explained in Section 2.3.3.

3.5 Lamellar tissue assessment at the field emission scanning electron microscope (FESEM)

Cancellous bone behaviour has been studied for years owing to the relevance of its mechanical properties and understanding its failure mechanisms. Over the years, meso- and macroscale bone numerical analyses have been carried out mainly considering two different material properties definition: using isotropic or anisotropic elastic properties. Lamellar tissue mechanical response has been evaluated by different techniques, such as experimental tests, imaging techniques, or numerical models, and the evidence is that cancellous tissue

is arranged orderly. Because of the great controversy between researchers on this issue, we have decided to evaluate the bone samples used in this work. Checking cancellous tissue structure enables us to make a better approach in our numerical models of the natural arrangement of the bone tissue in order to improve the results predicted by these numerical models.

3.5.1 Cancellous bone sample preparation procedure for FESEM

In this section, lamellar tissue organisation of cancellous bone samples have been analysed at the field emission scanning electron microscope (FESEM). This research required adhering to a stringent and systematic procedure due to the sensitivity of the microscope and the need to have a clean bone structure for obtaining great quality images. Figure 3.20 presents the scheme of the procedure followed from bone sample cleaning to FESEM image acquisition.
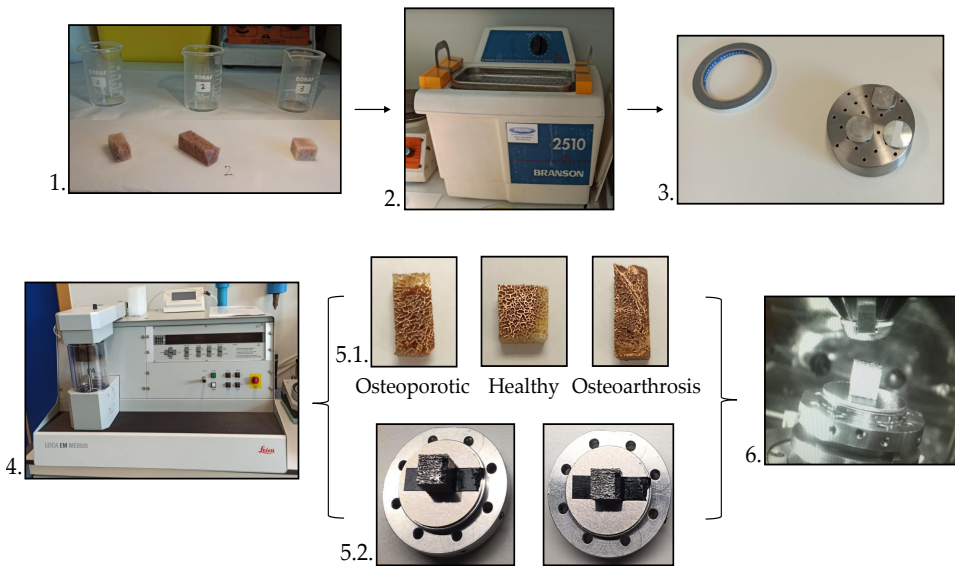
Figure 3.20: Scheme of the procedure followed in cleaning and preparing cancellous bone samples for getting images at the field emission scanning electron microscope (FESEM). 1) Cleaning of the specimens, 2) ultrasound cleaner machine, 3) FESEM setup for cancellous bone samples, 4) vacuum machine, 5) gold coating (5.1) and platinum coating (5.2) for the cancellous bone samples and 6) cancellous bone sample tilted inside of the FESEM.

Swine and human cancellous bone samples have been observed at the FESEM ULTRA 55 (ZEISS, Jena, Germany) at the microscopy service of the UPV. On the one hand, swine cancellous bone samples come from the lumbar vertebrae, whereas human bone comes from the femoral heads of three types of patients: healthy, osteoporotic, and osteoarthrosic. The starting point of the procedure is cleaning the bone samples in order to remove all the organic remains and blood (Figure 3.20.1). To this end, bone samples were immersed in distilled water inside bakers and placed inside the ultrasonic cleaner machine (see Figure 3.20.2) between 10 to 20 minutes controlling the temperature. This process has to be repeated several times owing to the nature of cancellous bone, which is highly porous and hinders cleaning, as the waste remains in the voids of the bone framework. Before each ultrasound bath, distilled water must be changed to ensure good cleaning. When the bone sample changes its reddish colour to white and distilled water after the ultrasound bath is almost transparent, the cleaning process is over. The following step is preparing the samples for the FESEM. For this purpose, it is essential to carry out the following assignments: assemble cancellous bone in a metal sample holder, bring it to vacuum, and apply a metal coating.

The following step is to place the specimens in the sample holders. There are two usual methods: adhesive tape, which is usually made of carbon, and conductive cement, of which silver is the most widely used. Due to the high porosity of the specimens, conductive cement is not the best option; for this reason, we have used adhesive carbon tape (see the setup in Figure 3.20.3).

One essential feature that must be considered is that the FESEM works in vacuum conditions to ensure that nothing inside the microscope chamber can deflect the electron beam. For this purpose, once bone specimens are fixed in the sample holder, they are introduced in a vacuum machine (Figure 3.20.4) to dry them and remove the last residues and moisture. Subsequently, the non-conductive nature of the samples requires to apply a metal coating, usually gold or platinum. Henceforth, the specimens are conductive, so they need to be grounded, and the carbon adhesive tape performs this function. In the beginning, the applied coating was platinum, as shown in Figure 3.20 5.2, but in order to enhance the obtained images, we tried gold coating (Figure 3.20 5.1). The main reason is that gold particles are smaller than platinum ones; thus, it is possible to reach more magnification in the microscope without observing the coating particles on the bone surface.

At this point, bone samples are ready to be introduced in the FESEM. As aforementioned, this microscope works in vacuum conditions, so once the sample is in, the vacuum starts until the pressure reaches 10^{-7} mbar. Lastly, for

this type of specimen, the sample is tilted between 8 to 10 degrees (see Figure 3.20.6). This intermediate tilt angle falls between the low and high tilt angles and offers a balance between surface visualization and internal structural analysis. This moderate tilt angle can enhance surface visualization and obtain information about the bone surface. This is really useful for studying surface features and potential changes in the surface due to several factors, such as bone remodelling or disease. Furthermore, by using this tilt angle, it becomes easier to analyse the trabeculae alignment and orientation, which is one of the main targets of this chapter. Working conditions also include using 3 kV voltage and a working distance between 6 and 8 mm.

3.5.2 Imaging assessment of lamellar tissue structure

The main target is to browse the lamellar structure in order to assess the preferred orientation of cancellous tissue. The knowledge extracted from the FESEM images will be used to establish cancellous tissue properties and to apply homogenization methods. This permits to develop an accurate numerical model of cancellous bone in an upper length scale that considers cancellous tissue properties.

Swine vertebral cancellous bone samples were the first ones to be observed at the FESEM. Figure 3.21 illustrates three relevant sites for evaluating cancellous tissue: in the surrounding of voids, in branching structures and in a trabecula. This image reveals how lamellar tissue has been deposited in agreement with bone growth and tissue location. What is shown in each image of Figure 3.21 is the mineralised skeleton of cancellous tissue because the specimens are cleaned, and each organic remains, such as collagen fibrils, has been removed. Figure 3.21 a) shows how and where the osteoblast deposited the new bone material, and it is clarified that lamellar tissue is deposited surrounding the hole. Figure 3.21 b) shows how and where the collagen fibrils were deposited in a branch. It is possible to appreciate that lamellar tissue reaches the branch with the orientation of the trabecula. However, lamellar tissue has to adapt when both trabeculae converge at the branch, resulting in a homogeneous zone without a clear orientation.

Figure 3.21 c) and d) show a single trabecula, with the only distinction being the magnification, facilitating a clearer assessment of the arrangement of lamellar tissue. In the images, the lamellar tissue is observed to be arranged in successive layers, aligning the collagen fibrils longitudinally along the trabecula.
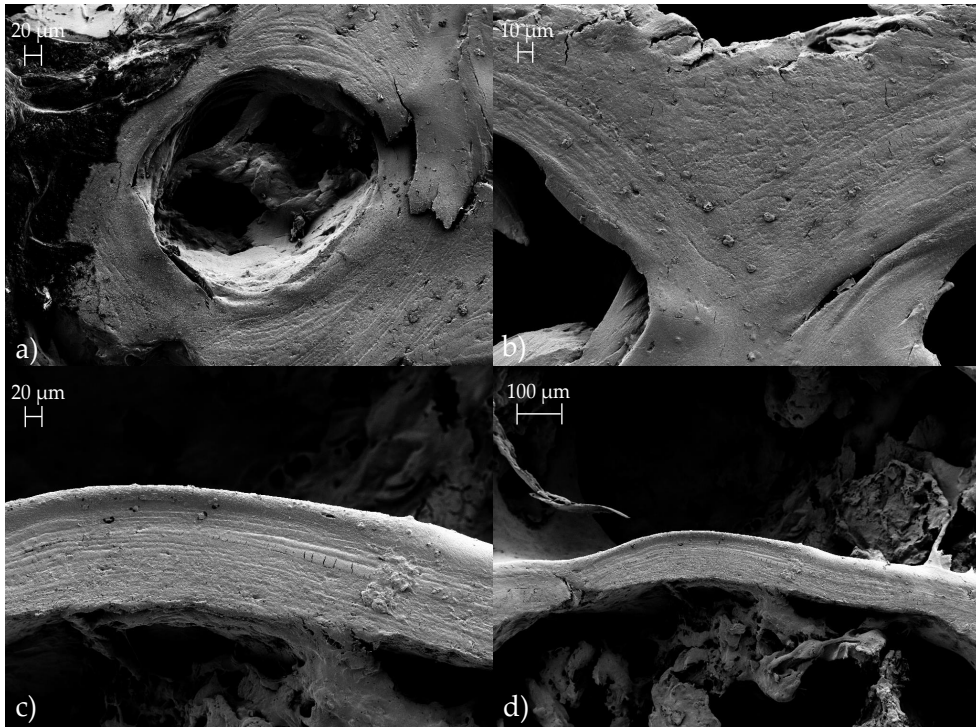
Figure 3.21: Lamellar tissue orientation evaluated at the field emission scanning electron microscope (FESEM). a) Lamellae arranged circumferentially around the hole, b) lamellae orientation in a brach, where two trabeculae join, c) lamellae arranged longitudinally along the trabecula and d) single trabecula.

Increasing the magnification, the canaliculi lattice can be observed, shown in Figure 3.22. This whole string framework is the calcophore canaliculi network which consists of tiny channels, which pass through the calcified matrix of the bone and connect bone cells to each other, called osteocytes. The canaliculi constitute a tridimensional network that allows communication and exchange of nutrients, metabolites, and signals between bone cells.

In conclusion, the examination of the lamellar tissue surface has provided insights into the mineral deposition and arrangement in bone tissue. While the lamellae align with the trabeculae from which they originate, there is a lack of dominant orientation at points where trabeculae converge. Thus, it has been shown that lamellar tissue is arranged according to the structures which
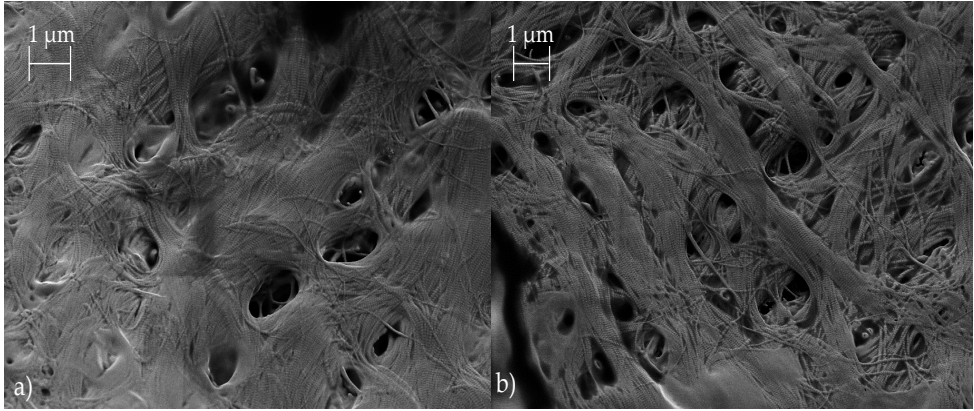
Figure 3.22: Calcophore canaliculi network seen at the field emission scanning electron microscope (FESEM).

form it. This finding highlights the need of considering material properties oriented according to the microstructure.

The knowledge of lamellae orientation has a significant role in lamellar tissue properties definition. Mineralised collagen fibrils direction are parallel within the lamellae; therefore, this will be the stiffest direction of cancellous bone. Cancellous bone presents anisotropic behaviour, which could be simplified to transversely isotropic behaviour due to the similar behaviour in two of the three orthogonal directions, corresponding to the bone matrix. As a result of imaging evaluation of lamellar tissue structure, we know how to orientate the lamellae in the trabeculae and surrounding holes, and then define the transversely isotropic properties in the numerical models. Nevertheless, lamellae lack of main direction in branches, resulting in a homogeneous region in which isotropic properties can be assumed.

3.5.3 Imaging assessment of lamellar tissue porosity

Once lamellar orientation has been clearly defined, it is important to consider another essential tissue feature, that is the porosity at tissue level. This section assesses cancellous tissue porosity at the FESEM, considering swine and human trabecular bone samples. Two sources of porosity have been distinguished: natural tissue porosity and porosity due to bone diseases, such as osteoporosis.

Cancellous bone inherently exhibits greater porosity than compact bone. The presence of trabeculae imparts structural support while facilitating processes such as nutrient diffusion and bone remodeling. Nonetheless, excessive porosity surpassing physiological thresholds could compromise the strength and stability of bone tissue. The primary influence of porosity on bone tissue manifests through its effect on mechanical properties, with an inverse relationship observed as porosity increases. Furthermore, bone porosity directly affects strength, stiffness, and the entire structural integrity of bone tissue.

Matínez-Reina *et al.* [44] established the main sources of tissue porosity for cortical bone as the sum of canaliculi porosity (P_{can}), lacunae porosity (P_{lac}) and vascular porosity (P_{vas}). Regarding cancellous bone, the natural source of porosity is the lacunocanalicular system formed by P_{can} and P_{lac} amounts about 5 % of tissue porosity. Another source which incorporates porosity to lamellar tissue could be due to some bone diseases, such as osteoporosis. The imbalance of the remodelling cycle at osteoporosis implies a loss of bone mass. In the most severe cases, the rapid activity of the osteoclasts produces depth cavities at the tissue level leading to trabecular bone perforation. This phenomenon is referred to as osteoclastic perforation, which instigates a significant decline in the mechanical characteristics of the bone.

Figure 3.23 presents the primary sources of porosity found in swine cancellous tissue. Both Figures 3.23 a) and b) exhibit the ellipsoidal lacunae that harbour osteocytes. In his work, Marotti [55] defined approximately the lacunae diameters as 4 x 9 x 22 μm. Furthermore, in these images, it is possible to appreciate that these lacunae are arranged in the lamellar direction or circumferentially to the holes, such as the lamellae. In addition, Figures 3.23 c) and d) show small pores which correspond to the canaliculi system. These pores have been found both in lamellar surface, as in Figure 3.23 c), and inside the trabeculae, such as in Figure 3.23 d). Finally, it is important to emphasise that these cancellous samples come from healthy mature swine.

As the magnification increases, it is possible to see clearly the pores at lamellar tissue due to the canaliculi system, such as in Figure 3.24. Owing to the possibility of measuring on the FESEM images, in Figure 3.24 a) is presented one pore measurement, which is less than 1 μm. The pores dimensions in Figure 3.24 b) are in the same order of magnitude as the measured in Figure 3.24 a). At this scale, these pores concern the natural porosity of lamellar tissue, specifically, all the voids of the canaliculi system.

The previous images correspond to healthy cancellous bone samples, swine and human, respectively. Regarding diseased bone, Figure 3.25 shows three
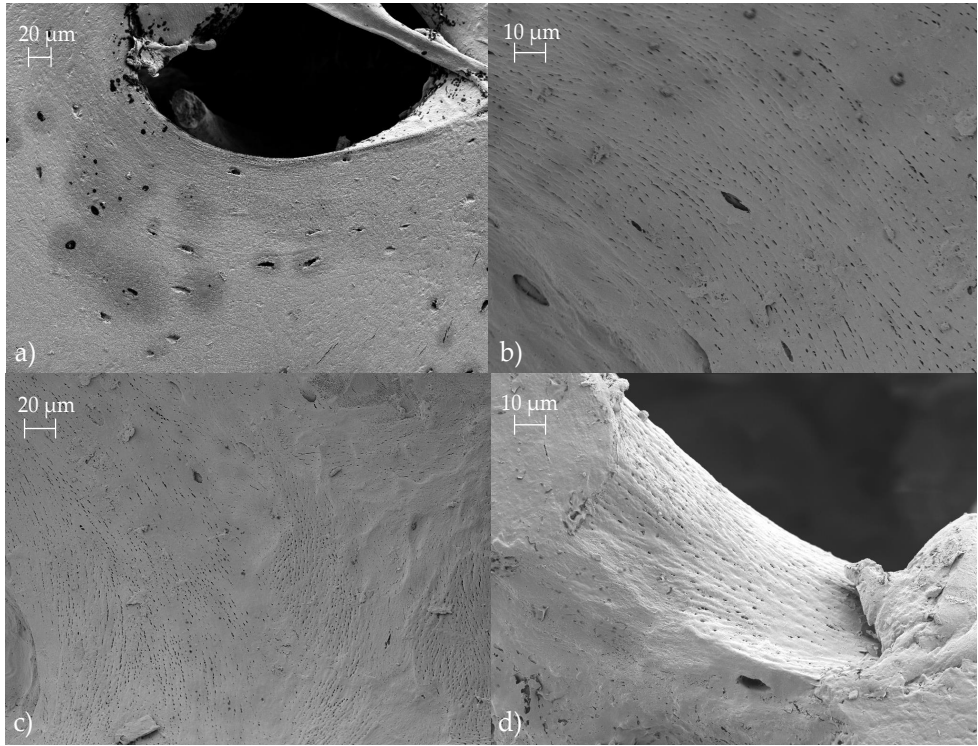
Figure 3.23: Lamellar tissue porosity evaluated at the field emission scanning electron microscope (FESEM) of swine vertebral cancellous samples. a) lacunae that harbour osteocytes circumferentially arranged around the holes, b) and c) present lamellar tissue natural porosity and lacunae and d) natural porosity of the lamellar tissue observed in a single trabecula.

images of osteoporotic lamellar tissue. Noticeably, a large quantity of gnawed tissue surface is observed. These large holes appear could be attributed to the disease because the osteoclasts activity is greater than the osteoblast one. This negative balance in the bone remodelling cycle ends in a lower quantity of bone mass, leading to this gnawed tissue, know as osteoclastic perforation. This huge porosity drastically affects bone mechanical properties by reducing them severely.

Some researchers only consider in their studies the macroscopic porosity, which is related to the deterioration and degradation of bone architecture and results in the reduction of struts thickness, greater separation between trabeculae, or
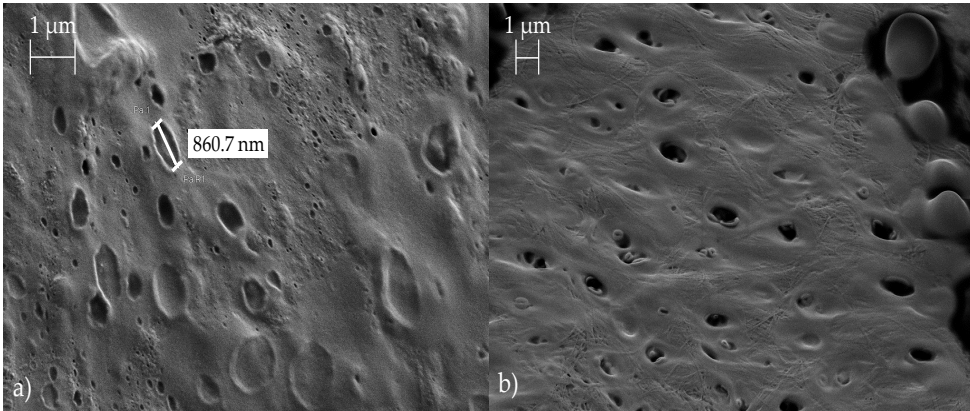
Figure 3.24: Lamellar tissue pores, corresponding to the voids of the canaliculi system, found at lamellar tissue evaluated at the field emission scanning electron microscope (FE-SEM) of human cancellous samples from femoral heads.

less framework connectivity. This porosity type is easily evaluated, such as the stereomicroscope or using micro-CT, examining some morphometric parameters such as the previously mentioned. However, pores, cavities, and perforations have a strong effect on tissue properties and, therefore, on bone stiffness and resistance. For all these reasons, it is essential to consider cancellous tissue porosity to study bone mechanical properties.

Finally, the porosity assessed in the osteoporotic cancellous samples is not classified as natural bone porosity because it is specific to the diseased bones. The holes found at the tissue surface are much bigger than the little pores due to lacunocanalicular system. Therefore, the amount of this type of porosity will be assumed in the further chapters between 5 % and 25 %, i.e. when the percentage of porosity exceeds 5 %, the cancellous bone sample has some bone disease.

3.6   Conclusions

In this chapter, we have evaluated swine and human cancellous specimens using different imaging techniques: the stereomicroscope, micro-CT (μ-CT), and field emission scanning electron microscopy (FESEM). The specimens examined are from different body locations, including lumbar vertebrae and femoral heads. The anatomy and the trabecular orientation of the vertebra and the femoral head have been defined. The vertebral specimens belong to
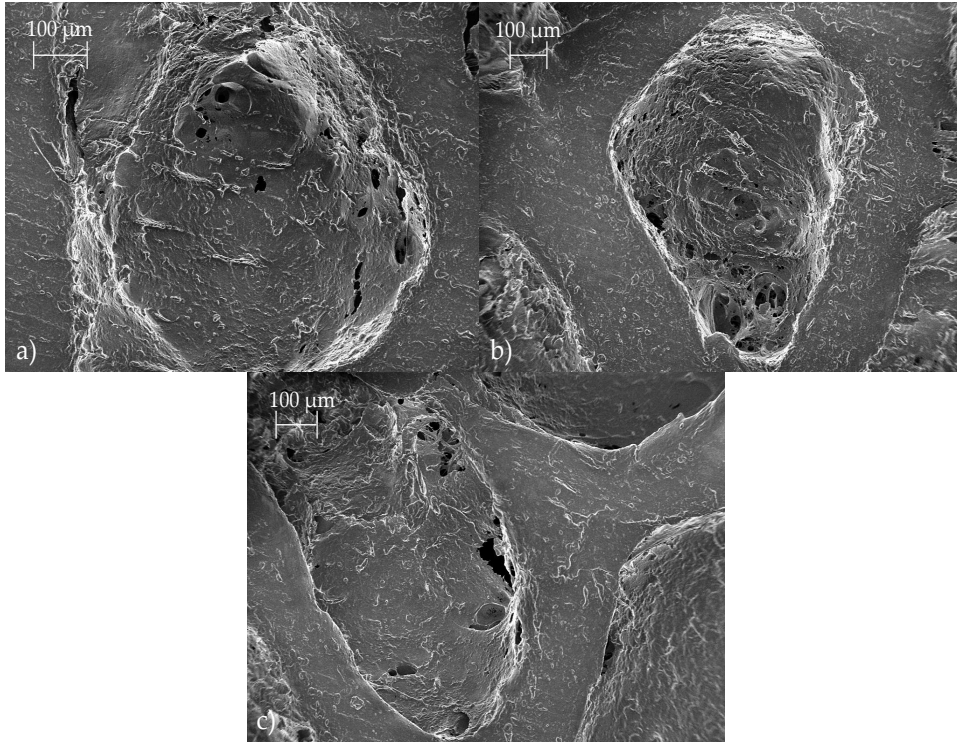
Figure 3.25: Osteoclastic perforation observed at lamellar tissue evaluated at the field emission scanning electron microscope (FESEM) of human cancellous samples from osteoporotic femoral heads.

a skeletally mature swine, and the human femoral heads are provided by the Hospital Universitario Infanta Leonor of Madrid, which have been extracted during the total hip replacement. Human femoral heads were classified into three groups based on the patient's pathology, which can be osteoarthrosis (OA) or osteoporosis (OP), or healthy individuals (HG).

Regarding the stereomicroscope, we have revealed the trabecular microarchitecture of the vertebral and femoral specimens. First of all, the lumbar vertebral specimens have shown a predominant direction, the samples longitudinal direction. In addition, such direction is the stiffest and mainly composed of a plate-like structure. By contrast, struts and rods constitute the trabecular lattice in the other two orthogonal directions of the specimens. Moreover, struts and rods also joint the plates in the longitudinal direction. On the other hand,

femoral cancellous specimens predominant direction depends on the region of the femur. In the femoral heads, the trabeculae are oriented in several directions to withstand all the daily stresses the femur has to deal with. For this reason and regarding the cutting plane, cancellous specimens from the femoral heads present different orientations, mainly in an oblique direction.

Furthermore, the stereomicroscope software allows for measuring the image, and then we acquired several values for the trabecular thickness (Tb.Th) of the different specimens. Our measurements for the vertebral specimens give a trabecular thickness (Tb.Th) of $165.67 \pm 58.53 \ \mu$m, which is in agreement with the findings in the literature, such as Poilliot *et al.* work that presents $160 \pm 20 \ \mu$m, or Nazarian *et al.* [24] with $146 \pm 10 \ \mu$m. For the femoral specimens, the trabecular thickness measured was $279.64 \pm 62.036 \ \mu$m for HG, $203.83 \pm 36.05 \ \mu$m for OA and $149.54 \pm 52.70 \ \mu$m for OP. The lowest trabecular thickness was presented in the osteoporotic specimens due to the degraded microarchitecture because of the pathology. However, between HG and OA specimens sometimes exist overlapping because of some Tb.Th are higher for OA specimens than for HG groups, as Ding and Overgaard indicated in their work [20]. The reason is that osteoarthrosis triggers a large deposition of mineral. Therefore, in the regions where bone is most affected by the disease, the trabecular thickness is slightly higher than in healthy specimens.

On the other hand, the DICOM images obtained from μ-CT scanning revealed structural differences, which enable us to distinguish between the three groups of femoral cancellous samples. The trabecular thickness, the separation between trabeculae, or localized vast regions of mineral has been identified in DICOM images. Images with high trabecular thickness, lower separation between them, and a high quantity of rods and struts represent the HG group. The images that show regions with high mineral content and the rest of the trabeculae are slightly thin than the HG, are mainly from the OA group. Lastly, images with less number of trabeculae, thinner than the others with a high separation between them, and sometimes with holes within the specimen, are indeed osteoporotic specimens. In addition, some other microarchitecture features are revealed in the DICOM images, such as big holes in specimens, which usually belong to OP samples, and the bone growth line, which is where the bone has been growing during childhood and adolescence, and is closed in the when the bone matures to adulthood. Finally, the relevance of an exhaustive cleaning of the specimens has been stated. If the specimens have rests of organic remains, they appear on the DICOM images in greyish depending on their density and are part of the greyscale of the DICOM image.

Ultimately, vertebral and femoral cancellous samples have been examined at the FESEM. On the one side, the lamellar tissue has been assessed, emphasizing the lamellar orientation. In addition, the lamellar tissue porosity, called microporosity, has been observed. All this information will be used to improve the numerical models of the specimen to make them more realistic and better capture the mechanical behavior of those samples. Lamellae orientation is mainly arranged along the trabeculae direction and circumferential to holes, while in branches, this lamellae orientation is not as clear. Regarding microporosity, the natural porosity of the tissue is composed of the lacunae, after osteocytes death, and the canaliculi network that connects the osteocytes. Then, this natural tissue porosity is caused by the so-called lacunocanalicular system. On the other hand, when bone suffers a pathology, such as osteoporosis, besides the reduction of trabecular thickness, big holes and deep cavities arise at the lamellar tissue. This porosity is called osteoclastic perforation. The images captured at the FESEM have allowed us to evaluate all the microarchitecture, lamellar tissue, and microporosity of the vertebral and femoral cancellous specimens.

Chapter 4

Explicit expressions for the estimation of the elastic constants of lamellar bone as a function of mineral content and porosity

4.1 Introduction

Elastic and strength properties of lamellar tissue are essential to analyse the mechanical behaviour of bone at the meso- or macro-scale. Although many efforts have been made to model the real architecture of cancellous bone, in most cases, isotropic elastic constants are assumed for tissue modelling. In such cases, its non-isotropic behaviour has been neglected, together with the influence of the bone mineral density and porosity on its mechanical response. Hence, usually, isotropic damage laws are used to estimate bone failure.

In this chapter, the non-isotropic terms of the stiffness matrix for the lamellar tissue are derived as explicit functions of the volumetric bone mineral density and microporosity at tissue scale ($1 - 5$ % for normal bone and up to 25 % for osteoporotic bone) by considering a multiscale approach. Microcomputed tomography (μ-CT) scans have been performed to obtain the micro-finite element (μ-FE) model of the representative volume of cancellous bone from the lumbar vertebra of one skeletally mature swine specimen. The numerical model has been analysed under quasi-static tension and compression load cases. In this model, the elastic constants and the inferred strength limits of lamellar tissue are defined by considering a unidirectional layer pattern being the mineralised collagen fibrils oriented in the most representative geometrical feature of the trabeculae network. In this study, we have considered the Hashin's orthotropic interactive failure criterion for estimating the initiation of the tissue failure. In addition, in order to analyze the damage evolution, a Material Property Degradation (MPDG) approach has been implemented. A detailed study about the influence of the damage parameters on the bone mechanics behaviour is also given.

The main contributions of the research presented in this chapter can be summarized in: (1) it addresses the numerical modelling of the cancellous bone mechanical behaviour. In this case, not only considering the microstructure, as usually done in literature, but also the non-isotropic elastic tissue properties, as a function of bone mineral density (BMD) and microporosity. (2) It includes the orientation of the mineralised collagen fibrils in the main geometrical feature of the trabeculae network. (3) It also proposes to use an interactive failure criterion based on the inferred orthotropic lamellar strength limits. (4) The post-yield behaviour is also addressed in a sensitivity analysis by means of an efficient technique, based on the elastic property degradation.

The objective of this chapter becomes even more important when characterising the mechanical competence of bone that exhibits certain pathologies. In osteoporosis, for example, the presence of "non-healthy" micro pores by the osteoclastic perforation as a consequence of the bone turnover unbalanced process [52–54] is scarcely addressed in literature from a mechanical point of view. These pores, as in any structural material, will undermine the mechanical functionality of bone. In addition, in this pathology, the increase of the mineral content in certain regions causes more heterogeneity and weakens the mechanical behaviour of bone. In order to deal with these phenomena from a numerical point of view, non-isotropic detailed constitutive models are needed.

4.2 Explicit modelling of porosity at tissue level

Cancellous bone is highly porous and heterogeneous, primarily located at the epiphysis and metaphysis of long bones and within vertebral bodies. Adult bone tissues, including cortical and cancellous bone, exhibit a laminated structure at the microscale. This laminated structure consists of lamellae, constituting the lamellar bone tissue, where mineralised collagen fibrils are the main component. Therefore, lamellar tissue stiffness and strength properties are crucial to studying and understanding bone mechanical behaviour at the meso and macro-scale.

Lamellar tissue porosity directly affects bone mechanical properties, reducing them as porosity increases. Lamellar tissue has an inherent source of porosity due to the lacunocanalicular system, which consists of lacunae and the canaliculi system. Moreover, when any bone disease is developed can produce large voids which accumulate porosity at lamellar tissue. For example, in osteoporosis, the high activity of the osteoclasts produces the so-called osteoclasts perforation, which causes big voids within lamellar tissue. These porosity sources will be explicitly modelled to develop equations of lamellar tissue properties as a function of bone mineral density (BMD) and porosity.

Regarding the numerical models, with the recent advances in acquisition techniques of high-resolution medical image and postprocessing software, the numerical analysis of the strength of trabecular bone through μ-FE models has become an interesting option. Non-linear μ-FE models were used to simulate pre- and post-yielding cancellous bone behaviour [97, 105, 209, 210, 309, 310]. In this numerical context, an option to simulate the bone failure is the Continuum Damage Mechanics (CDM) approach. In this approach, the initiation and propagation of cracks is based on a smeared crack approach [97, 210, 212, 213, 311]. In a quasi-static loading case, isotropic damage laws are often used to represent the non-linear behavior of cancellous bone [97, 105]. In addition, finite element deletion technique is also considered to model the complete fracture of the trabeculae [210].

Concerning the strength of trabecular bone, a detailed review of several failure criteria applied in material science is reported in Oftadeh *et al.* work [59], that have been considered for the study of the bone mechanics under multi-axial stresses. In that work, it is also highlighted that bone mechanical behaviour is highly dependent on tissue properties.

In order to implement a damage evolution law in a three-dimensional numerical analysis, the Material Property Degradation (MPDG) is a procedure

very efficient computationally. This method can simulate the post-damage degradation of brittle anisotropic materials. The MPDG results in a nonlinear evolution where the damage variable, d, takes predefined discrete values depending on the dominant failure mode, and assumes an instant stiffness reduction of the material. In contrast, in the Continuum Damage Mechanics (CDM) approach, the damage variable gradually increases with the amount of fracture energy dissipated. The discrete damage method is also applied to the study of progressive failure in laminate structures.
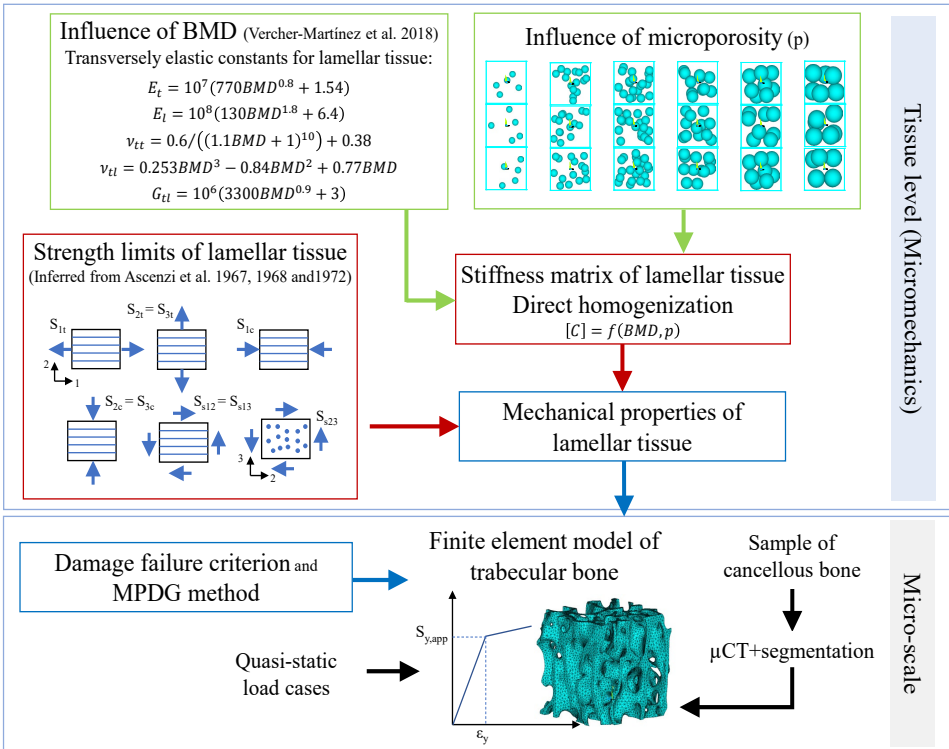
Figure 4.1: Work flow of the analysis performed in this work, from tissue micromechanics characterisation to the μ-FE numerical model.

The scheme shown in Figure 4.1 depicts the work flow of the numerical study carried out in this chapter. As a starting point, we consider the equations for the estimation of the non-isotropic elastic constants of lamellar tissue as a function of the BMD [46]. Subsequently, the influence of the microporosity on the elastic constants is also included explicitly in the numerical models and, therefore, the new homogenization stiffness matrices are derived as a function

of BMD and porosity p. On the other hand, the tissue strength limits have been inferred from the literature [312–314]. Hence, the resulting mechanical properties of lamellar tissue are applied to the μ-FE model of a representative volume of trabecular bone from swine lumbar vertebra. As a first approximation, in the numerical model, the bundles of fibres are oriented following the predominant direction of the trabeculae network. Then, Hashin's orthotropic three-dimensional quadratic failure criterion for fibre composites [315] has been implemented to estimate the onset of the failure in quasi-static displacement-controlled tension and compression numerical simulations. Finally, the damage evolution law follows the Material Property Degradation (MPDG) method. A study of the influence of the damage parameters is also performed.

4.2.1 Modelling porosity at tissue level

Lamellar tissue porosity has been defined and evaluated in the previous chapters. The lacunocanalicular system tissue porosity and osteoclasts perforation will be explicitly modelled in this section. The porosity ranges from 1 to 5 % for natural tissue porosity and from 5 to 25 % for a diseased bone, whose porosity is due to a bone illness such as osteoclasts tissue perforation.

In Figure 4.2, the mineralised skeleton of a swine vertebral trabecular bone sample is observed using the field emission scanning electron microscope (FE-SEM) of the Microscope Service at the Polytechnical University of Valencia. These images show that lamellar tissue deposition exhibits a predominant multilayer arrangement. The lamellar nature of the cancellous tissue is clearly manifested at certain regions (Fig. 4.2 (a-d)). In contrast, some regions show a more homogeneous appearance (Fig.4.2 (e)). The lacunocanalicular porosity at tissue level is also observed (see Fig.4.2 (f)). Furthermore, in Fig.4.3 empty lacunae are clearly distinguished.

In the present study, the porosity at tissue level is explicitly modelled by subtracting non-overlapping spheres randomly distributed from a representative elementary volume of lamellar tissue model. The different values of porosity considered are 1, 5, 10, 15, 20 and 25 % [44]. In order to obtain averaged properties, 10 models with random distribution of spheres have been analyzed for each value of porosity. In Figure 4.4 (a), three models out of the ten random distributions of voids are shown for each porosity. The numerical model of a representative volume of porous lamellar tissue is depicted in Figure 4.4 (b), where the elastic properties for the non-porous part of the lamellar tissue are estimated as a function of BMD, using the equations proposed in [46]:
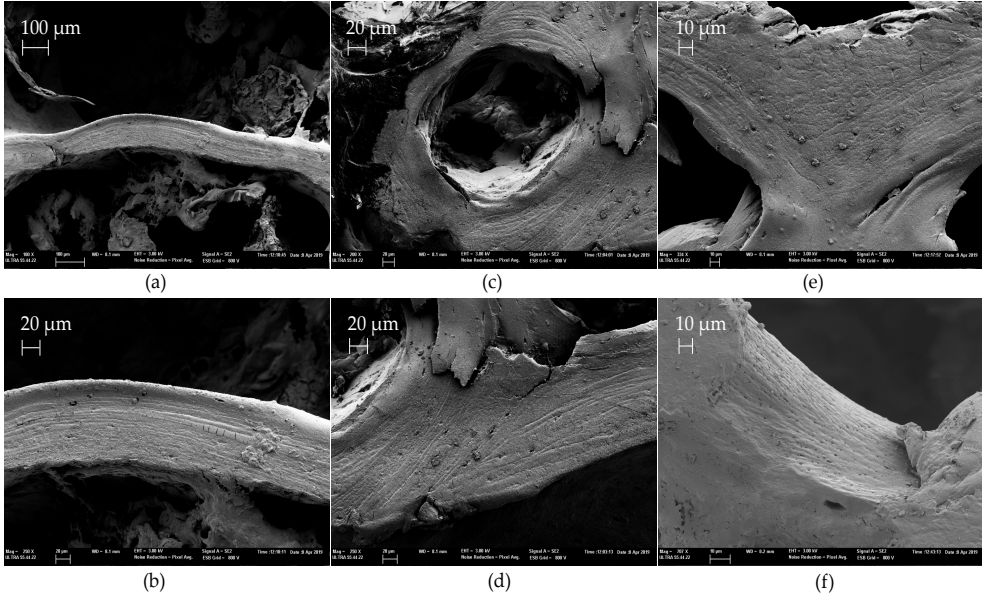
Figure 4.2: Mineralised skeleton of the lamellar tissue deposition in a swine vertebral trabecular bone sample (Field Emission Scanning Electron Microscope - FESEM). (a) Cross section of a plate structure showing a prone multilayer lamellar tissue deposition. (b) A magnification of (a). In (c) lamellar arrangement exhibits a circumferential pattern around a cavity. (d) A magnification of (c). In (e) a branched region is localized showing a more homogeneous tissue arrangement. In (f), the surface of a strut is observed. Microporosity due to lacunocanaliculli system is clearly identified.

$$E_l^{lam} = 10^8 (130 \, \mathrm{BMD}^{1.2} + 6.4) \tag{4.1}$$

$$E_t^{lam} = 10^7 (770 \, \mathrm{BMD}^{0.8} + 1.54) \tag{4.2}$$

$$\nu_{tl}^{lam} = 0.253 \, \mathrm{BMD}^3 - 0.84 \, \mathrm{BMD}^2 + 0.77 \, \mathrm{BMD} + 0.01 \tag{4.3}$$

$$\nu_{tt}^{lam} = \frac{0.6}{(1.1 \, \mathrm{BMD} + 1)^{10}} + 0.38 \tag{4.4}$$

$$G_{tl}^{lam} = 10^6 (3300 \, \mathrm{BMD}^{0.9} + 3) \tag{4.5}$$

132
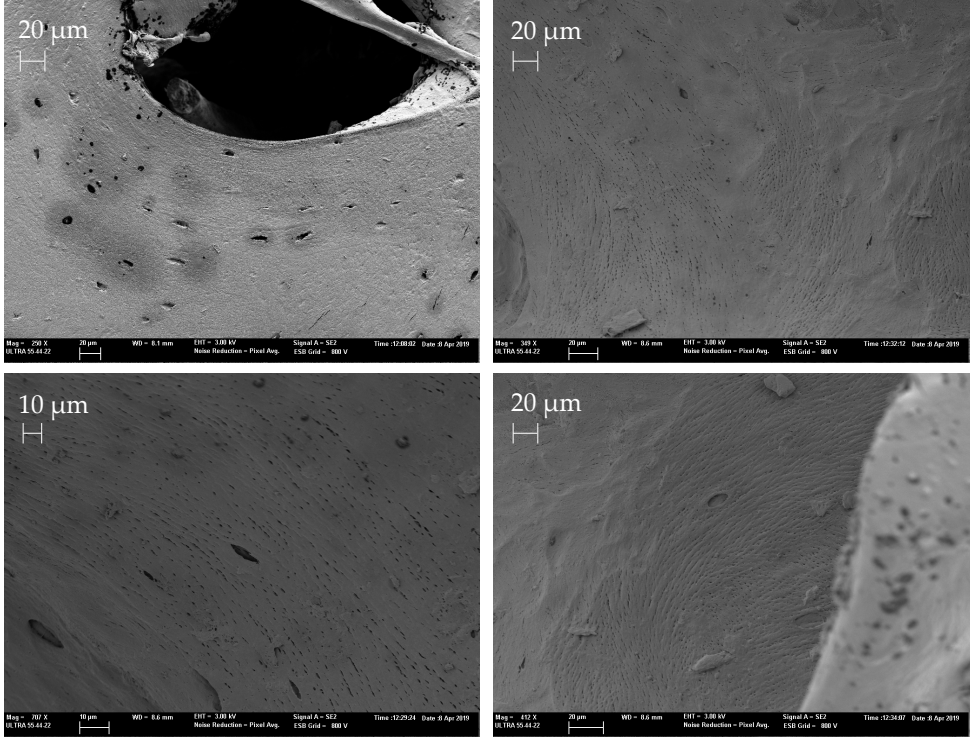
Figure 4.3: Porosity due to the lacunocanalicular system in cancellous bone from swine vertebral sample (Field Emission Scanning Electron Microscope - FESEM).

$$G_{tt}^{lam} = \frac{E_t^{lam}}{2(1 + \nu_{tt}^{lam})} \qquad (4.6)$$

where E is the Young's modulus, ν represents the Poisson's ratio and G is the shear modulus. In addition, subscripts l and t indicate the longitudinal and transverse directions of the fibre bundles and lam indicate that the properties are estimated for non-porous lamellar tissue.

In Figure 4.4 (c), the reference system (x, y, z) corresponds to an orientated reference system where 1 indicates the longitudinal direction of the mineralised collagen fibrils (l), 2 and 3 are two orthogonal or transverse directions (t) of the fibril array. This reference system is only used to set the transversely isotropic elastic properties and strength limits for lamellar tissue.
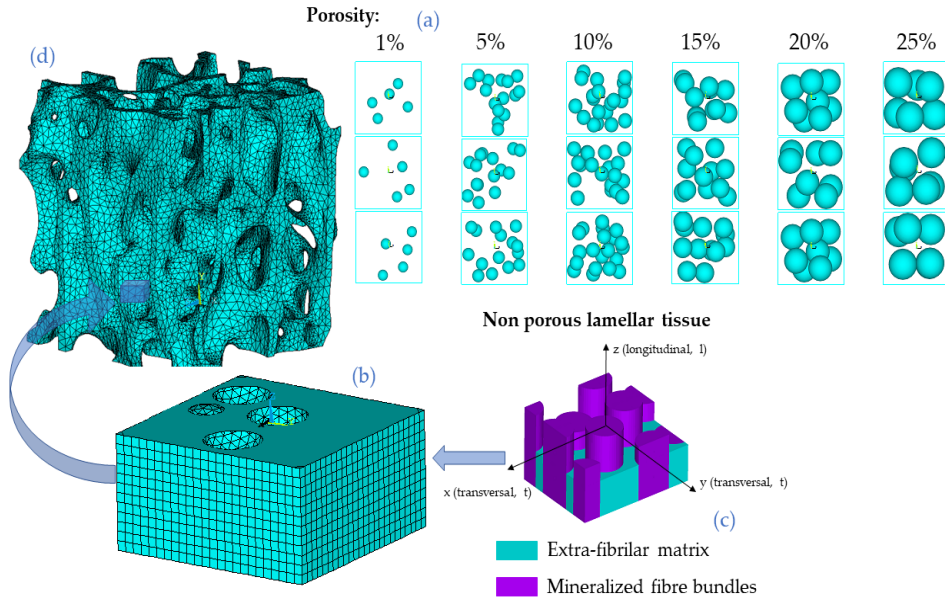
Figure 4.4: (a) Random distribution of non-overlapping spheres representing the voids. Three examples of the ten models for each level of porosity (plane view projections). (b) Numerical model of the representative elementary volume of porous lamellar tissue. (c) Transversely isotropic elastic properties of lamellar tissue as a function of BMD at tissue level [46]. (d) μ-FE model of trabecular bone with homogenized tissue elastic properties. Note that reference system (x, y, z) corresponds to an orientated reference system where 1 indicates the longitudinal direction of the fibrils, 2 and 3 are two transverse directions.

Cancellous tissue is less mineralised than cortical bone, mainly due to a higher activity of the bone turnover in the trabeculae network. Therefore, considering the work by Koller and Laib [316], the minimum value for the BMD at tissue level is assumed $0.653\,\mathrm{g/cm}^3$ and the maximum is derived from the work by Yu *et al.* [317] being $1.5\,\mathrm{g/cm}^3$. Table 4.1 summarizes the numerical values of porosity and BMD at tissue level that have been analyzed in the present work.

In order to estimate the averaged apparent stiffness of the porous lamellar tissue the following procedure has been carried out. First, a direct homogenization technique has been applied by means of the finite element method. Periodic boundary conditions are enforced, guaranteeing that the hexahedron analyzed behaves as a continuum domain. The displacement gradients along the corresponding external surfaces must be equal, and, for this purpose, the

Table 4.1: Values of BMD (g/cm^3) and porosity (%) at tissue level considered for estimating the elastic constants of lamellar tissue.

BMD	0.653	0.75	0.85	0.95	1.05	1.16	1.24	1.32	1.39	1.44	1.48	1.50
Porosity					1, 5, 10, 15, 20, 25							

equations established in Hohe [318] are employed. Assuming the linear elastic Hooke's law (Eq. 4.7)

$$\sigma_{ij} = C_{ijkl}\, \varepsilon_{kl} \tag{4.7}$$

where σ_{ij} and ε_{kl} are the stress and strain tensors, the elements of the constitutive elastic tensor C_{ijkl} are derived applying six independent unitary strain fields.

Lastly, the elastic constants are explicitly expressed as a function of BMD and porosity, p, using non-linear multi-variable regressions. These equations will be provided in the following Section 4.3.1, and applied to define the elastic properties of lamellar tissue for the μ-FE model (see Figure 4.4 (d)).

4.2.2 Strength limits inferred of lamellar tissue

In the secondary osteons, lamellae arrange circumferentially around the Havers canal. Within a lamella, mineralised collagen fibrils maintain their orientation constant and change it across the radial direction of the osteon in successive lamellae building the so-called rotated plywood pattern. In the work of Giner *et al.* [319] the lamellar structure observed in a secondary osteon, was condensed in two equivalent layers: the thin and thick lamellae. In the thin lamellae, fibrils are mainly aligned with the circumferential direction of the osteon and in the thick lamellae, fibrils are roughly parallel to the long axis of the osteon (see Figure 4.5). Thin and thick lamellae do not have any direct application on the trabecular bone numerical model, we use them only to estimate the strength limits of lamellar tissue.

The in-plane strength properties for lamellar tissue were derived from several works of Ascenzi and Bonucci in which tensile and shear loading were applied on different types of isolated osteons [312, 314], with the circumferential $\sigma_{\theta\theta}$, radial σ_{rr} and shear $\sigma_{r\theta}$ stresses (see Figure 4.5) and their respective strength limits.

135
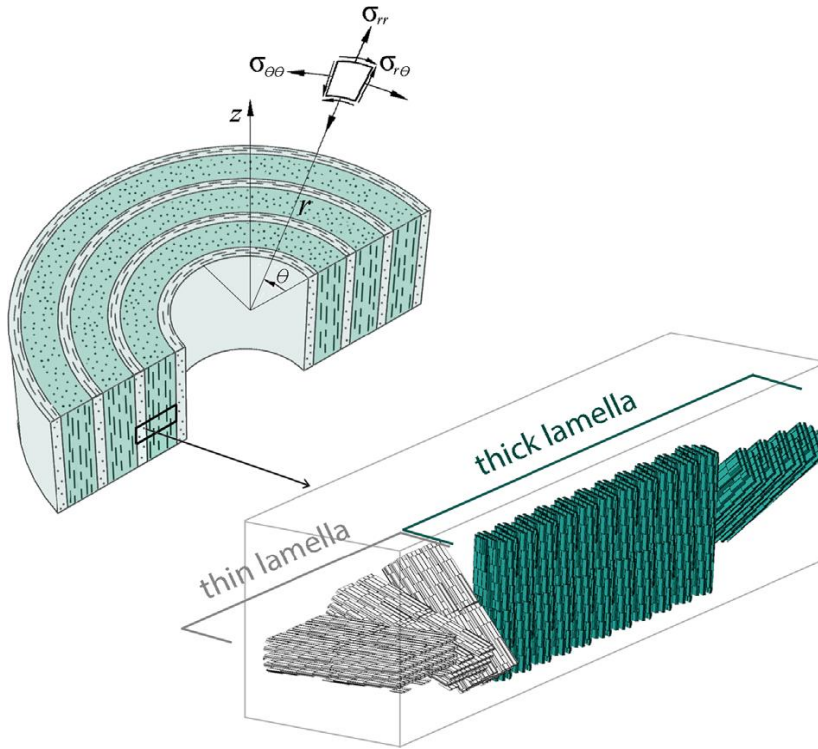
Figure 4.5: Model of an osteon showing the cylindrical reference system (r, θ, z). The thin and thick lamellae are defined bunching the layers where mineralised collagen fibrils are orientated in a predominant direction [319].

In this work, the strength limits of an orthotropic material S_{1t}, S_{2t}, S_{3t}, S_{s23}, S_{s13} and S_{s12} depicted in Figure 4.6 (following the customary terminology in structural composite materials), are inferred: the circumferential tensile strength $S_{\theta\theta,t}$ for thin lamellae derived in Giner *et al.* [319] corresponds to S_{1t} whereas $S_{\theta\theta,t}$ for thick lamellae corresponds to S_{2t} and S_{3t}. Additionally, the shear strength $S_{r\theta,s}$ for thick lamellae is equivalent to S_{s23} and for thin lamellae is S_{s12} and S_{s13} (see Figure 4.5 and Figure 4.6).

In order to infer the strength limits under compressive loading, the work of Ascenzi and Bonucci [313] has been considered. In their work, the stress-strain curves for compressive loading tests in the longitudinal direction of the osteon were obtained for different degrees of calcification and ages. The experimental analysis were developed for different types of osteons, classified
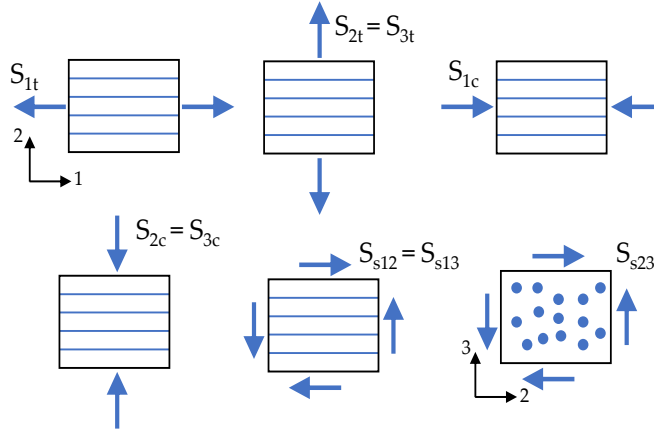
Figure 4.6: Schematic representation of the strength limits in an orthotropic material following customary terminology in structural composite materials. Reference system (1,2,3) corresponds to the orientated reference system where 1 indicates the longitudinal direction of the fibrils, 2 and 3 are two orthogonal directions (see Figure 4.4).

according to the predominant orientation of the mineralised collagen fibrils, in osteons of type I, II and III. In type I osteons, fibrils are mainly orientated in the circumferential direction of the osteon, consequently, the strength limit inferred from the stress-strain curve corresponds to $S_{2c} = S_{3c}$. Additionally, in type III osteons, fibrils are mainly aligned with the longitudinal direction of the osteon, hence, the strength limit S_{1c} can be estimated.

Table 4.2: Strength limits for fully calcified lamellar tissue. Approximated from Ascenzi and Bonucci [312–314].

$S_{1t} = 120\text{MPa}$	$S_{2t} = S_{3t} = 50\text{MPa}$
$S_{1c} = -115\text{MPa}$	$S_{2t} = S_{3t} = 50\text{MPa}$
$S_{2c} = S_{3c} = -160\text{MPa}$	$S_{s12} = S_{s13} = 46\text{MPa}$
$S_{s23} = 38\text{MPa}$	

Ascenzi and Bonucci works of tensile [312], compressive [313], and shear [314] properties from single osteons provided their results in different graphics. The results were presented separately depending on the disposition of the osteon trabeculae, whether they were air-dried or wet, and the level of calcium, the initial stage of calcification or fully calcified. For the present work, the nu-

merical values considered are an intermediate value of the range recorded by Ascenzi and Bonucci. The numerical values come from the graphics of fully calcified osteons in wet conditions and are summarized in Table 4.2.

4.2.3   Micro-FE of trabecular vertebral specimen

The trabecular bone sample was prepared at Instituto de Biomecánica de Valencia (IBV) from lumbar vertebrae of one skeletally mature swine recently euthanised. The parallelepiped-shaped sample, was at least 10 mm side.

The specimen was scanned by μ-CT (Skyscan 1172, Bruker, Kontig, Belgium) at the Estación de Bioloxía Mariña de A Graña (Universidad de Santiago de Compostela, Spain) μ-CT service, with an isotropic voxel resolution of 13.58 μm (voltage 100 kV, intensity 100 μA, Al/Cu filter). μ-CT images were segmented using ScanIp software (Simpleware, UK). Before generating the mesh, the geometrical model was cut leading to a cube shaped volume with approximately $2 \times 2 \times 2$ mm side.

μ-FE mesh was generated using ScanIP Software (Simpleware, UK), leading to a mesh of 3D linear elements. The finite element model of the specimen was able to reproduce with good accuracy the heterogeneous microstructure of cancellous bone (see Figure 4.7). The numerical model is built in a global reference system (x, y, z) where loads and constraints will be applied. In this mesoscale finite element model, y direction denotes the principal bone direction where plates predominate. Instead, x and z directions show a higher porosity and a strut-like structure.

The stiffness matrix for bone tissue has been estimated considering the approach developed in this work, assuming uniform reference values for bone mineral density (BMD) and porosity at tissue level: 0.85 g/cm^3 and $p = 5$ %. Regarding the strength limits, values summarized in Table 4.2 are specified in the numerical model. As a first approximation, we have assumed that the fibril bundles are unidirectionally orientated following the predominant direction of the trabecula [62]. Consequently, local material reference systems are defined with the purpose of considering the non-isotropic lamellar tissue properties, both elastic and strength features, in the μ-FE model.
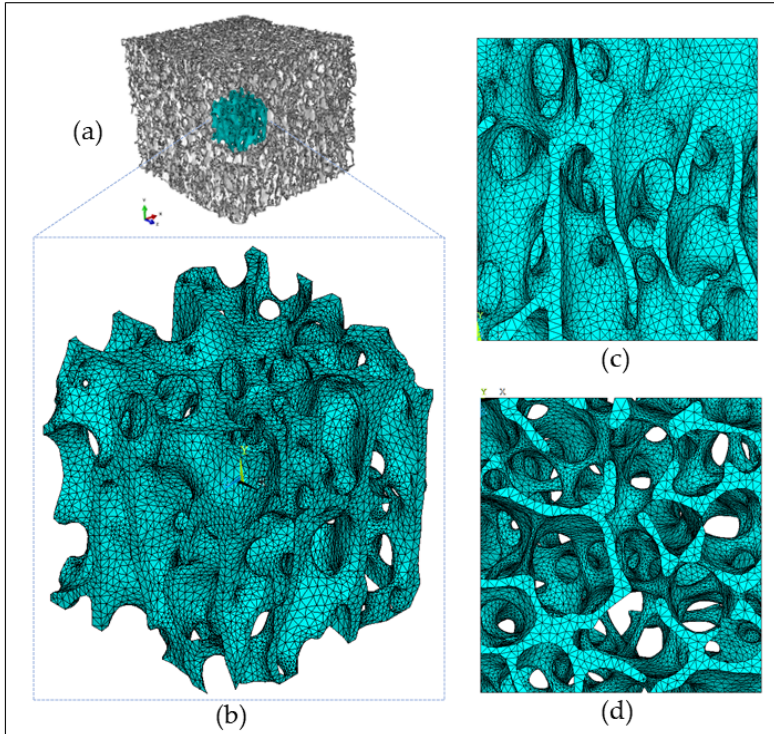
Figure 4.7: μ-FE model of a lumbar vertebra trabecular bone. (a) Geometrical model from segmentation of μ-CT images, (b) isometric, (c) front and (d) top view. The numerical model has been analyzed with $Ansys^{\copyright}$ APDL Software.

4.2.4 Bone failure modelling

In this section an orthotropic failure criterion is presented for defining the failure onset. Owing to the possibility of considering lamellar tissue as a laminate structure, the Hashin criterion [315], which is widely used in analysis of structural composite materials to predict intralaminar failure, is an interesting option to analyze the failure initiation at tissue level. The Hashin failure criterion is specially formulated to account for different damage mechanisms. Matrix failure is associated with intralaminar transverse and shear loads, whereas fibre failure is related to longitudinal tension.

The three-dimensional formulation of this orthotropic failure criterion is given by the following equations:

$$f_f = \left(\frac{\sigma_{11}}{X_t}\right)^2 + \frac{(\tau_{12}^2 + \tau_{13}^2)}{S^2}; \quad \sigma_{11} > 0 \qquad (4.8)$$

$$f_f = \frac{\sigma_{11}}{X_c}; \quad \sigma_{11} < 0 \qquad (4.9)$$

$$f_m = \frac{(\sigma_{22} + \sigma_{33})^2}{Y_t^2} + \frac{(\tau_{23}^2 - \sigma_{22}\sigma_{33})}{Q^2} + \frac{(\tau_{12}^2 + \tau_{13}^2)}{S^2}; \quad \sigma_{22} + \sigma_{33} > 0 \qquad (4.10)$$

$$f_m = \frac{(\sigma_{22} + \sigma_{33})}{Y_c}\left[\left(\frac{Y_c}{2Q}\right)^2 - 1\right] + \frac{(\sigma_{22} + \sigma_{33})^2}{4Q^2} + \frac{(\tau_{23}^2 - \sigma_{22}\sigma_{33})}{Q^2} + \frac{(\tau_{12}^2 + \tau_{13}^2)}{S^2};$$
$$\sigma_{22} + \sigma_{33} < 0 \qquad (4.11)$$

where the subscript f corresponds to fiber failure and m refers to matrix failure. In addition, $X_t = S_{1t}$, $X_c = S_{1c}$, $Y_t = S_{2t}$, $Y_c = S_{2c}$, $S = S_{s12}$ and $Q = S_{s23}$ are the strength limits for lamellar tissue detailed in Section 4.2.2.

The most critical of the failure modes is selected by means of:

$$f = \max(f_f, f_m) \qquad (4.12)$$

Note that in the above equations, f denotes the inverse of reserve factor, hence, critical values are greater or equal to one.

4.2.5 Material property degradation MPDG for damage evolution law

Once the failure has initiated, the damage evolution law based on the material property degradation MPDG method is considered. In this smeared crack approach, the discrete domain is a continuum mesh where the continuity in the displacement field is preserved. In order to reproduce the presence of cracks, the material stiffness is reduced, once the failure is achieved according to a failure criterion. A scheme of the method is shown in Figure 4.8.

This progressive damage model is used to analyze the post-damage degradation of brittle anisotropic materials. The instant stiffness reduction is applied by means of the degradation parameter d that affects the element stiffness
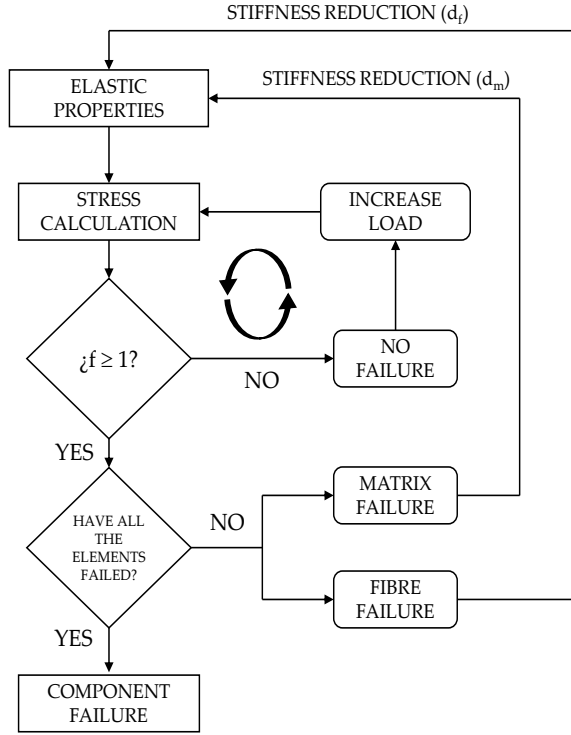
Figure 4.8: Scheme of the material property degradation MPDG method.

matrix. In the damage model, no tissue properties that could influence on the bone fracture toughness are considered.

Assuming a linear elastic behavior, $\widetilde{\sigma} = \mathbf{C}\epsilon$ is verified, where $\widetilde{\sigma}$ is the effective Cauchy stress (stress measured in the undamaged domain) and $\mathbf{C}$ is the undamaged constitutive matrix. Hence, the relationship for a damaged material is given by the following equation:

$$\sigma = \mathbf{C_d}\epsilon \tag{4.13}$$

where σ is the nominal stress (effective stress averaged over the entire domain, including both damaged and undamaged domains), ϵ is the strain and $\mathbf{C_d}$ is the damaged constitutive matrix. The relationship between the effective stress

141

$\widetilde{\sigma}$ and the nominal can be found in Barbero and Cabrera [320]. $\mathbf{C_d}$ can be written in terms of the damage variables as follows:

$$
\mathbf{C_d} = \begin{pmatrix}
\frac{S_{11}}{(1-d_f)} & S_{12} & S_{13} & 0 & 0 & 0 \\
S_{21} & \frac{S_{22}}{(1-d_m)} & S_{23} & 0 & 0 & 0 \\
S_{31} & S_{32} & \frac{S_{33}}{(1-d_m)} & 0 & 0 & 0 \\
0 & 0 & 0 & \frac{S_{44}}{(1-d_s)} & 0 & 0 \\
0 & 0 & 0 & 0 & \frac{S_{55}}{(1-d_s)} & 0 \\
0 & 0 & 0 & 0 & 0 & \frac{S_{66}}{(1-d_s)}
\end{pmatrix}^{-1}
\tag{4.14}
$$

where S_{ij} represent the terms of the the compliance matrix of the undamaged material $\mathbf{S}$ and d_f, d_m and d_s are the fiber, matrix and shear damage variables, respectively. Equation 4.14 represents the three-dimensional approach of the stiffness matrix for a damaged unidirectional lamina formulated under the plane-stress assumption in Matzenmiller *et al.* [321]. Valid values for the damage variables are between 0 and 1, where 0 implies no damage and 1 complete loss of stiffness in the affected mode. This method assumes four damage modes:

$$
d_f = \begin{cases} d_f^t & \text{if } \sigma_{11} \geq 0 \\ d_f^c & \text{if } \sigma_{11} < 0 \end{cases}
\tag{4.15}
$$

$$
d_m = \begin{cases} d_m^t & \text{if } \sigma_{22} + \sigma_{33} \geq 0 \\ d_m^c & \text{if } \sigma_{22} + \sigma_{33} < 0 \end{cases}
\tag{4.16}
$$

$$
d_s = 1 - \left(1 - d_f^t\right)\left(1 - d_f^c\right)\left(1 - d_m^t\right)\left(1 - d_m^c\right)
\tag{4.17}
$$

Note that the shear damage variable d_s is not an independent variable being determined by d_f and d_m by means of Equation 4.17 . Degradation parameters are scalar user-specified quantities. In this analysis, both the initiation failure criterion and the MPDG method have been implemented in the finite element code using scripts in Ansys APDL. Following a usual procedure in structural composite materials, the non-linear analyses are performed assuming certain parameter values. A sensitivity study on the post-yield behavior has been performed in the current work, considering different values for the damage parameters d_f and d_m. For the damage variable associated with the failure due to loads acting on the longitudinal direction of the fibrils, two values have been considered: $d_f = 0.9$ and $d_f = 0.9999$. In laminate strength analysis,

fibre failure is usually associated with a severe failure mode, hence, a high value is usually assumed. That means a very important reduction of element stiffness. In fact, the large value of the degradation parameter, $d_f = 0.9999$, entails the elimination of the element, producing an overload on the neighbour elements that will not be supported. This situation usually prompts a catastrophic failure. Regarding the damage variable d_m, this failure mode occurs mainly when loads are acting on the transverse direction of the fibrils or shearing. The numerical values here considered are: $d_m = 0.5, 0.95$ in the light of the possibility of redistributing the loads when matrix fails, being still able to bear certain level of load. Finally, the ply discount approach is also considered, being $d_m = 0.9999$ [320, 322]. In this later approach, for the sake of completeness, the stiffness of the element that reaches the damage onset as a consequence of transverse loading, is reduced almost to zero.

4.3   Results

In this section, the explicit expressions for the terms of the stiffness matrix as a function of bone mineral density (BMD) and microporosity are presented. These expressions have been used for studying the trabecular bone behaviour under tension and compression loads. Several degradation parameter values for fibers d_f and matrix d_m have been analysed to study failure in each orthogonal direction of the trabecular sample. Finally, the obtained results for the yield strain and the Young's modulus have been compared with those found in the literature.

4.3.1   Stiffness of lamellar tissue as a function of bone mineral density (BMD) and microporosity

From now on, subscript 1 denotes the longitudinal direction of the fibrils, subscripts 2 and 3 represent two orthogonal directions in the transverse plane of lamellar tissue as shown in Figure 4.4. In Figures 4.9-4.11, the orthotropic terms of the symmetric stiffness matrix of lamellar tissue are plotted, as a function of the variables BMD and porosity. The anisotropic terms are negligible. The markers correspond to the averaged results obtained from ten numerical homogenized random models. Nonlinear regressions are shown as solid lines, given in Eqs. 4.18 to 4.26.

As summarized in Table 4.1, the analyses have been performed for six values of porosity and, for each one, twelve values of BMD. Additionally, as detailed in Section 4.2.1, for each level of porosity, ten geometrical configurations with
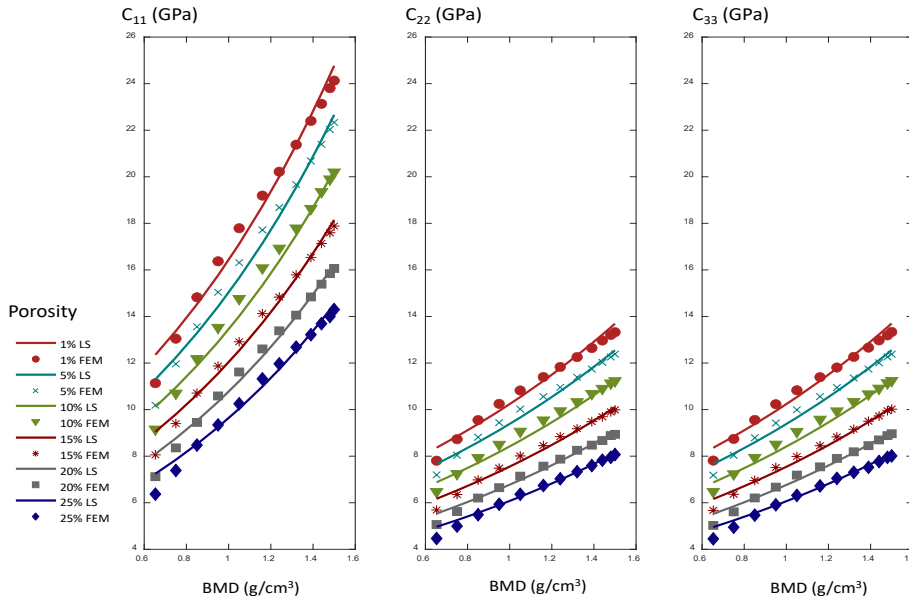
Figure 4.9: Evolution of the terms C_{11}, C_{22} and C_{33} of the stiffness matrix for lamellar tissue as a function of BMD and porosity. Markers denote the averaged results from ten numerical homogenized random FE models. Solid lines represent the least square fitting by an exponential function given in Eqs. 4.18 to 4.20.

randomly distributed voids have been analyzed. For this propose, scripts in $Matlab^{©}$ and $Ansys^{©}$ APDL have been programmed.

A consistent trend is observed in these results. The higher level of BMD makes the bone stiffer for all porosity values. Likewise, for a given value of BMD, the bone loses stiffness as the porosity increases. It should be highlighted the uniform trend of the principal diagonal terms of the stiffness matrix with both variables, BMD and porosity. A transverse isotropic behavior is observed, being the stiffest direction coincident with the mineralised collagen fibrils orientation (values of C_{11} are the highest, whereas C_{22} and C_{33} are very similar).

For the sake of clarity, in Figure 4.12 the multivarible regressions for the orthotropic terms of the stiffness matrix of lamellar tissue are depicted in three-dimensional plots. Numerical results are represented by blue markers and the regression fitted as a grey surface.
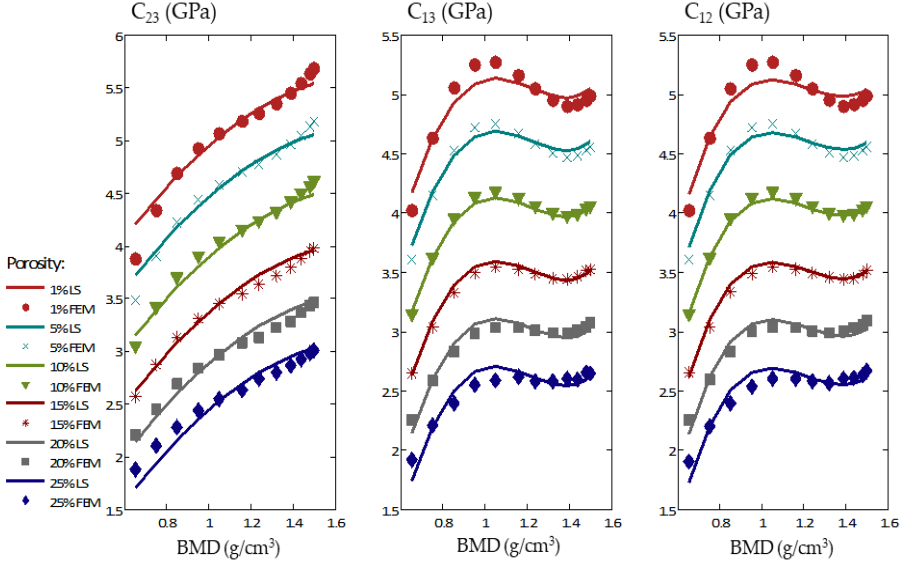
Figure 4.10: Evolution of the terms C_{23}, C_{13} and C_{12} of the stiffness matrix for lamellar tissue as a function of BMD and porosity. Markers denote the averaged numerical results from homogenization by FE. Solid lines represent the least square fitting given in Eqs. 4.24 to 4.26.

The equations that explicitly relate the stiffness terms with the variable BMD and porosity are derived using a least square fitting (note that results from Equations 4.18 to 4.23 are expressed in GPa and results from Equations are expressed in Pa):

$$C_{11} = 7.3876 \, e^{-0.022229 \, p} \, e^{0.82134 \, \text{BMD}} \qquad R^2 = 0.99 \qquad (4.18)$$

$$C_{22} = 5.4868 \, e^{-0.021726 \, p} \, e^{0.58165 \, \text{BMD}} \qquad R^2 = 0.99 \qquad (4.19)$$

$$C_{33} = 5.8386 \, e^{-0.021805 \, p} \, e^{0.58304 \, \text{BMD}} \qquad R^2 = 0.99 \qquad (4.20)$$

$$C_{44} = 1.3475 \, e^{-0.02013 \, p} \, e^{0.72977 \, \text{BMD}} \qquad R^2 = 0.99 \qquad (4.21)$$
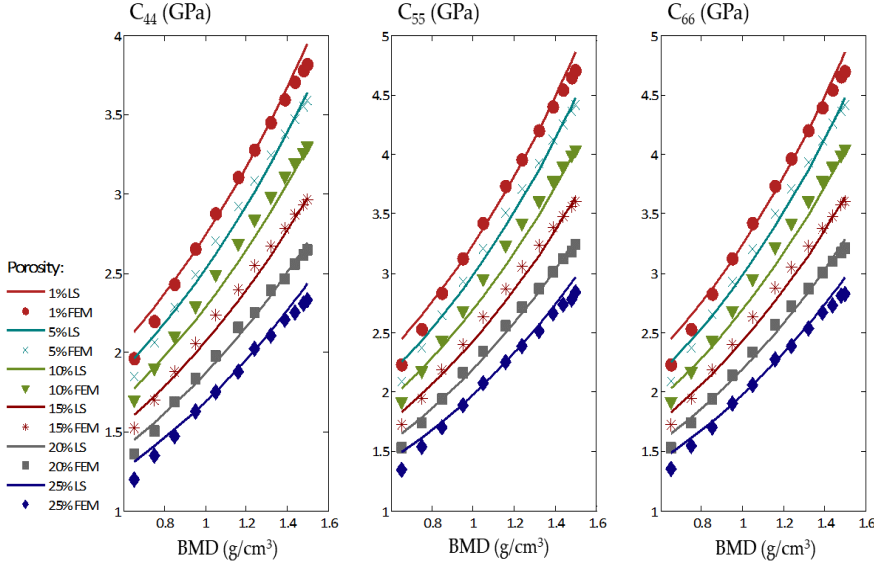
Figure 4.11: Evolution of the terms C_{44}, C_{55} and C_{66} of the stiffness matrix for lamellar tissue as a function of BMD and porosity. Markers denote the averaged numerical results from homogenization by FE. Solid lines represent the least square fitting by an exponential function given in Eqs. 4.21 to 4.23.

$$C_{55} = 1.4673\,e^{-0.02058\,p}\,e^{0.81231\,\text{BMD}} \qquad R^2 = 0.991 \qquad (4.22)$$

$$C_{66} = 1.4682\,e^{-0.02060\,p}\,e^{0.81189\,\text{BMD}} \qquad R^2 = 0.991 \qquad (4.23)$$

$$C_{23} = 2.1878 \times 10^9 - 1.2627 \times 10^8\,p + 8.4022 \times 10^5\,p^2 + 4.0292 \times 10^9\,\text{BMD}$$
$$-1.1405 \times 10^9\,\text{BMD}^2 \qquad\qquad R^2 = 0.992$$
$$(4.24)$$

$$C_{13} = -6.6623 \times 10^9 - 1.1082 \times 10^8\,p - 3.9345 \times 10^5\,p^2 + 30227\,p^3$$
$$+3.0459 \times 10^{10}\,\text{BMD} - 2.5596 \times 10^{10}\,\text{BMD}^2 + 7.0279 \times 10^9\,\text{BMD}^3$$
$$R^2 = 0.995$$
$$(4.25)$$
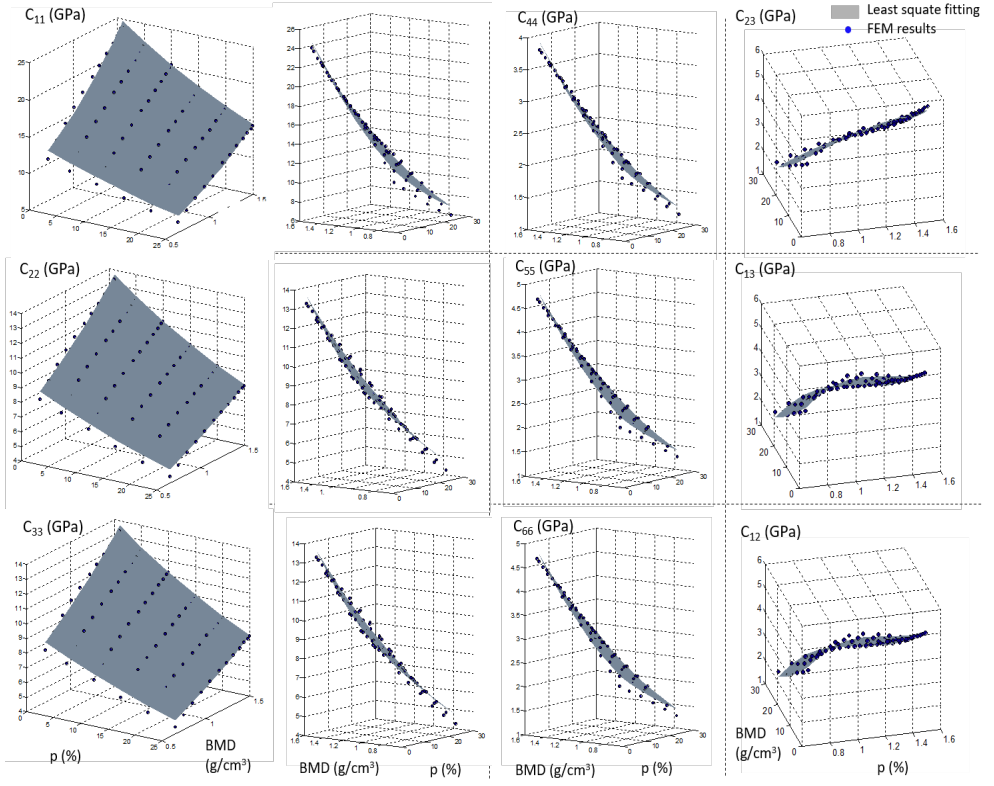
Figure 4.12: Three-dimensional representation of the orthotropic stiffness matrix terms for lamellar tissue as a function of BMD and porosity.

$$C_{12} = -3.6721 \times 10^9 - 1.0889 \times 10^8\, p - 6.1566 \times 10^5\, p^2 + 36350\, p^3$$
$$+ 1.9131 \times 10^{10}\, \mathrm{BMD} - 1.0812 \times 10^{10}\, \mathrm{BMD}^2 + 5.8818 \times 10^8\, \mathrm{BMD}^3$$
$$R^2 = 0.995$$
$$(4.26)$$

147

4.3.2   Numerical modelling of the trabecular bone strength

In this section, the finite element model of a representative volume of trabecular vertebral bone from a swine specimen (see details in Section 4.2.3) is analyzed under displacement controlled tension and compression loading. Assuming quasi-static conditions, the bone strength assessment in longitudinal and transversal directions is under scope. Through Equations 4.18 - 4.26 we estimate the stiffness properties assuming uniform values of BMD and porosity: BMD $= 0,85$ g/cm^3 , $p = 5$ %. Strength properties for lamellar tissue are summarized in Table 4.2. As mentioned in Section 4.2.3, custom reference systems are defined to align the element coordinate systems considering that the mineralised collagen bundles are orientated parallel to the main geometrical feature of the trabecula. Therefore, transversely isotropic elastic properties and strength limits of lamellar bone, defined in an orientated reference system (1,2,3) (see Figure 4.4), are currently oriented in the mesoscale model. The bone failure onset and the post-yield regime are analyzed through the Hashin criterion and Material Property Degradation method, respectively. Besides, the influence of the damage variables d_f and d_m (see details in Section 4.2.5) is also analyzed. The numerical values considered are $d_f = 0.9, 0.9999$ and $d_m = 0.5, 0.95, 0.9999$.

The graphs shown in Figures 4.13 - 4.15 outline the stress-strain relationships for the tensile and compressive loading, where the apparent stress is estimated from the resultant force on the supported area in the same direction of the applied displacement. It is remarkable the non-isotropic mechanical behavior of trabecular bone being able to identify approximately an orthotropic trend.

If we compare the results shown in Figure 4.13 (a) and (b), the damage parameter d_f presents an important influence on the longitudinal tensile and compressive mechanical behavior (y direction of the model). These results are expected because the mineralised bundles of fibres are mainly orientated in that direction. In general, the graphs of Figure 4.13 (a) show an elastic regime followed by a damage zone where the elements progressively fail simulating the presence of diffuse microcracks. Then, a more generalized element failure is observed suggesting that bone fracture initiates. Further material softening and densification is observed for $d_m = 0.95$ and 0.9999, whereas strain hardening behavior is noticeable for $d_m = 0.5$. The yield strain can be estimated as $\epsilon_y^+ = \left|\epsilon_y^-\right| = [0.0058 - 0.0071]$, resulting similar for the different values of d_m analyzed. The compression yield stress is slightly higher than the tension yield stress, for $d_m = 0,5$: $S_y^+ = [6.41 - 7.08]$ MPa and $\left|S_y^-\right| = [6.41 - 7.22]$ MPa.
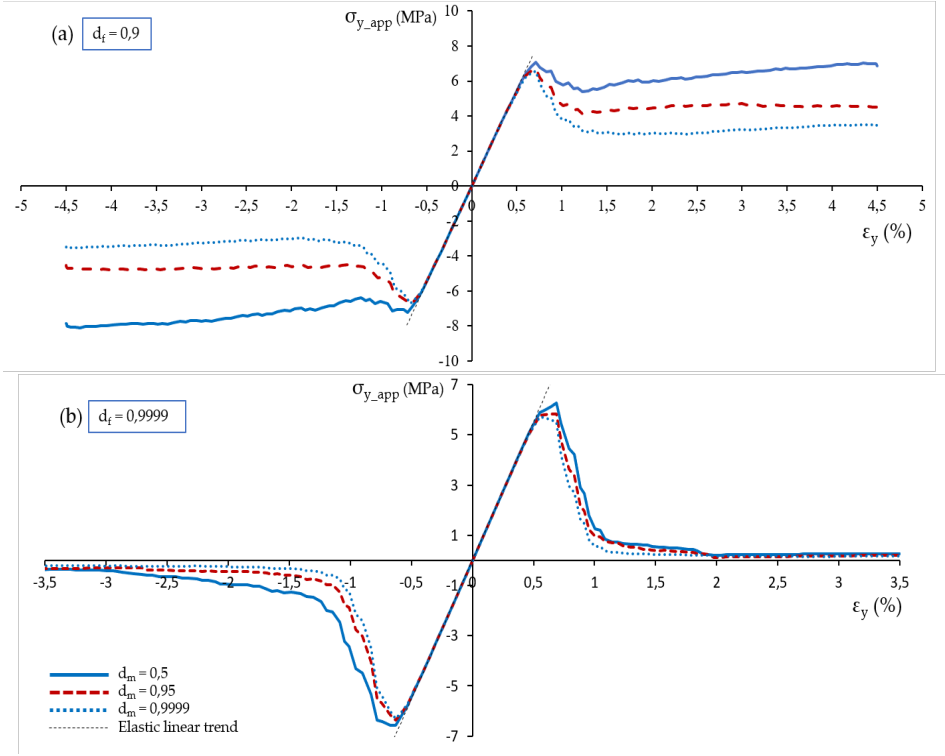
Figure 4.13: Tensile and compressive stress-strain relationships under displacement control in y direction of the model for (a) $d_f = 0.9$ and (b) $d_f = 0.9999$. Results for different values of the degradation parameter $d_m = 0.5$, 0.95 and 0.9999.

In Figure 4.13 (b) a quasi-brittle response is observed for tensile and compressive loading. This situation is promoted by the damage parameter value $d_f = 0.9999$ that gives rise to the elimination of elements just after failure initiation. The elastic linear zone is followed by a small damage mechanics regime. In this case, we observe that the resistance of the sample in the y direction is fully conditioned by the strength of the bundles in longitudinal direction, leading abruptly to a catastrophic failure when elements begin to fail. In tensile load, and considering $d_m = 0.5$, the yield strain is estimated as $\epsilon_y^+ = [0.0052 - 0.0068]$, and for compressive load as $\left| \epsilon_y^- \right| = [0.0056 - 0.0068]$.

The apparent elastic moduli in the longitudinal direction results equal for both tension and compression loading cases, being estimated in $E_{y,app} = 1104$ MPa.
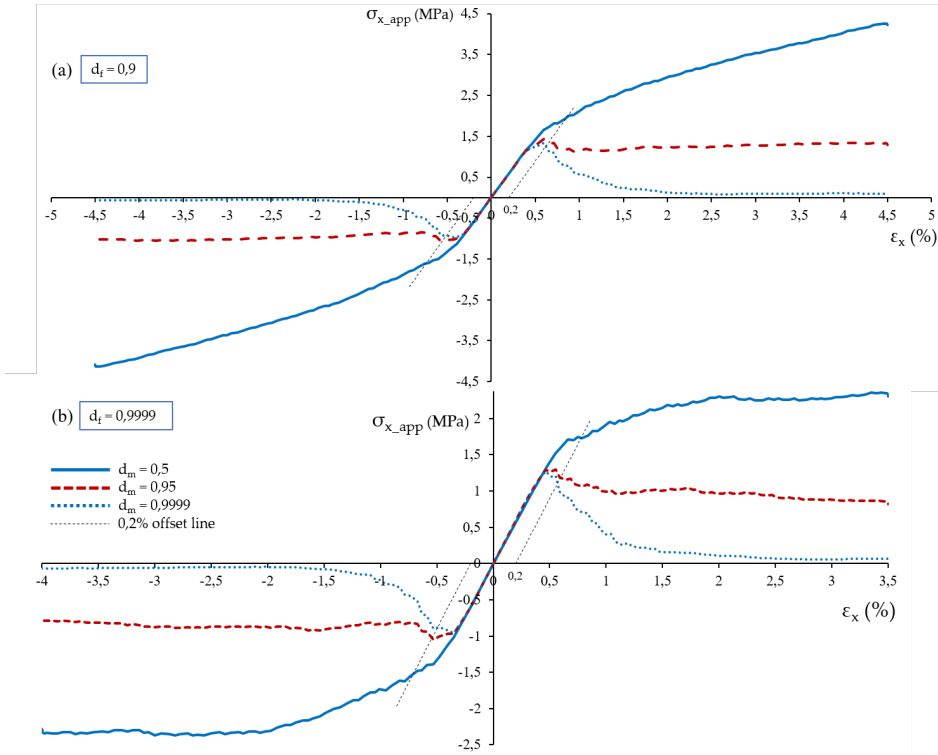
Figure 4.14: Tensile and compressive stress-strain relationships under displacement control in x direction of the model for (a) $d_f = 0.9$ and (b) $d_f = 0.9999$. Results for different values of the degradation parameter $d_m = 0.5$, 0.95 and 0.9999.

In Figures 4.14 - 4.15 the results for tensile and compressive loading in x and z transverse directions are shown. A high influence of d_m on the post-yielding is observed independently of d_f. A quasi-brittle behavior is obtained only when the ply discount is assumed, i.e. removing the element when the transverse failure mode occurs, $d_m = 0.9999$. In the other two situations, an important damage mechanism regime is observed. The post-yielding behavior changes with d_m. For $d_m = 0.5$ a strain hardening behavior is exhibited and for $d_m = 0.9$ the relationship indicates an increment of elongation at an almost constant stress value without strain hardening regime.

The maximum yield strain is reached for $d_m = 0.5$. For this case, it can be defined the elastic limit at the 0.2 % of strain. The averaged transverse yield
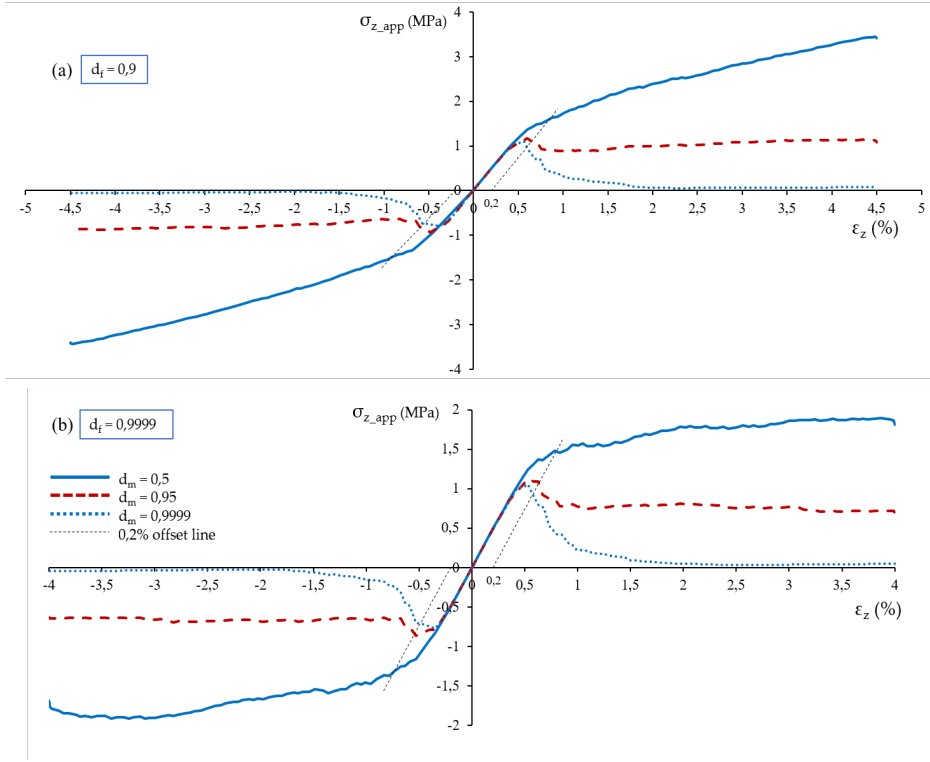
Figure 4.15: Tensile and compressive stress-strain relationships under displacement control in z direction of the model for (a) $d_f = 0.9$ and (b) $d_f = 0.9999$. Results for different values of the degradation parameter $d_m = 0.5$, 0.95 and 0.9999.

strain is $\epsilon_y^+ = [0.0079 - 0.0084]$ in tension and $\left|\epsilon_y^-\right| = [0.0075 - 0.0085]$ in compression.

The apparent elastic moduli in the transversal x and z directions are estimated as $E_{x,app} = 292$ MPa and $E_{z,app} = 252$ MPa. These values are the same both for tension and compression.

In our results, it is observed the quasi-brittle stress-strain behavior of bone described in Zioupos [112] assuming the damage parameter $d_f = 0,9999$ in case of longitudinal load and $d_m = 0,9999$ for transverse load. When an element fails, such a large stiffness reduction is equivalent to the elimination of the element, hence the remaining elements are not able to withstand the overload, which causes a generalized fail.

On the other hand, regarding the elastic regime, results shown in Table 4.3 highlight the influence of the non-isotropic elastic properties of lamellar tissue on the elastic behavior of cancellous bone at mesoscale. Results shown in series with markers are obtained considering Equations 4.18 - 4.26 for BMD = 0.653, 0.85, 1.05, 1.24, 1.39 and 1.48 g/cm^3 and natural values of porosity $p = 1$, 2.5, 5, 7.5 and 10 %.

When isotropic properties for tissue are defined in the numerical model, $E = 10$ GPa and $\nu = 0.3$ [323], the apparent moduli result $E_{x,app}^{iso} = 428.7$ GPa, $E_{z,app}^{iso} = 367.9$ GPa and $E_{y,app}^{iso} = 1164.6$ GPa. As it can be appreciated, stiffness in the transverse directions of the sample (x and z directions) can be easily overestimated, particularly for increasing levels of microporosity. In the longitudinal direction (y direction), the apparent modulus can be reasonably estimated for regular values of BMD and natural microporosity considering isotropic properties for tissue. However, when bone is highly mineralised, the differences increase following a potential law in both variables, bone mineral density and porosity.

Convergence analyses have been performed in order to guarantee the results accuracy. The energy norm of the estimated solution, $||U||$, has been obtained as a function of the total number of degrees of freedom (DOF) in the numerical model (where $||U|| = \sqrt{2\Pi}$, being Π the computed total strain energy expressed in mJ). The influence of the discretisation has been analysed applying a quasi-static compression load in the three orthogonal directions of the sample. To this aim, isotropic properties have been defined in the model. Note that the total DOF may vary slightly for each load case because the number of constraints is different. The strategy is based on a uniform mesh refinement. Values summarized in the Table 4.4 show that the assumed discretisation provides accurate results without compromising the computational cost.

In Table 4.5 the results presented in the current work are summarized, together with reference values found in the literature.

4.3.3 Discussion of the obtained results

Bone fracture risk assessment is nowadays a prominent topic of interest in an increasingly aged population. In this sense, many enhancements in high-resolution image acquisition and its treatment have been made to capture the patient specific real architecture of bone. This enables to perform numerical analysis of detailed micro-finite element (μ-FE) models. At this point, in most

Table 4.3: Evolution of the apparent moduli in x, y and z directions of the cancellous bone numerical model considering two approaches to define the lamellar tissue elastic properties. Results shown in series with markers are obtained considering the Eqs. 4.18 - 4.26 presented in this work which estimate the stiffness matrix of lamellar tissue as a funtion of BMD and porosity at tissue level. The dotted black line shows the numerical solution when isotropic elastic properties are defined for lamellar tissue: $E = 10$ GPa and $\nu = 0.3$ [323].
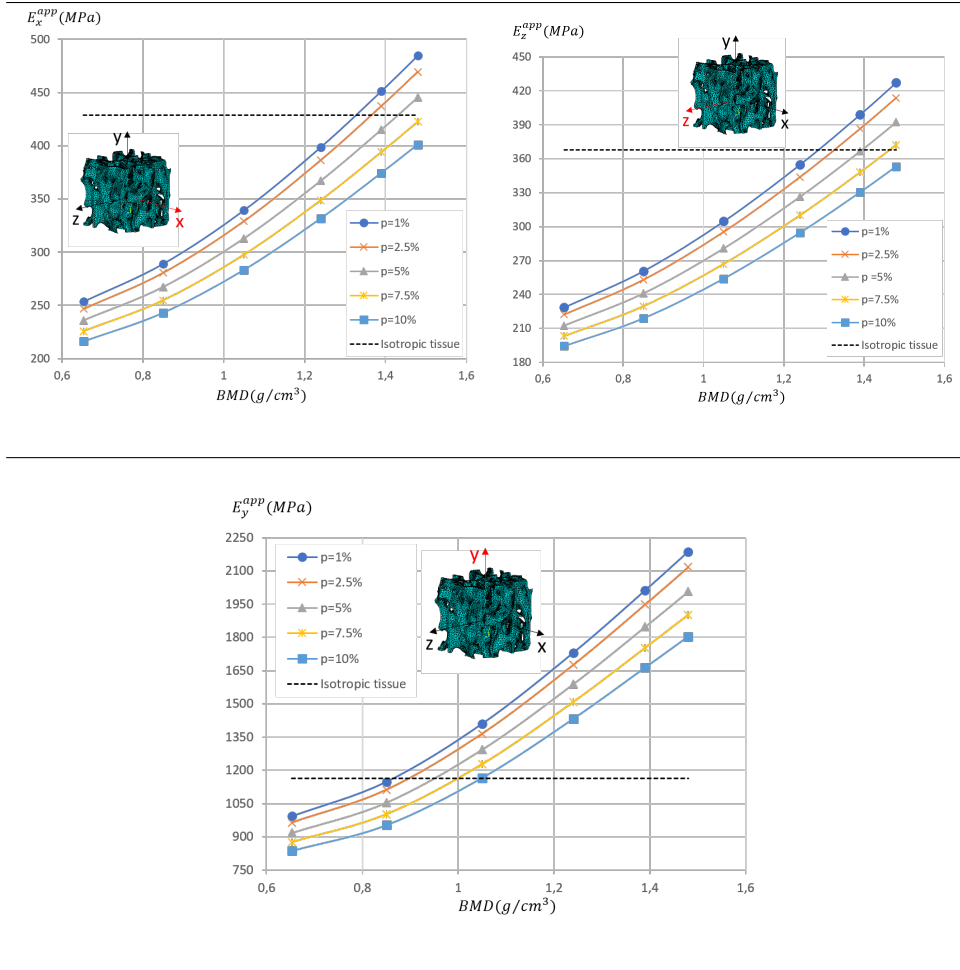
cases, isotropic elastic constants are assumed for tissue modelling, neglecting its anisotropic behavior, mineral content and the porosity influence on its mechanical response. In fact, isotropic damage continuum approaches are

Table 4.4: Estimated solution in energy norm, $||U||$, for different discretizations in the x, y, z directions. DOF represents the number of degrees of freedom in the numerical model.

x-direction		y-direction		z-direction	
DOF	$||U||$	DOF	$||U||$	DOF	$||U||$
5.10×10^4	1.8	5.10×10^4	3.0	5.12×10^4	1.7
6.46×10^4	1.8	6.39×10^4	3.0	6.42×10^4	1.7
1.01×10^5	1.7*	1.00×10^5	2.9*	1.01×10^5	1.7*
6.11×10^5	1.6	6.11×10^5	2.9	6.12×10^5	1.6
1.85×10^6	1.6	1.85×10^6	2.9	1.86×10^6	1.5

* Results obtained for the mesh refinement used in this work

often used to estimate bone failure through numerical modelling [97, 210, 310, 311, 323].

On the other hand, slow bone loss is associated with an incomplete osteoblastic deposition and leads to thinner structural elements. This is one characteristic indicator of an age-related or senile osteoporotic bone. This bone feature is revealed at micro scale length and can be included in a micro-numerical model obtained from processing μ-CT images. Essential morphometric parameters can be then captured. However, a very important impact on the porosity at tissue level is observed when a rapid bone loss accounts as a result of a deeper osteoclastic perforation that can generate discontinuities in the bone structure. This occurs most commonly in postmenopausal women, induced by the abrupt reduction of estrogens [52]. For the moment, the influence of the porosity at tissue level on the elastic behaviour of bone has not been addressed in the literature. It is essential to characterise the mechanical properties of bone tissue with prevalence of osteoclastic perforation [54] in the post menopausal women with osteoporosis, where BMD and microporosity values are altered as a consequence of an unbalanced bone turnover process.

The transversely isotropic model for the elastic tissue properties presented in this work addresses the non-isotropic behaviour due to mineralised collagen fibrils orientation, the bone mineral density and microporosity. In addition, in a trabecular bone numerical model at mesoscale, the main fibrils orientation is also considered. In [80], an isotropic Young's modulus for tissue was calibrated from experimental compression tests. Results of that work highlighted that different Young's moduli for tissue in the three orthogonal directions of the sample were to be inferred in order to reproduce the experimental results. A

Table 4.5: Results summary. Estimation of yield strain and Young's moduli (apparent values) for trabecular bone and comparison with some reference values from literature.

Longitudinal loading case (*y-direction*)				
	Tension		Compression	
	Thesis	Literature	Thesis	Literature
Yield strain*	[0.0052-0.0071]	0.0078 ± 0.0004 [74][(1,m)] 0.0078 ± 0.0004 [74][(3,m)] 0.0072 [107][(1,m)] 0.0078 ± 0.00041 [323][(1,c)]	[0.0052-0.0071]	0.0124 ± 0.00197 [324][(4,m)] 0.0109 ± 0.0012 [74][(3,m)] 0.0084 ± 0.0006 [74][(1,m)] $[0.0046\text{-}0.0063]$ [105][(3,m)] 0.0081 [107][(1,m)] 0.00951 ± 0.00125 [323][(1,c)] $0.00119 \quad - \quad 0.0168$ $[80, 309]$[(2,m)]
Young's modulus (MPa)*	1104	384.1 ± 155.1 [107][(1,m)] 1017 ± 0.088 [64][(5a,c)] 1800 ± 0.058 [64][(4b,c)] 908.2 [309][(2,c)]	1104	309 ± 109 [74][(1,m)] 384.4 ± 162.9 [107][(1,m)] 1017 ± 0.088 [64][(5a,c)] 1800 ± 0.058 [64][(5b,c)] 1265.2 [80][(2,m)] 908.2 [309][(2,c)] 1022.9 [309][(2,m)]
Transversal loading cases (*averaged values for x and z-directions*)				
	Tension		Compression	
	Thesis	Literature	Thesis	Literature
Yield strain*	[0.0079-0.0084]	≈ 0.007 [107][(1,m)] 0.00899 ± 0.00181 [323][(1,c)]	[0.0075-0.0085]	≈ 0.0082 [107][(1,m)] 0.0105 ± 0.00115 [323][(1,c)]
Young's modulus (MPa)*	$252 - 292$	129.7 ± 54.7 [107][(1,m)] $196 \pm 58 - 306 \pm 14$ [64][(5a,c)] $499 \pm 63 - 538 \pm 70$ [64][(5b,c)] $361.04 - 382.66$ [309][(2,c)]	$252 - 292$	119.5 ± 74.2 [107][(1,m)] $196 \pm 58 - 306 \pm 14$ [64][(5a,c)] $499 \pm 63 - 538 \pm 70$ [64][(5b,c)] $361.04 - 382.66$ [309][(2,c)] $328.1 - 346.0$ [309][(2,m)]

[(1)] Human vertebral trabecular bone

[(2)] Swine vertebral trabecular bone

[(3)] Bovine proximal tibia trabecular bone

[(4)] Bovine distal femora trabecular bone

[(5a)] Human vertebral bone T11/woman/60 years

[(5b)] Human vertebral bone T12/man/56 years

* Apparent values

m: Mechanical test; c: Computational analysis

plausible explanation is that the fibrils orientation varies with the direction and this is in consonance with the building substrucures of cancellous bone (plates and rods). Composition, distribution and architecture of lamellar tissue are very important to reproduce the micromechanics failure mode of trabecular bone [67].

We highlight different novelties of this analysis: (1) New explicit equations for the estimation of the elastic constants of lamellar tissue are provided. These equations have been obtained as a function of BMD and microporosity in a multiscale analysis, which enable to study the influence of these char-

acterising parameters on the mechanical behavior of bone particularly with certain pathologies, like osteoporosis. (2) The strength limits for fully calcified lamellar tissue have been inferred from literature. (3) The approach herein presented considers the orientation of the mineralised fiber bundles in the trabeculae network, which is essential for the implementation of elastic and strength tissue properties in the numerical model. (4) In accordance to the non-isotropic elastic and strength properties of lamellar tissue, an orthotropic failure criterion is proposed to analyze the damage onset of cancellous bone. The Hashin's interactive failure criterion is considered. (5) The Material Property Degradation (MPDG) method is used to model numerically the damage evolution law at tissue level. A detailed study about the influence of the damage parameters on the mechanical post-yielding response of trabecular bone is also presented.

In Section 4.3.1, Equations 4.18 - 4.26 provide the terms of the stiffness matrix of lamellar tissue as a function of two essential tissue parameters, the bone mineral density (BMD) and the microporosity. In the main terms, a power regression in BMD is observed. There are previous studies that show a similar tendency for the Young's moduli of lamellar tissue [46, 47]. Additionally, we observe an inverse power relationship for the microporosity.

Results summarized in Table 4.3 show the influence of the non-isotropic elastic properties of lamellar tissue on the apparent moduli of the cancellous bone at mesoscale. When isotropic tissue properties are assumed, stiffness can be frequently overestimated in the transverse directions. In the longitudinal direction, stiffness equally exhibits a high dependence on BMD and microporosity although isotropic tissue properties can be reasonable for values of BMD and microporosity within a natural range.

On the other hand, in Section 4.3.2, numerical results show that small differences are found for apparent yield strain between tension and compression for the sample analyzed, in agreement with [74] and [107]. It is known that, although yield strain represents a pretty uniform failure property, it is more influenced by the apparent density in compression than in tension, especially in less dense bone [74]. This can be the main reason for some discrepancies observed in the literature for the apparent yield strain in compression [309, 324]. In tension, the apparent yield strain estimated in this work is also in good agreement with values found in the literature (see Table 4.5), and confirms the tendency to a more uniform value, being less sensitive to the apparent density and anatomical site [80].

In addition, in accordance with [107] no relevant differences between apparent moduli in tension and compression were observed, for both longitudinal and transverse direction of the trabecular bone sample. The apparent elastic moduli estimated in this work are, in general, in good agreement with the values reported in literature [64, 309]. However, our results differ from others [74, 107]. This can be motivated by differences in the mineral content of the samples, anatomic site, bone volume fraction, shape complexity of the structure or experimental conditions.

Nevertheless, this study presents some limitations. Bone surfaces present a high activity of bone remodelling. Consequently, lamellar tissue is often renewed at surfaces, leading to a lower mineral content than through in the core. Hence, the tissue elastic constants change through a cross section of a trabecula. For example, a higher elastic modulus (between 5 to 12 %) was found at the core than at the cortex of a trabecula. Additionally, values for the strength limits of lamellar tissue summarized in Table 4.2 correspond to fully calcified tissue and assume healthy bone porosity. However, strength limits are strongly dependent on the degree of calcification [313] and on the degree and shape of porosity. Further investigations will be necessary to quantify the influence of the presence of micropores on the strength limits for lamellar tissue. These considerations should be addressed in a more general context. As aforementioned, orientation of the mineralised collagen fibrils in the trabeculae network has been estimated based on the main geometrical feature. A more refined strategy would be necessary to automatize the orientation of the elementary coordinate system, considering the predominant geometrical definition [63], but also including information based on the main pattern that osteocyte long axis follows in the microstucture, what effectively will provide information about how mineralised collagen fibrils are aligned. Besides, BMD and porosity vary within the trabeculae architecture and, in contrast, these values have been assumed homogeneous in our numerical mesoscale trabecular bone model. Lastly, the influence of the penalization parameters on modelling the post-yield behavior has been addressed. However, a more refined mesh should be necessary for a more detailed analysis.

4.4   Conclusions

This chapter addresses the numerical analysis of the mechanical response of cancellous bone including a new approach for the elastic and strength lamellar tissue properties. The non isotropic elastic behaviour of lamellar tissue deals with the influence of the bone mineral density and, as a novelty, the microporosity or porosity at tissue level. In addition, according to the strength limits inferred from literature, the failure onset is modeled by means of the Hashin failure criterion in combination with the Material Property Degradation (MPDG) method. The value of the degradation parameters can simulate different post yielding scenarios compatible with the bone damage mechanisms observed in literature, as a quasi-brittle failure or significant loss of stiffness, due to smeared crack regions where the presence of multiple microcracks reduces the load transmission capability.

Results show that, when isotropic elastic tissue properties are considered, the anisotropic ratio of the apparent moduli of cancellous bone is, in general, undervalued, particularly when microporosity increases. Not only the microstructure but tissue properties govern the elastic response of bone at the mesoscale.

On the other hand, the yield strain for tension and compresion quasistatic loadings has been estimated in the three orthogonal directions of the bone sample. Results indicate that, for the cancellous bone analyzed, there are no significant differences between tension and compression behavior for each direction. These results are in agreement with several works found in literature (see Table 4.5) and they are also compatible with the evidence that a higher apparent density in bone results in a higher yield strain in compression than in tension.

To conclude, the approches presented in this chapter enable to deal with a scarcely treated topic from the mechanical point of view: the undermined capabilities of osteoporotic bone due to severe alterations in parameters, such as bone mineral density (BMD) and porosity at tissue level. Adaptation of the morphometric parameters at micro scale level is commonly investigated under this pathology, but neglecting the underlying changes at the tissue level.

Chapter 5

Estimation of the strength limits of lamellar bone as a function of mineral content and porosity

5.1 Introduction

In this chapter, we aim to define the strength limits for the lamellar tissue as a function of the bone mineral density (BMD) and the microporosity, such as in Chapter 4. In this thesis, an exhaustive analysis of the cancellous bone is carried out. To achieve this goal, we have studied the elastic and strength properties of lamellar tissue in depth. With this information and a homogeneous procedure, we can go up in the hierarchical bone scale to study cancellous bone, considering its lower-level behavior.

The hierarchical nature of bone is attributed to the variable proportions of their main constituents and its changing spacial arrangement through different scale lengths. Hence, the main structural unit varies from the sub-microscale

to the macroscale. Lamellar tissue constitutes the building block in the sub-microscale length (1 - 10 μm), for both cortical and cancellous bone, although its arrangement is different (see Figure 5.1). While in cortical bone, lamellar tissue is placed following circumferential patterns around the principal vascularisation channels (secondary osteons or Haversian system), in cancellous bone, lamellar tissue is deposited in units of parallel layers (hemiosteons). The main constituents of lamellar tissue are fiber bundles of collagen type I, mineral (in crystal and amorphous phase) and water. Lamellar tissue is composed of thin substructures called lamellae (of a few microns in thickness), within which the mineralised collagen fibers course unidirectionally. At this length scale, osteocytes are found. They are bone cells interconnected through the canaliculi calcoforo network, that live in the small ellipsoidal cavities called lacunae. Osteocyte-canaliculi system controls the bone turn over process and ensure the bone remodeling activation under a threshold stimulus of mechanical strain.
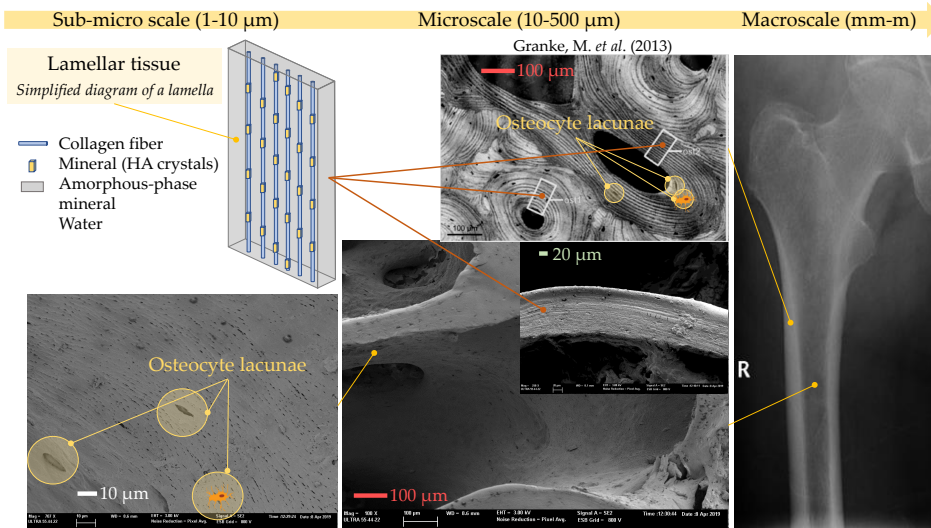
Figure 5.1: Lamellar tissue arrangement in the hierarchical organisation of bone from the sub-microscale to the organ - or - macro-scale. The lacunae that hosted the osteocyte introduce porosity at the tissue level. Compact bone image taken from Granke *et al.* work [143].

Marotti measured the dimensions of the ellipsoidal lacunae are D1 $\approx$ 22 μm, D2 $\approx$ 4 μm and D3 $\approx$ 9 μm [55]. The major axis, D1, is aligned with the longitudinal direction of the mineralised collagen fibrils, the minor axis, D2, is perpendicular to the lamellar plane and the intermediate, D3 is perpendicular

to the axis-1 and contained in the lamellar plane, as shown in Figure 5.2. Porosity associated with the lacunocanalicular system is in the range 1 - 5 %, according to Cowin and Martinez-Reina *et al.* works [44, 56].
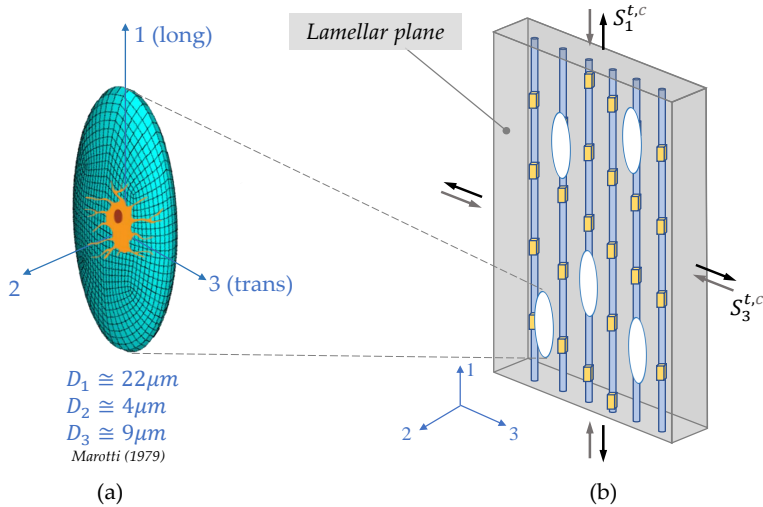
Figure 5.2: (a) Model of the ellipsoidal osteocyte lacunae and the reference system (1, 2, 3) used to define the orientation of the ellipsoid within lamellae (Marotti, 1979 [55]). (b) Definition of the lamellar plane and the terminology used for the in-plane utlimate normal strength $S_1^{t,c}$ and $S_3^{t,c}$.

Bone strength is highly dominated by its hierarchical arrangement. At the different scale lengths, diverse failure mechanisms seem to govern the mechanical response of bone under loading, from the inelastic behavior at the nano-scale passing through the emergence of microcracks at the microscale until the brittle mechanical response at macro or organ level.

As a biological tissue, bone is constantly remodeling, carried out by the osteocyte cells' activity. The osteocyte-sensory role is mainly based on the capability of these cells to detect the fluid flow inside the lacuno-canaliculi network due to the deformation of the lacunae. An increment of the stress (and strain) around the lacunae can trigger the bone remodelling process (see Figure 5.3). In this context, ellipsoids will act as "natural" amplifiers of strains. Osteocyte-canaliculi system controls the bone turn over process and ensure the activation of the bone remodelling under a threshold stimulus of mechanical strain. Cowin *et al.* [325] suggest that, a very small strain would be enough to activate the osteocyte activity. Assuming an elastic behavior of the extracellu-

lar matrix [326], the local strain field around the lacunae will disappear when the load is released, returning the ellipsoids to their original shape. When the load increases excessively, microcracks can initiate and are particularly dense at osteocyte lacunae [327,328]. A plausible explanation for this phenomenon is that lacunae act as stress contentrators, which are reinforced by microdamage zones around these cavities.
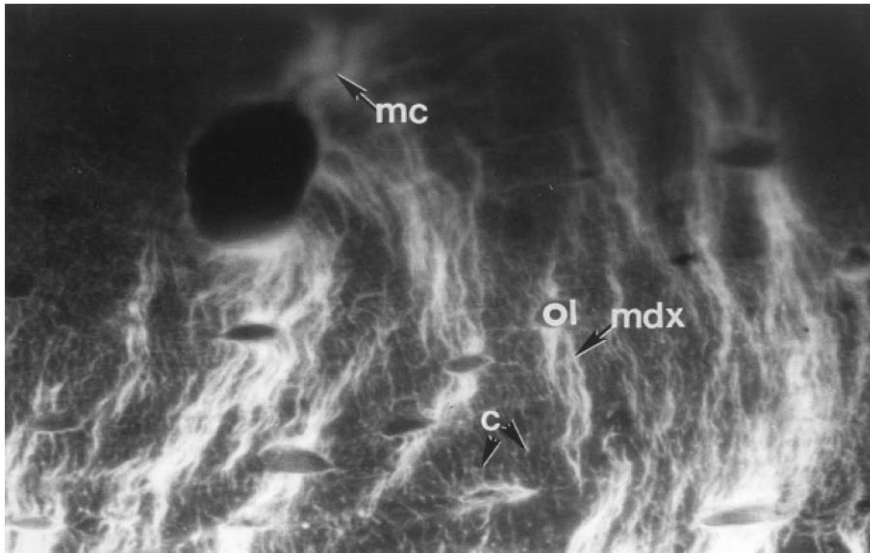
Figure 5.3: Confocal micrograph of the tensile surface of a beam specimen of bovine tibia. MC: macrocrack, OL: osteocyte lacunae, MDX: microdamage, and C: canaliculus. Image extracted from [327].

In Ebacher *et al.* [329], the importance of canaliculi network in the intralamellar cracking is analyzed. In their findings, through images from a laser scanning confocal microscope, show the interaction of microcracks with osteocyte lacunae and also with canaliculi. Voite *et al.* [330] state in their work that osteocyte lacunae do not stop the crack growth but rather provide guidance for microcrack propagation.

On the other hand, *in-silico* analysis of the bone failure process is nowadays widely used in order to evaluate the risk of bone fracture, to understand how bone microarchitecture and the concentration of bone constituents can influence the mechanical properties and mechanisms failure, to simulate the interaction between scaffolds or implants and bone, etc. All these topics involve

the need of using micromechanical models to define the elastic and strength properties of bone tissue.

In finite element simulation, the continuum damage mechanics approach is an option to evaluate the bone failure onset. The initiation and propagation of cracks is based on a smeared crack approach [97, 210, 212, 213, 309, 311]. In this approach, despite lamellar tissue is a non-isotropic material, an isotropic failure criterion is considered, defining an equivalent strain. In Megías *et al.* [331] the orthotropic Hashin's criterion was considered to capture the failure onset at tissue scale. In this work, the strength limits were inferred from Ascenzi & Bonucci works [312, 313]. Recently, Casari *et al.* [332] considered Hashin's criterion also, being shear strength components deduced from literature and the tensile and compressive strength were calibrated from microtensile test on a dry ovine osteonal bone at the length scale of a single lamella. Samples with osteocyte lacunae were neglected.

Additionally, the mineral content and the porosity at the lamellar tissue level (microporosity) are two essential parameters related to the bone mechanics behavior. It is well known that an increase in the volumetric bone mineral density (BMD) has a direct implication on the rise of the stiffness and strength [47–50, 333]. Porosity induces a strong influence on the strength and stiffness of bone. These mechanical properties vary inversely with increasing porosity [48, 49].

The main goal of the present work is to estimate the in-plane ultimate strength of lamellar tissue (see Figure 5.2 b): $S_1^{t,c}$, $S_3^{t,c}$ and S_{s13} as a function of the mineral content BMD and level of natural tissue porosity owing to the lacunae concentration. Superscripts t and c denote tensile and compressive, respectively.

The methodology followed in this work is schematically depicted in Figure 5.4. Ascenzi and Bonucci [312, 313] performed mechanical tests under tensile and compressive load until failure, of different types of wet osteons for two levels of mineralisation. Microporosity level due to lacunae concentration was not provided. From their results, we have inferred the homogenised ultimate stress of lamellar tissue attending to the fibers bundle orientation in the osteons tested. Moreover, the BMD is estimated, considering the slope of the elastic stress-strain curves and the micromechanical model provided in Vercher-Martínez *et al.* [46].

Then, a representative numerical model of lamellar tissue is considered. The element size is established through a convergence analysis. In this model,
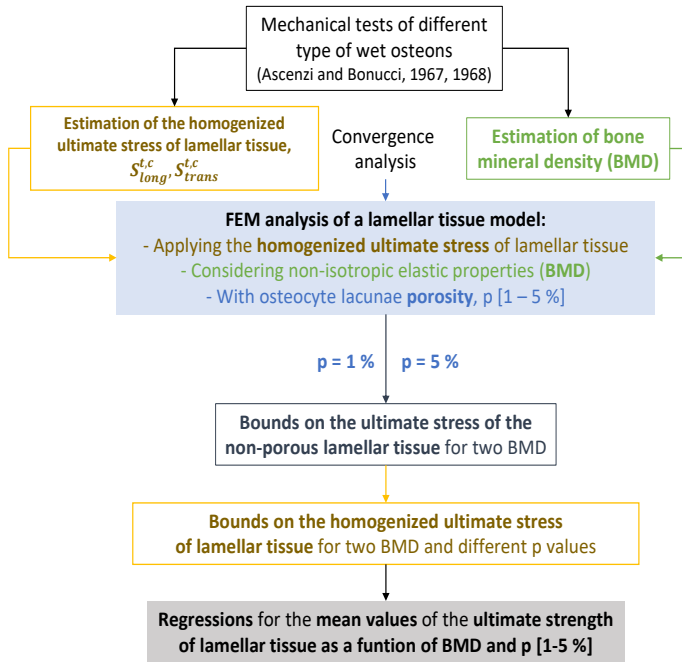
Figure 5.4: Scheme of the methodology followed to estimate the strength limits.

the non-isotropic elastic properties depend on BMD. The microporosity is modelled by subtracting ellipsoid voids corresponding to the variable osteocyte lacunae concentration. The homogenised ultimate stress of lamellar tissue is then applied to the finite element model.

Osteocytes produce stress gradients and failure occurs because the maximum local stress reaches the strength of non-porous lamellar tissue. In order to estimate it, we assume two scenarios: osteons present a minimum porosity level of $p = 1$ % and a maximum value of $p = 5$ %. Once we know the bound on material strength, the homogenised ultimate stress for lamellar tissue with other levels of porosity can be ascertained by finite element analysis. Lastly, we present the regression fitting of the results obtained in this work.

5.2   Finite element model description

In order to address the numerical estimation of the in-plane ultimate stress of lamellar tissue we model a volume of interest (VOI). It considers the lamellar tissue with lacunae explicitly modelled as discrete ellipsoids. Then, using the finite element method we estimate how a variation in the mineral content and the natural porosity affects to the ultimate stress of lamellar tissue. Ellipsoids are randomly distributed in the VOI, being their major diameters, D1, aligned. This direction will represent the longitudinal course of the mineralised collagen fibrils. The intermediate diameters of the ellipsoids, D3, are also aligned, hence, the lamellar plane D1 - D3 is established, such as in Figure 5.2. The homogenised elastic properties of lamellar tissue have been estimated through Equations 4.1 to 4.5 from Vercher *et al.* work [46], presented in Chapter 4. This model provides the transversely isotropic properties as a function of bone mineral density (BMD) and will be applied to the domain around ellipsoids. Consider that the longitudinal direction is parallel to axis-1 and the transverse is contained in the plane 2-3, as exhibited in Figure 5.2.

The VOI of lamellar tissue is a cubic control volume whose edge length, L_{VOI}, is obtained through Equation 5.1, setting a constant ratio between the number of ellipsoids, N_{Ellip}, and the volume fraction of voids, V_p, accordingly to the values summarised in Table 5.1. In Equation 5.1, Vol_{Ellip} represents the volume of an ellipsoid whose principal diameters are obtained from Marotti [55].

$$L_{VOI} = \left(\frac{Vol_{Ellip} N_{Ellip}}{V_p} \right)^{\frac{1}{3}} \tag{5.1}$$

Table 5.1: Relationship between the ellipsoid number, $N_{Ellip.}$ and the volume fraction of porosity, V_p, in the control volume or VOI of lamellar tissue

$N_{Ellip.}$	1	2	3	5	10	15	20	25
$V_p(\%)$	0.2	0.4	0.6	1	2	3	4	5

A convergence study has been made to determine the finite element size that guarantees a further accurate numerical solution, but also considering the computational cost associated. In order to avoid numerical singularities, the geometric model of the ellipsoid has been created deforming a sphere through the application of scaling factor. Figure 5.5 shows the $h-$refinement strategy

followed in this work. The variable h represents the element size near the ellipsoids and h' the element size in the outer areas of the control volume or VOI (both expressed in μm). Two parameters are defined: n is the ratio between the element sizes previously defined, and k controls the degree of refinement in successive iterations.

$$n = \frac{h_i}{h'_i} \tag{5.2}$$

$$k = \frac{h_i}{h_{i+1}} \tag{5.3}$$
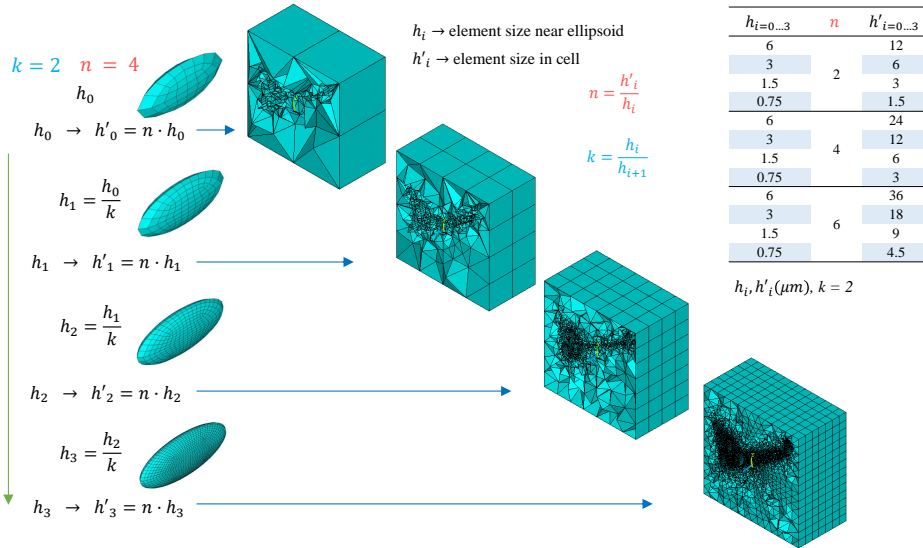
Figure 5.5: H-refinement strategy followed for the convergence analysis.

The convergence is analysed by maintaining a uniform refinement in each step $k = 2$ for different element size ratios $n = 2, 4, 6$. Figure 5.6 shows the evolution of the relative error in energy norm (left) and the number of degrees of freedom (right) with the inverse of element size in the VOI, h', for a value of porosity $p = 1$ %. The analysis has been performed for linear and quadratic solid elements. Smooth marks on the graph correspond with the solution for the parameters adopted in the current work: linear interpolation element, $h = 1$ μm and $h' = 6$ μm. As it can be seen, for these parameters, the relative error in energy norm is lower than 2 % and the computational

cost is feasible. It is worthy to mention that the numerical error tends to remain or decrease when the level of porosity increase, because, despite the higher stress gradients, more ellipsoids imply a much more quantity of small elements. However, computational cost will become excessive if lower element sizes or quadratic interpolation is chosen.
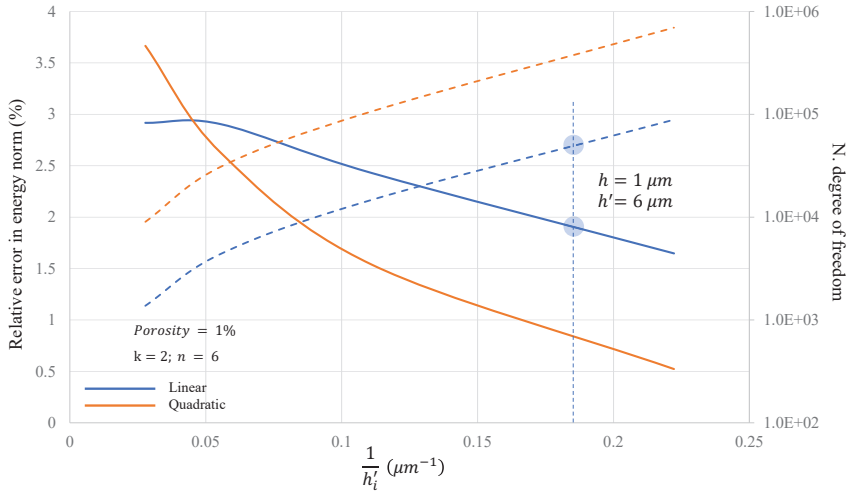
Figure 5.6: Evolution of the relative error in energy norm (%) (left) and number of degrees of freedom (right) with the inverse of the element size h'. Analysis performed for $p = 1$ % (5 ellipsoids), the solutions are the averaged from 5 models with a random distribution of ellipsoids. Refinement parameters: $k = 2$ and $n = 6$. Solutions for linear and quadratic element interpolation.

5.3 Bounds on the ultimate tensile strength of non-porous lamellar tissue for different bone mineral content

In the present work, the bounds on ultimate tensile strength of non-porous lamellar tissue have been estimated considering as starting point the Ascenci & Bonucci work's [312] where different wet osteons were tested until failure.

In Figure 5.7 (a and c), the mean stress-strain curves for several osteons with fibers bundles having a longitudinal spiral course with different degree of calcification are depicted [312]. In the current work, fully calcified has been denoted as BMD_{max} and the initial stage of calcification as BMD_{min}. Note that

for this kind of osteons, the tensile stress applied during the mechanical test is transferred to the longitudinal direction of the fibers bundles of the lamellae. Considering the linear-elastic regime, the estimated mean values for the elastic modulus and ultimate tensile strength result: $E_{long} = 119.400$ kg/cm^2 (11, 71 GPa) and $S_{long}^t = 11.65$ kg/mm^2 (114.28 MPa) for BMD$_{max}$ (Figure 5.7 (a)), and $E_{long} = 61.100$ kg/cm^2 (5, 99 GPa) and $S_{long}^t = 10.95$ kg/mm^2 (107.42 MPa) for BMD$_{min}$ (Figure 5.7 (c)), values from Ascenci & Bonucci [312]. Substituting the elastic modulus for different mineral content in Equation 4.1, the values of BMD can be inferred: BMD$_{max}$ = 0.875 g/cm^3 and BMD$_{min}$ = 0.477 g/cm^3.
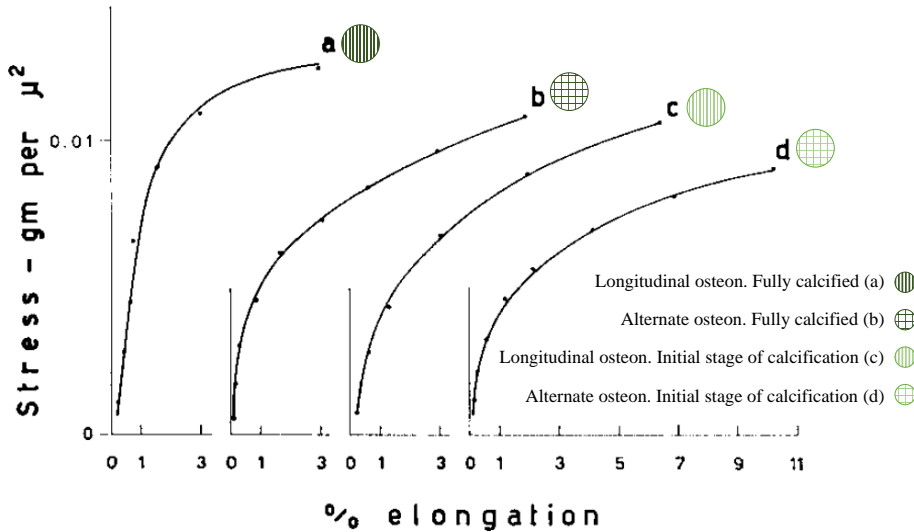
Figure 5.7: Tensile stress-strain curves of wet osteons with different orientation of fibers bundles in successive lamellae and degree of calcification (30-year-old man). Note: $1g/\mu m^2 \approx 10^4$ MPa. Reprinted from Ascenci & Bonucci [312] with permission of John Wiley and Sons.

Figure 5.7 (b and d) represent the stress-strain curves for osteons with fibers bundles running alternately in successive lamellae. In Ascenci & Bonucci [312], it is stated that these osteons present the same degree of calcification as longitudinal (a and c), hence, the same values for BMD$_{max}$ and BMD$_{min}$ will be assumed. In these osteons, the tensile stress applied is transferred as a transverse load into the lamellae whose fibers bundle roughly curse 90°. Since these stress-strain curves exhibit a pronounced plastic behavior, ultimate strength was approximated in 50 MPa [319]. Following a composite analysis

Table 5.2: BMD and ultimate tensile strength for both longitudinal and transverse direction of lamellar tissue. Values inferred from mechanical testing until failure of longitudinal and alternate osteons with different stage of calcification [312].

BMD (g/cm^3)	0.477	0.875	BMD (g/cm^3)	0.477	0.875
S_{long}^t(MPa)	107.42	114.28	S_{trans}^t(MPa)	30.75	32.96

approach, the failure would firstly occur in the lamellae whose fibers round at an angle of 90º, hence, the ultimate tensile strength in the transverse direction of the lamellar tissue can be estimated from Equation 5.4.

$$S_{trans}^t = \frac{50 \ E_{trans}}{E_{app}} \ \text{MPa} \tag{5.4}$$

Where E_{app} is the elastic modulus of the whole alternate osteon in the direction of the applied load and E_{trans} is the elastic modulus of the lamella in its transverse direction. Applying Equation 4.2, E_{trans} results 6.93 GPa for BMD$_{max}$ and 4.28 GPa for BMD$_{min}$. In order to determine E_{app}, the *rule of mixtures* has been considered (see Equation 5.5).

$$E_{app} = E_{long} \ V_{long} + E_{trans} \ V_{trans} \tag{5.5}$$

Where E_{long} represents the elastic modulus of the lamella in the longitudinal direction of the fibers bundles, being 11.71 GPa for BMD$_{max}$, and 5.99 GPa for BMD$_{min}$ (from Figure 5.7 (a and c)). V_{long} and V_{trans} are the volume fraction of lamellae whose fibers are aligned to the loading direction and forming an angle of 90º, respectively, and they result $V_{long} = 0.75$ and $V_{trans} = 0.25$ from Giner *et al.* [319].

Substituting previous values in Equation 5.4, the ultimate tensile strength in the transverse direction of the lamella is estimated: $S_{trans}^t = 32.96$ MPa for BMD$_{max}$ and 30.75 MPa for BMD$_{min}$. Table 5.2 summarises the values of BMD and the ultimate tensile strength acting on the longitudinal and transverse direction of lamellar tissue, that have been inferred from the empirical tests performed by Ascenci & Bonucci [312].

As described in Section 5.1, natural porosity in a healthy bone is in the range [1 − 5 %] and is mainly attributed to the lacuno-canaliculi system. In the previous approach from the Ascenci & Bonucci work [312] where different wet

osteons were tested until failure, no date about the degree of porosity was available, subsequently, healthy tissue can be assumed. Hence, bounds on ultimate tensile strength of non-porous lamellar tissue can be inferred assuming two scenarios: the natural porosity of lamellar tissue in osteons was the minimum $p = 1$ % (hypothesis 1) and the maximum $p = 5$ % (hypothesis 2).

Figure 5.8 illustrates a scheme of the workflow followed in order to estimate the mean value of the ultimate tensile strength in the longitudinal direction (a) and transverse direction (b) of the non-porous lamellar tissue. Firstly, a control volume of lamellar tissue is modeled assuming orthotropic elastic properties (Eqations 4.1 to 4.5). Then, accordingly with each hypothesis, five models with random distribution of ellipsoidal voids are generated. Secondly, the remote ultimate tensile strength for different mineral content from Ascenzi and Bonucci [312] is applied to the five models. Voids act as stress concentrators and also reduce the effective area. Subsequently, the nodal stress component aligned with the applied load will increase with a higher porosity level. The mean value of the maximum nodal stress component from the five models, will be identified as the corresponding ultimate strength for the non-porous tissue, the lower bound for hypothesis 1 ($\bar{S}_{long}^{t,low}(\mathrm{BMD}, p\_0$ %$)$, $\bar{S}_{trans}^{t,low}(\mathrm{BMD}, p\_0$ %$)$) and the upper bound for hypothesis 2 ($\bar{S}_{long}^{t,upp}(\mathrm{BMD}, p\_0$ %$)$, $\bar{S}_{trans}^{t,upp}(\mathrm{BMD}, p\_0$ %$)$).

5.4 Bounds on ultimate compressive strength of non-porous lamellar tissue for different bone mineral content

In this section, the bounds on the ultimate compressive strength of non-porous lamellar tissue have been estimated. For this proposal, the Ascenci & Bonucci work [313] was considered.

Figure 5.9 (a and b) represents the range of the stress-strain curves under compressive load resulting from testing several osteons, with fibers bundles showing a transversal spiral course in successive lamellae. Different degree of calcification is also considered [313]. For these sort of osteons, the compressive stress applied during the mechanical test is entirely transferred to the lamellae acting in the transverse direction of the fibers. As in Section 5.3, the linear-elastic regime enables to estimate the mean values for the elastic modulus and ultimate compressive strength: $E_{trans} = 94.905$ kg/cm^2 (9.3 GPa) and $S_{trans}^c = 16.70$ kg/mm^2 (163.83 MPa) for BMD_{max} (Figure 5.9 (a)), and $E_{trans} = 73.662$ kg/cm^2 (7.22 GPa) and $S_{trans}^c = 10.02$ kg/mm^2 (98.29 MPa) for BMD_{min} (Figure 5.9 (b)), values from Ascenci & Bonucci [313].

(a)

(b)

Figure 5.8: Scheme of the methodology followed for the estimation of the mean bounds on ultimate tensile stress in the longitudinal (a) and transverse (b) direction of non-porous lamellar tissue. S^t_{long}, S^t_{trans}, BMD$_{max}$ and BMD$_{min}$ are inferred from tensile test until failure of wet longitudinal and alternate osteons with different mineral content [312].

Hence, substituting the elastic modulus for different degree of mineralisation in Equation 4.2, the values of BMD can be inferred: $BMD_{max} = 1.264$ g/cm^3 and $BMD_{min} = 0.920$ g/cm^3.

Analogously, Figure 5.9 (e and f) represents the range of the stress-strain curves under compressive load resulting from testing several osteons, with fibers bundles showing a marked longitudinal direction in successive lamellae. In this case, the compressive stress applied during the mechanical test is transferred to the lamellae acting in the longitudinal direction of the fibers. From the linear-elastic regime, the mean values for the elastic modulus and ultimate compressive strength are again estimated: $E_{long} = 64.497$ kg/cm^2 (6.32 GPa) and $S_{long}^c = 11.20$ kg/mm^2 (109.87 MPa) for BMD_{max} (Figure 5.9 (e)), and $E_{long} = 49.063$ kg/cm^2 (4.81 GPa) and $S_{long}^c = 8.96$ kg/mm^2 (87.89 MPa) for BMD_{min} (Figure 5.9 (f)), values from Ascenci & Bonucci [313]. Replacing the elastic modulus in Equation 4.2 for different degree of mineralisation, the values of BMD can be inferred: $BMD_{max} = 0.502$ g/cm^3 and $BMD_{min} = 0.387$ g/cm^3.
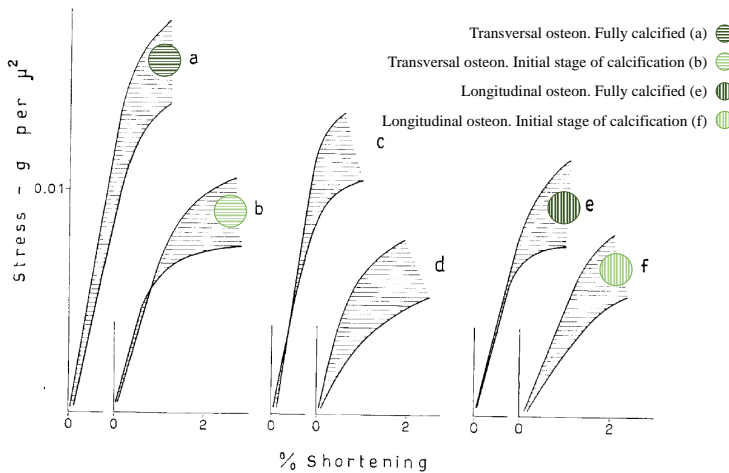
Figure 5.9: Range of compressive stress-strain curves of wet osteons with different orientation of fibers bundles in successive lamellae and degree of calcification (30-year-old man). Note: $1g/\mu m^2 \approx 10^4$ MPa. Reprinted from Ascenci & Bonucci [313] with permission of John Wiley and Sons.

Table 5.3 summarises the values of BMD and the ultimate compressive strength resulting on the longitudinal and transverse direction of lamellar tissue. These

Table 5.3: BMD and ultimate compressive strength for both longitudinal and transverse direction of lamellar tissue. Values inferred from mechanical testing until failure of longitudinal and transverse osteons with different stage of calcification [313].

BMD (g/cm^3)	0.387	0.502	BMD (g/cm^3)	0.920	1.264
S_{long}^c(MPa)	87.89	109.87	S_{trans}^c(MPa)	98.29	163.83

values have been deduced from the empirical tests performed by Ascenci & Bonucci [313].

Analogously as described in Section 5.3, mean bounds on ultimate compressive strength of non-porous lamellar tissue can be estimated assuming the two previous scenarios: the natural porosity of lamellar tissue in osteons was the minimum $p = 1$ % (hypothesis 1) and the maximum $p = 5$ % (hypothesis 2). Figure 5.10 illustrates a scheme of the workflow followed in order to estimate the mean value of the ultimate compressive strength in the longitudinal direction (a) and transverse direction (b) of the non-porous lamellar tissue. In this case, the remote ultimate compressive strength for different mineral content from Ascenci & Bonucci [313] is applied to the five models with randomly distributed ellipsoids. The mean value of the maximum nodal stress component (in absolute value) aligned with the applied load direction will be identified as the corresponding ultimate strength for the non-porous tissue, the lower bound for hypothesis 1 ($\bar{S}_{long}^{c,low}$(BMD, p_0 %), $\bar{S}_{trans}^{c,low}$(BMD, p_0 %)) and the upper for hypothesis 2 ($\bar{S}_{long}^{c,upp}$(BMD, p_0 %), $\bar{S}_{trans}^{c,upp}$(BMD, p_0 %)).

5.5   In-plane ultimate strength of porous lamellar tissue considering mineral content and lacunae concentration

5.5.1   Tensile and compressive strength

In this section, the methodology followed for studying the influence of the porosity owing to osteocyte lacunae on the lamellar tissue strength will be detailed.

Figure 5.11 summarises the procedure considered for the tensile load analysis (analogous to the compressive load). Firstly, for each degree of porosity ($p_1...p_n$) (see Table 5.1), five numerical models of a control volume or VOI of lamellar tissue with randomly distributed ellipsoids are generated.

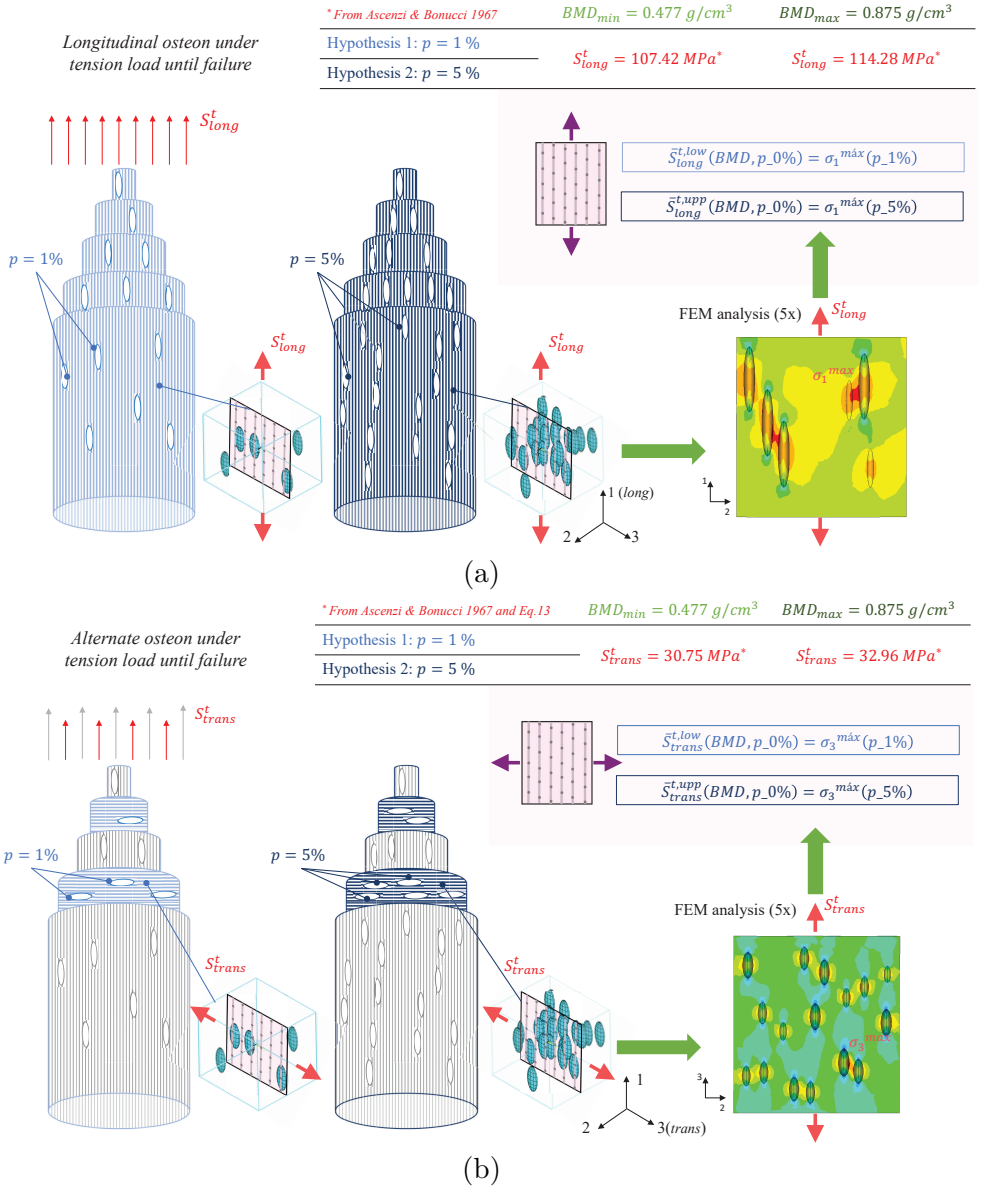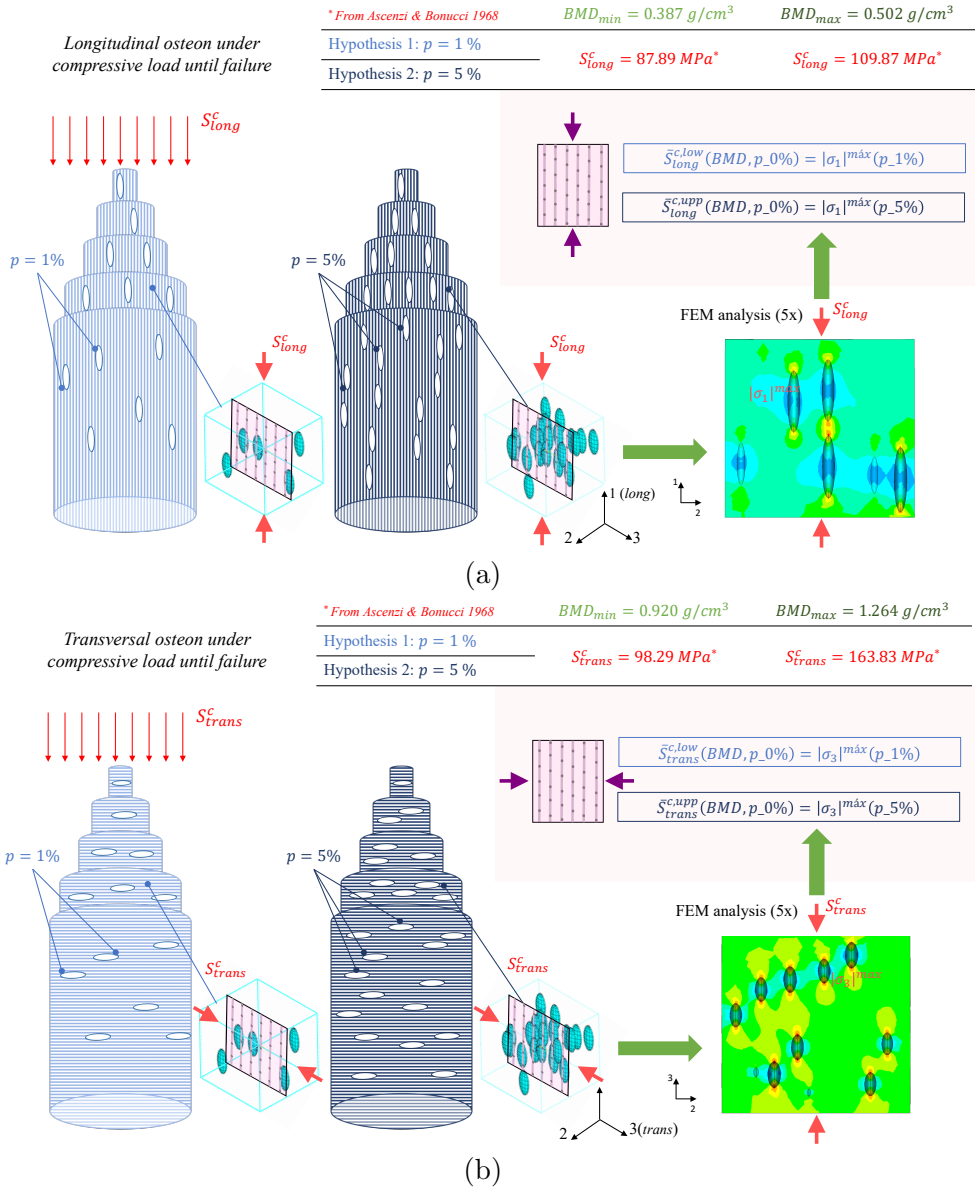**Figure 5.10:** Scheme of the methodology followed for the estimation of the mean bounds on ultimate compressive strength in the longitudinal (a) and transverse (b) direction of non-porous lamellar tissue. S_{long}^c, S_{trans}^c, BMD$_{max}$ and BMD$_{min}$ are inferred from compressive test until failure of wet longitudinal and transversal osteons with different mineral content [313].

Mechanical properties of lamellar bone at the tissue level are specified in the finite element models in the domain around the voids: the elastic properties as a function of BMD are defined through Eqs. 4.1 to 4.6 and the strength properties (non-porous tissue) that have been estimated as described in Section 5.3 and 5.4 (arrows in purple in Figure 5.11).
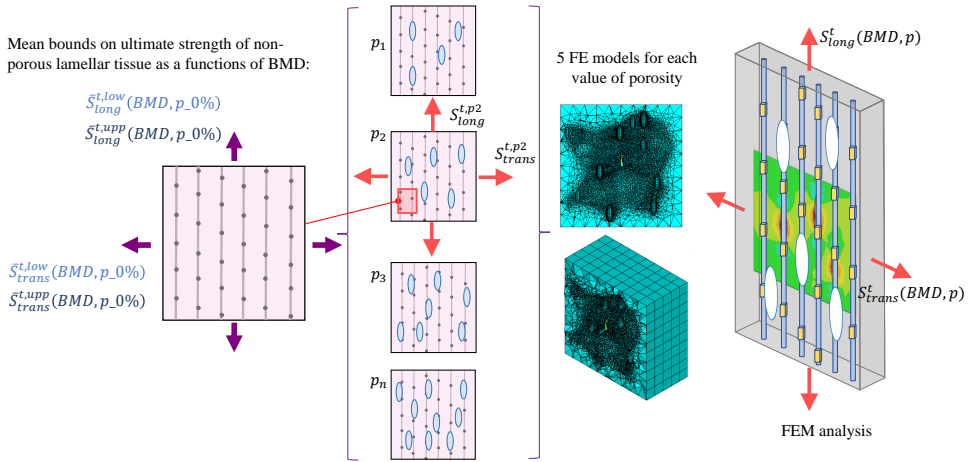
Figure 5.11: Scheme of the methodology followed to estimate the in-plane ultimate strength of lamellar tissue considering porosity due to lacunae concentration. The analysis sequence is reproduced for different mineral content (BMD_{max} and BMD_{min}) and lower and upper bounds on the ultimate strength of non-porous lamellar tissue.

Subsequently, the remote load to be applied for achieving the failure, that means the corresponding ultimate strength at tissue level (non-porous), will determine the lamellar tissue strength for each degree of porosity (arrows in red in Figure 5.11). Every analysis is performed considering the bounds on ultimate strength for non-porous material and two mineral content values.

5.6   Results obtained for in-plane strength limits

5.6.1   Ultimate strength of non-porous lamellar tissue

Table 5.12 presents the bounds on ultimate tensile/compressive strength in the longitudinal and transverse directions of non-porous lamellar tissue. Solid markers represent the averaged values of lower and upper bounds from five models with ellipsoids randomly distributed.

Notice that these results correspond with the maximum nodal stress component aligned with the loading direction considering hypotheses 1 and 2, where the porosity of the tested osteons from Ascenzi & Bonucci [312, 313] was assumed to be $p = 1$ % and $p = 5$ %, respectively (see Sections 5.3 and 5.4). Nodal stress increases near ellipsoids as a result of the stress concentration. Porous lamellar tissue will fail under certain remote uni-axial load, when maximum nodal stress reaches the ultimate strength of the material, this is the non-porous lamellar tissue.

Results are obtained for two stages of mineralisation. The micromechanic model for elastic properties used (Equation 4.1 to Equation 4.5) includes the BMD influence on the orthotropic elastic properties of lamellar tissue. Hence, as seen in Figure 5.12, strength increases with BMD because more load is transferred when bone tissue is stiffer.

The Table 5.4 summarises the mean and standard deviation of the ultimate tensile/compressive strength for the longitudinal and transverse directions of non-porous lamellar tissue, for two stages of mineralisation.

Theoretically, under pure compressive load, the maximum shear stress occurs at 45° from the direction of the applied load, such in the longitudinal as in the transverse direction of compression loading, as shown in Figure 5.13. Failure of the lamellar tissue under compressive load can be attributed to this shear stress. Table 5.5 summarises the mean and standard deviation of the maximum shear stress, τ_{45^o}, when the remote failure load is applied [313], for different stages of mineralisation of the bone tissue.
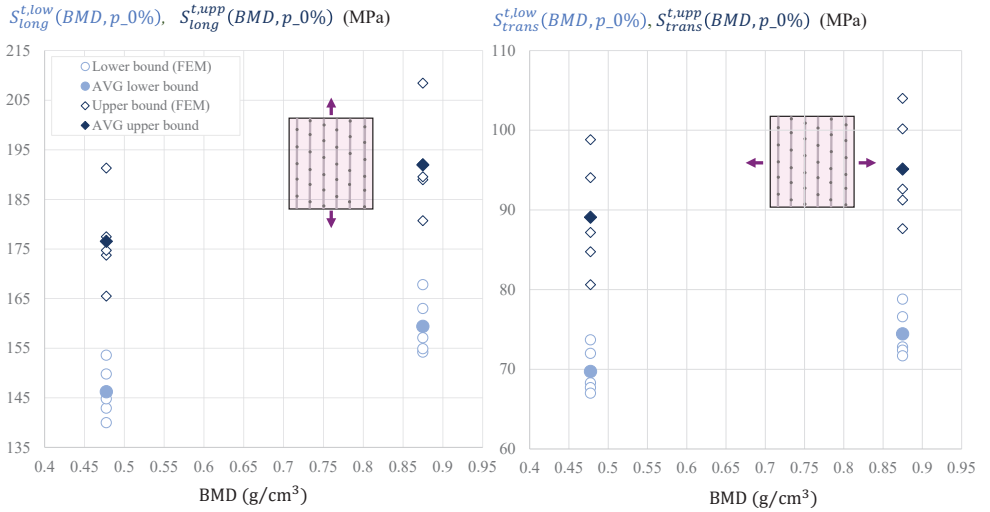
(a)
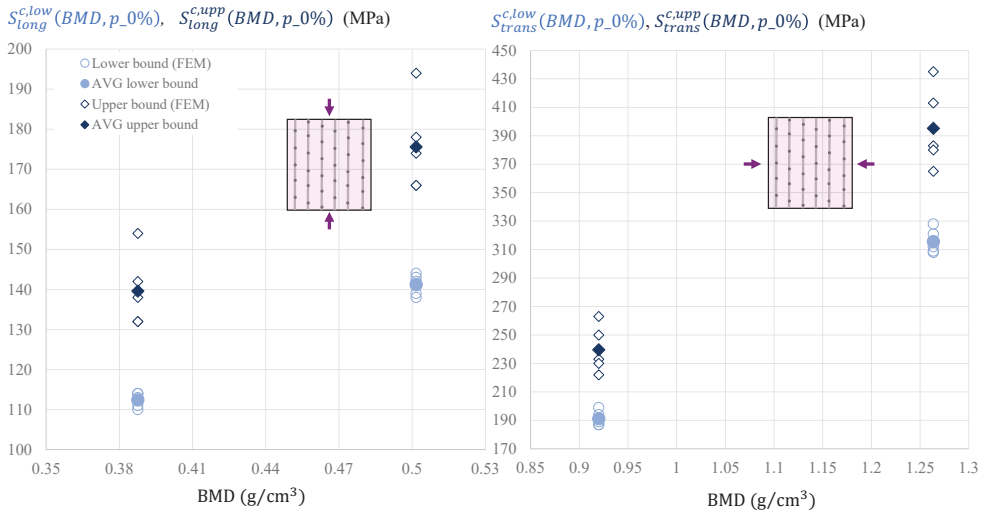
(b)

Figure 5.12: Bounds on ultimate tensile (a) / compressive (b) strength (in MPa) for non-porous lamellar tissue ($p = 0$ %) in the longitudinal (left) and transverse (right) direction, for two degree of mineralisation, BMD (g/cm^3).

Table 5.4: Ultimate tensile/compressive strength (MPa) in the longitudinal and transverse direction of non-porous lamellar tissue ($p = 0$ %) for different mineral content (g/cm^3) (mean values and standard deviation).

BMD (g/cm^3)	0.477	0.875
$\bar{S}^t_{long}\pm$ SD (MPa)	161.39 ± 15.17	175.69 ± 16.29
$\bar{S}^t_{trans}\pm$ SD (MPa)	79.41 ± 9.67	84.80 ± 10.34
BMD (g/cm^3)	0.378	0.502
$\bar{S}^c_{long}\pm$ SD (MPa)	126.00 ± 13.60	158.40 ± 17.20
BMD (g/cm^3)	0.920	1.264
$\bar{S}^c_{trans}\pm$ SD (MPa)	215.40 ± 24.20	355.40 ± 39.80

Table 5.5: Mean and standard deviation of the maximum shear stress acting on 45° (MPa) for compressive load.

BMD (g/cm^3)	0.378	0.502	0.920	1.264
$\bar{\tau}^{max}_{45^o}\pm$ SD (MPa)	63.9 ± 7.69	79.9 ± 9.47	96.0 ± 9.89	162.2 ± 20.06

5.6.2 In-plane ultimate strength of lamellar tissue considering mineral content and lacunae concentration

After estimating the ultimate tensile/compressive strength at the tissue level, the main goal of the present work can be addressed. In the following sections, the results for the in-plane ultimate strength of lamellar tissue considering the porosity due to the lacunae concentration and mineral content are presented.
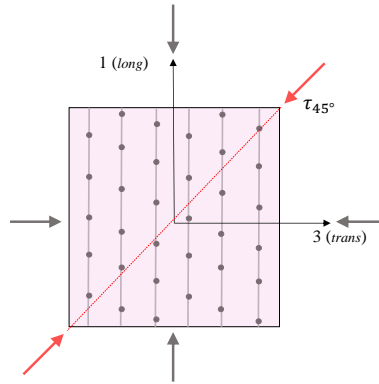
Figure 5.13: Scheme showing the direction where maximum shear stress is produced when compressive loading is applied.

5.6.2.1   Ultimate tensile and compressive strength

In Figures 5.14 and 5.15 results for the ultimate tensile and compressive strength are depicted. The objective is to determine the remote tensile load (arrows in red) to be applied to the porous lamellar tissue with certain mineral content, needed to reach the ultimate strength at tissue level (see Section 5.6.1). The methodology followed to obtain these results has been described in Section 5.5 and summarised in Figure 5.11.

In the graphs, light and dark blue represent the solutions for the lower and upper bounds, the solid line indicates the averaged ultimate strength. Results show that strength is highly reduced when porosity is considered, being remarkable the strong gradient when it initiates. This behaviour is motivated by the stress concentration attributed principally to the ellipsoidal geometry of the voids. As the porosity is higher, the number of ellipsoids increases (all of them being equal) and, hence, the effective area is reduced. This is the factor that will predominantly cause the smoother reduction of the strength when increasing porosity.

Subsequently, the averaged values are fitted using a potential multi-variable nonlinear regression in Matlab, being the parameters: BMD and porosity. To this aim, two conditions are added: the tissue strength should be equal to the strength of the hydroxiapatite crystal when, being the porosity equal to zero, the BMD reaches its maximum value (the hydroxyapatite density). Additionally, when porosity tends to be the maximum ($p = 100$ %), then, the

179
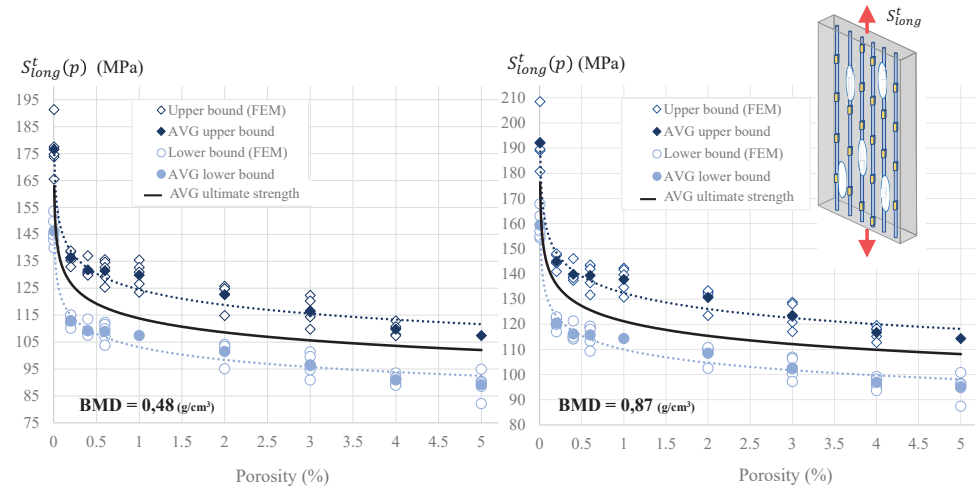
(a)
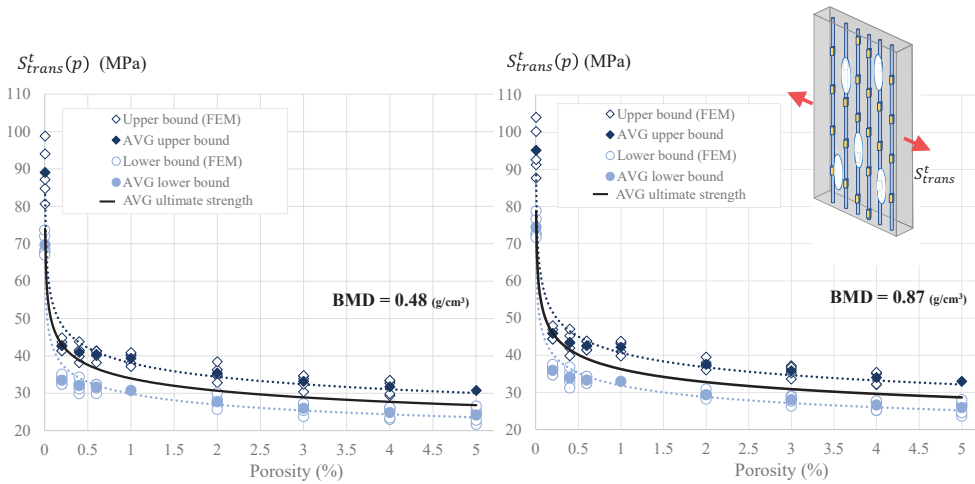
(b)

Figure 5.14: Bounds and averaged (AVG) ultimate tensile strength (in MPa) of lamellar tissue in the longitudinal (a) and transverse (b) direction as a function of the porosity due to osteocyte lacunae concentration, for two degree of mineralisation.
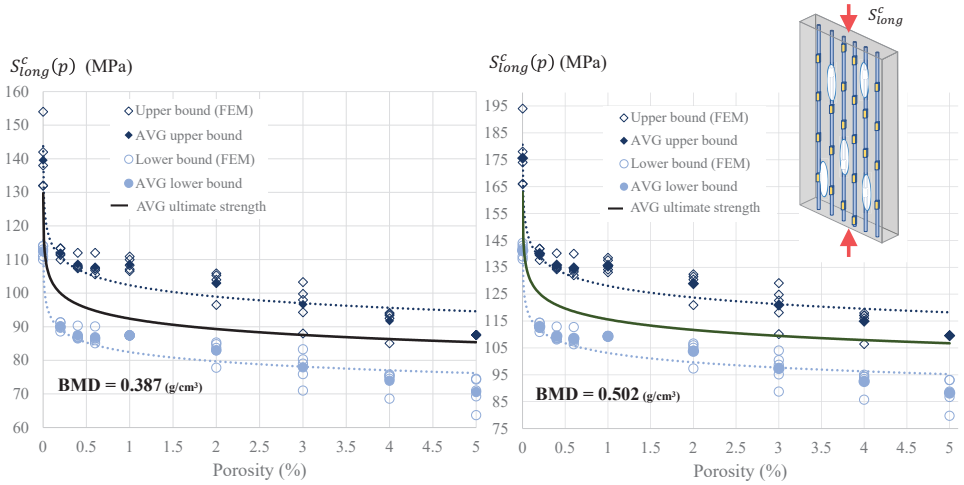
(a)
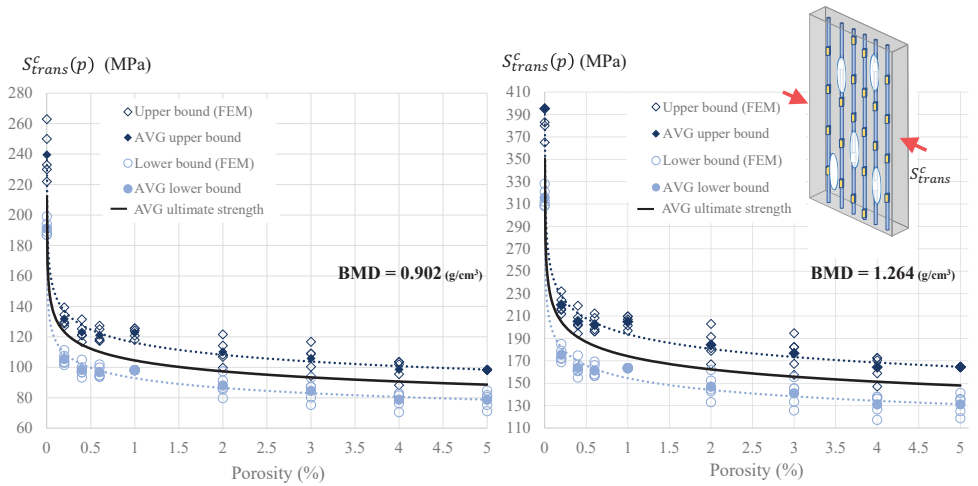
(b)

Figure 5.15: Bounds and averaged (AVG) ultimate compressive strength (in MPa) of lamellar tissue in the longitudinal (a) and transverse (b) direction as a function of the porosity due to osteocyte lacunae concentration, for two degree of mineralisation.

fitting should fulfill that the strength tissue will become zero. Equations 5.6 and 5.7 contain the regressions for the ultimate tensile strength and Equations 5.8 and 5.9 for ultimate compressive strength, both in the longitudinal and transverse direction of lamellar tissue.

$$S^t_{long}(BMD, p) = S^t_{HA} \left(\frac{BMD}{\rho_{HA}} \right)^{0.11024} \left(1 - \frac{p}{100} \right)^{0.29755} \text{MPa} \qquad R^2 = 0.985$$
(5.6)

$$S^t_{trans}(BMD, p) = S^t_{HA} \left(\frac{BMD}{\rho_{HA}} \right)^{0.5025} \left(1 - \frac{p}{100} \right)^{0.11559} \text{MPa} \qquad R^2 = 0.915$$
(5.7)

where ρ_{HA} and S^t_{HA} are the density and ultimate tensile strength of the hrydroxyapatite (3.6 g/cm^3 and 190 MPa, respectively [334]). BMD is the bone mineral density (in g/cm^3) and p represents the porosity due to lacunae concentration (in %).

$$S^c_{long}(BMD, p) = S^c_{HA} \left(\frac{BMD}{\rho_{HA}} \right)^{0.90634} \left(1 - \frac{p}{100} \right)^{0.33564} \text{MPa} \qquad R^2 = 0.988$$
(5.8)

$$S^c_{trans}(BMD, p) = S^c_{HA} \left(\frac{BMD}{\rho_{HA}} \right)^{1.0076} \left(1 - \frac{p}{100} \right)^{0.16183} \text{MPa} \qquad R^2 = 0.946$$
(5.9)

in this case, S^c_{HA} is the ultimate compressive strength of the calcium hrydroxyapatite mineral (900 MPa [334]). As in the corresponding expression for the tensile strength, BMD is the bone mineral density (in g/cm^3) and p is the porosity due to lacunae concentration (in %).

The first exponent near one in Equations 5.8 and 5.9, denotes that lamellar compressive strength is highly dominated by the mineral phase. In Figures 5.16 and 5.17 results from the regressions obtained are depicted.
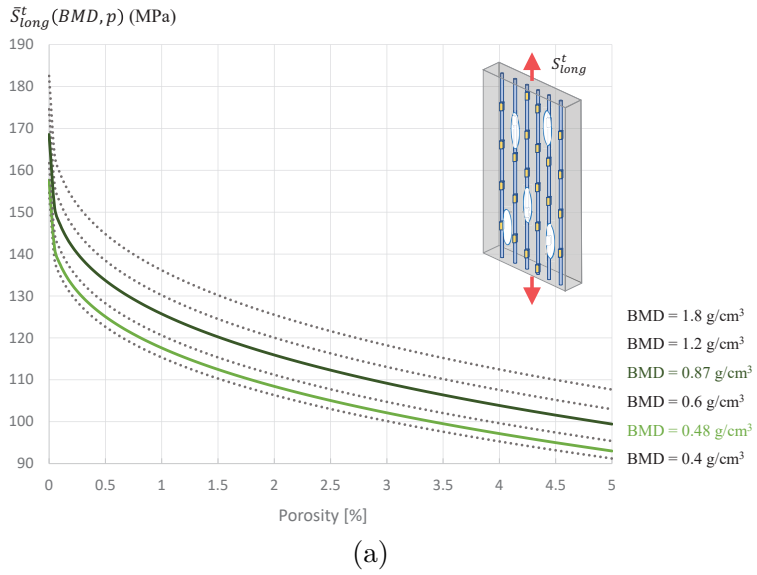
(a)
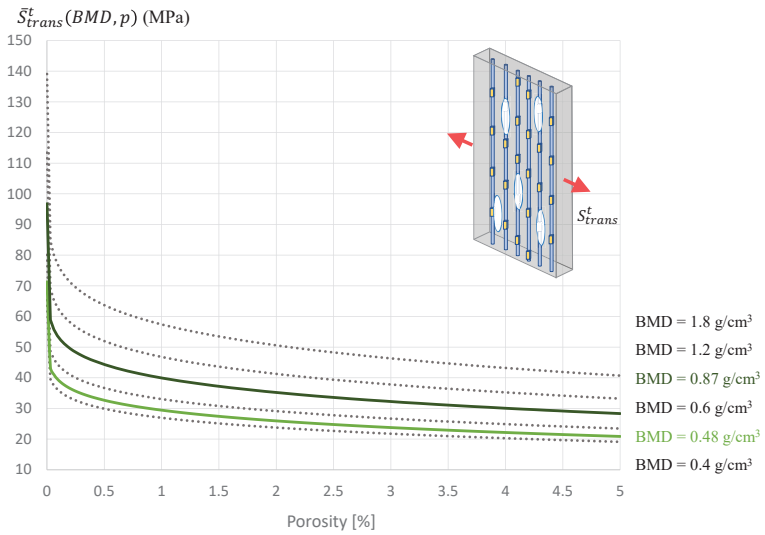
(b)

Figure 5.16: Results from the regressions for the ultimate tensile strength (in MPa) of lamellar tissue in the longitudinal (a) and transverse (b) direction, as a function of the mineral content (BMD) and porosity due to osteocyte lacunae concentration (Equations 5.6 and 5.7).
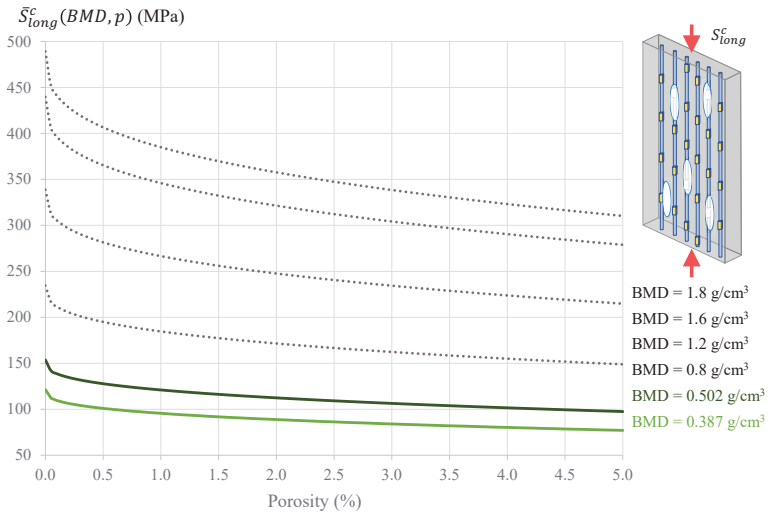
(a)
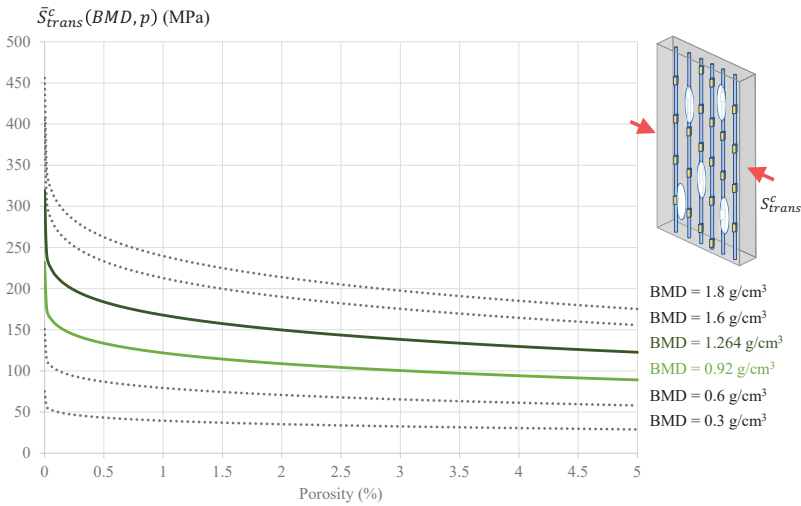
(b)

Figure 5.17: Results from the regressions for the ultimate compressive strength (in MPa) of lamellar tissue in the longitudinal (a) and transverse (b) direction, as a function of the mineral content (BMD) and porosity due to osteocyte lacunae concentration (Equations 5.8 and 5.9).

5.6.2.2   Intralamelar shear stress evolution with porosity and mineral content

Results from the numerical compressive stress analysis in the longitudinal and transversal direction of lamellar tissue, show that for a given compressive load σ^c, the maximum intralamella shear stress at tissue level increases with the porosity and mineral content. In Figure 5.18, the finite element solution for the ratio $\dfrac{\tau_{13}}{BMD\,\sigma^c}$ has been fitted with a multi-variable nonlinear model considering as variables BMD and porosity. The relationship of the in-plane shear component τ_{13} with these parameters is given in Equation 5.10.

$$\tau_{13} = \left(0.091\,BMD\,p^{0.381} + 0.12678\,BMD^{-0.293}\right)\sigma^c \quad \text{for } p \leq 5 \qquad R^2 = 0.980 \tag{5.10}$$

where σ^c is the remote compressive load applied in the longitudinal or transverse direction of the lamellar tissue.
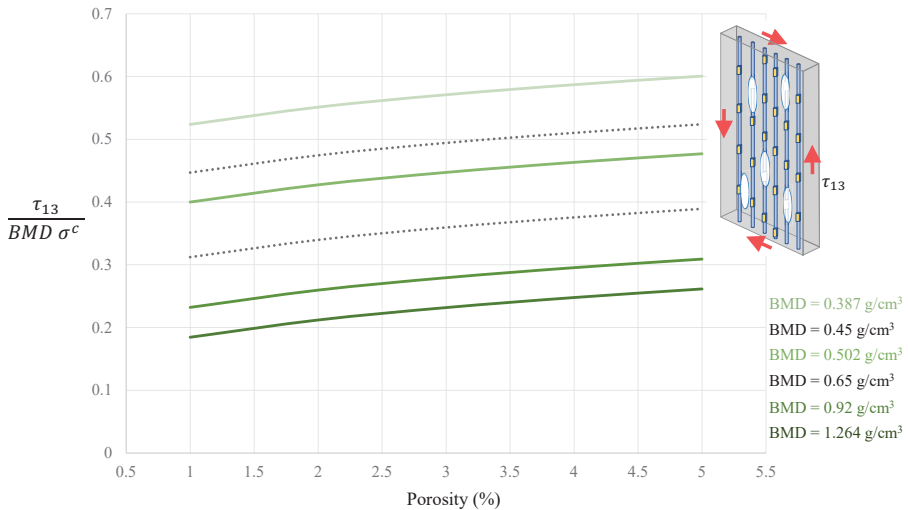
Figure 5.18: Evolution of the ratio $\dfrac{\tau_{13}}{BMD\,\sigma^c}$ as a function of the degree of porosity within the natural range due to lacunae concentration.

5.7 Discussion

In this work, a micromechanical model for evaluating the tensile/compressive ultimate stress of lamellar tissue is proposed. This novel approach includes the influence of the bone mineral density BMD and micro-porosity p values within the range of a healthy bone.

A representative volume of lamellar tissue has been numerically modelled. The elastic properties of the bone for different mineral content have been defined from Vercher-Martínez *et al.* [46] and the porosity due to osteocyte lacunae has been explicitly modelled creating a random distribution of smooth ellipsoids with dimensions and orientation in the lamellar plane known from Marotti [55]. Subsequently, we have inferred the failure stress acting on the longitudinal and transverse directions of the lamellar tissue from Ascenzi and Bonucci [312,313]. In their work, mechanical tests of quasi-static tensile/compressive load were applied to wet osteons with different orientation patterns of the fibers bundles in the successive lamellae, for both fully calcified and at the initial stage of mineralisation. In order to include the micro-porosity in the micromechanical model, two scenarios have been considered: the first assumes that osteons have a minimum porosity level, $p = 1$ %, and the second, a maximum porosity level, $p = 5$ %, always considering healthy bone tissue. These hypotheses allow to obtain the bounds on the ultimate stress of non-porous tissue.

The ultimate stress of non-porous tissue ($p = 0$ %) increases with higher mineral content, reaching a value of $\bar{S}^c_{trans} = 355.40 \pm 39.80$ MPa for compression in the transversal direction of the fiber bundles, being BMD = 1.246 g/cm^3. Similar values have been reported in the literature. In Casari *et al.* [332] the yield stress for compressive load for transverse specimens in dry conditions was 300 ± 20 MPa, however, no data about mineral content is available. In the present work, the longitudinal to transverse strength mean ratio for tension is 2.47:1 and for compression is 1.55:1, evaluated for the values of porosity $p = 0$ %, 1 % and 5 % and considering a mineral content BMD = 1.2 g/cm^3. These values are in agreement with Casari *et al.* [332], where the corresponding strength ratios are 2.7:1 for tension and 1.25:1 for compression.

Additionally, the shear stress acting at 45° from the compressive load direction is also increasing with the mineral content and reaches $\bar{\tau}^{max}_{45^o} = 162.2 \pm 20.06$ MPa for BMD = 1.246 g/cm ^{3}. The osteons tested under compressive load in Ascenzi and Bonucci [313] exhibit fissures oriented roughly $30^o - 35^o$, for both longitudinal and transverse samples. Based on that empirical evidence, although the micro-bending of the collagen fibers bundles can occur

under compressive longitudinal load, the shear component causes bone tissue failure.

From Fig. 5.14, the longitudinal tensile strength is significantly higher than in the transverse direction. This is in agreement with the highest tensile strength in the osteons with fibers roughly aligned with the osteon axis observed by Ascenzi and Bonucci [312]. Considering results from Fig. 5.15, it is not possible to establish a direct comparison because the mineral content of the osteons tested in the longitudinal and transverse directions is different. This drawback is avoided when considering the results from the multi-variable regressions (Fig. 5.17). Nevertheless, the compressive strength is considerably increased with the increment of mineral content.

Results obtained in this work show that the strength of lamellar bone decreases potentially with the lacunae porosity concentration. This behaviour is in accordance with Sang *et al.* [335] where the strain amplification around osteocytes is potentially related to the lacunae volume.

The evolution of the intralaminar shear stress τ_{s13} has been analyzed in this study, although the corresponding ultimate shear strength is not addressed. Following the composite materials approach, it can be estimated as $S_{s13} \approx \frac{1}{2} \bar{S}^c$, being $\bar{S}^c = \frac{S^c_{long} + S^c_{trans}}{2}$. Another limitation of this work is that it considers all the ellipsoids with the same dimensions, while morphological modifications can occur due to physiological or pathological conditions. In future work, the random generation code will incorporate the variability of morphology. On the other hand, no porosity due to the canaliculi calcoforo system is included, although its effect as stress concentrator, would not be so critical as lacunae. However, the reduction of the effective cross-section should be quantified. More experimental data from mechanical testing can be considered for compressive load [336]. Lastly, an elastic linear constitutive model has been assumed for the lamellar tissue. This is admissible for fully calcified tissue, i.e. the common situation in an adult bone.

5.8 Conclusions

A novel micromechanical model for evaluating the tensile/compressive ultimate stress of lamellar tissue is proposed, including the bone mineral content and micro-porosity p. This approach can be implemented in micro- or meso-numerical models of cancellous bone, obtained from processing clinical images, in order to enhance the results derived from numerical simulations.

The strength micromechanical model given in this work (Eqs. 5.6 to 5.9), provides the expressions to estimate the tensile/compressive ultimate stress in the longitudinal and transverse direction of lamellar tissue as a function of BMD and micro-porosity due to osteocyte lacunae. From these equations (graphically represented in Figs. 5.16 and 5.17), a higher strength in compression than in tension, for both longitudinal and transverse directions of the lamellar tissue, is clearly observed. This difference is more pronounced when BMD increases and porosity is low. This is compatible with the mechanical function of the hydroxyapatite mineral phase under compressive load because collagen fibers tend to bend and failure can occur earlier [313].

The results shown in this work reveal the strong influence of the porosity due to osteocyte lacunae on the increase of the stress at the tissue level, causing a decrease of apparent strength. This trend is observed regardless of the mineral content. Ellipsoidal lacunae act as stress concentrators around osteocytes, and also reduce the effective cross-section, causing a potential reduction of the lamellar bone strength as porosity increases. Our findings confirm that the stress and strain increase around osteocytes rather than other locations of the extracellular matrix, being the most potential location for microcracks.

Chapter 6

Experimental characterisation and numerical simulation of the mechanical behaviour of osteoporotic, osteoarthrosic and healthy cancellous human bone

6.1 Introduction

In this chapter, the aim is to characterise the mechanical behaviour of healthy and diseased cancellous human bones. For this purpose, cancellous bone samples have been prepared from femoral head specimens. The samples have been divided into three groups depending on the bone state: healthy, osteoarthrosic and osteoporotic bone. Different approaches have been employed to study the mechanical behaviour of these three types of cancellous bones: experimental

tests, finite element (FE) simulations and imaging techniques. To obtain the cancellous bone specimens geometry, we scanned the samples using a micro-CT with 13.5 μm isotropic resolution. To study the mechanical behaviour, we tested the cancellous specimens under quasi static compression loads. From these compression tests, we obtained the stress-strain curves with the compression response. To estimate the elastic and failure properties of the human cancellous samples, we used the stress-strain curves of the experimental tests to calibrate the numerical models.

This PhD thesis is focused on two bone diseases: osteoporosis and osteoarthrosis. The first one is the most prevalent bone pathology in society and consists in a negative imbalance in the remodelling cycle of bone, resulting in a degraded structure. Regarding osteoarthrosis, during the initial phase, there is a notable increase in the remodelling of the subchondral bone tissue. These changes result in a temporary reduction in bone mass, increased porosity and decreased bone density [337]. Nevertheless, in the final stages, the remodeling intensity decreases, leading to an increase in bone density and volume, so-called sclerosis. When comparing bone volume and density of osteoarthrosis patients and healthy individuals, it has been determined that patients with osteoarthrosis present a 15 % rise in bone density and 30 % in bone volume [338–340].

Intending to clarify and establish some terminology that will be used throughout this section, it is important to consider that in this thesis, the term OA will be related to osteoarthrosis, defined as a degenerative joint disease [341–343]. A great amount of English-speaking authors misuse the term osteoarthritis to design both an inflammatory bone disease, usually known as arthritis, and the chronic degenerative joint disease, so-called arthrosis. The suffix "*-itis*" implies the presence of inflammation, which is not involved in arthrosis. This improper use of osteoarthritis has led to confusion about what bone disease is referred to. Many researchers, at the beginning of their studies, explain which type of osteoarthritis is addressed, inflammatory or degenerative [20,337,344]. To avoid this confusion, from now on, we will use osteoarthrosis (OA) for the degenerative joint bone disease without an inflammatory implication.

6.2   Methodology to obtain the cancellous bone samples

In this chapter, human cancellous bone samples are analysed. The specimens come from human femoral heads extracted during total hip arthroplasty surgery in the Hospital Universitario Infanta Leonor of Madrid. We divided the specimens into three groups according to the doctors' criterion based on the classification of bone fracture presented by the patients: healthy group (HG), osteoarthrosic group (OA), and osteoporotic group (OP). The definition of each group is defined in section 3.2.2.1 in Chapter 3.

Besides the femoral head samples, some relevant information from the donors is available to study the specimens with bone diseases. The donors are anonymous, but they have filled out a survey with the signed consent and some information about their clinical history, which consists of several questions as follows:

– The study group (HG/OA/OP).

– Initials identifying the sample (ie: LCFB, MPR, AMMT).

– Age.

– Sex (male/female).

– Imaging technique employed for the diagnosis (RX/RM/TAC).

– Prescribed medicines.

– Whether they have previously undergone any protracted treatment.

– Whether they suffer any disease.

– Whether they have ever been immobilised.

– Whether they have a family history of osteoporosis.

– What kind of diet they follow (vegetarian, mediterranean, high in fat, processed food).

– Whether they smoke.

– Whether they do any kind of physical exercise.

The information extracted from the patient's survey is highly relevant because some points directly influence bone state. For example, it is widely known

that osteoporosis has a greater impact on women than in men [345], and therefore, high likelihood of suffering a bone fracture [5]. In addition, age is also relevant, i.e. in women age can be used to establish whether they are pre- or post-menopausal women. We know that there are risk factors that can increase the probability of developing osteoporosis, such as genetics, smoking, long periods of immobilisation, some diseases and drugs [218]. For this reason, we have asked the patients for their familiar clinical history, medicines, and daily routines (regarding food, sport, smoking), to understand the obtained results and whether any risk factor has directly influenced them.

Figure 6.1 presents the procedure followed. Firstly, the cancellous samples from the femoral heads were prepared. Then, they were scanned by the μ-CT with an isotropic resolution of 13.5 μm. On the one hand, quasi static compression tests were carried out until fracture load levels were reached. After the segmentation of the images, the morphometry of the cancellous bone samples was studied and the finite element (FE) models were used to estimate the elastic and failure properties.
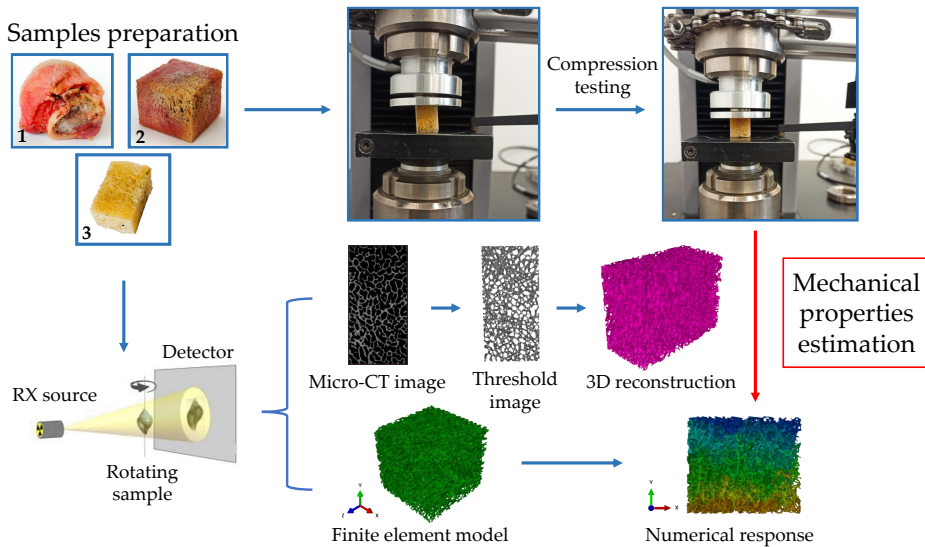
Figure 6.1: Procedure followed to study the compression mechanical behaviour and morphometry of healthy (HG), osteoarthrosic (OA) and osteoporotic (OP) human cancellous bone.

The starting point is the preparation of the cancellous bone samples. From the hospital, we received each femoral head wrapped in gauze individually

stored in a jar with the following information: study group, surgery date and the patient's initials that identify the samples (see Figure 6.2.1). It is only needed the cancellous bone of the femoral heads. The first step is to remove the cortical bone of the outermost part of the specimen. For this task, it was have employed a metallographic cutting saw TR100 Evolution Remet (Italy) (see Figure 6.2.3). From these cuts, we obtained a cancellous bone cube, such as the one illustrated in Figure 6.2.4. In addition, opposite faces of the cancellous samples are required to be parallel to apply perpendicular the loads to the specimen at the testing machine. For this task, we have used a Microtom Struers saw (Struers, Copenhagen, Denmark), such as the one shown in Figure 6.2.5. The cancellous bone samples studied in this section are such as the one shown in Figure 6.2.6. Finally, to remove the organic remains and blood, the samples underwent ultrasound baths in distilled water.
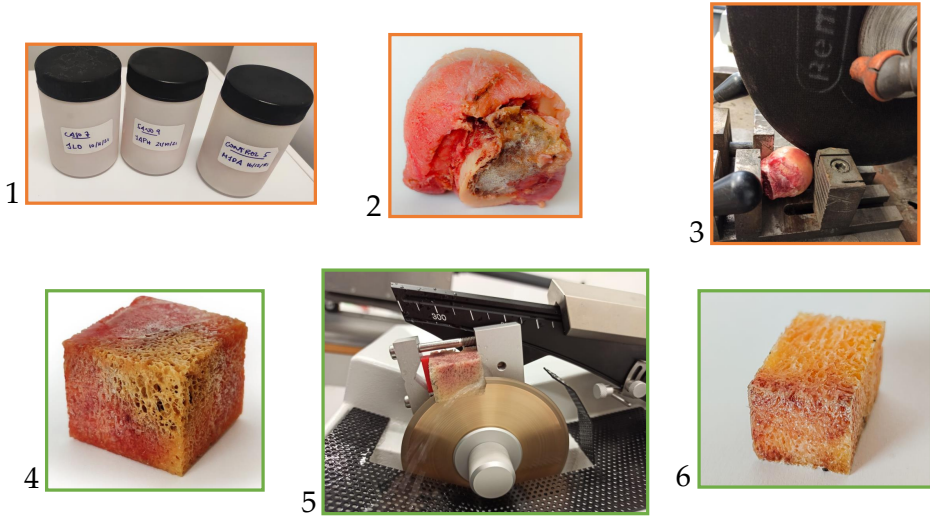
Figure 6.2: Cutting procedure to obtain cancellous samples from femoral heads.

6.3 High resolution scanning, image segmentation and morphometric characterisation

This section presents the morphometric analysis of the human cancellous specimens from the femoral heads. To achieve this purpose, we have scanned the cancellous samples using the μ-CT scanner. We segmented the images using

a global manual thresholding procedure, allowing the 3D reconstruction geometry of the specimens to be available. With the geometry, we study the cancellous morphometry and generate the FE models.

6.3.1 Micro-CT image segmentation

With the aim of characterising the 3D bone microarchitecture and generating the FE models with high resolution, we have scanned the cancellous samples using the μ-CT technique. We have used the μ-CT scanner from the Estación de Bioloxía Mariña at A Graña (University of Santiago de Compostela). They have a Skyscan1172 (Bruker, Kontig, Belgium), which can obtain images with an isotropic resolution of 13.5 μm (voltage 100 kV, intensity 100 μA, Al/Cu filter).

We have used ScanIP software (Simpleware, UK) and a global manual thresholding procedure for image segmentation. The format of the scanned images is DICOM (see Fig. 6.3 a), which contains all the information about the image, such as voltage, intensity, specimen identification, image number, resolution, etc. Firstly, we have to delete the black in the outer region of the scan to keep only the area of the image containing the cancellous sample (see Fig. 6.3 b). This procedure is important for two reasons: we will use this geometry to generate the FE models, so if we have parallel faces, we could apply the load better; secondly, we will use the images to analyse the morphometry of the samples: too much black background can lead to false voids and holes.

Then, the threshold to segment the images must be chosen. This part of the procedure is essential so as not to thicken nor thin the geometry of DICOM image. Whether we enlarge or slim the cancellous geometry, we will be misrepresenting morphometric information. Figures 6.3 d and e exhibit two masks with different thresholds, being wider the red mask. To compare and evaluate the differences, Figure 6.3 f presents overlapping masks. It is possible to appreciate that the red mask is thicker than the blue mask. Therefore, between these two masks, we will choose the blue mask, which neither overestimates, nor underestimates trabecular thickness.

Then, we apply the "Flood fill" command to the selected mask to delete the unconnected parts of the geometry, pointed out in Figure 6.4 with red arrows. After this process, the small parts usually at the corners or edges of the cancellous samples, disappear, and we obtain an entirely connected cancellous geometry. The obtained 3D reconstructed geometry (see Fig. 6.4) will be used to generate the FE models. The last step is to apply a binarisation
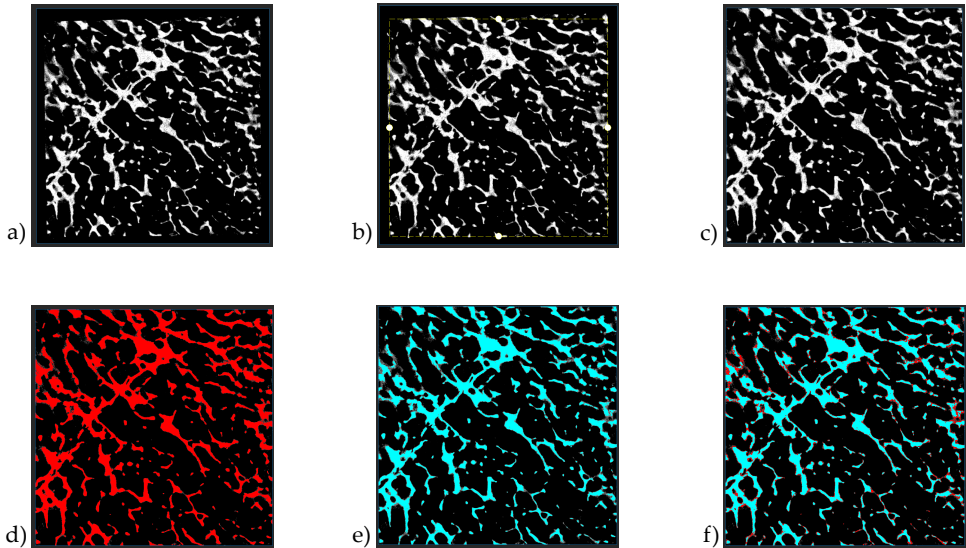
Figure 6.3: Global manual thresholding segmentation procedure. a) DICOM image, b) crop process, c) cropped image with parallel faces, d) mask 1 with larger threshold, e) mask 2 with smaller threshold and f) mask 1 and mask 2 overlapped.

filter and then export the mask with the voxels resolution because it will be used to analyse the cancellous specimens morphometry at BoneJ software.

6.3.2 Assessment of the bone mineral density using micro-CT images

Micro-CT images provide much information about the scanned specimen and the acquisition features. When we scan the specimen through μ-CT we obtain a three-dimensional matrix, wherein each voxel is assigned the attenuation coefficient value associated with the scanned material, directly linked to material density. Calibration phantoms are materials with a previously known density. They must be scanned using the same acquisition configuration as the studied specimens because the acquisition parameters, such as voltage, intensity, or integration time, highly influence the attenuation coefficient. Phantoms allow us to estimate the density of the scanned specimens because of the relationship that we can establish between them.

The most common phantoms employed to determine the bone mineral density (BMD) are both hydroxyapatite (HA) and dipotassium phosphate (K_2HPO_4).
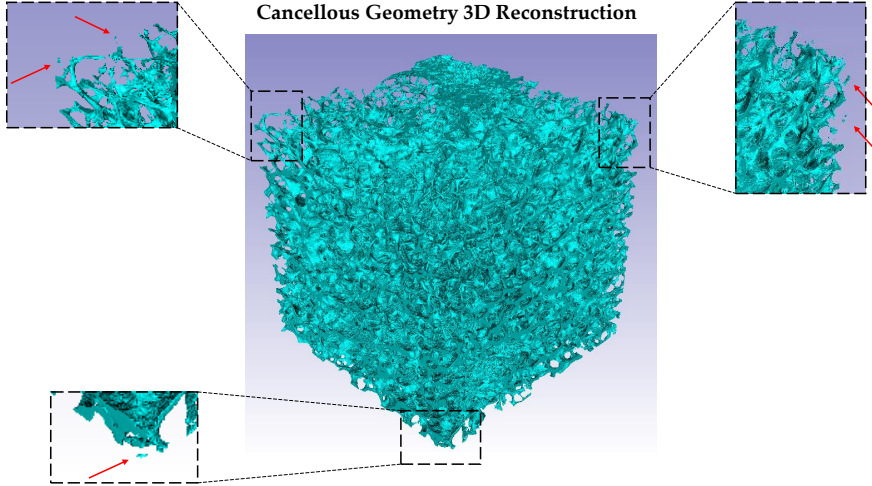
Figure 6.4: Cancellous geometry 3D reconstruction. Zoomed squares show the unconnected parts of the geometry removed after applying the 'Flood fill' procedure.

The first one (HA), is widely known because it is the mineral component of bone tissue, while K_2HPO_4 is also employed due to its comparable features to HA when referring to the effective atomic number or density [346].

To estimate the bone mineral density (BMD) of the studied specimens, we have scanned two hydroxyapatite (HA, $Ca_5(PO_4)_3OH$) phantoms with 250 and 750 mg HA/cm^3 of density (see Figure 6.5 left). These phantoms were scanned with an isotropic resolution of 13.5 μm with the equipment described in Section 6.3.1, the same configuration employed to scan the cancellous bone specimens. Figure 6.5 (right) shows the calibration relationship between the grey scale value (GS) and the mask density. The linear relationship between both parameters is presented in Equation 6.1:

$$\rho = 1.1575\ GS + 781.87 \tag{6.1}$$

Subsequently, we need to estimate both apparent and tissue properties from the micro-CT data. On the one hand, to determine the apparent properties, we will use the pre-segmented micro-CT images because they consider all the image content, which includes both bone and holes. The cleaning of the
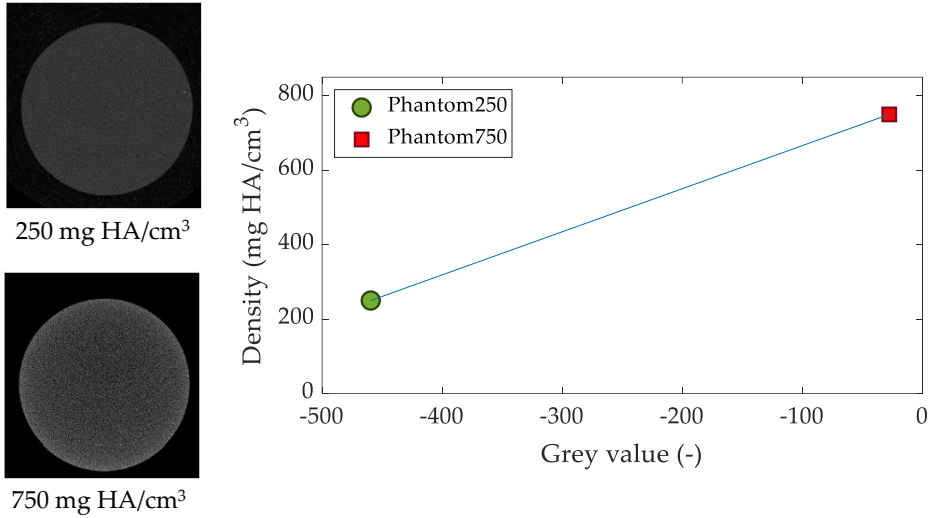
Figure 6.5: Micro-CT images of HA phantoms used to the calibration (left) and relationship established between both phantoms to calibrate density (right).

sample directly influences these results. If the marrow and the organic waste are not properly removed, they will appear in the μ-CT images. That means adding different grey values to the image that do not belong either to the bone or the background (holes and voids). With the grey scale values (GS), we aim to determine the apparent density (ρ_{app}) and the apparent Young's modulus (E_{app}). On the other hand, we use the mask GS, which only contains information about bone, to estimate the bone mineral density (BMD) of the specimens and Young's modulus at the tissue level (E_{tis}). Given that mask GS information is only related to bone, not the whole specimen (considering voids), the parameters obtained from this value will be related to bone tissue.

Several studies in the literature have explored formulations for stiffness-density relationships [203, 347], but there is no overall agreement on this issue. In the same line, Morgan and colleagues [202] observed variations in stiffness-density relationships depending on the skeletal location of the specimens. Schileo *et al.* [347] provided a procedure for estimating stiffness using density measurements. They reported several expressions that relate the phantom density with the ash density for both cortical and trabecular bone, and also a combined expression. In this study, we will only use the trabecular expression (Eq. 6.2) due to the nature of our specimens.

197

$$\rho_{\mu\mathrm{CT}} = -0.05 + 0.98 \; \rho_{\mathrm{ash}} \qquad (6.2)$$

$$\frac{\rho_{\mathrm{app}}}{\rho_{\mathrm{ash}}} = 0.6 \qquad (6.3)$$

Since Morgan *et al.* [202] stated that the skeletal location presents differences once estimating stiffness-density, we employ their expression for the femoral neck, depicted in Eq. 6.4, to determine the Young's modulus.

$$E = 6850 \; \rho_{\mathrm{app}}^{1.49} \qquad (6.4)$$

The procedure begins using Eq. 6.1 and obtaining the micro-CT density ($\rho_{\mu\mathrm{CT}}$), which will be applied in Eq. 6.2 to obtain the ash density (ρ_{ash}). Substituting in the Eq. 6.3, we find the apparent density (ρ_{app}) to be used in Eq. 6.4 and determine Young's modulus. It is essential to highlight that if in Eq. 6.1 is used the pre-segmented GS grey values we will obtain apparent results (see Table 6.1), whereas if we employ the mask GS, we will estimate tissue parameters (see Table 6.3).

The apparent parameters estimated using the grey scale (GS) mean values of the raw micro-CT images are collected in Table 6.1. The analysed specimens are from the different study groups: six osteoporotic (OP), seven osteoarthrosic (OA) and six healthy (HG). In order to have an overview of the obtained results, we have presented the mean values and the standard deviation of each parameter (see Table 6.2).

The presented results are apparent, meaning that the sample's architecture influences them. For this reason, we have developed an ANOVA statistical analysis to evaluate whether there are significant differences between groups due to bone diseases that affect the bone microarchitecture. The ANOVA analysis concluded that all the studied parameters (GS, ρ_{app} and E_{app}) present significant differences between HG and both diseased groups, OA and OP. ρ_{app} for HG is 23.79 % higher than OA and 36.95 % than OP. In the case of E_{app}, HG is 30.57 % greater than for the OA specimens and 49.13 % higher than OP. The interpretation of the results is that we can differentiate between healthy and diseased cancellous specimens with any of these apparent parameters. This seems logical due to the vast differences between their cancellous microarchitecture, where HG samples have a large amount of material compared to the pathological groups. It is possible to appreciate that the most significant dif-

ferences are between HG and OP because the osteoporotic structure is severely degraded, and this reality is directly reflected in the apparent results.

Table 6.1: Apparent density (ρ_{app}) and apparent Young's modulus (E_{app}) estimation from the grey scale values for the three study groups.

Sample ID	Group	Grey value (-)	ρ_{app} (g/cm^3)	E_{app} (MPa)
LCFB_P1	HG	-432.67	0.478	2281.03
MPR_P1	HG	-418.16	0.507	2488.64
MPR_P2	HG	-485.16	0.375	1586.95
MPR_P3	HG	-477.56	0.389	1682.21
JIMA_P1	HG	-476.38	0.392	1697.19
JIMA_P2	HG	-441.56	0.461	2157.68
AM_P1	OA	-484.93	0.375	1589.80
AM_P2	OA	-505.51	0.335	1340.86
AM_P3	OA	-487.69	0.369	1555.59
AM_P4	OA	-488.89	0.367	1540.75
AFA_P1	OA	-542.52	0.262	930.05
AFA_P2	OA	-546.98	0.253	884.01
AFA_P4	OA	-468.95	0.407	1792.34
FMF_P1	OP	-545.87	0.255	895.46
FMF_P2	OP	-586.33	0.176	512.83
ESR_P1	OP	-513.89	0.318	1243.56
ESR_P2	OP	-553.71	0.239	815.97
MADL_P1	OP	-531.81	0.283	1043.87
MCRC_P1	OP	-489.07	0.367	1538.60

Several researchers have found similar values for the apparent density ρ_{app}, such as Ranjanomennahary *et al.* [348] who stated for femoral head 0.417 ± 0.134 g/cm^3 for healthy specimens which agrees with our HG result. Gujar and Warhatkar [349] found for human femoral neck specimens results between 0.485 and 0.747 g/cm^3. Abdullah *et al.* [350] and Auger *et al.* [351] studied osteoarthrosic (OA) specimens, obtaining apparent density values from 0.28 to 0.34 g/cm^3 and 0.37 ± 0.08 g/cm^3, respectively, which are in the same range of our estimated values for the OA group. Regarding the E_{app} estimated

through the grey scale values (GS), Gujar and Warhatkar [349] presented results between 1880.96 and 3079.01 MPa, resulting in 2479.99 ± 599.027 MPa for healthy human femoral neck specimens, which is close to our HG results.

Table 6.2: Mean values and standard deviation for the grey scale values (GS), apparent density (ρ_{app}) and apparent Young's modulus (E_{app}) for HG, OA and OP specimens presented in Table 1.1.

	Grey value (-)	$\rho_{\mathbf{app}}$ **(g/cm^3)**	$E_{\mathbf{app}}$ **(MPa)**
HG	-455.23 ± 27.99	0.434 ± 0.055	1982.28 ± 375.24
OA	-503.64 ± 30.05	0.338 ± 0.060	1376.20 ± 346.56
OP	-536.78 ± 33.61	0.273 ± 0.066	1008.38 ± 355.82

Conversely, we have estimated the mineral content of the human cancellous samples and tissue Young's modulus based on the segmented mask of the micro-CT images, which only considers bone content. For this reason, the extracted results from this value are at the tissue level and are cancellous bone features. We have evaluated six specimens per group and the results are exhibited in Table 6.3. We have presented the mean values and the standard deviation of each study group in Table 6.4.

The results present a mineral content between 1.149 and 1.837 g/cm^3 for human cancellous femoral head specimens. Pumarino *et al.* [352] studied the most preferred skeletal sites to study bone mineral density: the spine and the femoral head or neck. They obtained a BMD mean value for the femoral neck of 0.931 g/cm^3. Kröger *et al.* [353] studied both spine and femoral neck bone density, and for the last ones, they registered values between 0.6 to 1.40 g/cm^3. Cossio-Bolano and colleagues [354] studied bone density and mineral content in the Chilean population from 5 to 80 years old. For the range of age of our specimens, they obtained values of BMD between 1.26 and 1.47 g/cm^3. In addition, in their work, it is possible to appreciate that after the age when bone finishes growing, the BMD has a stabilisation that is not present during the growth of bone.

Regarding the results obtained for the tissue Young's modulus, our values are between 14290.10 and 16957.24 MPa, except for one sample that manifests the lowest values with 8425.83 MPa. Zysset *et al.* [91] found similar results, 11.4 ± 5.6 GPa. Other researchers, such as Zlámal *et al.* [355] registered 12.582 ± 2.18 GPa for the elasticity modulus at tissue level.

Table 6.3: Bone mineral density (BMD) and tissue Young's modulus (E_{tis}) estimated from the segmented mask values for HG, OA and OP specimens.

Sample ID	Group	Segmented mask (mg HA/cm^3)	BMD (g/cm^3)	E_{tis} (MPa)
LCFB_P1	HG	194.548	1.713	15272.23
AMMT_P1	HG	-91.802	1.149	8425.83
AMMT_P2	HG	157.356	1.639	14309.78
MPR_P1	HG	167.925	1.660	14581.19
MPR_P2	HG	170.132	1.665	14638.07
JIMA_P1	HG	238.493	1.799	16435.66
AM_P3	OA	256.477	1.835	16919.82
AM_P4	OA	225.015	1.773	16075.85
AFA_P1	OA	176.302	1.677	14797.49
AFA_P3	OA	229.042	1.781	16183.08
JJCM_P1	OA	176.723	1.678	14808.39
JJCM_P2	OA	226.389	1.775	16112.41
ESR_P2	OP	257.860	1.837	16957.24
FMF_P1	OP	206.572	1.736	15587.76
FMF_P2	OP	253.750	1.829	16846.10
MADL_P1	OP	241.207	1.805	16508.43
MADL_P2	OP	225.368	1.773	16085.24
JLO_P1	OP	156.587	1.638	14290.10

We have developed an ANOVA analysis to assess the statistical differences between HG, OA and OP tissue results. The study reveals that no statistical differences are found between any group or parameter. These results state that even though some specimens have pathologies at the tissue level, there are no differences that allow us to distinguish between healthy and diseased groups or discern between pathologies. It is important to point out that the mineral content does not vary significantly, despite the cancellous bone suffers osteoarthrosis or osteoporosis.

In agreement with our results, other researchers have found similar results for healthy and osteoporotic specimens, such as Carretta *et al.* [99] who presented 16.24 ± 2.47 and 16.85 ± 2.1 GPa, respectively. Tkhia *et al.* [356] found the

Table 6.4: Mean values and standard deviation for the segmented mask, bone mineral density (BMD) and tissue Young's modulus (E_{tis}) for HG, OA and OP specimens.

	Segmented mask (mg HA/cm^3)	BMD (g/cm^3)	E_{tis} (GPa)
HG	139.44 ± 116.96	1.60 ± 0.23	13.94 ± 2.81
OA	214.99 ± 31.97	1.75 ± 0.06	15.82 ± 0.84
OP	223.56 ± 37.86	1.77 ± 0.07	16.05 ± 0.99

same trend in their results for the iliac crest for healthy and osteoporotic patients being 15.6 ± 1.2 and 15.7 ± 1.3 GPa, respectively. Regarding the mineral content, it is important to consider that the studied specimens belong to bone-mature patients, which may be the reason why we found similar BMD.

The estimated apparent Young's modulus will be compared in Section 6.4 with the results obtained from the quasi static compression tests for this same parameter to assess differences between the methods. Analogously, we will compare the estimated tissue Young's modulus with the calibrated values obtained from the finite element models in Section 6.6.

6.3.3 Morphometric analysis of the human cancellous bone specimens

In this section, we have analysed the morphometry of twenty one cancellous bone specimens: four from the healthy group (HG), eight from the osteoarthrosic group (OA) and nine from the osteoporotic group (OP). The morphometric parameters studied are the following:

- **Degree of anisotropy (DA)**: the fabric tensor measures the extent of material anisotropy in orthotropic substances, such as cancellous bone [133]. For cancellous bone, the mean intercept length (MIL) representation using a histological section of the cancellous specimen yields an ellipse whose major axis is aligned with the primary trabecular orientation. These findings were demonstrated by Harrigan and Mann [357] and can be indicated as presented in Equation 6.5 or as a tensor (Equation 6.6).

$$ax^2 + bxy + cy^2 = k \qquad (6.5)$$

$$[M] = \begin{bmatrix} a & b/2 \\ b/2 & c \end{bmatrix} \tag{6.6}$$

Using the mean intercept length on a 3D mask of cancellous bone results in an ellipsoid aligned in accordance with the favored trabecular direction. The significance of anisotropy plays a crucial role in the analysis of cancellous bone [358]. Some researchers associate it with the mechanical condition, along with apparent density or volume fraction, whereas others have established its correlation with the elastic stiffness matrix.

- **Connectivity density (Conn.D)**: this morphometric parameter was assessed using BoneJ software [185], relying on Toriwaki and Yonekura [359] and Odgaard and Gundersen [183] works. To determine the connectivity the Euler-Poincaré equation 6.7 is applied, which relies on the topological invariant Euler characteristic number (χ):

$$\chi = \beta_0 - \beta_1 - \beta_2 \tag{6.7}$$

where β_0 represents the number of parts in a structure, β_1 denotes the connectivity and β_2 indicates the number of empty spaces enclosed by bone. For cancellous bone, it is presumed to exhibit a singular connected structure ($\beta_0 = 1$), without any enclosed voids due to its open-cell nature ($\beta_2 = 0$). The connectivity density is determined by normalizing Eq. 6.7 to the volume (V), as expressed in Equation 6.8:

$$\text{Conn.D} = \frac{1 - \chi}{V} \tag{6.8}$$

The determination of Euler number in a 3D digitised image is defined in Equation 6.9:

$$\chi = n_0 - n_1 + n_2 - n_3 \tag{6.9}$$

where n_0 denotes the number of vertices in the object, n_1 represents the number of edges, n_2 is the amount of faces and n_3 is the number of voxels. These values are influenced by the definition of connectivity neighborhood (as illustrated in Figure 6.6). This definition determines whether each voxel entity defines the same aspect of the 3D object or es-

6-neighborhood   18-neighborhood   26-neighborhood
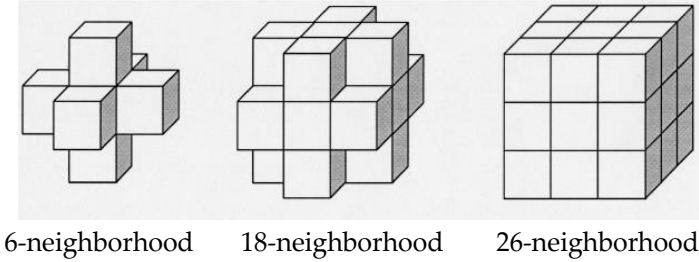
Figure 6.6: Three types of neighborhood. Image extracted from Toriwaki and Yonekura work [359].

tablishes a connection between voxels, without contributing to the Euler number (χ).

- **Fractal dimension (D)**: the concept of fractal dimension was introduced by the mathematician Benoit Mandelbrot with the main goal of accurately measuring the intricate complexity of nature through relatively simple mathematical expressions. The fractal dimension serves as an exponent that provides insight into how space is occupied when the length scale of analysis changes. In nature, it is possible to find fractal geometries, and cancellous bone manifests certain characteristics of fractals.

Namely, for cancellous bone, which is the subject of this research, the box-counting fractal dimension is calculated. Considering an object of Euclidean dimension D, e.g. square of side size 1, and then, divide it by a factor $1/\lambda$ at each direction. Hence, $N = \lambda^D$ boxes are needed to cover the object perimeter. The Euclidean or topological dimension would be defined as presented in Equation 6.10.

$$D = \frac{\log N(\lambda)}{\log 1/\lambda} \qquad (6.10)$$

Extending the same reasoning to a fractal object, adjusting the characteristic length (λ) of analysis, the data will conform to the expression given in Equation 6.11.

$$\log N = -D \log \lambda + k \qquad (6.11)$$
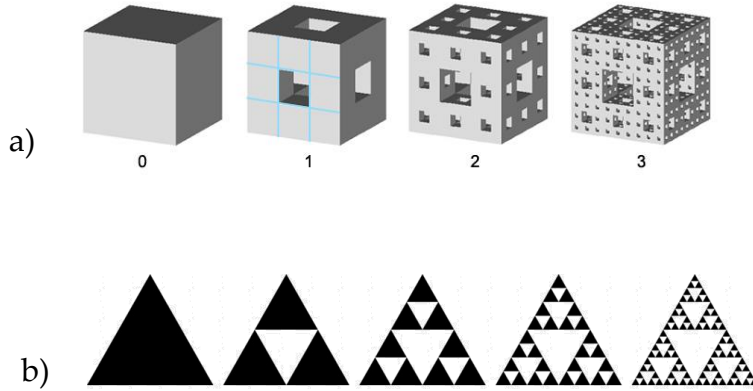
Figure 6.7: Fractal development illustrations. a) Menger Sponge [360] and b) Sierpinski Triangle [361].

where N is the number of boxes required to encompass the perimeter, D represents the fractal dimension, λ denotes the characteristic length under analysis, and k stands as a constant of proportionality.

- **Bone volume fraction (BV/TV)**: is the ratio between the bone tissue voxels and the total number of voxels (see Eq. 6.12) within the volume of interest (VOI). This parameter is calculated using the 3D segmented mask, and it can be presented both in percentage (%) or dimensionless (-).

$$\text{BV/TV} = \frac{\text{number of bone tissue voxels}}{\text{number of total voxels}} \qquad (6.12)$$

- **Bone surface area to volume ratio (BS/BV)**: represents the relationship between the outer surface area of bone and its corresponding volume (Equation 6.13), and it is expressed in mm^{-1}. BS/BV is obtained by calculating bone surface from the surface mesh, where A_i denotes the discretised surface mesh area, whereas N represents the total number of surfaces. Bone volume (BV) is determined by cancellous bone mask voxel counting.

$$BS/BV = \frac{\sum_{i=1}^{N} A_i}{\text{number of bone voxels}} \qquad (6.13)$$

- **Mean trabecular thickness (Tb.Th)**: this parameter determines the trabeculae thickness and is usually presented in mm. Tb.Th is the mean distance between the contour of the bone mask and its skeleton, as shown in Figure 6.8. The approach to determine the mean trabecular thickness involves fitting spheres of the maximum radius within the trabecular structure [184], as exhibited in Figure 6.8b (left). This method enables the calculation of Tb.Th without making any assumptions beforehand about the nature of the analysed structure. Unlike some methods in the literature, which tend to overstate Tb.Th [135], this is a fully three-dimensional (3D) method.

- **Mean trabecular separation (Tb.Sp)**: it represents the average size of gaps within the cancellous bone marrow and is usually measured in mm, although it is possible to find it in microns (μm). The computation method is analogous to that of Tb.Th, but it involves applying the process to the negative of the 3D segmented mask. This entails swapping 1s with 0s and vice versa.

  Figure 6.8b shows the procedure to compute the Tb.Sp. In this case, the spheres fit the spaces between trabeculae. Concerning the results, in Figure 6.9 one slice of the segmented mask is shown with the mean trabecular thickness and the mean trabecular separation. In Figure 6.9a, the brighter colours are referred to higher trabecular thickness (Tb.Th), whereas for the mean trabecular separation (Tb.Sp), brighter colours represent the larger separation between trabeculae.

- **Trabecular number (Tb.N)**: this is the ratio between the bone volume fraction (BV/TV) in the VOI and the trabecular thickness (Tb.Th), such as presented in Equation 6.14, and is expressed in mm^{-1}.

$$Tb.N = \frac{BV/TV}{Tb.Th} \qquad (6.14)$$
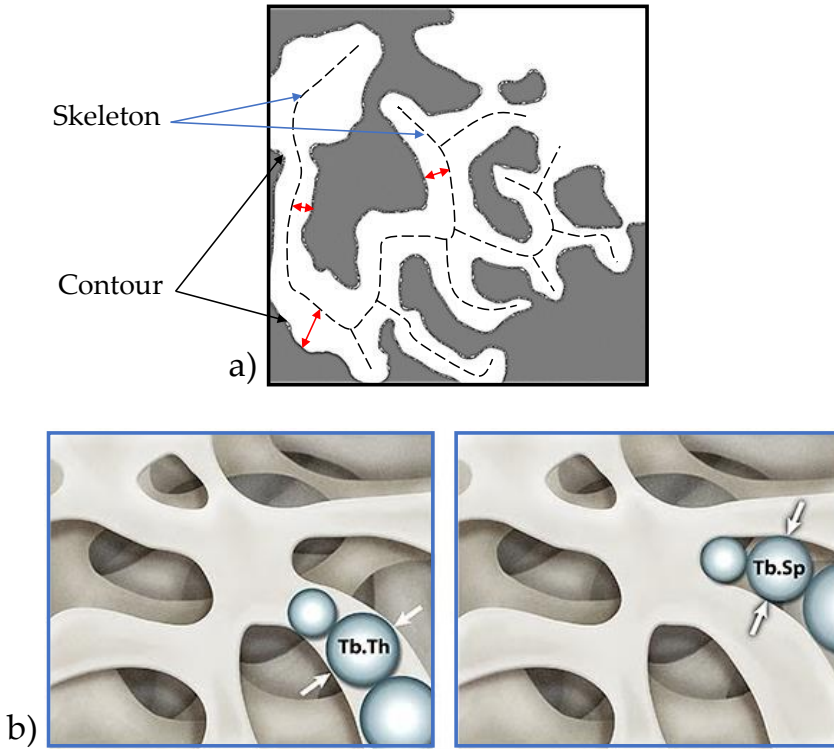
Figure 6.8: a) The contour and skeleton of a cancellous bone sample and b) procedures to determine the mean trabecular thickness, Tb.Th (left) and mean trabecular separation, Tb.Sp (right). Image a) taken from [362] and image b) extracted from [363].

6.3.3.1 Morphometric results of the healthy, osteoarthrosic and osteoporotic cancellous bone specimens

The aforementioned defined morphometric parameters have been evaluated for twenty-one cancellous bone samples divided into four healthy (HG), eight osteoarthrosic (OA), and nine osteoporotic (OP). The analysed morphometric parameters have been determined using the software ImageJ and BoneJ. We have carried out a statistical ANOVA analysis for every morphometric parameter to determine if the obtained results are statistically different between groups and if it is possible to differentiate each group according to each parameter. Table 6.5 collects the morphometric parameters results with the mean value and the standard deviation and the results of the ANOVA statistical analysis, that indicates significant differences between groups.

a) Tb.Th   b) Tb.Sp
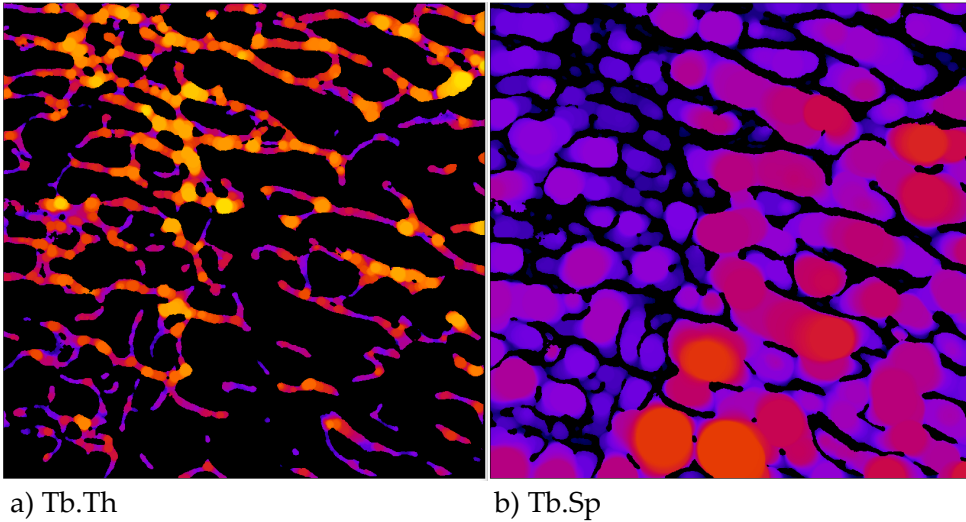
Figure 6.9: Same slice of the segmented mask of a cancellous bone sample obtained at BoneJ. a) Mean trabecular thickness (Tb.Th) and b) mean trabecular separation (Tb.Sp).

Figure 6.10 presents the results of the degree of anisotropy (DA), connectivity density (Conn.D), fractal dimension (D) and bone volume fraction (BV/TV) for the three study groups. In this study, we have obtained DA $= 1 -$ long axis eigenvalue / short axis eigenvalue, which means that values close to 0 indicate an isotropic distribution and 1 an anisotropic distribution. Most of the results are in the range of 0.45 to 0.55, indicating the preferred oriented direction for each cancellous bone sample. It seems that OA is the least anisotropic distributed group, but it is important to consider that in some cases the samples have calcified regions, which are translated to denser regions. This can be one of the factors that lead to these results in the OA group. Regarding HG and OP, the latter seems to present higher values. The ANOVA analysis revealed significant differences between OA and OP.

Concerning connectivity density results, the highest values are presented by the OA specimens. The ANOVA analysis revealed significant differences between HG and OA, 41.27 % higher for the OA samples. The statistical analysis for the fractal dimension D shows differences between HG and OA cancellous specimens specimens.

Ending with the results depicted in Figure 6.10, the bone volume fraction is one of the most common analysed parameters. In this case, the trend is as

Table 6.5: Morphometric results presented as mean values and standard deviation for human cancellous specimens belonging to the three study groups HG, OA and OP. The ANOVA analysis column determines which groups have statistically significant differences, presenting the p-value < 0.05.

Morphometric parameters	HG	OA	OP	ANOVA analysis
Degree of anisotropy (-)	0.525 ± 0.073	0.465 ± 0.049	0.434 ± 0.064	OA-OP
Connectivity density (mm^{-3})	4.72 ± 2.38	8.04 ± 2.14	6.14 ± 1.34	HG-OA
Fractal dimension (-)	2.48 ± 0.05	2.51 ± 0.02	2.45 ± 0.02	OA-OP
Bone volume fraction (%)	25.20 ± 3.99	21.78 ± 3.39	17.94 ± 2.97	HG-OP OA-OP
Surface ratio (mm^{-1})	15.05 ± 1.59	18.76 ± 2.59	19.36 ± 2.73	HG-OA HG-OP
Mean trabecular thickness (mm)	0.217 ± 0.024	0.177 ± 0.020	0.177 ± 0.025	HG-OA HG-OP
Mean trabecular separation (mm)	0.728 ± 0.102	0.749 ± 0.032	0.811 ± 0.088	-
Trabecular number (mm^{-1})	1.18 ± 0.19	1.23 ± 0.11	1.02 ± 0.11	HG-OP OA-OP

expected. The higher values of the BV/TV are for healthy (HG) specimens and the lowest for OP. It is important to highlight that the specimens have, as far as possible, the same dimensions. Table 6.6 shows the results for the total volume (TV), and it is possible to appreciate that the mean values are almost equal. The ANOVA results support that evidence because TV results do not present differences. Therefore, the differences are observed in the quantity of bone, as can be recognised in Figure 6.12 in BV graph. BV/TV presents statistical differences between HG-OP and OA-OP, which means that with this morphometric parameter, it is possible to distinguish an osteoporotic specimen from the other two. HG presents 28.81 % more bone volume fraction than the osteoporotic samples, whereas OA specimens are only 13.61 % lower than HG.

Figure 6.11 shows the other morphometric parameters analysed: surface ratio (BS/BV), mean trabecular thickness (Tb.Th), mean trabecular separation (Tb.Sp) and trabecular number (Tb.N). The surface ratio (BS/BV) presents the opposite trend to BV/TV, which is logical given the results. The ANOVA analysis results presented in Table 6.6 state that no significant differences exist in BS results. Then, if BS is almost the same and bone volume is different, being the lowest values for OP, BS/BV present totally the opposite trend.
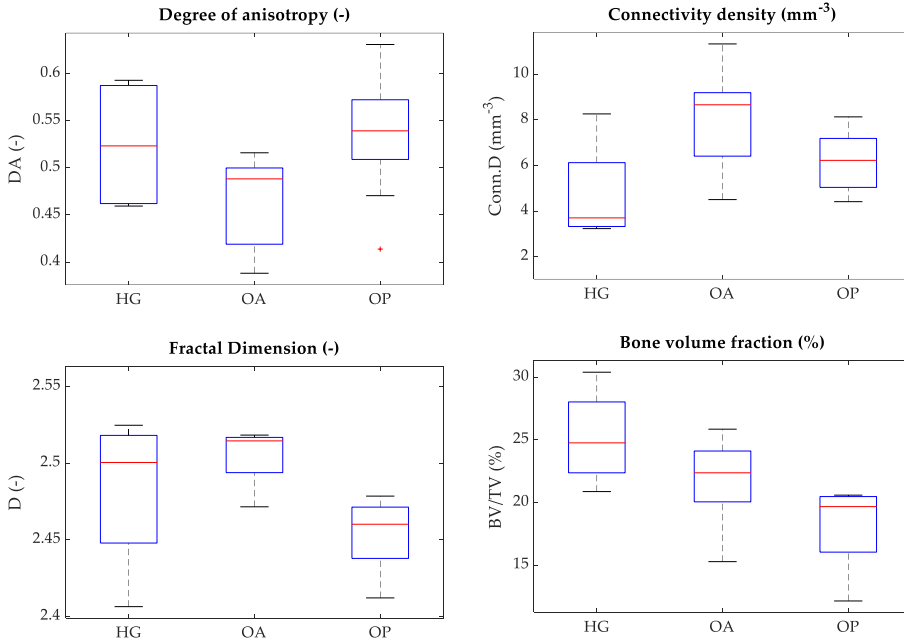
Figure 6.10: Degree of anisotropy (DA), connectivity density (Conn.D), fractal dimension (D) and volume fraction (BV/TV) results obtained from HG, OA an OP cancellous bone samples.

The ANOVA analysis of BS/BV concludes that there are differences between HG-OA and HG-OP, which means that this morphometric parameter can be used to distinguish healthy specimens from pathological specimens. This can be really useful in clinical diagnosis.

Regarding the trabecular parameters, the mean trabecular separation (Tb.Sp) does not present differences between groups. The mean trabecular thickness (Tb.Th) presents the highest values for HG, and similar lower values for both OA and OP. The ANOVA highlights this difference by stating statistical differences between HG and the pathological groups. Hence, this morphometric parameter is helpful in distinguishing between healthy and pathological cancellous bone samples. HG has a mean thickness of 217 μm, whereas OA and OP have 176.49 and 176.60 μm, respectively, which results in a thickness difference of 18.43 % between healthy and pathologic groups. Finally, the lowest values for the trabecular number (Tb.N) are manifested in OP specimens. This parameter presents significant differences between OP and the other two groups,
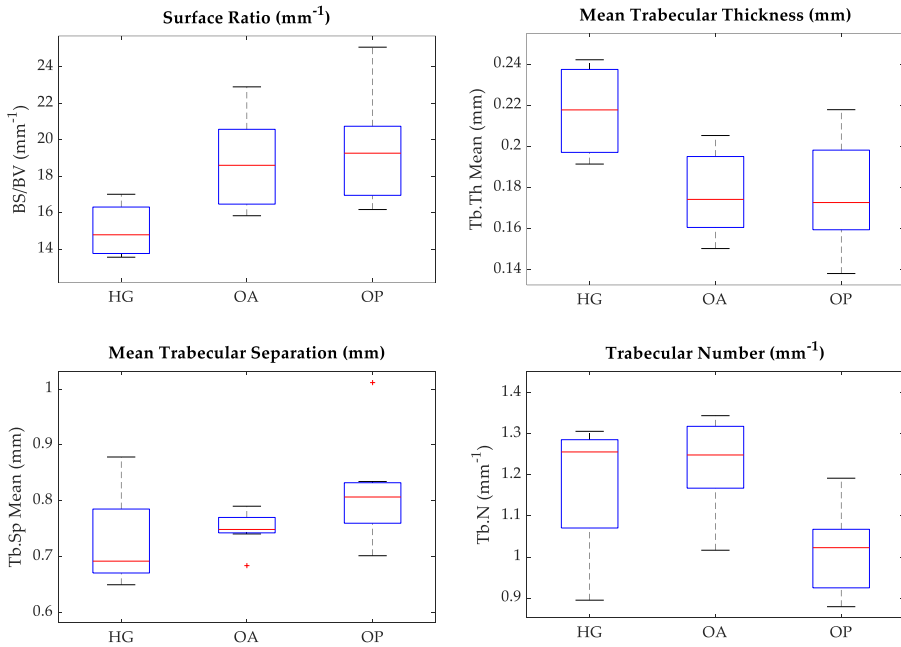
Figure 6.11: Surface ratio (BS/BV), mean trabecular thickness (Tb.Th), mean trabecular separation (Tb.Sp) and trabecular number (Tb.N) results obtained from HG, OA an OP cancellous bone samples.

leading to the ability to distinguish the osteoporotic cancellous samples from the other two groups. The highest values are registered for OA samples, which are 17.21 % higher than OP values.

Figure 6.12 and Table 6.6 show the microarchitectural parameters that are bone volume (BV), surface area (BS) and total volume (TV) of human cancellous bone. They can also be classified as morphometric parameters, but they have been employed to determine other more relevant parameters, such as BV/TV or BS/BV. For this reason, we present them apart from the analysed morphometric parameters.

Several researchers have analysed cancellous bone morphometry [20,21]. They study rheumatoid arthritis (RA), OA, OP and control specimens from femoral heads, and stated some similar conclusions, such as they do not find differences between groups in morphometric parameters such as DA, fractal dimension (D), connectivity density (Conn.D) or mean trabecular separation

Table 6.6: Microarchitectural properties presented as mean values and standard deviation for bone volume (BV), surface area (BS) and total volume (TV) used to estimate some of the morphometric parameters. The ANOVA analysis column determines which groups have statistically significant differences, presenting the p-value < 0.05.

Microarchitectural properties	HG	OA	OP	ANOVA analysis
Bone volume (mm^3)	715.98 ± 11.56	627.99 ± 166.41	486.68 ± 81.70	-
Surface area (mm^2)	10767.39 ± 1081.45	11582.93 ± 2567.80	9480.09 ± 2291.22	-
Total volume (mm^3)	2857.72 ± 354.87	2915.55 ± 748.86	2797.38 ± 739.86	HG-OP OA-OP

(Tb.Sp). Li *et al.* [306] studied OP and different stages of OA and presented similar values for trabecular thickness for OP and OA in the first and medium stages. Montoya *et al.* [190] analyse OA and OP patients with hip fractures and present similar values for Tb.N and Tb.Th to ours.
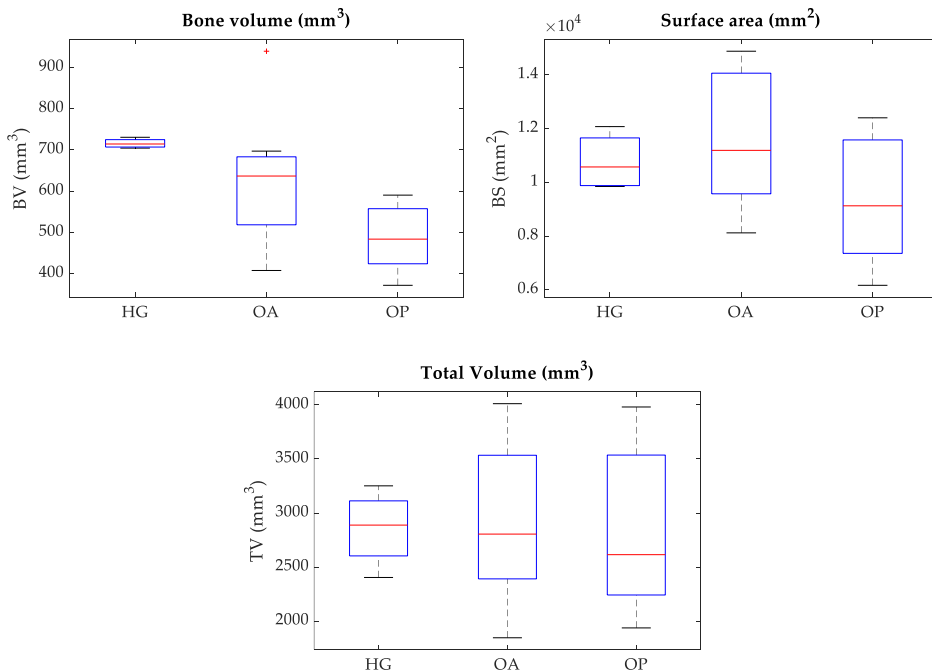
Figure 6.12: Bone volume (BV), bone surface (BS) and total volume (TV) results obtained from HG, OA an OP cancellous bone samples.

To sum up, this section has reflected the need to study the morphometry of bone because of the complete information we can extract about the architectural state of bone. The results and some parameters have been analysed, such as BV/TV or Tb.Th, permit to evaluate the degeneration of the cancellous architecture. The stage of the microarchitecture directly influences the apparent level mechanical results that will be presented in the following section. Lastly, we have carried out a statistical analysis ANOVA of the results and we conclude that the best morphometric parameters to distinguish between healthy and diseased bone specimens are the surface ratio (BS/BV) and the mean trabecular thickness (Tb.Th). Furthermore, both the trabecular number (Tb.N) and the bone volume fraction (BV/TV) permit to differentiate osteoporotic specimens from the other groups.

6.4 Compression mechanical characterisation of human cancellous bone specimens

This section presents the results concerning the experimental tests where the cancellous specimens were subjected to quasi static compression loads. In the first instance, we tested the three orthogonal directions of the cancellous samples in the elastic range. Then, we applied compression load levels until fracture in one of the three orthogonal directions. We tested the samples in two rounds, where the first batch of specimens was tested until fracture in the stiffest direction, whereas the last batch was tested in the largest direction.

The specimens were stored in a freezer at -20 ℃ until the day before they were tested. Cancellous samples were defrosted around 12-24 hours before the tests and kept them at 4-6 ℃. The compression tests were carried out in an electromechanical testing machine MTS Criterion C42 (MTS Systems, USA), with aluminum compression platens (see Figure 6.13 a). The quasi static tests were conducted using a displacement control with a 1 mm/min speed. A contact deflectometer (MTS ref.:632.06H-20) was employed to measure the displacement between both compression platens as shown in Figure 6.13 b.

Prior to the tests, we applied a preload between 10 and 20 N to ensure that both compression platens touch both sides of the specimen entirely. During the tests, we recorded the displacement u using the contact deflectometer and the applied force by the testing machine F.

Derived from the registered response, we can deduce the stress-strain curve, which allows the study of the mechanical behaviour of the cancellous bone samples. Regarding the elastic range tests, we can obtain the apparent elastic
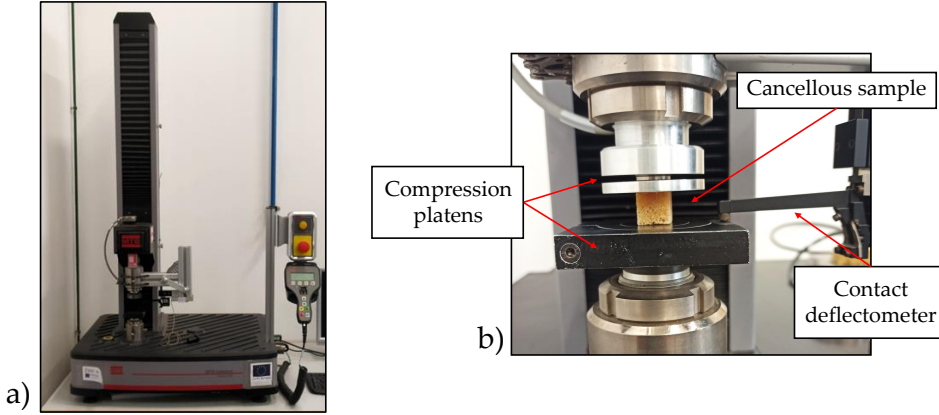
Figure 6.13: a) Electromechanical testing machine MTS Cirterion C42 and b) assembly employed to perform the quasi static compression tests.

modulus (E_{app}) of each orthogonal direction, whereas from the fracture compression tests, we can calculate the final stress (σ_{f}) and the strain (ε_{f}) reached at the final stress. We will also calculate E_{app} from the fracture test to analyse any difference from the test method.

6.4.1 Apparent elastic modulus (E_{app}) estimation

The elastic apparent modulus (E_{app}) has been obtained for eighteen cancellous bone samples: six healthy (HG), six osteoarthrosic (OA) and six osteoporotic (OP). The compression elastic tests consist of 10 cycles of a load level within the elastic range. The minimum and maximum displacement applied at each cycle depends on the tested dimension, as in Equation 6.15 and 6.16.

$$\text{Minimum displacement} = 0.003L_0 \qquad (6.15)$$

$$\text{Maximum displacement} = 0.015L_0 \qquad (6.16)$$

where L_0 is the dimension of the sample. As we obtained ten E_{app} results per sample, we have established that the average value of the elastic cycles will be the apparent elastic modulus of the sample. In addition, as we have conducted compression tests until fracture load levels, we want to compare both obtained

E_{app} to evaluate any differences between them. Table 6.7 presents the apparent elastic modulus for the three orthogonal directions obtained from both elastic cycles and fracture tests. As fracture tests are destructive, we only have this value for one of the three orthogonal directions. For the directions that we do not have, both E_{app} are combined to show the elastic test result.

It is observed that the apparent modulus in both transversal directions is predominately lower than the obtained values for the fracture direction. These findings agree with the results obtained in other research about cancellous bone [80]. Regarding the comparison between both E_{app} of the fracture direction, it is recognised that the prevailing trend is that the fracture tests results are higher than the elastic tests results. There are several explanations for the found evidences, such as the applied displacement implies a very low load level, which entails that E_{app} is evaluated in the lowest regions of the linear behaviour of the samples. On the contrary, the apparent modulus of the fracture direction is evaluated in the medium or high region of the linear elastic behaviour range of the samples, once the cycles have finished. This hypothesis can explain the underestimation of the apparent elastic modulus when it is evaluated using the elastic tests. The variations presented by the apparent elasticity modulus of the fracture direction are around 1 - 30 %, and only in a few specific cases exceed this percentage.

Furthermore, it can be appreciated that in specific cases occurs the opposite and the E_{app} from the elastic tests is greater than the calculated at the fracture tests. It is essential to consider that in the experimental tests, there are several artifacts that can affect the tests and, hence, the results. At the beginning of the tests, it is possible that the sample was not completely in contact with both compression platens or in some samples, the applied load level triggered damage on the specimens. All these possibilities introduce variability in the results. In any case, it is possible to appreciate an overall trend.

Regarding the numeric values obtained for the apparent elasticity modulus (E_{app}) in the fracture direction, it can be appreciated that the highest values correspond to the healthy group (HG) and the lowest values correspond to the osteoporotic group (OP). It is essential to highlight that the architecture of the specimens directly influences these results. Therefore, it is reasonable to expect that the highest values emerge in HG specimens because they have a strong and non-degenerated architecture that grows optimally to support the mechanical loads. However, both OA and OP specimens have a degenerated structure, which causes a decrease in the apparent modulus. This expected trend is in line with the findings of Metzner *et al.* [364] and Homminga *et al.* [365].

Table 6.7: Apparent elastic modulus (E_{app}) for the three orthogonal directions for eighteen cancellous bone samples divided into six healthy (HG), six osteoarthrosic (OA) and six osteoporotic (OP). E_{app} results are regarding the elastic and fracture tests.

Sample	$E_x app$ (MPa)		$E_y app$ (MPa)		$E_z app$ (MPa)	
	Elastic tests	Fracture tests	Elastic tests	Fracture tests	Elastic tests	Fracture tests
HG - LCFB P1	762.64	1394.10	275.03		849.11	
HG - MPR P1	552.43		1055.32	1321.8143	615.95	
HG - MPR P2	330.20		720.26	887.25	175.60	
HG - MPR P3	290.75		730.73	1093.33	181.95	
HG - JIMA P1	543.65	680.93	370.63		334.40	
HG - JIMA P2	808.79		752.57	759.49	591.88	
OA - EHG P1	546.13	770.00	647.65		487.86	
OA - JJCM P1	561.68	845.30	270.40		287.75	
OA - JJCM P2	580.57	594.41	958.85		406.15	
OA - AMM P1	693.30	900.55	370.21		216.73	
OA- AMM P2	584.42	845.28	211.61		478.31	
OA - AFA P1	618.53		696.58		829.49	769.95
OP - FMF P1	412.98		515.98	388.72	299.87	
OP - FMF P2	112.04		343.63	237.78	146.49	
OP - MCRC P1	418.13		723.66	663.46	247.3	
OP - MCRC P2	1066.10	655.84	130.30		404.81	
OP - MADL P2	660.44		661.40	570.42	339.78	
OP- JLO P1	240.46		645.86	785.44	153.93	

In OA specimens, we can find both extremes because of the different stages of the disease. On the one hand, at the beginning of the disease, the patient experiences a negative balance in the remodelling cycle, which leads to a thinning of the trabeculae. On the other hand, in the final stages, an increase in bone material deposition produces a thickening of bone architecture. Considering these two stages of the OA, we can find higher or lower results in this study group. Concerning the OP specimens, the disease triggers a devastating degeneration of bone architecture, leading to weakness and high fragility of the bone structure. In addition, owing to the high misalignment in the bone remodelling cycle, in the most severe cases, the disease causes high levels of porosity, that the bone architecture seems to be gnawed, the so-called osteoclastic perforation. Apparent modulus of elasticity obtained from the fracture tests seems to be a better estimation than the results obtained from the elastic test. The main reason is because it is estimated in a higher area of the elastic behaviour of the specimens when the test is much more representative than in the cycles performed in the lowest region of the elastic behaviour range.

6.4.2 Compression mechanical behaviour of human cancellous bone up to failure

This section presents the results obtained from the compression tests up to fracture. The current findings correspond to twenty-three tested specimens, divided into six HG, eight OA and nine OP.
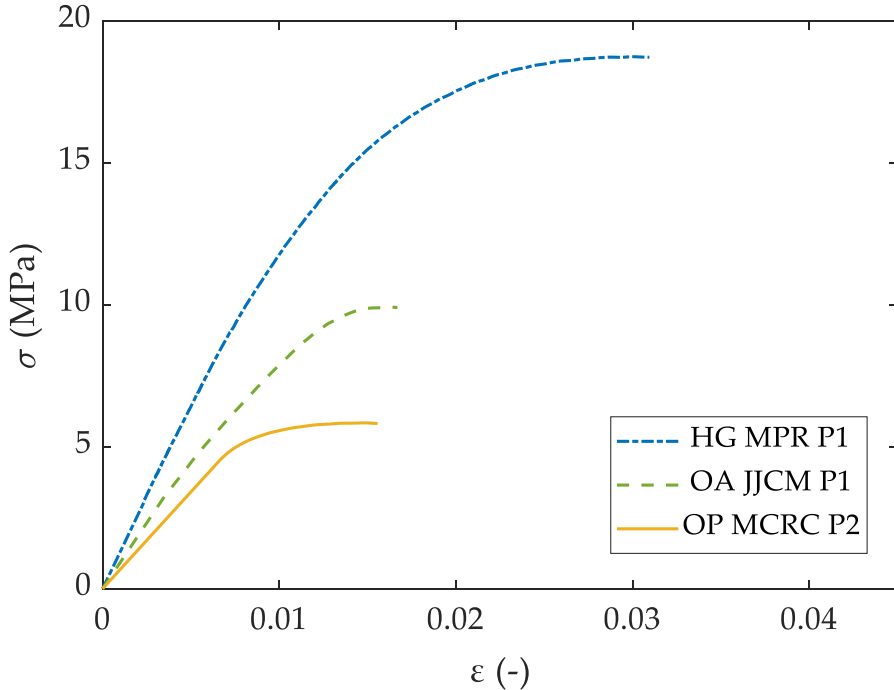
Figure 6.14: Exameples of compression stress-strain curves for each studied group. The healthy specimen (HG) is represented in blue by a dashed-dotted line, osteoarthrosic specimen (OA) is represented by a green dashed line and osteoporotic specimen (OP) is represented by a yellow continuous line.

Figure 6.14 depicts one stress-strain curve per study group to show the overall behaviour of each group. As expected, the healthy (HG) specimen is stiffer than the diseased specimens. Between pathology cancellous samples, the osteoarthrosic (OA) specimen can withstand a higher stress level than the osteoporotic (OP) bone sample. It is important to consider that the apparent behaviour of the cancellous specimens is directly related to the bone architecture features.

The results obtained from the compression tests are presented in Table 6.8 including the mean value and the standard deviation. These results concern six healthy, eight osteoarthrosic and nine osteoporotic cancellous bone samples. The highest values for the three obtained parameters from the mechanical response are registered for HG specimens, whereas the smallest are for OP. These evidences are directly related to the bone architecture conditions. In the healthy group (HG), the cancellous lattice is strong, thick and grows optimal to withstand the mechanical loads. However, both diseased groups have a degraded bone structure due to the pathology. The most severely affected specimens are the osteoporotic ones. When osteoporosis develops, not only do the struts reduce their thickness, triggering a great level of macro porosity in the bone structure. This pathology affects the balance of the bone remodelling cycle, depositing less material than the removed, leading to the emergence of large voids and holes that can be appreciated at the tissue level, such as shown in Chapter 3. The lamellar tissue is thoroughly gnawed in the harshest cases due to the high osteoclast activity, producing significant porosity levels.

Table 6.8: Results obtained from the compression experimental tests for the three main parameters obtained from the stress-strain curves: failure stress (σ_{f}), failure strain (ε_{f}) and the apparent elasticity modulus (E_{app}). The results are presented by the mean value and the standard deviation.

Group	σ_{f} (MPa)	ε_{f} (-)	E_{app} (MPa)
HG (n=6)	10.93 ± 4.57	0.024 ± 0.0070	1022.82 ± 295.58
OA (n=8)	7.80 ± 2.50	0.016 ± 0.0047	876.25 ± 277.15
OP (n=9)	6.18 ± 1.65	0.018 ± 0.0033	645.47 ± 219.27

It can be seen that the results obtained for OA specimens are between HG and OP values, being closer to the last ones. It is crucial to consider the nature of the pathology. In the first stages of osteoarthrosis (OA), it is present a negative bone remodelling balance, like in osteoporosis, which triggers a bone mass loss. However, in the last stages, large quantities of bone material are deposited, so calcified areas arise. This explains why OA cancellous specimens can withstand higher stress levels than OP.

HG human cancellous specimens can withstand stress levels of 43.46 % more than OP samples, considering the mean values of Table 6.8. Because of the degraded OP microarchitecture, HG cancellous lattice can withstand nearly the double level of stress, which is relevant considering possible bone fractures. Compared to OA specimens, HG can withstand 28.63 % higher stress levels. E_{app} results show the same trend as the final stress. HG specimens registered

a mean value of E_{app} of 1022.82 MPa, which, compared with OA and OP, is 14.33 % and 36.91 % higher, respectively. In the case of the failure strain (ε_f), the results are more differentiated between healthy and diseased groups. OA and OP exhibit 0.016 and 0.018 for the mean values, respectively, showing a little difference of 11 % between them. However, HG presents a larger mean value, 0.024, which is 33.33 % greater than for OA cancellous samples. These results manifest that HG specimens deform much more before they suffer the final catastrophic failure than both pathologic groups OA and OP.
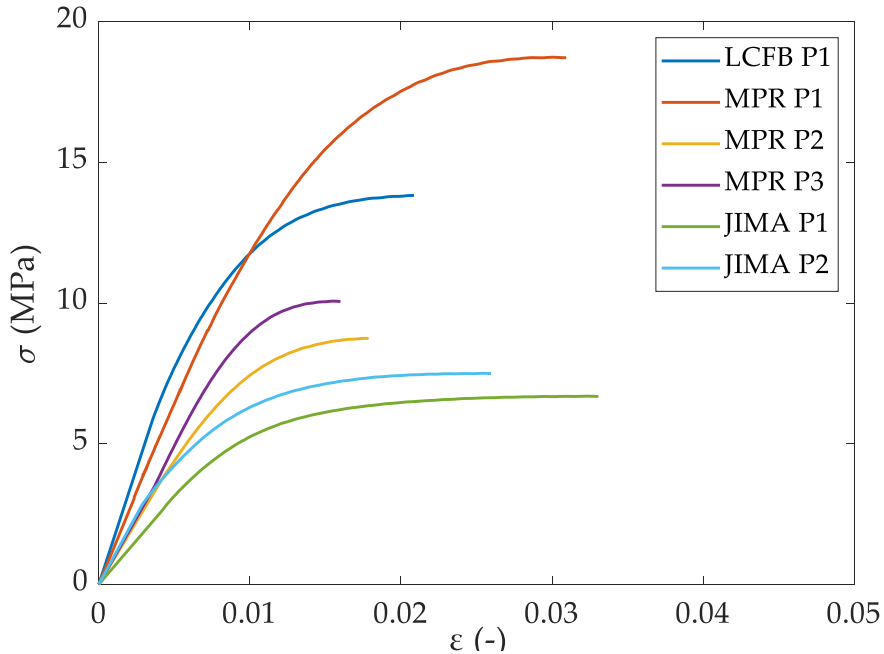
Figure 6.15: Compression stress-strain curves for the six healthy (HG) tested specimens.

Furthermore, we have developed an ANOVA statistical analysis of the results to analyse if there are significant differences between the obtained results for the three groups. We found statistical differences between HG and OP for the failure stress (σ_f) and the apparent modulus of elasticity (E_{app}). However, the failure strain (ε_f) presents significant differences with both OA and OP. This statistical analysis reveals that the stress components (E_{app}, σ_f) allow to distinguish between healthy and osteoporotic cancellous samples, whereas the strain component (ε_f) permits to differentiate healthy specimens from the diseased samples.
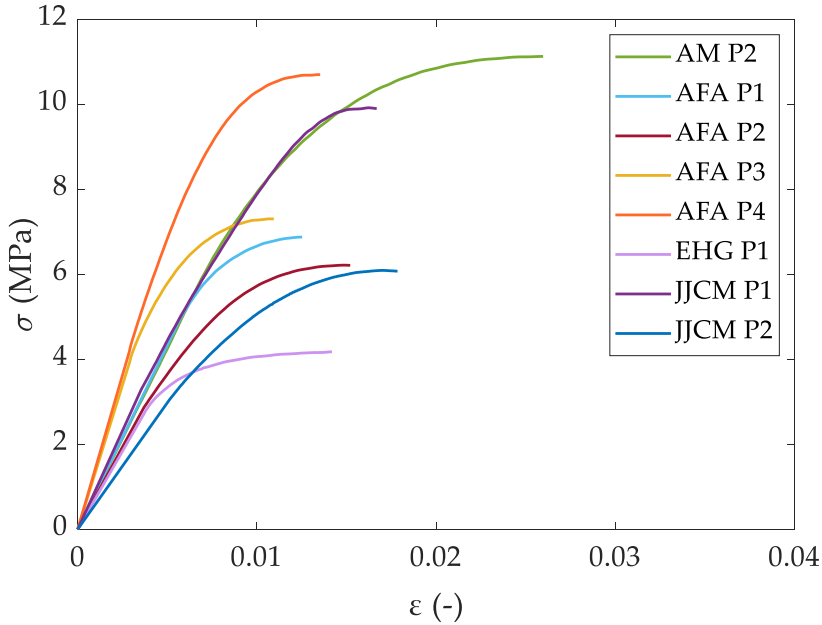
Figure 6.16: Compression stress-strain curves for the eight osteoarthrosic (OA) tested specimens.

We have reviewed other works to compare our results, and we found that some authors, such as Morgan and colleagues [202], registered for the femoral neck values for the apparent Young's modulus for healthy specimens between 500 and 1200 MPa. Regarding diseased specimens, Sun *et al.* [366] presented values for the apparent Young's modulus for OP specimens around 580 MPa and around 950 MPa for OA. These results are quite similar to the ones that we have measured. Finally, Ding and Overgaard [21] provided failure stress values of 17.36 ± 4.36 MPa for HG, 9.81 ± 5.50 MPa for OA and 5.88 ± 1.56 MPa for OP. Their HG results are greater than ours, but both OP and OA agree with our findings.

Figures 6.15 to 6.17 show the compression stress-strain curves of the HG, OA and OP tested specimens. Some specimens have less failure strain than others, e.g. in Figure 6.15 sample MPR P3 compared to JIMA P2. Once sample MPR 3 reaches the maximum stress, it fails without a significant strain level; however, sample JIMA P2 presents greater strain levels before reaching the final stress. These differences between specimens of the same study group can

also be observed in Figure 6.16 with samples AFA P4 and EHG P1 and in Figure 6.17 between samples ESR P2 and FMF P1.
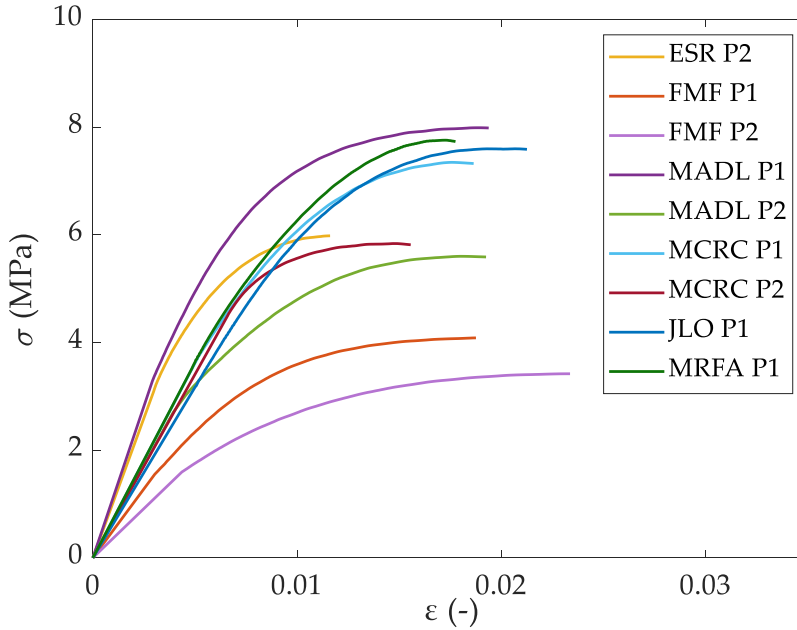
Figure 6.17: Compression stress-strain curves for the nine osteoporotic (OP) tested specimens.

Lastly, in Figures 6.15 to 6.17, it is possible to appreciate the behavior differences between samples of the same group. At first sight, differences in the stiffness between specimens can be seen, whereas the most remarkable variation is in the failure stress levels. For HG samples, the failure stress range is from 5 MPa to around 17 MPa, for OA specimens ranges from less than 4 MPa to 11 MPa, and for OP the results go from around 3 MPa to 8 MPa. It is interesting to note that the interval is reduced from the healthy samples to the osteoporotic specimens.

6.5 Correlation between morphometric parameters and apparent properties of human cancellous bone

In the previous sections 6.3.3.1 and 6.4.2, we have stated the relevance of studying the morphometry of bone because of the amount of information that we can extract to understand the mechanical bone behaviour, especially in bone diseases when the microarchitecture changes. The apparent properties of bone are usually obtained during the experimental tests or through density estimation, namely compression properties due to the nature of the applied load. These properties are directly influenced by bone structure. Therefore, we would like to study the relationship between the morphometric parameters and the mechanical response of bone. The main goal is to assess which morphometric parameters are more significant to the mechanical behaviour of cancellous bone.

Table 6.9: Results of the Pearson correlation coefficient (R^2) of the linear regression calculated between morphometric and elastic and failure parameters for human cancellous bone. These results are considering the three study groups together: HG, OA and OP.

	Correlation coefficient (R^2)		
	σ_{f}	ε_{f}	E_{app}
DA	0.041	0.017	0.029
Conn.D	0.005	0.004	0.026
D	0.261	1.16E-05	0.320
BV	0.008	0.041	0.039
BS	0.0002	0.079	0.054
BV/TV	0.179	0.010	0.099
TV	0.095	0.078	0.023
BS/BV	0.015	0.002	0.0002
Tb.Th Mean	0.003	0.005	0.049
Tb.Sp Mean	0.503	0.003	0.442
Tb.N	0.421	0.008	0.465
σ_{f}	1	0.390	0.403
ε_{f}	sym.	1	0.012
E_{app}	sym.	sym.	1

In this section, twenty-two human cancellous samples have been studied. The specimens were divided into six HG, seven OA, and nine OP. This analysis

has a limitation regarding the number of the studied cancellous specimens. It is evidenced that there are few specimens, but it is essential to appreciate the difficulty of obtaining human specimens from three different types. The established relationships should be confirmed in further studies with a large amount of specimens.

We have confronted the morphometric parameters with the elastic and failure properties obtained from the compression tests. In addition, we have included the correlation coefficient of the elastic and failure properties themselves. Tables 6.9 and 6.10 collect the results obtained for the Pearson correlation coefficient (R^2). The strong correlations, those with p-value < 0.05, have been marked in bold.

Firstly, we have analysed all the studied groups together. In this case, we do not obtain a strong influence between results, as observed in Table 6.9. The reason could be due to the vast differences between the cancellous microarchitecture of the groups. Therefore, in the following analyses each group has been evaluated individually.
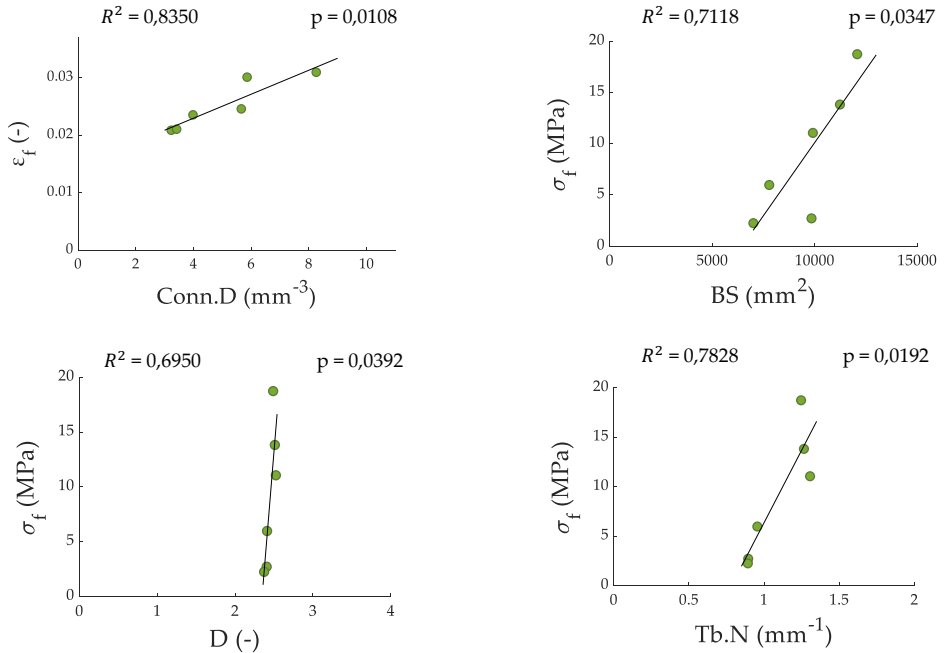
Figure 6.18: Significant correlations (p-value < 0.05) between morphometric parameters and the mechanical response for HG cancellous specimens.

The results for the Pearson correlation coefficient (R^2) for each group are presented in Table 6.10. The significant correlations, those with p-value < 0.05, are marked in bold. For HG specimens, the failure stress σ_f shows strong relationships with bone surface BS, the trabecular number Tb.N and the fractal dimension D. In addition, failure strain ε_f correlates with the connectivity density Conn.D (see Fig. 6.18).

Regarding OP specimens, it has been found correlations with the same morphometric parameters for both σ_f and E_{app} (see Figure 6.19). The relationships are presented with the trabecular separation Tb.Sp and the trabecular number Tb.N. It can be appreciated that the OP samples that reach higher stress levels exhibit greater trabecular number and lower trabecular separation. This means that the specimens with better structure can withstand large stress levels, while the samples with the most degraded microarchitecture can reach lower stress levels. The same trend is presented for the apparent Young's modulus.
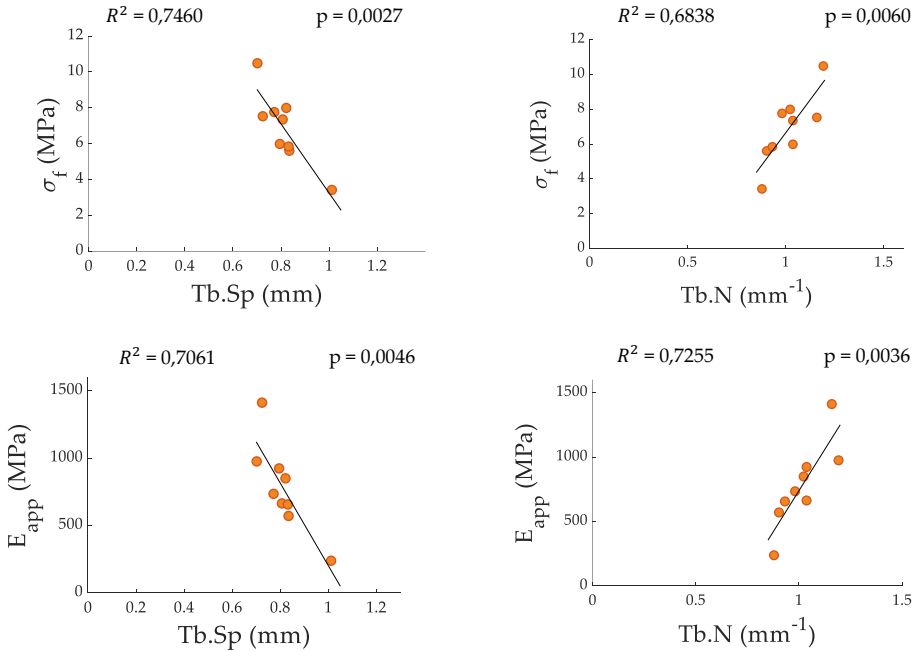
Figure 6.19: Significant correlations (p-value < 0.05) between morphometric parameters and the mechanical response for OP cancellous specimens.

Table 6.10: Results of the Pearson correlation coefficient (R^2) of the linear regression calculated between morphometric and elastic and failure parameters for human cancellous bone. These results are presented individually for each group: HG (n=6), OA (n=7) and OP (n=9). Significant correlations (p-value < 0.05) are marked in bold.

	Correlation coefficient ($\mathbf{R^2}$)								
	σ_f			ε_f			E_app		
	HG	OA	OP	HG	OA	OP	HG	OA	OP
DA	0.292	0.537	0.116	0.289	0.597	0.002	0.038	0.003	0.0007
Conn.D	0.135	0.036	0.007	**0.835**	0.002	0.044	0.057	0.034	0.007
D	**0.695**	0.088	0.121	0.058	0.001	0.118	0.461	0.460	0.322
BV	0.379	0.507	0.188	0.197	0.607	0.012	0.249	0.016	0.065
BS	**0.712**	0.512	0.0005	0.019	0.625	7.08E-06	0.624	0.014	0.0008
BV/TV	0.407	0.009	0.527	0.176	0.004	0.058	0.184	0.128	0.328
TV	0.041	**0.701**	0.0882	0.076	0.610	0.030	0.085	0.026	0.089
BS/BV	0.104	0.039	0.271	0.452	0.037	0.018	0.034	0.0003	0.110
Tb.Th	0.010	0.124	0.072	0.479	0.092	0.010	0.002	0.020	0.006
Tb.Sp	0.629	0.057	**0.746**	0.025	0.057	0.444	0.364	0.280	**0.706**
Tb.N	**0.783**	0.386	**0.684**	0.004	0.084	0.319	0.516	0.586	**0.725**
σ_f	1			0.528	**0.727**	0.072	**0.804**	0.192	0.405
ε_f	sym.			1			0.179	0.005	**0.693**
E_app	sym.			sym.			1		

Osteoarthrosic (OA) cancellous specimens present just one correlation between the failure stress σ_f and the total volume of the samples TV. This lack of strong correlations could be related to the huge differences in the microarchitecture between the specimens of this group. This bone disease has two differentiated stages. In the first one, it is presented a negative bone remodelling cycle where a bone loss mass occurs. However, in the later stages, there is an overproduction of material leading to regions with high concentrations of mineral.

These large variations in the trabecular structure of the samples may be the reason why it is more difficult to correlate morphometry and mechanical response in this group.
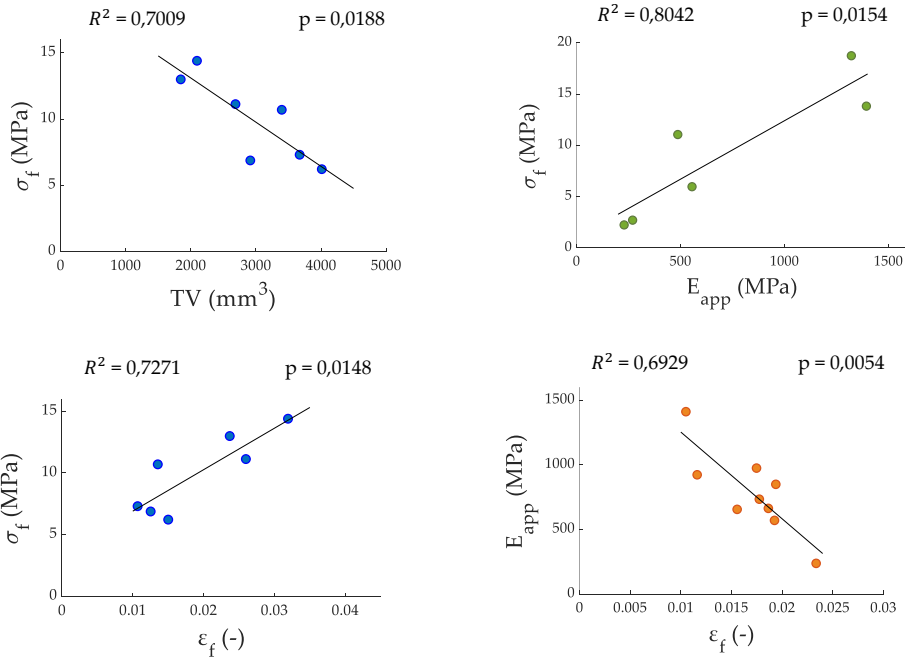
Figure 6.20: Significant correlations (p-value < 0.05) between morphometric parameters and the mechanical response for OA cancellous specimens and relationships between the mechanical response parameters between themselves (HG is represented in green, OA in blue and OP in orange).

Finally, we have also correlated the mechanical response parameters between themselves. We have found one correlation per group, as seen in Figure 6.20. HG present a significant correlation between the apparent Young's modulus

and the failure stress. This correlation enables to estimate the failure stress with the apparent Young's modulus. For OA specimens, the relationship is obtained between the failure stress and the failure strain. It can be seen that for higher stress levels the cancellous samples fail at large strains. These results manifest that OA specimens have ductile behaviour. Regarding OP samples, the relationship found is between the apparent Young's modulus and the failure strain. It is evidenced that for greater apparent modulus the samples fail at lower strain levels. This means that the disease embrittles the cancellous specimens.

The correlations obtained in this section allow the estimation of the mechanical response using the micro-CT images. Thus, the experimental tests would not be necessary to obtain the mechanical behaviour of cancellous bone. In addition, the relationships between the mechanical response parameters themselves have manifested the behaviour of each group, being more ductile or brittle depending on the pathology.

6.6   Numerical modelling and calibration of the elastic and failure properties of human cancellous bone

This section presents the finite element (FE) models generated to estimate the elastic and failure properties of healthy and diseased cancellous bone specimens. The numerical models reproduce the elastic and failure behaviour of the cancellous bone samples. The models have a high degree of discretisation, allowing us to define the cancellous bone architecture accurately.

6.6.1   Finite element model generation and failure criterion

The FE models were generated from the μ-CT images, which allows us to obtain the architecture of the cancellous specimens. The FE meshes were developed using ScanIP software (Simpleware, UK), leading to meshes with approximately between 5.6M and 10.7M nodes, which implies between 2.69M and 6.03M quadratic tetrahedral elements (C3D10 in Abaqus).

To generate the numerical models, we start with the segmentation of the μ-CT images, developed in Section 6.3.1. The next step is to generate the numerical models, carried out in ScanIP software in the FE module. Some of the relevant choices we made are the following: we use the coordinate system of the image (not the global one), and we define FE-free (not grid) and quadratic

tetrahedral elements. Once all the options are selected, we generate the full FE model, such as the one shown in Figure 6.21 (left).
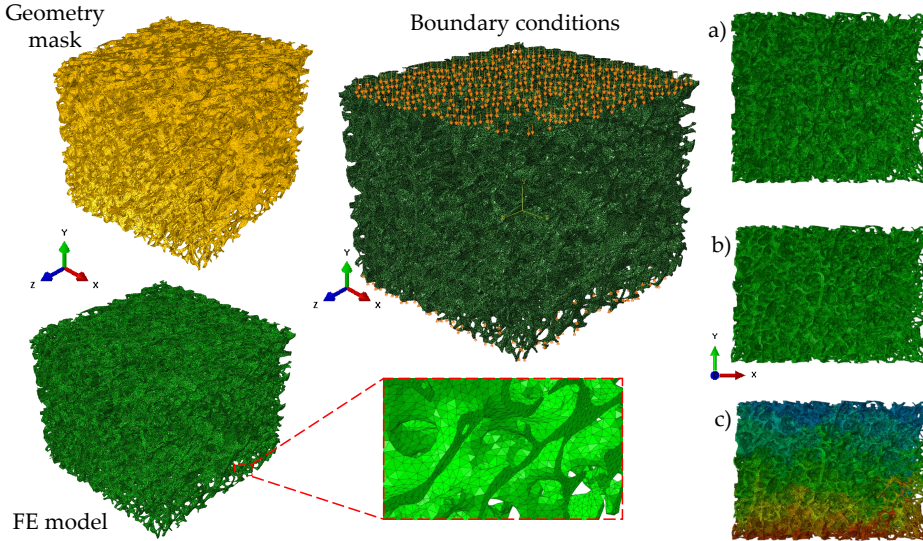
Figure 6.21: Finite elements models of the cancellous bone specimens. Mask with the cancellous microarchitecture obtained after image segmentation and finite element models meshed with quadratic tetrahedra (left). Boundary conditions were applied to the FE model to simulate the compression experimental tests (middle). a) Non-deformed FE model, b) deformed FE model after applying the compression load and c) displacement obtained after applying the compression load (right).

We have defined the behaviour of cancellous bone as a homogeneous isotropic linear-elastic material. Some researchers, such as Kabel *et al.* [367], stated that this assumption is enough to estimate the apparent stiffness of cancellous bone. Concerning boundary conditions, we define the appropriate ones to simulate the quasi static experimental compression tests. To this end, we prescribed a controlled displacement in the upper face nodes of each FE model, whereas the nodes of the opposite face of the applied displacement were constrained in the compression direction (see Fig. 6.21 middle). Some results of the numerical analyses were shown in Figure 6.21, such as the deformed shape of the cancellous sample or the displacement field shown in Fig. 6.21c.

An inverse analysis was carried out to estimate the elastic and failure properties. We have inferred values for the estimated parameters and made several iterations until the numerical response matches the experimental stress-strain curve. To calibrate Young's modulus at the tissue level, we captured the re-

sponse at the elastic range of the stress-strain compression curve. The other elastic parameter defined in the FE model is the Poisson's ratio, which was set to 0.3 for all the cancellous specimens [368]. Then, we must match the initial failure strain (ε_y), at the yield point, when the behaviour changes from linear-elastic to non-linear behaviour. The third calibrated parameter is the final fracture strain (ε_f), which corresponds to the value when the cancellous samples collapse and fail. In order to study cancellous bone damage, we have to define a failure criterion. In this thesis, we have used a failure criterion based on the equivalent strain.

In this research, the modeling of compression failure follows the principles of continuum damage mechanics. Within the context of a continuum damage methodology, modelling failure involves the degradation of the mechanical properties upon reaching critical values. This is achieved by implementing an Abaqus user's subroutine (USDFLD), where material degradation is incorporated to simulate the gradual reduction in stiffness resulting from the propagation of microcracks and porosity voids. The variations in the microarchitecture result in material stiffness degradation, which is evidenced at the macroscale [369]. The process of bone failure is controlled by strains, as documented in [74,370], and thus, our methodology relies on an equivalent strain (ε_{eq}).

Lemaitre [311] described the elastic isotropic relationship within the context of damage mechanics in the quasi-static domain:

$$\sigma_{ij} = (1 - D)C_{ijkl}\varepsilon_{kl} \tag{6.17}$$

where D is defined as the damage variable, C_{ijkl} is the constitutive elastic tensor, σ_{ij} and ε_{kl} are the stress and strain tensors, respectively. In accordance with Hambli works [97,210], we consider an isotropic damage law at the tissue level, which is empirically fitted and can be formulated as follows:

$$D = \begin{cases} 0 & \varepsilon_{eq} \leq \varepsilon_{y,c} \\ D_c(\frac{\varepsilon_{eq}}{\varepsilon_{f,c}})^n & \varepsilon_{y,c} < \varepsilon_{eq} < \varepsilon_{f,c} \\ D_c & \varepsilon_{eq} \geq \varepsilon_{f,c} \end{cases} \tag{6.18}$$

based on an equivalent strain, following Equation 6.19.

$$\varepsilon_{eq} = \sqrt{\frac{2}{3}\varepsilon_{ij}\varepsilon_{ij}} \tag{6.19}$$

In this study of cancellous bone specimens, we have defined the damage at compression fracture D_c as 0.95 [212, 213] and the damage exponent n as 2 [107] following the literature.

To mitigate the influence of mesh dependency on damage propagation, we implemented a linear weighting strategy for the strain at fracture. This weighting is based on the characteristic micro-FE length (L_{FE}) and the characteristic crack length specific to cancellous bone (L_{frx}), presented in Equation 6.20. The L_{FE} is calculated iteratively for each element throughout the simulation using Abaqus. The average crack lengths documented in the literature for cancellous bone fall within the range of 50 to 100 microns. Therefore, we choose the characteristic crack length as $L_{\text{frx}} = 0.075$ mm [371, 372]. Consequently, in the FE models, the failure strain (ε_{f}) at each element will be considered as follows:

$$\varepsilon_{\text{f}} = \varepsilon_{\text{f,c}} \left(\frac{L_{\text{frx}}}{L_{\text{FE}}} \right) \tag{6.20}$$

6.6.2 Elastic and failure properties using FE models for healthy and diseased human cancellous specimens

Table 6.11 summarises the mean values and the standard deviation of the calibrated Young's modulus (E_{cal}), the yield strain (ε_{y}) and the failure strain (ε_{f}). Seventeen cancellous bone samples have been calibrated, divided into six HG, six OA and seven OP. Regarding E_{cal}, which is Young's modulus at the tissue level, the results are in the range between 18053.82 and 20056.05 MPa (considering the average values of each group). The ANOVA analysis revealed that there was no significant difference between groups, which means that the mineral content at the tissue level is the same, even for both pathologies considered.

Table 6.11: Calibration of the elastic and failure properties of the HG, OA and OP cancellous bone specimens. Results of the calibrated elastic modulus (E_{cal}), yield strain (ε_{y}) and failure strain (ε_{f}) are presented as mean values with corresponding standard deviations.

Group	E_{cal} (MPa)	ε_{y} (-)	ε_{f} (-)
HG (n=6)	20056.05 ± 8149.47	0.0059 ± 0.0014	0.054 ± 0.017
OA (n=6)	18053.82 ± 6400.84	0.0051 ± 0.0025	0.035 ± 0.021
OP (n=7)	19181.89 ± 5169.33	0.0046 ± 0.0012	0.025 ± 0.020

Farlay *et al.* [373] investigated bone remodelling and bone matrix quality before and after menopause. They concluded that after menopause, there was not a variation in the degree of mineralisation (DMB) in the entire bone. They stated that bone preserves an optimal global DMB, maybe trying to offset the bone loss and the focal changes in the bone mineral matrix, with the final mission to optimise bone strength. An optimal balance between the area of new/interstitial bone could be adjusted, resulting in the preservation of a stable DMB.

Figure 6.22: Compression stress-strain curves from the experimental tests (continuous line) and the numerical calibration (dashed lines) for specimens of the healthy group (HG).

Morgan *et al.* [202] assessed the tissue modulus for the femoral neck, proximal tibia and greater trochanter. To compare similar skeletal locations, their results for the femoral neck were around 23 GPa, and they compared it with the obtained results of Kabel *et al.* [96] and Yang *et al.* [374], which were 17 GPa

and 27 GPa, respectively. Bayraktar *et al.* [95] obtained for human femoral neck values of tissue Young's modulus of 18 ± 2.8 GPa. Chevalier *et al.* [84] registered for human proximal femur values between 19.6 and 22.3 GPa, similar values as Smith *et al.* [375] whose results were 22.34 ± 3.01 GPa or Jirousek *et al.* [376] who obtained 16.34 ± 1.76 GPa. Finally, some authors find similar values for tissue Young's modulus both for healthy and osteoporotic femoral bone in agreement with our results, such as Carretta *et al.* [99], who state 16.24 ± 2.47 GPa for healthy specimens and 16.85 ± 2.1 GPa for osteoporotic samples. Tjhia *et al.* [356] obtained similar results both for HG and OP, for samples of the iliac crest, which were 15.6 ± 1.2 and 15.7± 1.3 GPa, respectively.
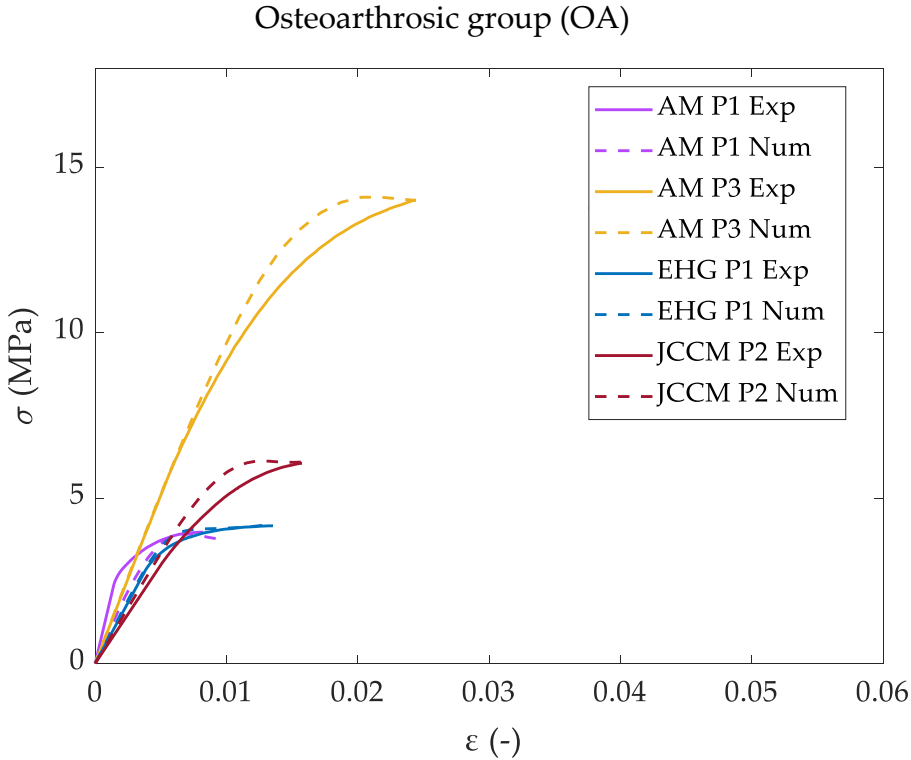
Figure 6.23: Compression stress-strain curves from the experimental tests (continuous line) and the numerical calibration (dashed lines) for specimens of the osteoarthrosic group (OA).

Regarding the results of the yield strain (ε_y), the mean values range between 0.0046 for OP and 0.0059 for HG. The ANOVA analysis stated that there are no significant differences between them. Therefore, the yield onset seems to be independent of the bone state (healthy or diseased) and is an intrinsic property of bone. Several authors have reported this bone behaviour dominated by strains, such as Morgan *et al.* [377] in their review of bone mechanical properties. They stated that high-density cancellous bone, where the femur is included, tends to have isotropic yield strains and, for compression, usually range between 0.65 % and 0.70 % for healthy specimens, which is close to our findings. In another work, Morgan *et al.* [82] registered higher values for the yield strain at the femoral neck, which were 0.85 ± 0.10 %. Bayraktar and Keaveny [378] report the same findings about the uniformity of yield strains in the cancellous bone at the human femoral neck. They established that while the strength and modulus of trabecular bone vary across different anatomical sites, the intra-site variations in yield strains are shallow, which can be considered constant. Lastly, the work of Kopperdahl and Keaveny [74] validates our assumption that strain dominates bone behavior. They studied the importance of using yield strains instead of failure strains when studying the relationship between strain and density.

The failure strain (ε_f) is the last calibrated parameter. As shown in Figures 6.22 to 6.24, this strain is the calibrated value at the maximum stress point. OA and OP present mean lower values for ε_f, 0.035 and 0.025, respectively, whereas HG presents a 0.054 mean value. This implies that HG cancellous samples fail at more than twice the deformation of OP, namely 53.71 % greater. The ANOVA analysis determined that significant differences exist between HG and OP. Hence, this failure strain allows to distinguish between healthy and osteoporotic specimens.

Figures 6.22 to 6.24 present the numerical calibration of several cancellous bone samples of each study. Compression stress-strains curves obtained at the experimental tests are represented as continuous lines, whereas the numerical calibration is displayed as dashed lines. Note that the numerical curve does not match 100 % with the experimental response. It is important to consider the issues that detract from the accuracy of the calibration, such as all the possible errors committed during the tests, the discretisation of specimens, or the failure criterion. We are calibrating three parameters, E_{cal}, ε_y, and ε_f. Hence, these three points are important to be matched. As can be appreciated, the main three points are captured, so the calibrated numerical models can represent the compression behaviour of human cancellous bone specimens.
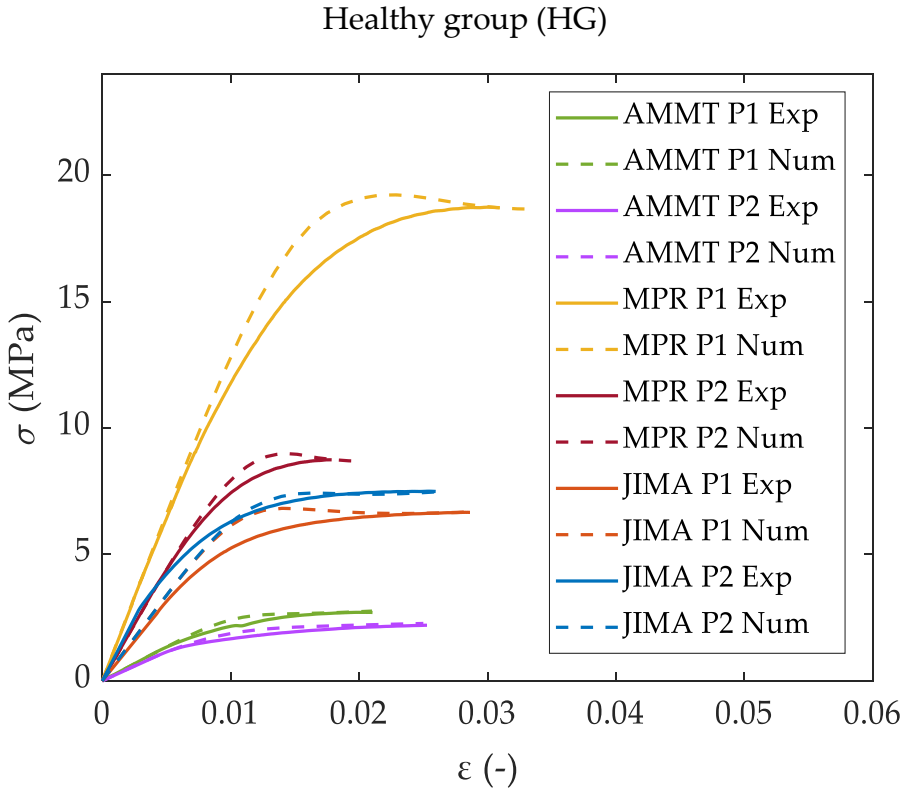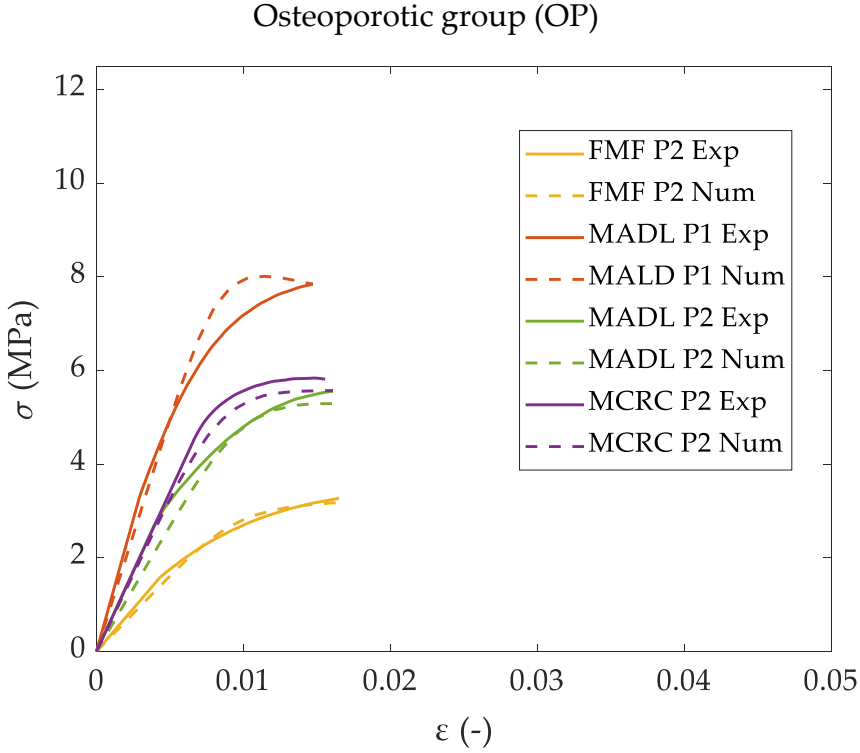
Figure 6.24: Compression stress-strain curves from the experimental tests (continuous line) and the numerical calibration (dashed lines) for specimens of the osteoporotic group (OP).

6.7 Comparison of apparent and tissue Young's modulus estimated by μ-CT, compression tests and FE models

In the previous sections, we estimated the apparent and tissue Young's modulus using different approaches. In Section 6.3.2, we use the grey scale values to estimate the apparent Young's modulus and the mask density to determine the tissue Young's modulus, both using the micro-CT images. In Section 6.4.2, we presented the apparent Young's modulus obtained from compression tests until the failure load. Lastly, in Section 6.6.2, we calibrated tissue Young's modulus using the stress-strain curve from the experimental compression tests and the FE models. In this section, we compare both tissue Young's moduli, the obtained from micro-CT images and the obtained calibrating the FE models,

to evaluate whether they are reliable methods to estimate apparent or tissue Young's modulus.

Table 6.12: Comparison of the apparent and tissue Young's modulus estimated throughout micro-CT images, compression tests and FE models.

	E_{app} (MPa)		E_{tissue} (MPa)	
	micro-CT	**Exp. tests**	**micro-CT**	**FE cal.**
HG	2281.03	1022.82 ± 295.58	13943.79 ± 2808.71	20056.05 ± 8149.47
OA	1376.20 ± 346.56	876.25 ± 277.15	15816.17 ± 843.94	18053.82 ± 6400.84
OP	1008.38 ± 355.82	645.47 ± 219.27	16045.81 ± 997.90	19181.89 ± 5169.33

At first glance, it is possible to see several differences between the same parameter estimated by different approaches. Starting with the apparent Young's modulus (E_{app}), the differences between the micro-CT and compression tests are 55.16 % for HG, 36.33 % for OA and 35.98 % for OP. In the case of HG, the difference percentage is unreliable because we have just one specimen with micro-CT results. E_{app} for this specific specimen registered from the tests has only a difference with the micro-CT results of 38.88 %, closer to the other two percentages. Therefore, we can conclude that E_{app} estimated using the experimental tests introduce artifacts, such as the loss of connectivity density of the trabecular lattice, leading to an underestimation of the results. From these results, it is essential to consider two facts. In this case, we have employed the grey scale values (bone and background), so the cleaning process of the specimens is really important. If the specimens have not been thoroughly cleaned, the remains will appear in the micro-CT images, polluting the information and the grey scale values. Regarding the experimental tests, many factors affect the results, such as the parallelism of the opposite faces, the test conditions, the storage, etc. The issues of both methods can explain the differences of 36-39 %. Even though the experimental tests can provide more information, the estimation of E_{app} using the micro-CT images can be an initial approach to the results.

Regarding the results of tissue Young's modulus (E_{tiss}), HG specimens present a 30.47 % difference between both procedures. Diseased groups present less differences, 12.34 % for OA and 16.35 % for OP. Micro-CT results were calculated using the density mask (only bone information), which avoids some of the conflictive points mentioned in the previous paragraph, such as the cleaning process, which helps to reduce the percentage of differences between methods. Calibrating E_{tiss} with the FE models also induces several issues. An essential point is the discretisation of the numerical model to have an accu-

rate precision of the cancellous geometry. In addition, as we have used the compression stress-strain curves from the experimental tests, all the artifacts that can introduce errors in the tests will also be transferred to calibration. Nevertheless, for diseased specimens, the differences between methods are between 12 and 16 %, which is admissible considering all the potential errors. Concerning HG, having just few samples makes it difficult to obtain reliable results.

To conclude, the approaches to estimate the apparent Young's modulus differ in a range of 36 to 39 %. The method that employs the grey scale values overestimates the results, probably due to the cleanliness of the samples. The methods to assess tissue Young's modulus present less differences for the diseased groups OA and OP, being 12.34 % and 16.35 %, respectively. E_{app} estimated using the micro-CT images can be used as an initial estimation of the results, whereas E_{tiss} calculated by micro-CT presents similar values to the FE models and could be used as adequate estimations.

6.8   Conclusions

In this chapter, we have assessed the mechanical behaviour of healthy (HG), osteoarthrosic (OA) and osteoporotic (OP) human cancellous femoral specimens. We have used different approaches, such as micro-CT, compression tests and finite element models, to estimate cancellous bone elastic and failure properties. We also analysed the relationship between the morphometric parameters and the apparent results (failure stress, failure strain and apparent Young's modulus) to evaluate their influence on each other.

After the segmentation, we estimate the apparent density ρ_{app}, the apparent modulus E_{app}, the bone mineral density BMD and tissue Young's modulus E_{tiss} using the calibration of the phantoms, the grey scale values and the mask density. We found that the results obtained with the grey scale values were apparent results because the images had information about bone and background, whereas the results obtained from the mask density were tissue results because they only had bone information. The ANOVA analysis revealed that the results estimated at the tissue level did not present significant differences between groups, whereas the apparent results did because they presented the information of the complete microstructure.

Regarding morphometric analysis, the main conclusions are that it is possible to distinguish osteoporotic samples from the HG and OA using the bone volume fraction (BV/TV) and the trabecular number (Tb.N). In addition, using

236

the surface ratio (BS/BV) and the mean trabecular thickness (Tb.Th), we can differentiate between healthy and diseased specimens.

From the compressive quasi static tests, the first information extracted was the apparent modulus (E_{app}) estimated at the elastic range. Then, we conducted in-direction compression tests until failure loads. Regarding experimental characterisation, failure stress σ_{f} ranged from 6.18 to 10.93 MPa, with the lowest values for OP specimens and the highest for HG samples. E_{app} is between 645.47 and 1022.82 MPa, following the same trend as the failure stress. However, the failure strain ε_{f} presented values between 0.016 for OA to 0.024 to HG. We also conducted an ANOVA analysis, which reveals statistical differences between HG and OP for both σ_{f} and E_{app}. This gives the possibility to distinguish OP from HG specimens with these two parameters. Concerning the failure strain, the ANOVA analysis stated that there were differences between HG and both OA and OP, which permits the differentiation of diseased cancellous samples from healthy specimens. On the other hand, the measured yield strain is very similar for the three groups analysed.

Once we had all this information, we analysed the relationships between the morphometric parameters and the elastic and failure properties obtained from the compression tests. We analyse the Pearson correlation coefficient R^2, first for all the samples together and then per separated groups. When we evaluated them all together, we did not find strong linear relationships between the parameters (p-value < 0.05). However, in the analysis per groups, we found that for HG specimens the failure stress σ_{f} correlates with fractal dimension D, bone surface BS and the trabecular number Tb.N. It is also found a relationship between the failure strain ε_{f} and the connectivity density Conn.D. In OP samples, both σ_{f} and E_{app} correlate with the same morphometric parameters, the trabecular separation Tb.Sp and the trabecular number Tb.N. These results manifest that the most degraded microarchitectures, with large trabecular separations and less trabecular number, present lower apparent modulus and can withstand lower stress levels. OA specimens are those that present fewer correlations, just one between σ_{f} and the total volume of the specimens TV. This lack of correlations may be due to the differences between the microarchitecture of the specimens from this group because of the pathology. These results evidenced that it is possible to estimate the mechanical response using the micro-CT images without the need to develop experimental tests.

In addition, the the elastic and failure properties obtained from the mechanical response have been related to themselves. HG samples present a linear relationship between σ_{f} and E_{app}, which allow to determine the failure stress using the apparent Young's modulus. OA group correlates σ_{f} with ε_{f}. The re-

sults show that the specimens that can withstand great stress levels also fail at higher strains. Hence, these cancellous specimens present ductile behaviour. Regarding OP samples, the correlation is between E_{app} and ε_f. In this group, as much apparent Young's modulus the specimens failed at lower strain levels. These results manifest that osteoporosis embrittles the cancellous bone specimens.

We generated finite element models with high discretisation using quadratic tetrahedra and 5.6M to 10.7M nodes. We have employed a failure criterion based on the equivalent strain to study the failure. Using the stress-strain curves obtained at the compression tests and the FE models, we have estimated elastic and failure properties. The results calibrated for E_{cal}, the Young's modulus at tissue level, ranged from 18 to 20 GPa. The ANOVA analysis revealed that the results did not present statistical differences between groups, which means that the mineral content at the tissue level is not different when a bone is healthy or diseased. The yield strain ε_y ranged from 0.0045 to 0.0059, and the ANOVA analysis stated that there are no significant between samples/groups. That means that the yield behaviour is not influenced by the architecture, but is a material condition. Hence, as several authors also confirmed, cancellous bone behaviour is dominated by strains, not by stresses. Lastly, the failure strain ε_f, registered values from 0.025 for OP, 0.035 for OA and 0.054 to HG. These values confirm that bone pathologies have a significant impact on the mechanical behaviour of cancellous bone, making it more brittle. The statistical analysis manifested differences between OP and HG. As a consequence, these parameters allow to distinguish between healthy and osteoporotic cancellous samples.

We conclude that the apparent modulus estimated with grey scale values differs from those obtained from the experimental tests between 36 and 39 %. These differences between the results may be explained due to the experimental artifacts as a consequence of the lack of connectivity of the trabecular lattice. Regarding the methods for estimating tissue Young's modulus, the results obtained by the FE models and the mask density differ between 12 and 16 %. Therefore, it is possible to estimate E_{tis} and E_{app} using micro-CT images, without the need of carrying out experimental tests.

Chapter 7

Mechanical characterisation of cancellous bone surrogates and gyroids made out of additive manufacturing. Experimental testing and numerical correlation

7.1 Introduction

In this chapter, we aim at characterising the elastic and failure properties of trabecular bone surrogates obtained by additive manufacturing (AM) using polylactic acid (PLA) as a material. For this purpose, three bone surrogates have been manufactured using the geometry of trabecular samples of a healthy swine specimen. The chosen AM technology is Fused Deposition Modelling (FDM), described in Chapter 2, one of their main procedures is 3D printing.

In addition, the capability of the Triply Periodic Minimal Surface (TPMS) structure for mimicking trabecular bone mechanical response has been analysed. The selected TPMS structure was the gyroid and has been obtained by FDM using PLA. Numerical models have been generated to estimate the material Young's modulus and yield and failure strains.

In the biomedical field, numerous areas have benefited from AM. Some of the advantages are the possibility of manufacturing organoids, the modelling and production of patient-specific implants, which enhance the osteointegration in the patient and in several cases with biomaterials that the body can soak, medical materials, blood vessels and so on.

Focusing on bone implants, the most commonly used structures have been the scaffolds over the years. Usually, the scaffolds are composed of a reticular structure. In bone fractures, they are used to maintain the structural integrity of bone through the healing process. The configuration consists of a set of bars vertically and horizontally criss-crossed (see Figure 7.1 a). The main problem of these implants is related to the joints of the bars, which are stress concentrators. At these geometric points, a significant increase in local stresses leads to a rise in fracture risk. This situation has motivated the research of new geometries that overcome those limitations. Triply periodic minimal surface (TPMS) structures have gained substantial attention in the scientific field in recent decades owing to their outstanding features. TPMS structures are three-dimensional geometries characterised by having the smallest possible surface area within a given volume and regularly repeating in three spatial directions (see Figure 7.1 b).

TPMS structures usually comprise interconnected elements or nodes that form a complex network with specific properties. Several advantages of their geometric conditions are the following: they are designed to minimise the amount of material on the surface, making them highly efficient in terms of material use; they can have complex geometries not found in other structures, which make them really useful at research; they are very lightweight; and they have the ability to absorb impacts or deform in a controlled manner, which can be advantageous in applications such as impact protection. Specifically for bone implants, these structures have good permeability, they enhance the bone growth and the remodelling process, leading to excellent osteointegration of the implant. The periodic geometry has a lower level of stress concentrators than other grid-based lattice structures, has a larger surface area compared to traditional single geometry implants, which allows for more efficient load distribution and improves implant stability, among some other. For all of the presented arguments, both bone surrogates and TPMS structures, namely the
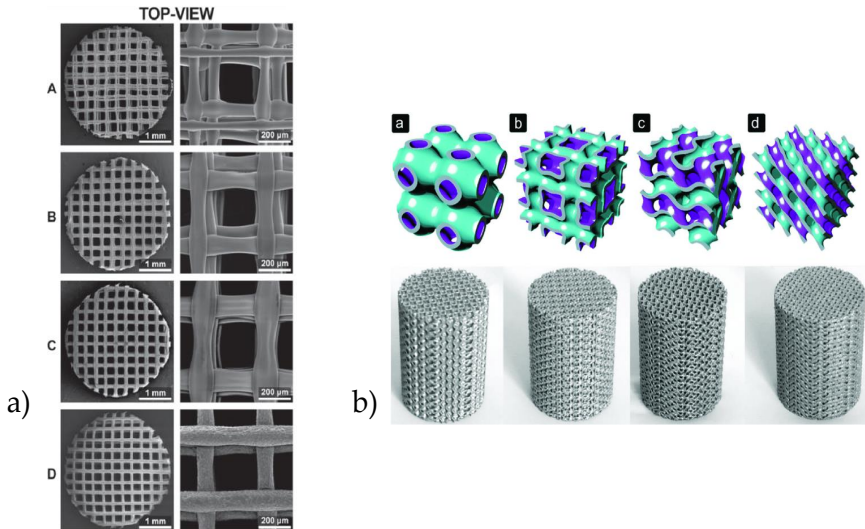
Figure 7.1: a) Scanning electron microscopy (SEM) images of the scaffolds [379] and b) selective laser melted Ti6Al4V porous biomaterials for bone regeneration based on triply periodic minimal surfaces, being (a) primitive, (b) I-WP, (c) gyroid and (d) diamond [380].

gyroid geometry obtained by additive manufacturing using PLA as a material, will be studied in this chapter.

7.2 Analysis of the compressive behaviour of cancellous bone surrogates

In this section, we have studied the behaviour of a cancellous bone surrogate obtained by additive manufacturing (AM) using polylactic acid (PLA) as material. To carry out this study, we have scanned a cancellous bone sample at the micro-CT scan, manufactured the bone surrogates in PLA with a 3D printer, carried out a compression test, and finally, generated the numerical models for calibrating the elastic and failure properties of the surrogates. The workflow followed to perform this work is shown in Figure 7.2.

As it is appreciated in Figure 7.2, the starting point is the cancellous bone sample. The specimen selected is from a healthy swine. The porcine cancellous samples were extracted from the lumbar region, so they have a predominant direction, as depicted in Chapter 3. The following steps are to scan the sam-
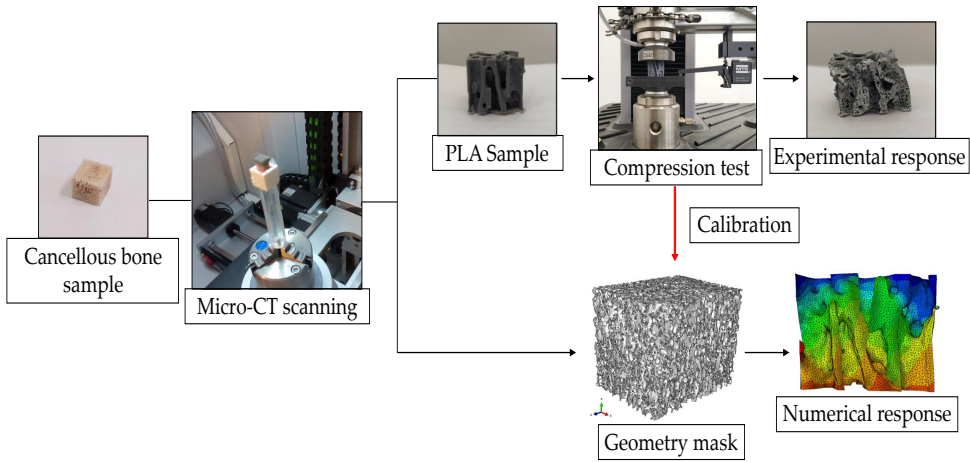
Figure 7.2: Scheme of the workflow followed to carry out the study of the cancellous bone surrogates obtained by additive manufacturing.

ples to dispose of the geometry of the specimens, to generate the numerical models and to print the bone surrogates. After printing, the samples have been subjected to quasistatic compression load until fracture in the three orthogonal directions. The experimental response permits to calibrate the elastic and failure properties of the numerical model.

7.2.1   Preparation and manufacture of bone surrogates

We have scanned the specimen using micro-CT in order to obtain the cancellous geometry. The micro-CT scanner was carried out at the Estación de Bioloxía Mariña de A Graña (Universidad de Santiago de Compostela). The scanner is a Skyscan1172 (Bruker, Kontig, Belgium), achieving images with an isotropic resolution of 13.58 μm (100 kV voltage, 100 μA intensity, Al/Cu filter). The image segmentation was performed using a global manual thresholding procedure at the ScanIP software (ScanIP, Simpleware, UK). After that, we generated the mask with the geometry of the cancellous specimen, which will be used both to generate the finite element models and to have the geometry for printing the bone surrogates.

The subsequent phase is manufacturing the cancellous bone surrogates to perform the experimental tests under quasistatic compression loads. The chosen

AM technology is Fused Deposition Modelling (FDM), whose main feature is that the component is manufactured layer by layer. For this assignment, we have used a commercial Ultimaker S3 3D printer (Ultimaker, Utrecht, Netherlands), presented in Figure 7.3.
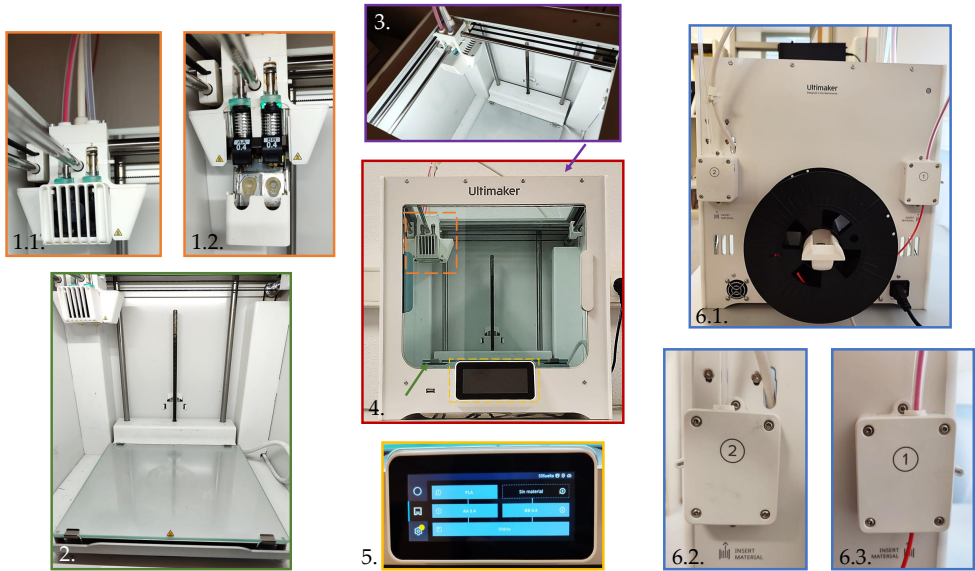
Figure 7.3: Components and parts of the Ultimaker S3: 1.1. print cores and cooling compartment closed, 1.2. print core 1 (left) and print core 2 (right) with their nozzles, 2. heated bed with the threaded rod mechanism that allows it to be raised and lowered, 3. straight bars and belts mechanism enabling movement in the print cores plane, 4. Ultimaker S3 3D printer, 5. control display, 6.1. the rear side of the printer with both feeders and the filament support, 6.2. feeder 2 and 6.3. feeder 1.

First of all, we made the printing setup at Ultimaker Cura 4.13.1. To this end, we can define the 3D printer that we have and then open the STL file with the geometry of the cancellous specimen. Then, it is time to define the sample's dimensions, the orientation on the printer heated bed, and the number of samples we want to print. In this case, owing to the trabecular network's intricate geometry, we have taken off a small cube of the whole specimen, whose dimensions are 2 mm per side. Afterward, the samples were scaled by a factor of 10 to be able to print them in high quality with the available printer. Consequently, the printed cubic samples will have 20 mm per side.

The next step is orienting the sample in the printer's heated bed at Cura. It is crucial to consider the printing direction; then, we have decided to place the
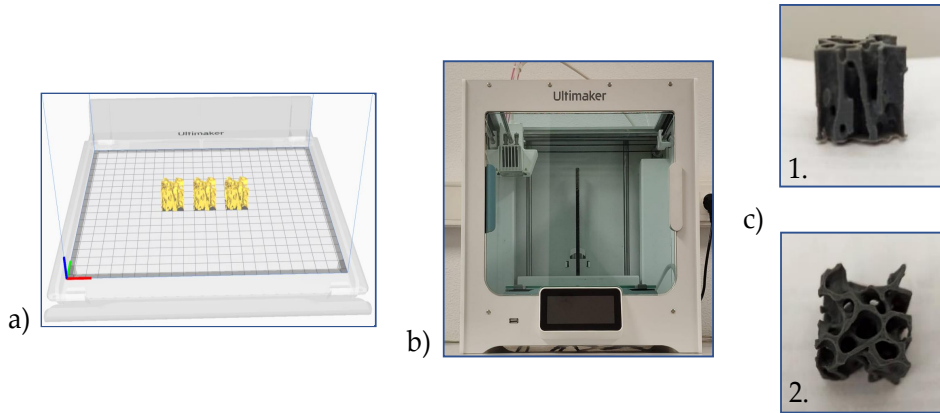
Figure 7.4: a) Cancellous bone samples at the Ultimaker Cura software to define the printing parameters, b) Ultimaker S3 3D printer and c) cancellous bone surrogates manufactured in PLA.

piece in the direction of the plates. Therefore, the 3D printer will deposit the material in the same direction as the bone grows. Then, the printer will not need support for printing the samples. It is essential to place the piece in the most conducive direction to manufacturing and not require material support because, in some cases, it is difficult to remove them, and maybe the quality of the piece will be reduced at the points where there was a support.

Table 7.1: Printing parameters defined for manufacturing the PLA samples.

Printing parameters		
Quality	Layer height	0.1 mm
Perimeter	Top/bottom thickness	1 mm
Infill	Infill density	100 %
Speed	Printing speed	30 mm/s
Material	Printing temperature	200 ºC
Nozzle	Retraction	enabled
Adhesion to the plate	Priming droplets	enabled
	Printing plate adhesion	skirt

Three samples were manufactured because we will study the specimen three orthogonal directions (see Figure 7.4 a). The next step is to configure the print settings, which involve the following points: quality, walls, top and bottom walls, infill, material, speed, displacement, cooling, supports, adhesion to the printing plate, double extrusion, special modes, and experimental. The printing parameters defined for manufacturing these samples are presented in Table 7.1. In relation to the adhesion to the heated bed, we selected the skirt option because PLA has enough adhesion without any adhesive.

Once the printing had finished, we obtained PLA cancellous bone surrogates, as presented in Figure 7.4c. As they are lumbar samples, it is possible to identify one main direction in which bone grows (see Figure 7.4c.1.), where the predominant structure is plates, whereas in the other two orthogonal directions, there are mainly rods and struts, such as exhibited in Figure 7.4c.2.

7.2.2 Experimental results of the cancellous bone surrogates subjected to compression load

In this section, the experimental results obtained after subjecting bone surrogates to quasistatic compression loads are presented. The compression tests were conducted in an electromechanical testing machine (MTS Criterion C42, MTS Systems, USA) with aluminium compression platens (MTS ref.: FYA502A). The tests were performed with displacement control at a 1 mm/min speed. The displacement between the compression platens was measured using a contact deflectometer (MTS ref.:632.06H-20), as exhibited in Figure 7.5. The deflectometer is fixed to the upper platen through tooling (see Figure 7.5).

We have carried out three destructive compression tests, one per each orthogonal direction of the sample. In each experimental test, we applied a preload of 10 N to settle the sample before starting the compression test and to ensure that both compression platens were entirely in contact with the specimen. The acquisition of displacements has been carried out through the signal recorded by the contact deflectometer. On the other side, the force applied by the testing machine on the specimen was recorded with a data acquisition frequency of 10 Hz. We obtain the stress-strain curve from the recorded response that allows us to study the behaviour of the PLA cancellous bone surrogates.

The compression response of the bone surrogates is presented in Figure 7.6. The most important data extracted from these tests are the apparent elasticity modulus (E_{app}), calculated at the linear region of the curve, and the so-called
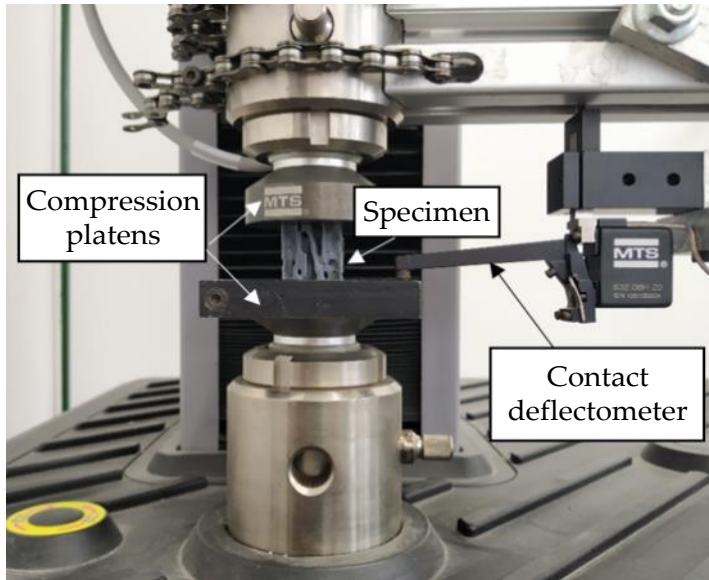
Figure 7.5: Configuration used for the bone surrogates compression testing on the electromechanical testing machine MTS.

final point, where the maximum stress (σ_f) is reached, and the strain (ε_f) achieve at this point.

The response of each sample direction has been represented in different strokes in Figure 7.6. The longitudinal direction of the sample, which corresponds to the plate direction of the specimen, is described in green with a continuous line. For the y direction, we plotted the response in red with dashed dots, while the x direction was presented in blue with dashed lines.

At first sight, several conclusions can be extracted from Figure 7.6, such as the plate direction is the most resistant. This direction can withstand 68.65 % more stress level than the x direction, whereas concerning the y direction, this value decreases to 60.84 %. That means the plate direction can withstand more than twice as much stress as the other two. Regarding the transversal directions, it is appreciated that both have similar behaviour, although the y direction can support a 19.95 % more stress level than the x direction.

The experimental results obtained for the compression tests of the cancellous bone surrogates are exhibited in Table 7.2. The numerical values manifest
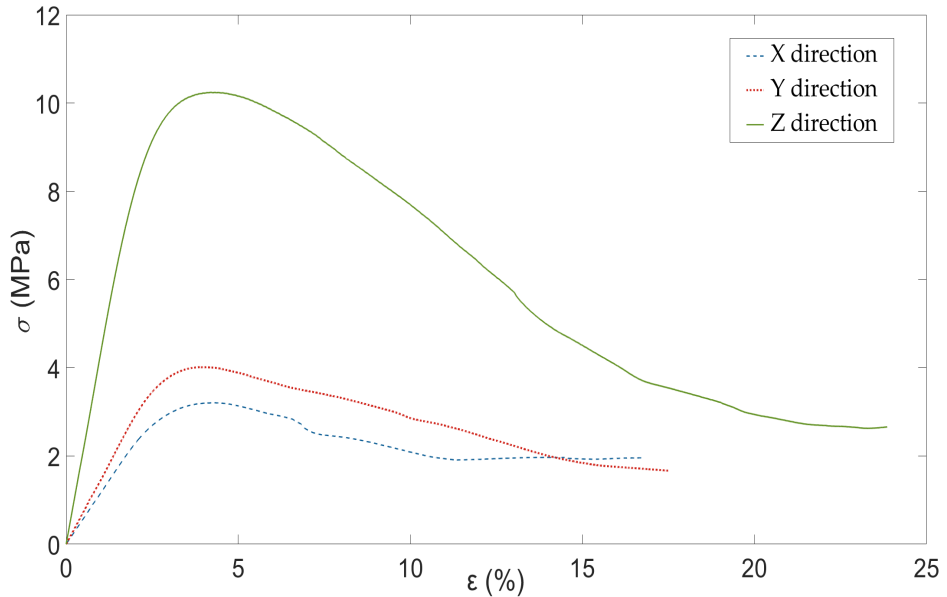
Figure 7.6: Experimental response under compression loads of the cancellous bone surrogates.

some interesting results that may not be appreciated in Figure 7.6, such as the strain at failure present similar values between them, while the stresses are highly different between the specimen directions, which means that the strain dominates the behaviour of the sample. This means the maximum stress value is reached at a similar strain point, approximately around a strain value of 0.040.

Table 7.2: Results of failure stress (σ_f), failure strain (ε_f), and compression apparent elasticity modulus (E_app) for each orthogonal direction of the sample after subjecting cancellous bone surrogates to quasistatic compression load.

	x direction	y direction	z direction
σ_f **(MPa)**	3.21	4.01	10.24
ε_f **(-)**	0.043	0.039	0.042
E_{app} **(MPa)**	115.35	144.27	432.38

The apparent modulus of elasticity (E_app) follows the same trend as the failure stress (σ_f), where the maximum value is reached in the z direction, whereas

the lowest values are manifested in the transversal directions of the specimen. In agreement with the failure stress results, the apparent elasticity modulus for the transverse directions is slightly different, being 20.05 % higher in the y direction. The more significant difference is between the z and x directions, 73.32 %.

On the other hand, we have compared the cancellous bone surrogate's apparent elasticity modulus with those of several cancellous bone specimens [80], and are presented in Table 7.3. To consider the body location, both samples have been extracted from a healthy swine's lumbar spine vertebra. At first glance, it is appreciated that the ratio between the apparent modulus of the transversal x and y directions and the z direction is maintained. In detail, the ratio of the bone surrogate is 3.05, whereas the cancellous bone's ratio is 3.30. Therefore, just by scaling Young's modulus to that of the cancellous bone, it is possible to have the bone's apparent modulus of elasticity.

Table 7.3: Comparison of the compression apparent elastic modulus (E_{app}) obtained for the cancellous bone surrogate and a cancellous bone from a healthy swine. Both specimens are from the lumbar region.

	Surrogate E_{app} (MPa)	Bone E_{app} (MPa)*
x direction	115.35	346.0 ± 81.9
y direction	144.27	328.1 ± 82.2
z direction	432.38	1022.9 ± 199.4

*Taken from [80].

To conclude, it is important to highlight that additive manufacturing (AM) has enabled the study of the fracture behaviour of a cancellous bone specimen. Compression tests are destructive, so it is impossible to perform such experimental tests in cancellous bone specimens. In addition, this work can reinforce the statement of using non-isotropic properties in cancellous bone or even in the macroscopic scale because it shows a strong relationship between the cancellous architecture and several parameters, such as the failure stress (σ_{f}) or the apparent modulus of elasticity (E_{app}). Furthermore, it has been stated that the polylactic acid (PLA) behaviour is dominated by the strains, which can be useful when using this material.

This study of a local region of the cancellous bone can be used to analyse critical parts, such as fractures, to design patient-specific implants. It might be employed to study the trabecular network with an isotropic material, which

is much easier to control the behaviour than an anisotropic or orthotropic material, such as bone.

7.2.3 Calibration of elastic and failure properties of cancellous bone surrogates

In this section, the elastic and failure properties of cancellous bone-like surrogates manufactured in polylactic acid (PLA) have been assessed using the compression response obtained from the experimental tests and the numerical model. To obtain the finite element model, we segmented the micro-CT images, and then we obtained the mask with the geometry of the cancellous specimen (ScanIP, Simpleware, UK). Hence, we generated the mesh of the numerical model with linear tetrahedra (element type C3D4 in Abaqus), obtaining a total of 225,369 elements and 67,725 nodes (see Figure 7.7 a).
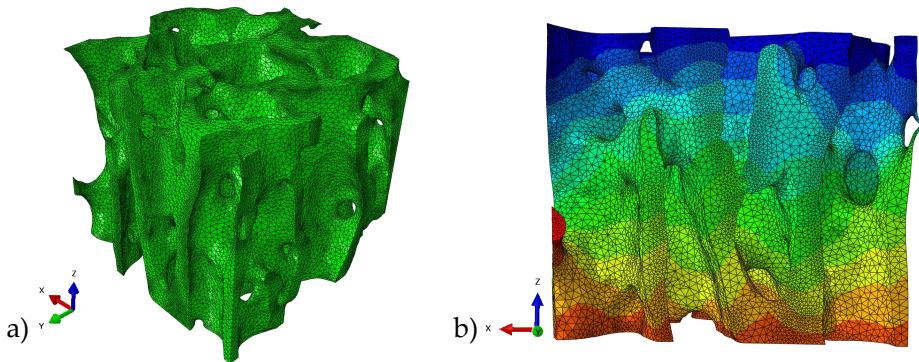
Figure 7.7: a) Finite element model of the cancellous bone surrogate in isometric view and b) front view when compression displacement has been applied on the numerical model.

The FE models have been simulated in the finite element software Abaqus/-Standard (SIMULIA, Dassault Systèmes, Vélizy-Villacoublay, France) to calculate the elastic and failure properties. As in the experimental tests, the numerical models have been subjected to quasistatic compressive load with displacement control, and the compression result is shown in Figure 7.7 b. On the same FE model, we have applied the displacements in each of the three specimen's orthogonal directions separately to assess the properties of each one.

As appreciated in the previous section, the sample behaviour is dominated by the strain; hence we have used a strain failure criterion based on the calculation

of the equivalent strain, such as in Chapter 6. The experimental response and the numerical calibration are represented in Figure 7.8 in continuous solid and dashed lines, respectively. For both transversal directions, the calibrated response passes right over the experimental response; then, it is possible to state that we have caught the surrogate behaviour in both directions.
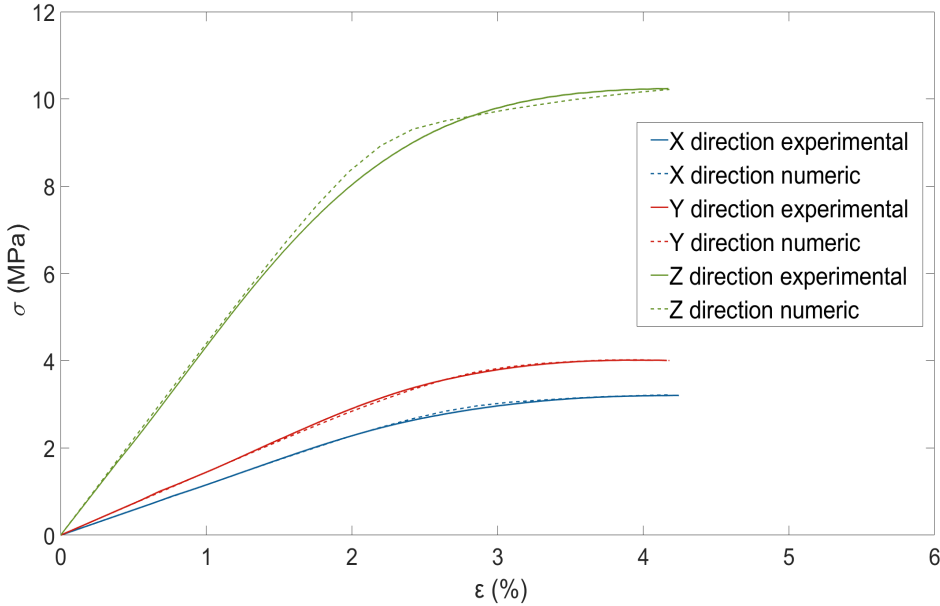
Figure 7.8: Experimental response and numerical calibration for each orthogonal direction of the PLA cancellous bone surrogate.

On the other hand, in the z direction, there are some parts of the curve that the calibrated response does not pass right over. However, the calibrated properties are the yield onset strain (ε_y), the failure strain (ε_f), and the calibrated modulus of elasticity (E_{cal}), hence these are the essential points that we must capture in the numerical model. For the yield strain (ε_y), we need to catch the failure onset. The next crucial point is the failure strain (ε_f), which is registered when the stress reaches the maximum value. The linear response permits the assessment of the modulus of elasticity (E_{cal}). As can be seen in Figure 7.8, the three essential points previously commented are perfectly captured, and we only have a slight deviation in some parts of the curve.

Regarding mechanical parameters calculation, the obtained numerical values are collected in Table 7.4. The yield local strain or at material level (ε_y) approximately matches for both directions. On the contrary, the z direction,

which is the plate direction, has been required to change the damage penalty when an element fails to capture the stress-strain curve. For this reason, the value for the yield strain (ε_y) in the z direction is different and can not be compared with the other two. On the other hand, the failure strain (ε_f) results are more scattered, making it more challenging to draw conclusions.

Table 7.4: Results of the yield strain (ε_y), the failure strain (ε_f), and the material elastic modulus (E_cal) calibrated for each orthogonal direction of the sample after applying a compression displacement on the numerical model.

	x **direction**	y **direction**	z **direction**
$\varepsilon_\mathbf{y}$ **(-)**	0.052	0.054	0.030
$\varepsilon_\mathbf{f}$ **(-)**	0.50	0.27	0.20
$E_\mathbf{cal}$ **(MPa)**	2288.1 $\pm$ 298.72		

The variation of the calibrated modulus can have several explanations, such as this parameter has been calculated using the experimental response, which can include experimental artifacts that would affect the calibration. The filament must be vacuum-packed after printing once we have finished printing for its good preservation. The elastic modulus provided by the PLA manufacturer is 2300 MPa. Therefore, compared with our calibrated results, it is possible to establish that the calibrated modulus is similar to the manufacturer's.

Several important conclusions can be extracted from this section. This study has proved that AM of cancellous bone specimens permits an experimental evaluation of different loading destructive loading conditions. Thus, it helps the analysis of the influence of cancellous bone architecture on the mechanical response. Specifically, plate-like structures undergo a different damage law evolution than strut-like structures.

7.3 Characterisation of the compressive behaviour of triply periodic minimal surface (TPMS) structures

Once we have the properties of a cancellous bone surrogate, we will study a triply periodic minimal surface (TPMS) structure, namely the gyroid, to analyse its capabilities to mimic the cancellous bone's behaviour. The starting point is to generate the gyroid geometry and we have used MSLattice free software [381]. Then, it is time to manufacture the gyroid samples using fused deposition modelling (FDM) technology, specifically by employing a 3D

printer. We have subjected the gyroid samples, manufactured in polylactic acid (PLA), to quasistatic compression loads. On the other hand, with the gyroid's geometry, we generated the finite element model to estimate the elastic and failure properties.

7.3.1 Introduction

Bone inherently possesses the ability to regenerate as a natural part of its healing mechanism when responding to injuries [382]. Nevertheless, large bone defects resulting from procedures such as bone tumor removals and severe nonunion fractures do not have the necessary framework for coordinated regeneration, necessitating surgical intervention. The established and most effective treatment method involves a procedure known as autografting. This process entails extracting bone from a non-weight-bearing area within the patient, often a readily accessible site like the iliac crest, and then transplanting it into the damaged area. These kinds of grafts yield the most favorable clinical results due to their dependable integration with the recipient's bone. This approach also eliminates the potential immune and disease-related issues associated with allogeneic bone (from human cadavers) or xenogeneic bone (from animals) [383].

In order to overcome the limitations of these bone grafts, scientists have created bone scaffolds and engineered bone tissues using biocompatible materials and bone cells [384]. Bone Tissue Engineering (BTE) is a field that creates and produces porous interconnected scaffolds. These structures facilitate the regeneration of bone tissues as cells can gradually and systematically fill the voids within the lattice structure [34]. A perfect tissue scaffold should present the following attributes, which must be considered in the design:

- The scaffold ought to possess a porous structure with significant porosity, facilitating cell proliferation, nutrient transport, and the removal of waste products.

- It should be both biocompatible and biodegradable, with degradation rates matching the pace of tissue growth, and any resulting degradation products must not interfere with tissue metabolism.

- The surface microstructure must encourage cell adhesion, growth, and specialisation.

- The scaffold's mechanical characteristics should closely resemble those of the surrounding tissue.

Triply periodic minimal surface (TPMS) are mathematically described as infinite and periodic surface curvatures, which can be configured in function of the curved shape, porosity or layer thickness [35]. These structures are widely used as bone scaffolds, starting from the design of the repeated unit cell [33]. Hence, using this method, the scaffolds can be customised to match the specific organ or tissue requirements they are intended for. This includes ensuring the scaffolds possess the necessary mechanical attributes such as stiffness and permeability (see Figure 7.9). This adaptability extends from the initial scaffold design to its practical use, making it a crucial factor for clinical application. When the mechanical behavior of a particular structure can be predicted and verified through numerical methods beforehand, it substantially enhances the likelihood of successful *in vitro* and *in vivo* clinical trials and subsequent implantation into the target organ or tissue. This reduces time-to-market and enhances the practicality of these innovative approaches [35].
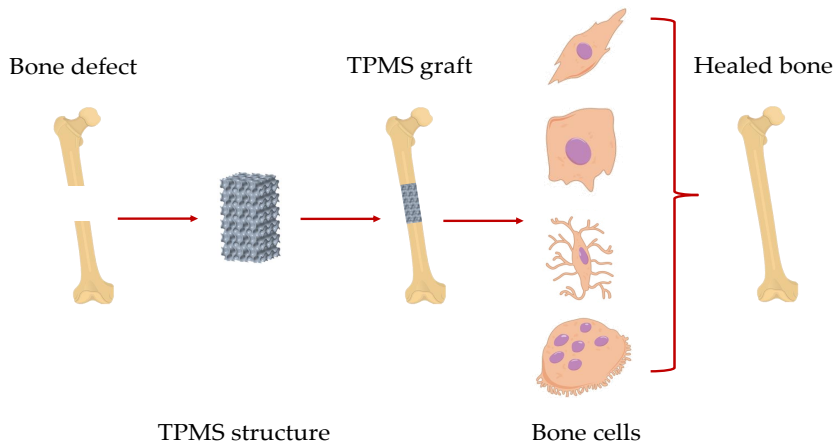
Figure 7.9: Scheme of the healing processes of a large bone defect using TPMS structures as a bone graft.

Furthermore, additive manufacturing (AM) has promoted the manufacturing of TPMS structures for bone implants. The broad range of manufacturing technologies and materials available makes AM suitable for the biomechanical field's requirements. Regarding the materials employed in implant manufacturing, in the past years, the materials created for implantation were primarily designed to be biologically inactive or "bio-inert." However, materials scientists have recently transitioned their focus to intentionally developing "bioactive" materials. These materials can interact with biological molecules or cells

and promote tissue regeneration. For bone-related materials, it is ideal that they are [383]:

- Osteoinductive: able to stimulate the differentiation of precursor cells towards becoming bone-forming cells.

- Osteoconductive: able to foster bone growth and facilitate the integration of adjacent bone.

- Capable of osseointegration: seamlessly merging with the surrounding bone.

7.3.2 Analysis and design of a gyroid TPMS

If a surface exhibits a mean curvature of zero at any given point, it is identified as a minimal surface. If this particular surface exhibits infinite and periodic characteristics in three dimensions, it is termed a Triply Periodic Minimal Surface (TPMS). These structures can be expressed through level-set approximation equations, which consist of a series of trigonometric functions defining an iso-surface at a specific iso-value.

Level-set equations consist of a collection of trigonometric functions that jointly fulfill the equation $\Phi(x, y, z) = c$. In this context, $\Phi(x, y, z)$ represents an iso-surface assessed at a specific iso-value, denoted as c. Some of the available TPMS structures at MSLattice are: Diamond, Primitive, Gyroid, I-WP, Neovius, Fisher Koch S, F-RD or PMY [381], exhibited in Figure 7.10.

In this section, the TPMS studied structure is the gyroid, whose level-set equation is defined in Eq. 7.1. In this equation, $X = 2\alpha\pi x$, $Y = 2\beta\pi y$, $Z = 2\gamma\pi z$, where α, β and γ are constants associated with the dimensions of the unit cell in the x, y, and z directions, respectively. When the level-set equation is assessed with a value of $c = 0$, it divides space into subregions of equal volumes by the iso-surfaces. These subregions can be managed by adjusting the iso-value constant, allowing for the expansion or contraction of their volumes by shifting away from or towards the zero value along the normal or reverse direction [381].

$$sinX cosY + sinY cosZ + sinZ cosX = c \qquad (7.1)$$

Moreover, it is possible to follow two different approaches to create a TPMS lattice. One approach involves considering one of the volumes separated by the
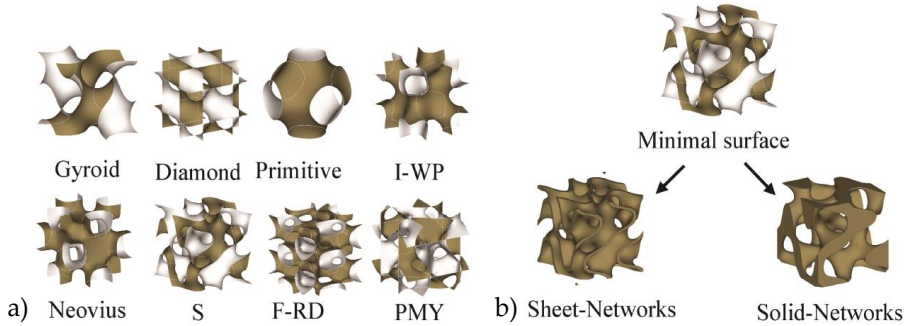
Figure 7.10: a) Unit cell examples of triply periodic minimal surfaces (TPMS) available in the library of the MSLattice and b) strategies to create lattices from a minimal surface: sheet and solid. Image extracted from [381].

minimal surface as the solid region and the other as the empty region. This is achieved by defining the volume enclosed by the minimal surface in such range $\Phi(x,y,z) > c$ or $\Phi(x,y,z) < c$, thereby creating a so-called solid-network lattice. The second method includes displacing the minimal surface in both its normal and reverse normal directions, forming a dual surface defined by solving the equation $-c \leq \Phi(x,y,z) \leq c$. The spatial points enclosed between these two dual surfaces form the solid region, representing a thicker shell or sheet-based lattice derived from the minimal surface [381]. We refer to this lattice as a sheet-network lattice (as depicted in Figure 7.10 b).

In this section, the main target is determining which of these two geometries more accurately replicates cancellous bone surrogates' behavior. For this purpose, we have manufactured both gyroid geometries in a 3D printer using polylactic acid (PLA), and then, we have carried out a quasi static compressive test to analyse the mechanical behaviour of these TPMS structures.

The first step is to generate the gyroid geometries in the MSLattice software. The surfaces developed in MSLattice were imported into ScanIP software to generate a solid 3D model. The process consisted of filling in the structure contained in the surface mesh. Once the solid geometries are developed, we export them in STL format to be able to print them out. Before printing, we must define the printing parameters and the number of printing pieces in the corresponding software, which in this case is Cura 4.13.1. The printed pieces with sheet and solid geometry are such as the presented ones in Figure 7.11 right, with 20 mm per side and 30 % volume fraction.
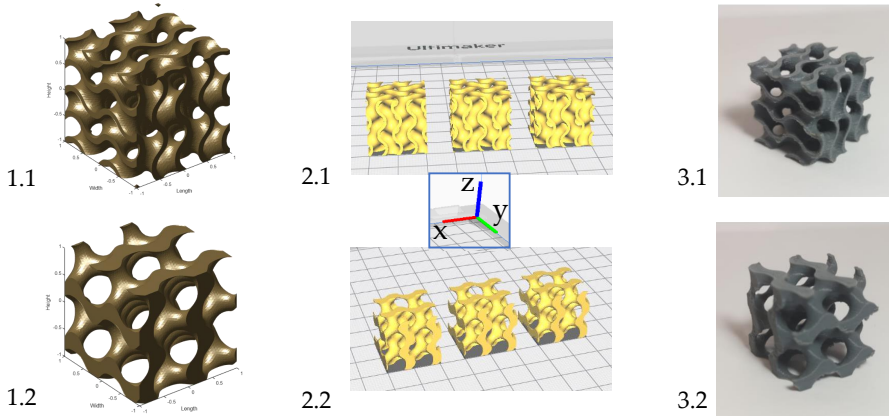
Figure 7.11: Procedure for generating and manufacturing gyroid structures. Geometry generation in MSLattice (left), the definition of printing parameters and the number of samples (middle), and PLA sheet and solid gyroids (right).

7.3.2.1 Experimental compression characterisation of sheet and solid gyroids

We have printed three sheet gyroids and three solid gyroids in polylactic acid (PLA) using a Ultimaker S3 3D printer. All the samples have been subjected to quasi static compressive loads using an electromechanical test machine (MTS Criterion C42, MTS Systems, USA) with a load-cell of 5 kN and aluminium compression platens (MST ref: FYA502A). We developed the compression tests in displacement control with a monitored speed of 2 mm/min and a data acquisition rate of 10 Hz. During the tests, we recorded the applied load in N and the displacement in mm using a contact deflectometer. The configuration of the testing machine is the same as the one showned in Figure 7.5.

As we printed three samples per gyroid geometry, we tested one in each orthogonal direction x, y and z. The behaviour curves obtained for the compression tests are presented in Figure 7.12 for each type of geometry and orthogonal direction. A characteristic feature of such structures is the triply periodicity, also manifested in the results. Regardless of the test direction, the three samples for each geometry present similar results with respect to the three orthogonal directions. Nevertheless, slight differences can be appreciated between the same gyroids' responses. They are mainly due to the experimental

tests' variability or possible defects during the printing, but it is manifested that they are not significant. The behaviour distinctions are primarily due to the microstructural differences of each typology of the gyroid.
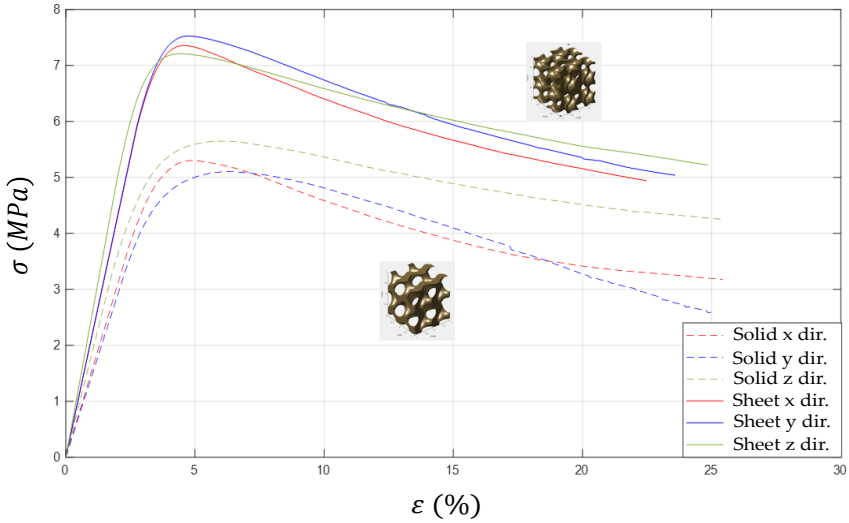
Figure 7.12: Experimental results obtained under compressive loads for sheet and solid gyroids. Sheet gyroids are represented in continuous stroke, while solid gyroids are represented in dashed stroke.

Table 7.5 collects the results obtained from the experimental tests, in which the most relevant parameters are the failure stress (σ_f), the strain at the failure stress (ε_f) and the apparent modulus of elasticity (E_{app}). It can be appreciated that sheet gyroids can withstand higher loads than solid gyroids. Sheet gyroids exhibit a failure stress mean value of 7.36 MPa, whereas solid gyroids have 5.34 MPa, that is a 27.5 % higher stress level for the sheet configuration. Following the same trend, the apparent modulus of elasticity (E_{app}) is slightly higher for sheet structures than solid ones. It is essential to consider that E_{app} is directly related not only to the material but also to the geometry of the sample. Sheet gyroids present a E_{app} mean value of 227.71 MPa, while solid gyroids exhibit a mean value of 153.95 MPa.

However, the strain at the failure stress (ε_f) results manifest the contrary trend, as can be appreciated both in Figure 7.12 and in Table 7.5. Solid gyroids achieve the failure stress (σ_f) at a higher strain (ε_f) than sheet gyroids. The

strain values for each group are pretty similar, whereas between typologies, solid gyroids present higher values. Sheet gyroids present a strain mean value of 0.046, while solid gyroids are 0.056, with the latter being 18.3 % higher.

Table 7.5: Experimental results of the failure stress (σ_f), the strain at the failure stress (ε_f) and the apparent modulus of elasticity (E_{app}) for sheet and solid gyroids.

	Sheet gyroid			Solid gyroid		
	x	y	z	x	y	z
$\sigma_{\mathbf{f}}$ **(MPa)**	7.36	7.53	7.21	5.30	5.10	5.62
$\varepsilon_{\mathbf{f}}$ **(-)**	0.046	0.048	0.044	0.049	0.063	0.057
$E_{\mathbf{app}}$ **(MPa)**	216.18	216.07	250.87	148.57	140.05	173.22

In Figure 7.13 a, it is presented both sheet and solid gyroids before and after the mechanical tests, conducted in the z direction. It can be noticed that for both sheet and solid gyroids, the failure onset appears in the areas where the cross-section is thinner. Consequently, these areas accumulate higher strain levels and plasticity. In addition, as the compression is applied in the same direction of the printing, all the layers are crushed, compacting the whole structure, as manifested in Figure 7.13 a.
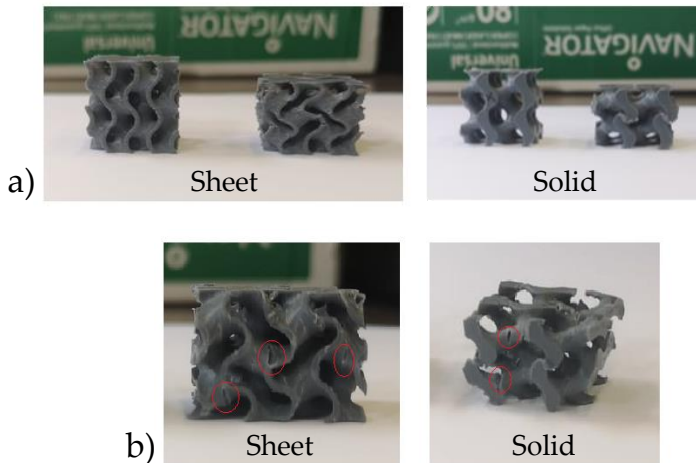
Figure 7.13: a) Non-deformed and deformed shapes of sheet and solid gyroids when testing in the printing direction and b) deformed shapes for gyroids tested in plane x and y directions.

On the other hand, in Figure 7.13 b, the gyroids are shown after the compression for both plane directions, x and y directions. In these cases, the compression is applied perpendicular to the printing direction, the consecutive layers split up, and consequently, cracks arise, such as in Figure 7.13. This evidence manifests the influence of the printing direction in the fracture paths, but not in the macroscale mechanical parameters.

In the biomechanical field, TPMS structures usually aim to mimic cancellous bone behaviour to develop bone implants with such geometries. Based on the results for the bone surrogates presented in Table 7.2 and intending to mimic that behaviour, we choose the sheet gyroid instead of the solid geometry.

7.3.2.2 Numerical estimation of elastic and failure properties of sheet gyroid

Once the experimental behaviour is characterised, we proceed with the numerical estimation of the elastic and failure properties. Unlike in the experimental section, we only study the sheet geometry of the gyroid. For the studied volume fraction the sheet gyroid presents better mechanical properties, such as higher stress values, which properly mimic the cancellous bone surrogate behaviour, thus, the cancellous bone behaviour.

The sheet geometry generated in the software MSLattice and post-processed and meshed in ScanIP (Simpleware, UK) with linear tetrahedra C3D4 elements. A mesh size analysis has been conducted to establish a suitable size element. The finite element model for the sheet gyroid has 252,129 nodes and 1,070,444 elements, presented in Figure 7.14 left. The compression load is applied through controlled displacements to simulate the quasi-static compression load in the testing machine. We have specified a displacement of 5 % of the lateral dimension of the gyroid, particularly in the z direction (see Figure 7.14 right). In the opposite surface to the compression displacement, we have constricted the displacement of the nodes in such direction.

To estimate the elastic and failure properties, isotropic elastic properties have been defined, namely Young's modulus for the material, in this case, the polylactic acid (PLA). In addition, for damage assessment, it is defined a failure criterion based on the equivalent strain ($\varepsilon_{\mathrm{eq}}$), the criterion used in Chapter 6. The non-linear response of the gyroid once the failure onset is reproduced using a failure criterion of degradation of the material elastic properties (PLA). This failure criterion is defined and explained in Section 6.6.1 in Equations 6.17 to 6.20.
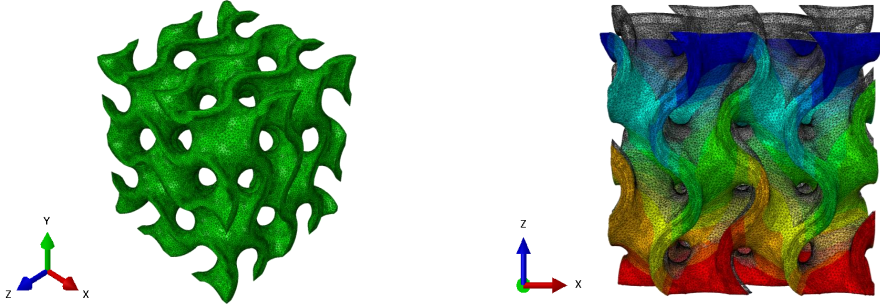
Figure 7.14: Isometric view of the finite element model of the sheet gyroid (left) and front view of the gyroid before and after applying the displacement (right).

Owing to the periodicity of the TPMS structures, we have only present the results of one direction of the gyroid, namely the z direction exhibited in Figure 7.15. The estimated parameters are the Young's modulus of the material (E_{cal}), the yield strain (ε_{y}) and the failure strain (ε_{f}), which are collected in Table 7.6.

The numeric calibration has been carried out until the maximum stress level. The numerical stress-strain curve must match the three relevant points: the linear range of the curve where the E_{cal} can be calculated, the strain at where the failure begins (ε_{y}) and the strain registered at the maximum stress level (ε_{f}). It can be appreciated in Figure 7.15 that the numeric calibration perfectly captures the three relevant parameters aforementioned and also the other parts of the curve.

Regarding the numerical values, Table 7.6 presents the estimated results for each parameter. In relation to the calibrated Young's modulus, it is illustrated that for the sheet gyroid, the E_{cal} is 2411.74 MPa, while the provided elasticity modulus by the manufacturer is 3300 MPa, available in the technical specifications sheet [385].

Table 7.6: Results of the yield strain (ε_{y}), the failure strain (ε_{f}), and the material elastic modulus (E_{cal}) calibrated for the z direction of the sheet gyroid.

	$\varepsilon_{\mathbf{y}}$ (-)	$\varepsilon_{\mathbf{f}}$ (-)	$E_{\mathbf{cal}}$ (MPa)
z **direction**	0.03	0.08	2411.74
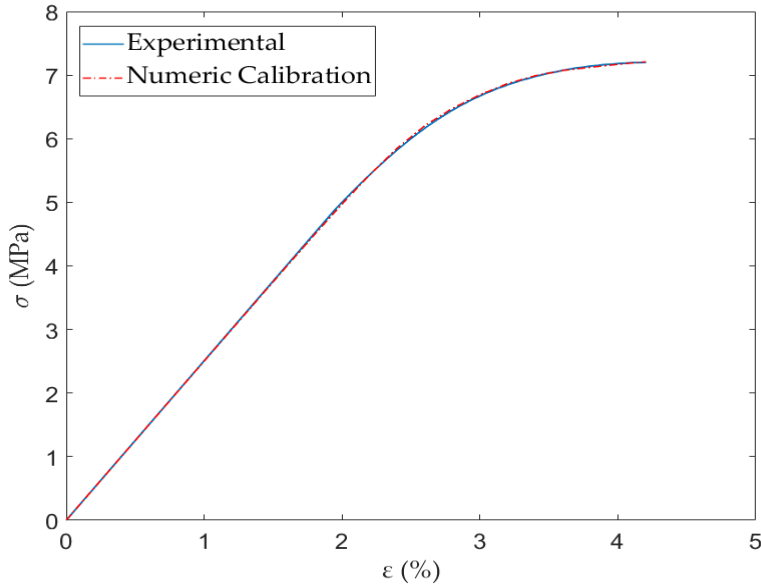
Figure 7.15: Experimental stress-strain curve for PLA sheet gyroid in the z direction represented in continuous blue stroke and numeric calibration of the compression stress-strain curve represented in dashed red stroke.

Recapitulating to the cancellous bone surrogate Section 7.2.3, the calibrated Young's modulus is 2288.1 ± 298.72 MPa. The calibrated Young's modulus (E_{cal}) are in the same line between them, both for the cancellous surrogate and sheet gyroid. It is essential to consider that the modulus is calibrated using the experimental response, so if any experimental artifact has occurred during the tests, it will directly affect the calibrated properties. The modulus provided by the manufacturer is the tensile Young's modulus, whereas we have conducted compression tests, so maybe the PLA behaviour is slightly different in tension than in compression, thus the differences found in the results.

7.3.3   Design and evaluation of non-isotropic gyroids

In this section, we propose a procedure to design patient-specific non-isotropic scaffolds. In this thesis, we have evaluated and discussed that morphometry controls the mechanical behavior. Following this idea, we propose that, to adjust the non-isotropic properties, the geometry can be modified. To address it, we have stretched one of the three orthogonal directions of the gyroid. Although the starting point is the same sheet gyroid studied in the previous section, once we have modified the triply periodicity of the sample, from now on, the generated geometries are not TPMS structures. However, the generated geometries keep the rest of the TPMS features, such as low levels of stress concentrators or the ability of cellular migration and osteointegration. Figure 7.16 presents the procedure followed to develop the analysis of these stretched sheet gyroids.
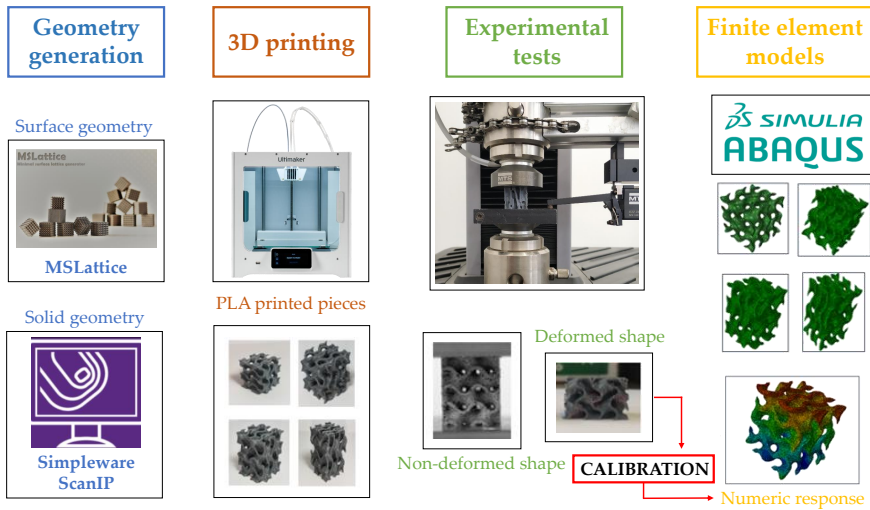
Figure 7.16: Scheme of the procedure employed to design and analyse the non-isotropic gyroids manufactured in PLA. The procedure can be divided into four blocks: geometry generation, 3D printing, experimental tests and finite element models.
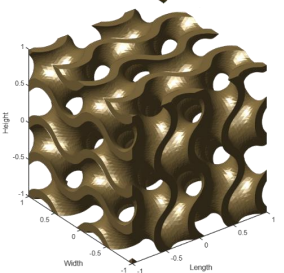
To evaluate the proposed procedure to design non-isotropic structures we generate three types of gyroids with a different distorsion value in the z direction, and then we print four pieces per type. Two pieces will be printed in the z direction, whereas the other two will be manufactured in the y direction. Once we have the printed samples, we subject them to quasi-static compression loads until fracture load levels. On the other side, after the generation

of the geometries, we have available the structures to develop the finite element models. Finally, with the experimental response obtained from the test, we will calibrate the elastic and failure properties of the non-isotropic sheet gyroids.

7.3.3.1 Geometric generation of non-isotropic sheet gyroids

In this section, we have generated the non-isotropic gyroids using the free software MSLattice [381]. For this study, we have generated the geometries using uniform relative density and the properties exhibited in Table 7.7. MSLattice establishes the structure limits with the defined parameters, then some unconnected corners appear in the upper and bottom extremes of the boundaries (see the image presented in Table 7.7), which must be removed in the post-processing.

Table 7.7: Defined properties to generate the gyroid's structure in the free software MSLattice using uniform relative density.

Gyroid's properties	
Relative density (%)	30
Unit cell size	1
Sample length (-)	2
Sample width (-)	2
Sample height (-)	2
Mesh density points	30

The relative density defined in Table 7.7 was the same as the volume fraction of the cancellous bone studied in Section 7.2 in order to be able to compare the mechanical behaviour. Regarding the mesh density points, this parameter is related to the quality of the generated TPMS structure, as more density mesh points more quality.

The post-processing was performed in ScanIP software, and the first step was to import the surface geometries created in MSLattice. Using the flood fill tool in ScanIP, we have removed the floating unconnected corners and generated the solid structures. Then, we applied a distorsion thorugh scaling the sheet gyroid in the z direction to try to adjust the non-isotropic behaviour of the cancellous samples. The dimensions of the sheet gyroid from which we started, from now on, the base gyroid, were 20x20x20 mm. We have generated three

new structures called S25, S50 and S100, depending on the applied scaling. The new z dimension is obtained as defined in Equation 7.2.

$$L' = L_0 + \beta L_0 \qquad (7.2)$$

where L_0 is 20 mm, the base gyroid (B) dimension and β is the scale factor. Table 7.8 collects the terminology for each new gyroid type, the scale factor used for generating the gyroids and the new z dimension L'_0 for each type. By scaling the geometry of the base gyroid (B) and not the mesh, we avoid the distortion of the meshed elements. Once the scaled process is done, we can export the solid geometries of the new gyroids to the STL file because it is the format used in the 3D printers for manufacturing.

Table 7.8: Scale factors applied to the z direction of the base-gyroid (B) to create stretched structures S25, S50 and S100.

Terminology	Scale factor	z dimension (mm)
B	0	20
S25	0.25	25
S50	0.5	30
S100	1	40

7.3.3.2 3D printing process to obtain the polylactic acid (PLA) samples

Using the STL files exported from ScanIP with the solid geometries and a 3D printer, we obtained the polylactic acid (PLA) samples. For manufacturing, we have employed an Ultimaker S3 3D printer and Ultimaker Cura 4.13.1 to define all the printing parameters and the positioning of the pieces in the hotbed. The printing parameters were the same as explained in Section 7.2.1. However, it is essential to highlight that we have printed the gyroids in two different directions to study the influence of layer deposition in the printing process.

As illustrated in Figure 7.17, we printed some pieces depositing each layer in the z direction, whereas some others were printed in the y direction. We printed two pieces per type and printing direction, and then, finally, we obtained twelve samples. It is possible to appreciate in the magnification sections of Figure 7.17, that in the z direction manufacturing, the layers are deposited
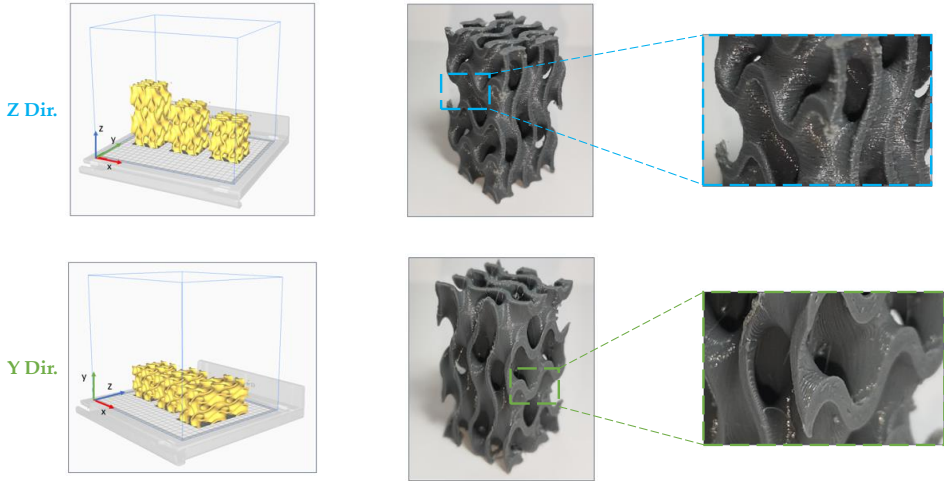
Figure 7.17: Printing directions to analyse the influence of the layer deposition on the gyroids mechanical behaviour.

along the stretched axis, whereas in the y direction manufacturing layers are parallel to the axis. In addition, it is important to consider that the load direction will be the same for all the samples, the scaled direction which corresponds to the z direction.
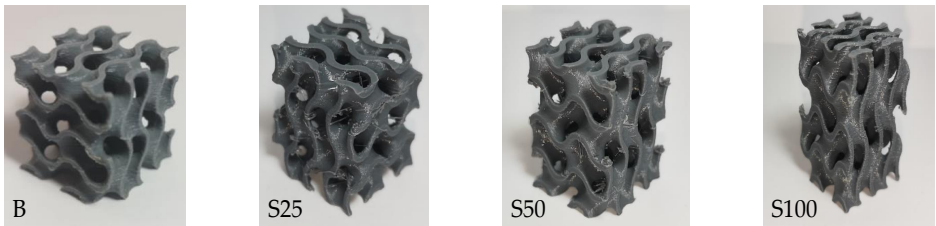
Figure 7.18: Base gyroid (B) and the new scaled gyroids: S25, S50 and S100 obtained by 3D printing using polylactic acid (PLA).

As with the gyroid and the cancellous bone surrogate, the structures were self-reliant and did not need any supports, which avoided the post-processing required to remove the supports. Figure 7.18 presents the base gyroid (B) used in the previous section and for scaling the geometry and the new gyroids: S25,

S50 and S100. It is possible to appreciate several PLA strings that remain in some holes in the structures. It is important to consider that this technology has associated a surface finish with certain inaccuracies. Nevertheless, they do not influence the mechanical properties, so they are only aesthetic but not mechanical drawbacks.

7.3.3.3 Analysis of the mechanical compression behaviour of non-isotropic sheet gyroids

In this section, we study the mechanical behaviour of the three new types of gyroids: S25, S50 and S100. To this end, we have carried out two analyses. First of all, we tested all the samples in the elastic range under quasi static compression loads. The aim is to study the influence of the material deposition in manufacturing and to obtain the apparent modulus E_{app} of the pieces. For these tests, we employed an electromechanical testing machine MTS Criterion C42 (MTS Systems, USA), with a load cell of low rated load, namely 5 kN (see Figure 7.19 left). On the other hand, we analyse the failure in the gyroids by subjecting the samples to high load levels until fracture occurs. The failure tests were conducted by applying quasi static compression loads in the z direction because it is the modified one. In this case, we used a servo-hydraulic testing machine INSTRON 8801 (Norwood, Massachusetts, USA) with a load cell of 100 kN that enables us to test the samples until the failure point (see Figure 7.19 right).

We have calculated the apparent elastic modulus (E_{app}) for each stretched gyroid S25, S50 and S100 in the three orthogonal directions. Moreover, the average apparent elastic modulus ($\bar{E}_{app}$) for samples with the same scaling factor and manufacturing direction are also estimated. Table 7.9 collects all the obtained results related to the elastic tests. Regarding the mechanical behaviour, in the columns of the average apparent elastic modulus ($\bar{E}_{app}$) in the x direction, it is easier to identify a clear trend in the results in both manufacturing directions. The apparent results for S25 manifest higher values than for S100 because of the changes in the morphometry.

We conducted an ANOVA statistical analysis to study whether the apparent Young's modulus collected in Table 7.9 present significant differences when comparing the same stretched structure manufactured in two different directions. The study has been developed in Statgraphics Centurion 18 (Statgraphics Technologies, Inc., Princeton, USA), and we state that significant differences exist when the p-value is lower than 0.05. Table 7.10 presents the p-values obtained from the ANOVA analyses.

Electromechanical testing machine   Servo-hydraulic testing machine

MTS C42 Criterion

INSTRON 8801

Figure 7.19: Electromechanical testing machine MTS C42 Criterion (left) and servo-hydraulic testing machine INSTRON 8801 (rigth).

We have manufactured in two different directions, as shown in Figure 7.17, to evaluate if the manufacturing direction has influence on the apparent behaviour of the stretched structures. The results of the ANOVA analyses reveal that the apparent Young's modulus (E_{app}) is statistically different for S50 when we tested them in one of the transversal directions, namely the x direction. The least stretched structure, S25, presents significant differences in E_{app} when they are tested in the y transversal directions and also in the stretched direction z. S100 does not exhibit significant differences. Therefore, this structure can be manufactured in either of the directions, and the E_{app} will be the same for both cases. These results lead us to conclude that maybe the number of samples is insufficient to establish whether these differences are really due to the influence of the layer deposition during the printing or is only the dispersion of the results. It is important to highlight that the manufacturing and experimental tests introduce several errors in the results. Therefore, we finally state that these differences are due to the artifacts introduced during the printing and the tests and not due to the layer deposition. Consequently, from now on, we will consider all the results together without separating them for manufacturing direction, we will only differentiate between scaled structures S25, S50 and S100.

Table 7.9: Results for the compression apparent elastic modulus (E_{app}) for S25, S50 and S100 stretched gyroids calculated at the three orthogonal directions of the samples and the averaged $\bar{E}_{app}$ for samples with same scaling factor and manufacturing direction.

Manufacturing direction		*z* direction		*y* direction	
Test direction	Tested structure	E_{app} (MPa)	$\bar{E}_{app}$ (MPa)	E_{app} (MPa)	$\bar{E}_{app}$ (MPa)
x direction	S25-1	225.40	227.66	225.43	219.54
	S25-2	229.92		213.66	
	S50-1	181.85	181.26	208.52	205.36
	S50-2	180.67		202.19	
	S100-1	168.78	163.44	167.15	147.92
	S100-2	158.09		128.68	
y direction	S25-1	264.91	269.28	230.71	232.32
	S25-2	273.65		233.93	
	S50-1	234.04	225.91	205.09	205.63
	S50-2	217.78		206.18	
	S100-1	177.60	171.47	147.18	151.23
	S100-2	165.34		155.29	
z direction	S25-1	305.24	292.04	402.06	400.21
	S25-2	278.84		398.36	
	S50-1	432.19	428.50	469.58	427.88
	S50-2	424.81		386.19	
	S100-1	524.82	525.33	484.88	502.36
	S100-2	525.85		519.85	

Owing to we will consider all the results together, we have averaged the results obtained for the apparent modulus per structure type for having the overall behaviour of each type of stretched structure, which are collected in Table 7.11. As can be appreciated, for the base gyroid (B), we only studied one sample per orthogonal direction, so we have the information limited to these results, which were presented in the previous section in Table 7.5. In addition, comparing the results obtained for the gyroid (B) and the scaled structures S25, S50 and S100, it can be seen that in x and y directions, the results for all the structures are pretty similar.

The bar graph exhibited in Figure 7.20 allows a better comparison between the studied structures. It is possible to visually assess how the stretched structures behave in relation to the base gyroid (B). One of the most relevant conclusions that can be extracted from this bar graph is that the scaling has enabled the adjustment of the non-isotropic properties according to the

Table 7.10: Summary of the p-values from the ANOVA statistical analysis when comparing the apparent Young's modulus (E_{app}) obtained for the stretched structures manufactured in different directions.

Structure	Test direction		
	x	y	z
S25	p=0.3269	**p=0.0155**	**p=0.0148**
S50	**p=0.0174**	p=0.1306	p=0.9896
S100	p=0.5183	p=0.1105	p=0.3275

Table 7.11: Averaged apparent modulus of elasticity for each tested direction for the stretched structures S25, S50 and S100.

	$\bar{E}_{\mathrm{app}} \pm$ standard deviation (MPa)			
	B	**S25**	**S50**	**S100**
x **direction**	216.18	223.60 ± 6.03	193.31 ± 12.26	155.68 ± 16.11
y **direction**	216.07	250.80 ± 18.77	215.77 ± 11.66	161.35 ± 11.38
z **direction**	250.87	346.12 ± 54.90	428.20 ± 29.60	513.85 ± 16.88

patient requirements. In addition, an ANOVA statistical analysis has been conducted to verify if the E_{app} results obtained for both x and y directions are statistically different or not. The results of the ANOVA conclude that the presented results for these two orthogonal directions do not present significant differences, which means that it has been achieved transversely isotropic properties. Moreover, the E_{app} results decrease for the highest scaling factor in these two orthogonal directions. This behaviour is related to the distortion introduced in the structure once the scaling of the gyroid geometry. By scaling the z direction, the gyroid architecture is oriented to a greater degree in such direction, which causes the transverse stiffness to decrease.

Finally, with the scaling procedure, we have managed to increase rigidity concerning the base gyroid (B) 27.52 %, 41.41 % and 51.18 % for S25, S50 and S100 structures, respectively. Regarding the difference between the results of the transverse directions and the scaled direction for each structure, from S25 to S100 are 31.47 %, 52.23 % and 69.15 % higher for the scaled direction. This study manifests that a distorted gyroid structure in one direction can take advantage of the TPMS features, such as less stress concentrators or a high surface area volume ratio, together with a controlled non-isotropic prop-
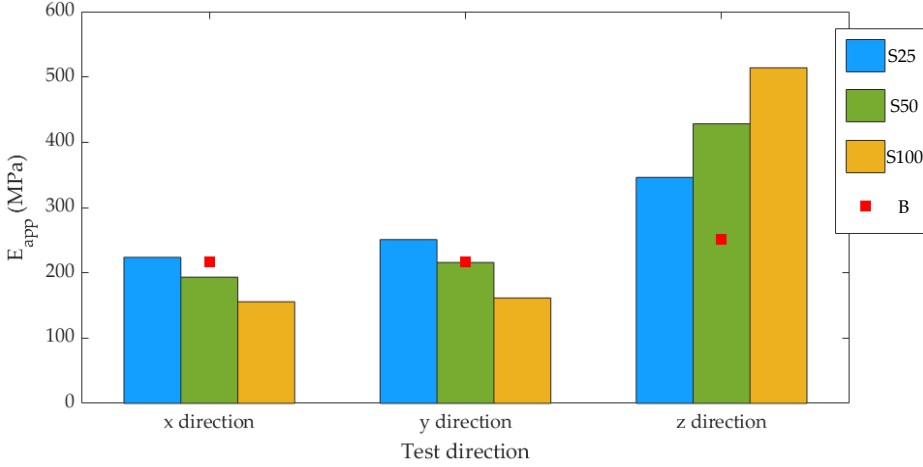
Figure 7.20: Summary of the apparent elastic modulus E_{app} for the gyroid (B) and the scaled structures S25, S50 and S100 for each test direction.

erties. This procedure could overcome the limitation that TPMS structures present to reproduce the cancellous bone behaviour.

Regarding the achieved non-isotropy, we have estimated the degree of anisotropy (DA) of each scaled structure S25, S50 and S100 using the averaged $\bar{E}_{\text{app}}$ values presented in Table 7.11. To estimate the degree of anisotropy (DA), we have defined the inverse of the ratio of the stiffness in the transverse to the longitudinal direction as defined in Equation 7.3.

$$DA = \frac{\bar{E}_{app-z}}{\frac{(\bar{E}_{app-x}+\bar{E}_{app-y})}{2}} \tag{7.3}$$

Figure 7.21 presents the estimated DA for each structure. It is essential to consider that the DA of the base gyroid (B) should be 1, but the possible experimental and manufacturing errors make the DA a bit higher, even though it is pretty near to one.

The degree of anisotropy (DA) has been represented against the scaling factor (β), as shown in the image exhibited in Figure 7.21. We have adjusted the results to a linear expression presented in Equation 7.4. As illustrated, as the scaling factor (β) increases, the degree of anisotropy (DA) also increases following the linear expression presented in Equation 7.4. Therefore, with this

Degree of anisotropy (DA)	
B	1.16
S25	1.46
S50	2.10
S100	3.24
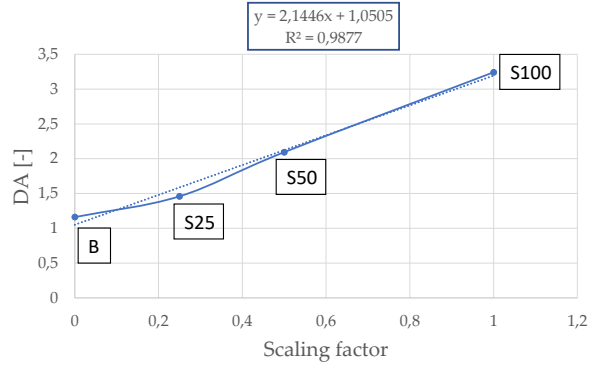
Figure 7.21: Degree of anisotropy (DA) estimated for the based gyroid (B) and the stretched gyroids: S25, S50 and S100.

expression, we can choose the desired DA depending on the bone specimen defect and then scale the gyroid with the corresponding scaling factor.

$$DA = 2.1446\beta + 1.0505 \tag{7.4}$$

In the following, the results obtained for the compression test until failure will be presented. It is crucial to emphasise that the compression tests until failure load levels have been carried out in the z directions, corresponding to the scaled direction for the S25, S50 and S100 structures. Figure 7.22 illustrates the averaged stress-strain curves for the scaled structures S25, S50 and S100 represented in a continuous line, whereas the strain-stress curve for the base gyroid (B) is represented in dashed line. The results manifested a direct relationship between architecture distortion and mechanical properties. The samples have higher values for the apparent elasticity modulus (E_{app}) and for the failure stress (σ_{f}). In addition, all the stretched structures can withstand higher load levels than the base gyroid (B) and are stiffer than B.

Regarding the numerical values, the averaged results are exhibited in Table 7.12 together with the base gyroid (B) values obtained in the previous sections. The trend of the presented results can be appreciated in Figure 7.22. However, the numerical values allow us to quantify the results. As visually evaluated, the greater values both for $\bar{E}_{\mathrm{app}}$ and $\bar{\sigma}_{\mathrm{f}}$ are for S100 structure. With the scaling, S100 structure can withstand 43.98 % more stress levels than the base gyroid (B) and 17.72 % more stress than S25. Regarding the apparent

271
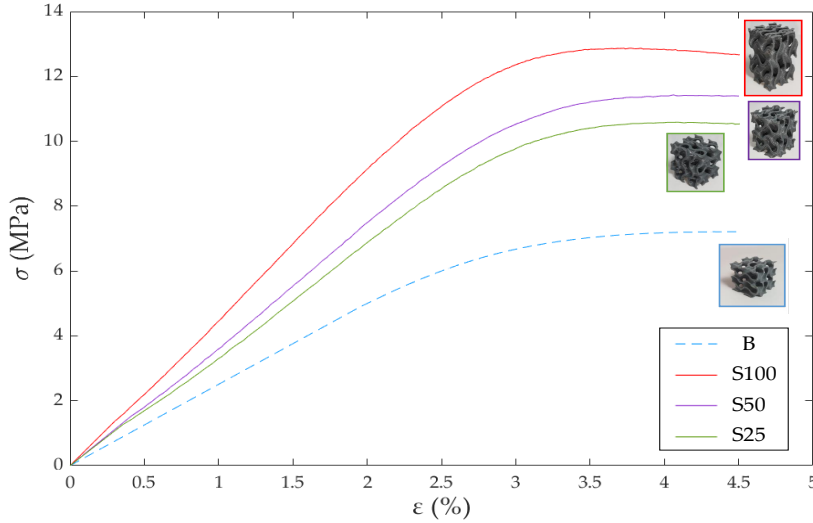
Figure 7.22: Averaged experimental stress-strain curves for the stretched structures S25, S50 and S100 and the stress-strain curve for the base gyroid (B).

Young's modulus, S100 structure is 46.15 % stiffer than the base gyroid (B) and 25.87 % more than S25.

Table 7.12: Experimental results obtained from the compression tests until failure load levels for the scaled structures S25, S50 and S100 and the results for the base gyroids (B) obtained in the previous sections.

	B	**S25**	**S50**	**S100**
$\bar{E}_{\mathbf{app}}$ **(MPa)**	250.87	345.33 ± 20	378.17 ± 25	465.85 ± 15
$\bar{\sigma}_{\mathbf{f}}$ **(MPa)**	7.21	10.59 ± 0.02	11.43 ± 0.33	12.87 ± 0.58
$\bar{\varepsilon}_{\mathbf{f}}$ **(-)**	0.044	0.041 ± 0.003	0.041 ± 0.006	0.038 ± 0.003

Concerning the failure strains ($\bar{\varepsilon}_{f}$), it can be appreciated that the strains are pretty similar for all the structures. Therefore, we conducted a statistical analysis to evaluate if they present significant differences. The analysis conclusion is that there are no significant differences, which means that failure strains are independent of the scaling, all the structures failed around 0.04. These results mean that the behaviour of these structures is dominated by the strain and not by the stress.

7.3.3.4 Numerical calibration of the elastic and failure properties of non-isotropic sheet gyroids

In order to obtain the numerical models, we used the finite element (FE) module in ScanIP to generate the meshes of the new gyroid geometries. The FE models were meshed with linear tetrahedron, type C3D4 in Abaqus, as presented in Figure 7.23. Analogously to the cancellous bone surrogate and the gyroid, we applied a controlled displacement to mimic the quasi static compression load of the experimental tests. The applied displacement is the 5 % of the z direction. In the opposite area, which corresponds to $z = 0$, we constricted the model to avoid any movement in the displacement direction. In FE models, it has been implemented a damage model that considers four levels of properties degradation when the elements begin to fail.
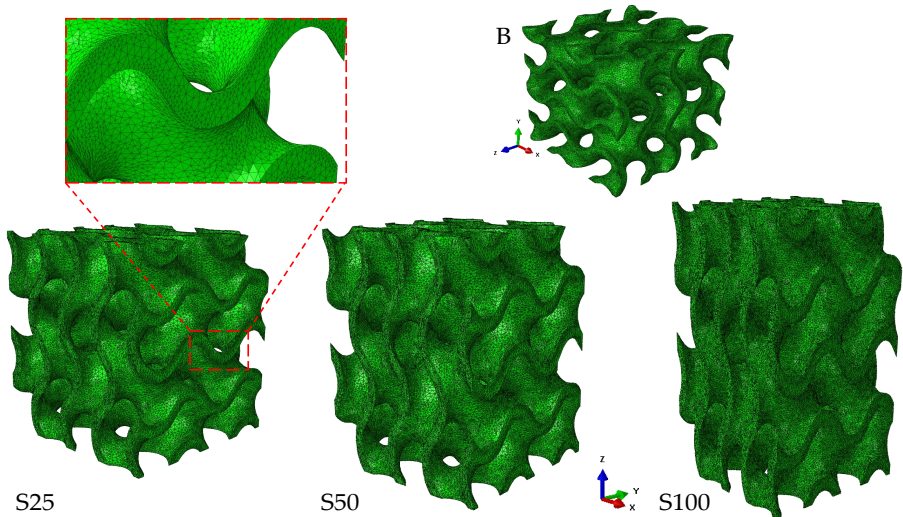
Figure 7.23: Finite element (FE) models for each scaled structure meshed with linear tetrahedron. Extended area to appreciate the spatial discretisation.

First of all, we have calibrated the Young's modulus of the materials. All the samples have been manufactured with the same type of filament: PLA, Antracite colour from Smart Materials 3D [385]. This parameter is estimated using the elastic range of the stress-strain curve. The calibrated E_{cal} for each scaled structures are presented in Table 7.13.

The calibrated elasticity modulus (E_{cal}) for all the analysed structures are pretty similar. We hypothesise that the differences observed rely on the inher-

Table 7.13: Summary of calibrated Young's modulus (E_{cal}) values of the material used for printing for the base gyroid (B) and the stretched structures S25, S50 and S100 and the averaged Young's modulus ($\bar{E}_{\text{cal}}$) for the PLA.

	B	**S25**	**S50**	**S100**
E_{cal} **(MPa)**	2411.74	2441.74	2570.66	2655.56
$\bar{E}_{\text{cal}}$ **(MPa)**	2519.925 ± 113.71			

ent variability in material characterisation. The obtained results are less than a 10 % difference between the highest and the lowest values. The estimated value for the base gyroid (B) is extracted from the previous sections when we calibrated such TPMS structure. In Table 7.13 is presented the average Young's modulus ($\bar{E}_{cal}$) for the printing material, the polylactic acid (PLA). The provided Young's modulus by the manufacturer is 3300 MPa, a 23.6 % higher than the average Young's modulus for the PLA.

Once we have estimated the Young's modulus of the PLA, it is time to calibrate the yield onset strain (ε_{y}) and failure failure strain (ε_{f}). In this process, to study the failure of the studied structures, we have also degraded the stiffness of each element when it fails. Table 7.14 presents the results for the calibrated failure strains ε_{y} and ε_{f}, as well as the degradation employed when the elements fail. In this section, we do not calibrate the base gyroid (B), we did it in the previous section, so the gyroid results are shown in Table 7.6, such as is indicated in Table 7.14.

Table 7.14: Element stiffness degradation used to calibrate the numerical models and the calibrates strains: yield strain (ε_{y}) and failure strain (ε_{f}).

	Element degradation				**Calibrated strains**	
	E1	E2	E3	E4	ε_{y} (-)	ε_{f} (-)
B	0.20	0.40	0.60	0.68	0.03 (Table 7.6)	0.08 (Table 7.6)
S25	0.15	0.25	0.65	0.70		
S50	0.18	0.30	0.60	0.65	0.03	0.08
S100	0.20	0.45	0.62	0.65		

One important conclusion extracted from these results is that the calibrated values for both ε_{y} and ε_{f} are the same for all the scaled structures, regardless of size, even for the base gyroid. These results reinforce the hypothesis manifested in the experimental results section, in which it had already been

observed that the scaled structures have approximately the same failure strain value. Thus, the failure of gyroid TPMS structures is governed by strain rather than stress. The failure criterion allows the identification of the elements that have failed in each load step. The stiffness of these elements is penalised, degrading it. Table 7.14 presents the stiffness degradation at each of the four steps when the element fails. As can be appreciated, the degradation percentage at each stage is almost the same. In the first stage, the degradation is around 18 %, in the second one, 35 %, whereas in the third and the fourth stages, the values are around 60 and 70 %. Owing to the calibrated Young's modulus is not exactly the same for each structure, it is permissible to have slight variations between the degradation percentage at the same stage.
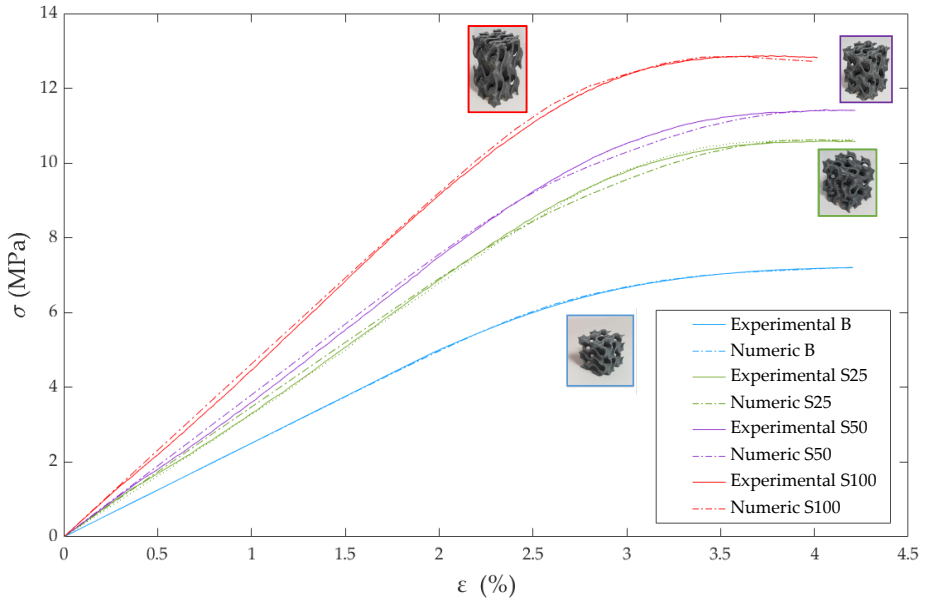
Figure 7.24: Experimental stress-strain curves and the numerical calibration for the base gyroid (B) and the Stretched structures S25, S50,S100.

Figure 7.24 presents the experimental stress-strain curves, represented in continuous stroke, for the base gyroid (B) and the scaled structures S25, S50 and S100, as well as the numerical calibrations, represented in dashed stroke. The experimental stress-strain curves correspond to the average stress-strain curves of the four studied samples per type. For this reason, in the elastic range of the curves, the numerical response is not exactly the same due to the average. As can be seen, the three relevant points of the curves are really well

captured by the FE models, so we can state that the FE models can represent the scaled structures' compression mechanical behaviour.

Finally, trying to fix the problem of reproducing the longitudinal direction behaviour, we have scaled the z direction of the gyroid with three different scaling factors (β) and we obtained the so-called S25, S50 and S100 stretched structures. We stated that S100 structures can support 43.98 % more stress level than the TPMS gyroid and also, the apparent Young's modulus is 46.15 % greater than the gyroids' modulus. To sum up, in Figure 7.25 we have presented the compression stress-strain curves for the experimental and numerical response for the z direction, the longitudinal direction from the cancellous bone surrogate and the scaled directions of the gyroid, to compare the difference and to conclude if we can reproduce the cancellous bone behaviour.

Table 7.15: Summary of the apparent modulus of elasticity (E_{app}), final stress (σ_{f}) and failure strain (ε_{f}) for the cancellous bone surrogate (CB), base gyroid (B), and the scaled structures little (P), medium (M) and big (G) obtained at the z direction.

	E_{app} **(MPa)**	σ_{f} **(MPa)**	ε_{f} **(-)**
CB	432.38	10.24	0.042
B	250.87	7.20	0.042
S25	345.33	10.59	0.041
S50	378.17	11.43	0.041
S100	465.85	12.87	0.038

The numerical values for the the apparent modulus of elasticity (E_{app}), failure stress (σ_{f}) and failure strain (ε_{f}) are collected in Table 7.15. As can be appreciated both in Figure 7.25 and in Table 7.15, the three stretched structures S25, S50 and S100 have greater values for the failure stress than the cancellous bone (CB) surrogate. Thus, any of the three scaled structures could be valid. However, one relevant point in the implants is to avoid stress-shielding, which requires similar Young's modulus between the implant and the surrounding bone. Therefore, the structure that meets the specifications is S100 geometry.

Concerning the failure strain values, it is concluded that all the structures failed at similar strain levels, around 0.04. Therefore, we can state that the behaviour of these PLA samples is governed by the strain and not by the stress. Finally, it is important to highlight that the generated FE models capture pretty good the compression stress-strain curves obtained at the compression

experimental tests. Figure 7.25 illustrates in dashed lines the calibration of the numerical models and all of them capture the three main points of the curves which are the Young's modulus of the material (E_{cal}) in the linear range, the yield strain (ε_{y}) and the failure strain (ε_{f}). Then, we have also validated our FE models to study such structures varying any parameter.
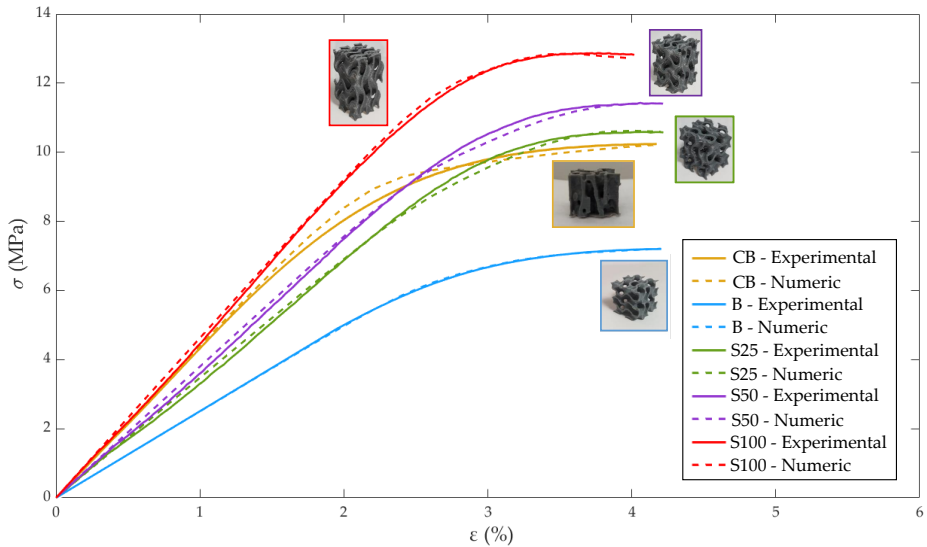
Figure 7.25: Experimental stress-strain curves and the numerical calibration for the cancellous bone surrogate (CB), base gyroid (B) and the stretched structures S25, S50 and S100 for the z direction.

7.4 Conclusions

In this chapter, we have studied the compression mechanical behaviour of cancellous bone surrogates, TPMS structures, namely sheet and solid gyroids and non-isotropic TPMS designs. PLA samples were subjected to quasi static compression loads until fracture levels. With the combination of the experimental stress-strain curve and the FE models, we have estimated the elastic and failure properties: the Young's modulus, the yield strain (ε_{y}) and the failure strain (ε_{f}).

As regards the study of the compression mechanical behaviour of the cancellous bone surrogates. Our study has permitted the evaluation of the influence of cancellous bone architecture on the mechanical response, overcoming some

of the limitations inherent to testing biological tissues under destructive conditions. Moreover, we have proposed a damage evolution law for rod-like and plate-like structures.

Once we are able to reproduce the cancellous bone behaviour with a surrogate, we would like to mimic this behaviour with structures that can be used as an implant in large bone defects. In recent years, the triply periodic minimal surface (TPMS) structures have gained huge importance due to their advantages against other reticular structures usually employed in scaffolds design. We concluded that sheet geometry is stiffer than solid geometry and can withstand greater stress levels. However, the symmetry of these structures implies an isotropic behaviour, equal in the three orthogonal directions of the sample. Hence, we have proposed a methodology that permits the adjustment of those non-isotropic properties patient-specific. It implies the geometry distortion to control morphometry variation along one axis. Our results reveal that the anisotropy degree can be adjusted between 1 to 3.26, thus overcoming an inherent limitation of usual TPMS structures.

Chapter 8

Thesis conclusions and main contributions

8.1 Conclusions

In this thesis, the lamellar tissue and the mechanical behaviour of human cancellous bone has been studied using different experimental and numerical approaches. The main conclusions and contributions extracted from the results are presented in this chapter.

Image analysis of cancellous bone

Human and swine cancellous bone specimens have been evaluated using imaging techniques, such as stereomicroscopy, micro-CT and Field Emission Scanning Electron Microscopy (FESEM). The lamellar tissue has been assessed at the FESEM to analyse the lamellae orientation. We observed that the lamellae are arranged circumferentially around the holes, and in the single trabecula, along the thickness parallel to the trabeculae surface. Where two trabeculae meet, there is no main orientation of the lamellae, so in such locations, they approximately present an isotropic behaviour due to the lack of orientation of

the lamellae. With the FESEM, we were able to capture the canaliculi network, which is one of the primary sources of porosity of the lamellar tissue. This information will be used to define the finite element models properties.

Estimation of equations for the elastic constants of lamellar tissue as a function of BMD and porosity

Equations for the elastic properties of the lamellar tissue as a function of the bone mineral density (BMD) and the porosity have been estimated. These expressions allow the study of diverse scenarios with a wide range of BMD and percentage of porosity, from the natural porosity of the lamellar tissue (healthy specimens) or high porosity levels due to bone disease.

The relevance of defining lamellar bone tissue properties as an orthotropic material has been evaluated and compared to isotropic tissue properties. The results reveal that the the apparent modulus of the transversal directions is overestimated, whereas in the stiffest direction of the cancellous specimen, the apparent modulus is underestimated when using isotropic tissue properties.

Estimation of equations for the strength limits of lamellar tissue as a function of BMD and porosity

Equations for the in-plane strength limits of the lamellar tissue as a function of the bone mineral density (BMD) and the microporosity have been estimated. These expressions are estimated for a BMD range between 0.4 to 1.80 g/cm^3 and a range of porosity between 1 to 5 %. This range of porosity only encompasses the natural porosity of the lamellar tissue. We have modelled the porosity as ellipsoids due to the geometry of the osteocyte lacunae.

The results present a strong influence of the porosity due to the lacunae and the stress concentration they cause at the lamellar tissue. This trend is evidenced irrespective of the mineral content. These cavities at the tissue reduce the effective cross-section and behave as a stress concentrator, leading to increased stress and strain levels around them. This phenomenon occurs around the lacunae rather than in other locations of the extracellular matrix, which is the most preferred location for microcracks to arise.

From the estimated equations, it has been evidenced that the compressive strength is higher compared to tensile strength in both the longitudinal and transverse orientations of the lamellar tissue. This contrast becomes more noticeable with higher bone mineral density (BMD) and lower tissue microp-

orosity. This aligns with the predominant mechanical role under compression of the hydroxyapatite mineral phase, as collagen fibers tend to bend and experience premature failure. To estimate shear strength, a composite material approach has been employed.

Mechanical behaviour characterisation of healthy, osteoarthrosic and osteoporotic human cancellous bone

The mechanical behaviour of healthy (HG), osteoarthrosic (OA) and osteoporotic (OP) human cancellous femoral specimens has been evaluated, using imaging techniques, compression tests and finite element models.

We have carried out compressive quasi-static tests. From the stress-strain curves, we have calculated the failure stress σ_{f} ranged between 6.18 to 10.93 MPa, the failure strain ε_{f} between 0.016 to 0.024 and the apparent Young's modulus E_{app} between 645.47 to 1022.82 MPa. The ANOVA statistical analysis stated that for the three analysed parameters, significant differences exist between HG and both OA and OP specimens. Therefore, the apparent results enable us to distinguish between healthy and diseased specimens. It is important to highlight that the microarchitecture of the specimens directly influences these results.

A morphometric analysis was developed with the cancellous specimens from the three study groups. The results showed we can differentiate between healthy and diseased cancellous samples with the surface ratio (BS/BV) and the mean trabecular thickness (Tb.Th). The osteoporotic samples can be differentiated from the HG and OA specimens using the bone volume fraction (BV/TV) and the trabecular number (Tb.N). We analysed the relationship between the studied morphometric parameters and the information extracted from the mechanical response. The strong correlations obtained for each group allow us to estimate the mechanical response using the micro-CT images without the need of experimental tests. In addition, the mechanical response parameters were related to each other. Results revealed different behaviours depending on the pathology. OA specimens showed more ductile behaviour, while OP samples were more brittle. The relation found for HG makes it possible to determine the failure stress using the apparent Young's modulus.

On the other hand, we generated numerical models to estimate the elastic and failure properties using the stress-strain curves from the compression tests. We estimated Young's modulus at tissue level E_{cal} ranged from 18 to 20 GPa, a yield strain ε_{y} between 0.0045 and 0.0059, and a failure strain ε_{f} between 0.025

to 0.054. We also developed an ANOVA analysis to evaluate the results, and it concluded that neither for E_{cal} nor ε_{y} presented significant differences between the results. Regarding E_{cal}, the results can be explained because the mineral content is the same at the tissue level regardless of the pathology. The results for ε_{y} revealed that the yield behaviour of the cancellous bone was similar for all the samples despite the bone condition. Lastly, ε_{f} statistical analysis presented significant differences between OP and HG specimens. Hence, it can be stated that the failure behaviour is the one that is different between samples and where the bone disease has an influence. Ductile specimens would admit higher strains, whereas brittle specimens failed at lower strain levels.

We also estimated apparent and tissue properties from the micro-CT images, and then we compared the results with those obtained from the compression tests and the numerical calibration. The apparent density ρ_{app} and the apparent modulus E_{app} of the cancellous specimens from the femoral heads have been determined. With the bone mask grey values, we have estimated the mineral density and Young's tissue modulus. We conclude that the estimation of the apparent Young's modulus through the experimental tests underestimates the obtained results. The estimation of the tissue Young's modulus with both methods only differs by 12-16 %.

Mechanical characterisation of cancellous bone surrogates and gyroids manufactured in PLA

The mechanical compression behaviour of cancellous bone surrogates and triply periodicity minimal surface (TPMS) structures obtained by additive manufacturing using polylactic acid (PLA) was analysed. Cancellous bone surrogates present an orthotropic behaviour, such as the cancellous bone specimens. Therefore, they can be used to perform previous studies when cancellous specimens are not available.

We have evaluated the TPMS structures as implants for large bone defects to replace the commonly used lattice scaffolds. We have analysed the gyroid structure, both their sheet and solid typologies. Owing to their triply periodicity, with TPMS structures, we can only mimic an orthotropic behaviour.

To overcome the limitation of reproducing the non isotropic behaviour of the cancellous specimens, we have proposed a methodology to adjust the orthotropic properties of TPMS bone scaffolds through the distortion of the structure by scaling one direction. We studied three scale factors, which are 25 %, 50 % and 100 %. The results show that the methodology proposed per-

mits the adjustment of the orthotropic properties of the scaffold and enable to design patient specific solutions that take into account the bone mechanical properties of the vinicity of the bone defect.

8.2 Main contributions of the thesis

- The lamellae orientation at the lamellar tissue has been evaluated using FESEM. We observed that the lamellae are oriented circumferentially to the holes and, in the single trabecula, are parallel to its surface. In a branch, where two trabeculae meet, there is a lack of orientation of the lamellae, so in such locations, the lamellar tissue approximately presents an isotropic behaviour.

- Using FESEM, we have captured the natural porosity of the lamellar tissue, whereas in diseased specimens, we were able to capture the degradation of the lamellar tissue due to the pathology.

- Equations for the elastic properties of lamellar tissue as a function of bone mineral density (BMD) and porosity have been estimated.

  - These equations enable the study of both healthy and diseased cancellous specimens, just changing the BMD and porosity values.

  - Failure was defined using the Hashin criterion in combination with the Material Property Degradation Method (MPDG). This criterion allows to distinguish between fibers and matrix failure.

- Equations for the in-plane strength limits at lamellar tissue as a function of BMD and microsporosity have been estimated.

  - We reported a high influence of the porosity due to the osteocyte lacunae on the increase of the stress at the tissue level. This trend is observed regardless of the mineral content.

  - Stress and strain increase around the osteocytes rather than other locations of the extracellular matrix being the most potential location for microcracks initiation.

  - The shear strength limit has been estimated using a composite materials approach.

- We have evaluated the mechanical behaviour of healthy (HG), osteoarthrosic (OA) and osteoporotic (OP) human cancellous femoral specimens,

using different approaches: imaging techniques, compression tests and finite element models.

- The ANOVA statistical analysis revealed that with the parameters obtained from the stress-strain curves (σ_f, ε_f and E_app), it is possible to differentiate between healthy and diseased cancellous specimens. The microarchitecture of the specimens directly influences these results.

- A morphometric analysis was developed and the results revealed that we can distinguish healthy samples from diseased ones with the surface ratio (BS/BV) and the mean trabecular thickness (Tb.Th). Osteoporotic cancellous specimens can be differentiated from the other two groups with the bone volume fraction (BV/TV) and the trabecular number (Tb.N).

- Strong correlations were found between several morphometric parameters and the mechanical response (σ_f, ε_f and E_app). These results allow us to estimate the mechanical response using micro-CT images instead of experimental tests.

- The mechanical response parameters were related to each other, and the results showed the behaviour of the specimens. Brittle behaviour for OP and ductile behaviour for OA. The failure stress can be estimated with the apparent Young's modulus for HG.

- The tissue Young's modulus was estimated between 18 to 20 GPa for all the groups. These results manifest that the tissue Young's modulus is similar for all the groups, irrespective of whether the bone suffers a pathology or not.

- The estimated yield strain resulted in 0.0045 to 0.0059, which means that the yield behaviour is similar for all the cancellous samples.

- Failure strain presents differences in the estimated results between groups. This evidence is in concordance with the behaviour of bone; some specimens present a brittle behaviour, whereas others are more ductile.

- The methods employed to determine the apparent Young's modulus revealed that the experimental tests underestimate the obtained results. Therefore, micro-CT images will be a better approach to

estimate the apparent Young's modulus. Regarding tissue Young's modulus, it is possible to achieve similar results with both methods.

- A methodology has been proposed to design patient-specific bone scaffolds to fix large bone defects using triply periodic minimal surface (TMPS) structures. This method allows to calibrate the orthotropic mechanical properties in each direction according to a specific bone.

Chapter 9

Future work

After developing this research, we found several issues that can be addressed in the future.

First of all, we intend to develop compression tests inside the scanner to provide more information during the compression tests. Therefore, we will acquire micro-CT images at each load step. This option enables the evaluation of trabecular failure and the representation of the local damage. In addition, we could relate the damage accumulation with the microarchitecture condition and compare healthy and diseased specimens.

In this thesis, we evaluated the morphometry of cancellous bone specimens obtained after replacing the femoral head with a prosthesis. With this method, we can just analyse the bone microarchitecture in that time step. We propose using photon-counting CT (PCCT) or high resolution peripheral quantitative computed tomography scanners, allowing continuous study over time. Throughout these cohort studies, we will be able to analyse the evolution of cancellous bone microarchitecture during a drug treatment for osteoporosis and study the effects and improvements produced in the bone. This analysis will be patient-specific and could overcome the advantages and disadvantages of a treatment for each patient. Moreover, doctors can monitor patients' bone status with periodic scans to assess the state of the cancellous bone and then diagnose any bone disease.

Regarding the estimated equations for the elastic properties of lamellar tissue as a function of bone mineral density (BMD) and porosity, we must extend the BMD range up to 1.80 or 1.90 g/cm^3 in order to apply these equations for cancellous bone specimens to different body locations. In this thesis, we have estimated BMD for cancellous femoral samples between 1.15 and 1.85 g/cm^3. The BMD upper limit for the estimated equations is 1.50 g/cm^3, which does not allow to calculate the elastic properties at the tissue level for several of our femoral specimens.

On the other hand, we have the equations to estimate the strength limits as a function of BMD and microporosity. In this case, the BMD upper limit is 1.80 g/cm^3. However, the porosity percentage only concerns natural tissue porosity. In order to use these equations to evaluate bone pathologies, such as the increase in tissue porosity due to the illness, we need to study higher porosity levels. Moreover, it is essential to consider the geometry of the pores when the source of porosity is a bone disease. In these cases, the sphere shape could better mimic this kind of pores.

In the same line, and trying to evaluate the porosity percentage, we can use FESEM images to this end. Quantifying the tissue porosity using FESEM images, we would know the percentage of porosity that we should include in the elastic and resistant equations to mimic the specimen conditions as much as possible to reproduce accurately its behaviour throughout the numerical models.

In order to study other types of osteoporosis, we can remake the criteria to divide samples into groups to include people younger than 65 years old in the osteoporotic group. With this new criterion, we can study how osteoporosis affects premenopausal women, which was not possible in our present research. We can divide the osteoporotic group by the patient's sex and age to analyse how osteoporosis affects bone morphometry and the behavior of bone depending on the stage of the disease and the sex because it is more severe for women than for men.

Similarly, we can divide the osteoarthrosis (OA) specimens depending on the grade of the disease because of the differences in the OA microarchitecture. In the first stage, bone loss material, whereas in the last stages of the disease, a calcification in localised regions is shown. These differences presented in the cancellous bone structure lead to different morphometric results and relationships with the apparent parameters. By further classifying the OA group, we could differentiate the results for each pathology phase, and we can state more consistent results than those obtained grouped all together.

With these specific divisions of the study groups, we suggest to study the morphometric parameters to analyse new relationships and confirm some others. Furthermore, we can also determine behaviour differences between the samples of the same group considering the stage of the disease in OA specimens or the age of the patient in OP. Even though we propose to enlarge the number of specimens to validate the results or to find new evidences that can be detected by increasing the number of specimens.

In order to generate patient-specific implants, starting from the CT image showing the bone defect, we can develop a specific implant that perfectly suits the patient's needs, which will ensure the fixation and the bone growth around the implant. In addition, as a result of this research, we can develop a non isotropic implant that could better suit the defect requirements.

Finally, with a large number of specimens and results, machine learning could enhance some of the processes that we have studied and developed in this research. First of all, we can predict elastic (E_{app}) and failure properties (σ_f, ε_f) based on the morphometric parameters of the cancellous bone. Therefore, we could also predict failure risk and potential bone fractures in patients concerning their bone microarchitecture. Regarding implants and machine learning, with a great database of information, we could choose the most suitable geometry for the implant, knowing the cancellous microarchitecture. This could reduce the implant design time and ensure that the implant will work and contribute to bone remodelling and growth.

List of publications

Research papers in JCR journals

Vercher-Martínez A., Megías R., Belda R., Vargas P., Giner E. *Estimation of the in-plane ultimate strength of lamellar tissue as a function of bone mineral density and osteocyte lacunae porosity.* Computer Methods and Programs in Biomedicine (2024) . Article in press.

Belda R., Megías R., Marco M., Vercher-Martínez A., Giner E. *Numerical analysis of the influence of triply periodic minimal surface structures morphometry on the mechanical response.* Computer Methods and Programs in Biomedicine 230 (2023) 107342.

Megías R., Vercher-Martínez A., Belda R., Peris J.L., Larrainzar-Garijo R., Giner E. Fuenmayor F.J. *Numerical modelling of cancellous bone damage using an orthotropic failure criterion and tissue elastic properties as a function of the mineral content and miroporosity.* Computer Methods and Programs in Biomedicine 219 (2022) 106764.

Belda R., Megías R., Feito N., Vercher-Martínez A., Giner E. *Some practical considerations for compression failure characterization of open-cell polyurethane foams using Digital Image Correlation.* Sensors (2020), 20, 4141.

Conference works

International conferences

Belda R., Megías R., Vercher-Martínez A., Giner E. *Estudio del fallo a compresión en estructuras triplemente periódicas con mínima superficie obtenidas por fabricación aditiva.* 5th Iberian Conference on Structural Integrity, Coimbra, Portugal, 30 March - 1 april 2022(ISSN: 2792-4246).

Megías R., Belda R., Vercher-Martínez A., Giner E. *Explicit expressions for elastic constants of osteoporotic lamellar tissue and damage assessment using Hashin failure criterion.* VI Eccomas Young Investigators Conference (YIC), Valencia, Spain, 7-9 July 2021 (ISBN: 978-84-9048-969-7).

Belda R., Megías R., Vercher-Martínez A., Giner E. *Non-isotropic elastic constants of cancellous bone tissue as a function of morphometry.* VI Eccomas Young Investigators Conference (YIC), Valencia, Spain, 7-9 July 2021 (ISBN: 978-84-9048-969-7).

Vercher-Martínez A., Megías R., Belda R., Giner E. *Numerical modelling of cancellous bone damage using an orthotropic failure criterion and tissue properties.* XXV Congress of the European Society of Biomechanics (ESB), Vienna, Austria, 7-10 July 2019 (ISBN: 978-3-903024-96-0).

National conferences

Megías R., Belda R., Vercher-Martínez A., Giner E. *Influencia de la morfometría y las propiedades aparentes en la integridad estructural del hueso trabecular humano sano y enfermo.* XXXX Congreso del Grupo Español de Fractura (GEF), Palma de Mallorca, Spain, 6-8 March 2024 (ISSN: 2792-4246).

Belda R., Megías R., Vercher-Martínez A., Giner E. *Diseño y caracterización de soluciones paciente-específicas basadas en estructuras triplemente periódicas con mínima superficie con propiedades no isótropas para el tratamiento de fracturas óseas de gran tamaño.* XXXX Congreso del Grupo Español de Fractura (GEF), Palma de Mallorca, Spain, 6-8 March 2024 (ISSN: 2792-4246).

Fresquet-Monter A., Belda R., Vercher-Martínez A., Megías R., Giner E. *Análisis del daño de andamios óseos paciente-específicos basados en estructuras triplemente periódicas con mínima superficie mediante ensayos cuasi-estáticos a compresión para el tratamiento de fracturas óseas de grandes di-*

mensiones. XXXX Congreso del Grupo Español de Fractura (GEF), Palma de Mallorca, Spain, 6-8 March 2024 (ISSN: 2792-4246).

Megías R., Belda R., Garrigós J.A., Vercher-Martínez A., Giner E. *Evaluación de la respuesta a compresión de hueso trabecular procedente de cabezas femorales humanas en condiciones normales y con patologías óseas.* XII Reunión del Capítulo Español de la Sociedad Europea de Biomecánica, Málaga, Spain, 2-3 Novimebre 2023.

Fresquet A., Belda R., Megías R., Vercher-Martínez A. *Diseño de un sustituto óseo de estructura triplemente periódica con mínima superficie para el tratamiento de defectos óseos de grandes dimensiones.* XII Reunión del Capítulo Español de la Sociedad Europea de Biomecánica, Málaga, Spain, 2-3 Novimebre 2023.

Megías R., Belda R., Vercher-Martínez A., Giner E. *Análisis del comportamiento a compresión de hueso trabecular femoral sano y enfermo.* XXIV Congreso Nacional de Ingeniería Mecánica, Las Palmas de Gran Canaria, Spain, 25-27 October 2023 (ISSN: 0212-5072).

Belda R., Megías R., Marco M., Vercher-Martínez A., Giner E. *Análisis numérico de la influencia de la morfometría de estructuras triplemente periódicas con mínima superficie en su respuesta elástica.* XXIV Congreso Nacional de Ingeniería Mecánica, Las Palmas de Gran Canaria, Spain, 25-27 October 2023 (ISSN: 0212-5072).

∗Megías R., Belda R., Garrigós J.A., Vercher-Martínez A., Giner E. *Estudio de la fractura a compresión de hueso trabecular sano, osteoporótico y artrósico procedente de cabezas femorales humanas.* XXXIX Congreso del Grupo Español de Fractura (GEF), Gijón, Spain, 22-24 March 2023 (ISSN: 2792-4246).

∗**Award-winning work**: Mejor trabajo presentado por un investigador no doctor en el XXXIX Congreso del Grupo Español de Fractura (GEF).

Megías R., Belda R., Garrigós J.A., Vercher-Martínez A., Giner E. *Estudio morfométrico de hueso trabecular sano, osteoporótico y artrósico de cabezas femorales humanas.* XI Reunión del Capítulo Español de la Sociedad Europea de Biomecánica, Zaragoza, Spain, 24-25 October 2022.

∗Vercher-Martínez A., Pérez F., Megías R., Belda R., Giner E. *Estimación de los límites resistentes del tejido lamelar en función de la porosidad y la densi-*

dad mineral ósea. XI Reunión del Capítulo Español de la Sociedad Europea de Biomecánica, Zaragoza, Spain, 24-25 October 2022.

∗**Award-winning work**: Mejor comunicación en tejido duro en la XI Reunión del Capítulo Español de la ESB 2022.

∗Megías R., Belda R., Vercher-Martínez A., Giner E. *Estudio del comportamiento mecánico de una muestra bioinspirada de hueso trabecular obtenida mediante impresión 3D en ácido poliláctico.* X Reunión del Capítulo Español de la Sociedad Europea de Biomecánica, Granada, Spain, 25-26 October 2021.

∗**Award-winning work**: Mención a trabajos que destacan por su excelencia en la X Reunión del Capítulo Español de la ESB 2021.

∗Megías R., Belda R., Vercher-Martínez A., Giner E. *Análisis experimental y correlación numérica de la respuesta a compresión de un simulante de hueso trabecular obtenido por fabricación aditiva.* XXIII Congreso Nacional de Ingeniería Mecánica, Jaén, Spain, 20-22 October 2021 (ISSN: 0212-5072).

∗**Award-winning work**: Primer premio a la mejor comunicación en Biomecánica en el XXIII Congreso Nacional de Ingeniería Mecánica 2021.

∗**Award-winning work**: Primer premio de investigación básica por la AEIM en el XXIII Congreso Nacional de Ingeniería Mecánica 2021.

Calvo J.V., Megías R., Feito N., Giner E., Miguélez M.H. *Análisis de la progresión del daño en laminados compuestos con concentrador de tensiones bajo cargas de tracción.* XXIII Congreso Nacional de Ingeniería Mecánica, Jaén, Spain, 20-22 October 2021 (ISSN: 0212-5072).

Megías R., Belda R., Vercher-Martínez A., Giner E. *Análisis del comportamiento elástico y la fractura a compresión de una muestra de hueso trabecular fabricada en ácido poliláctico.* XXXVII Congreso del Grupo Español de Fractura (GEF), (on-line), Spain, 7-8 June 2021 (ISSN: 2792-4246).

Megías R., Vercher-Martínez A., Belda R., Giner E. *Modelado numérico del daño del hueso trabecular utilizando un criterio de fallo ortótropo y las propiedades del tejido.* IX Reunión del Capçitulo Español de la Sociedad Europea de Biomecánica (ESB), Las Palmas de Gran Canaria, Spain, 24-25 October 2019 (ISBN: 978-84-09-15896-6).

Belda R., Megías R., Vercher-Martínez A., Giner E. *Estudio de la influencia de las microestructura en la respuesta elástica en hueso trabecular mediante elementos finitos.* IX Reunión del Capçitulo Español de la Sociedad Europea

de Biomecánica (ESB), Las Palmas de Gran Canaria, Spain, 24-25 October 2019 (ISBN: 978-84-09-15896-6).

Teaching conferences

Megías R., Belda R., Infante-García D., Feito, N., *Análisis del método de evaluación de las sesiones de prácticas en alumnos del Máster Universitario en Ingeniería Aeronáutica.* IX Congreso Nacional de Innovación Educativa y Docencia en Red (IN-RED), (443-450), Valencia, Spain. 13-14 July 2023.

Infante-García D., Megías R., Feito, N., Belda R. *Estudio comparativo de la opinión del alumnado respecto a la evaluación de las sesiones de laboratorio en el Máster Universitario de Ingeniería Aeronáutica.* IX Congreso Nacional de Innovación Educativa y Docencia en Red (IN-RED), (443-450), Valencia, Spain. 13-14 July 2023.

Belda R., Infante-García D., Megías R., Feito, N. *Aprendizaje basado en proyectos mediante aplicación de impresión 3D y modelos de elementos finitos en el Grado de Ingeniería Mecánica.* IX Congreso Nacional de Innovación Educativa y Docencia en Red (IN-RED), (903-914), Valencia, Spain. 13-14 July 2023.

Feito, N., Belda R., Megías R., Vila, C. *Aprendizaje basado en proyectos en asignaturas de ciclo de vida del producto en estudios de Máster de Diseño y Fabricación.* VII Congreso de Innovación Educativa y Docencia en Red (IN-RED), Valencia, Spain. 15-16 July 2021.

Bibliography

[1] Lee D.M. and Weinblatt M.E. Rheumatoid arthritis. *Lancet.*, **358**:903–911, 2001.

[2] Gardner D.L. The nature and causes of osteoarthrosis. *BMJ.*, **286**:418–424, 1983.

[3] Pereira D., Ramos E., and Branco J. Osteoarthritis. *Acta Med Port.*, **28**(1):99–106, 2015.

[4] Lane J.M., Russell L., and Safdar N.K. Osteoporosis. *Clin Orthop Relat Res.*, **372**:139–150, 2000.

[5] Willers C., Norton N., Harvey N.C., Jacobson T., Johansson H., Lorentzon M., McCloskey E.V., Borgström F., and Kanis J.A. Osteoporosis in Europe: a compendium of country-specific reports. *Arch Osteoporos.*, **17**:1–129, 2022.

[6] Nogués Solán X., Guerri R., Solé E., and Díez-Pérez A. Impacto socioeconómico de la osteoporosis. *Rev Osteoporos Metab Miner.*, **2**(Supl 3):S8–S11, 2010.

[7] Barrios-Moyano A. and De la Peña-García C. Prevalencia de osteoporosis y osteopenia en pacientes laboralmente activos. *Acta Ortop Mex.*, **32**(3):131–133, 2018.

[8] Plataforma para la prevención de fracturas por osteoporosis. La osteoporosis por el mundo. Fractura por osteoporosis: La osteoporosis por el mundo. https://fracturasporosteoporosis.com/fractura/mundo/.

[9] La osteoporosis a nivel mundial produce una fractura ósea cada tres segundos. iSanidad: Actualidad. https://es.overleaf.com/project/62d57b5561c48a50d88b2fe2, 23 october 2017.

[10] Boyce B.F., Rosenberg E., de Papp A.E., and Guong L.T. The osteoclast, bone remodelling and treatment of metabolic bone disease. *Eur J Clin Invest.*, **42**(12):1332–1341, 2012.

[11] Mulvihill B.M. and Prendergast P.J. Mechanobiological regulation of the remodelling cycle in trabecular bone and possible biomechanical pathways for osteoporosis. *Clin Biomec.*, **25**:491–498, 2010.

[12] McNamara L.M. and Prendergast P.J. Perforation of cancellous bone trabeculae by damage-stimulated remodelling at resorption pits: A computational analysis. *Eur J Morphol.*, **42**(1/2):99–109, 2005.

[13] Adams J.E. *Dual-Energy X-Ray Absorptiometry. In: Guglielmi, G. (eds) Osteoporosis and Bone Densitometry Measurements. Medical Radiology.* Springer, Heidelberg. ISBN: 978-3-642-27883-9, Berlin, 2013.

[14] Shanks G., Sharma D., and Mishra V. Prevention and treatment of osteoporosis in women. *Obstetrics, Gynecology and Reproductive Medicine*, doi.org/10.1016/j.ogrm.2019.04.001:1–6, 2019.

[15] Arlot M.E., Sornay-Rendu E., Garnero P., Vey-Marty B., and Delmas P.D. Apparent Pre- and Postmenopausal bone loss evaluated by DXA at different skeletal sites in women: The OFELY cohort. *J Bone Miner Res.*, **12**(4):683–690, 1997.

[16] Woodson G. Dual X-ray absorptiometry T-score concordance and discordance between hip and spine measurement sites. *J Clin Densitom.*, **3**(4):319–324, 2000.

[17] Chu Lau E.M. and Cooper C. Risk factors for osteoporosis in Europe. *J Bone Miner Metab.*, **19**:142–145, 2001.

[18] Golding P.H. Dual-energy X-ray absorptiometry (DXA) to measure bone mineral density (BMD) for diagnosis of osteoporosis - experimental data from artificial vertebrae confirms significant dependence on bone size. *Bone Rep.*, **17**:101607, 2022.

[19] Olson A.F. Osteoporosis detection: Is BMD testing the future? *The Nurse Practitioner*, **32**(6):20–27, 2007.

[20] Ding M. and Overgaard S. 3-D microarchitectural properties and rod- and plate-like trabecular morphometric properties of femur head cancellous bones in patients with rheumatoid arthritis, osteoarthritis, and osteoporosis. *J Orthop Translat.*, **28**:159–168, 2021.

[21] Ding M. and Overgaard S. Degeneration in global morphometry of cancellous bone in rheumatoid arthritis, osteoarthritis, and osteoporosis of femoral heads are similar but more severe than in aging. *Calcif Tissue Int.*, **110**:57–64, 2022.

[22] Stauber M., Rapillard L., van Lenthe G.H., Zysset P., and Müller R. Importance of individual rods and plates in the assessment of bone quality and their contribution to bone stiffness. *J Bone Miner Res.*, **21**(4):586–595, 2006.

[23] Stauber M. and Müller R. Volumetric spatial decomposition of trabecular bone into rods and plates - A new method for local bone morphometry. *Bone*, **38**:475–484, 2006.

[24] Nazarian A., Stauber M., Zurakowski D., Snyder B.D., and Müller R. The interaction of microstructure and volume fraction in predicting failure in cancellous bone. *Bone*, **39**:1196–1202, 2006.

[25] Garzón-Alvarado D.A. and Linero D. Comparative analysis of numerical integration schemes of density equation for a computational model of bone remodelling. *Comput Methods Biomech Biomed Engin.*, **15**:11:1189–1196, 2012.

[26] Baldonedo J., Fernández J.R., and Segade A. Numerical analysis of a bone remodeling model with damage. *Comput Methods Appl Mec Engrg.*, **367**:113113, 2020.

[27] Anitha D., Kim K.J., Lim S.K., and Lee T. Implications of local osteoporosis on the efficacy of anti-resorptive drug treatment: a 3-year follow-up finite element study in risedronate-treated women. *Osteoporos Int.*, **24**(12):3043–3051, 2013.

[28] Rho J.Y., Kuhn-Spearing L., and Zioupos P. Mechanical properties and the hierarchical structure of bone. *Med Eng Phys.*, **20**:92–102, 1998.

[29] Barkaoui A., Tlili B., Vercher-Martínez A., and Hambli R. A multi-scale modelling of bone ultrastructure elastic properties using FE simulations and neural network method. *Comput Methods Programs Biomed.*, **134**:69–78, 2011.

[30] Sabet F.A., Najafi A.R., Hamed E., and Jasiuk I. Modelling of bone fracture and strength at different length scales: A review. *Interface Focus*, **6**:20150055, 2016.

[31] Choi K., Kuhn J.L., Ciarelli M.J., and Goldstein S.A. The elastic moduli of human subchondral, trabecular and cortical bone tissue and the size-dependency of cortical bone modulus. *J Biomech.*, **23**(11):1103–1113, 1990.

[32] Bikas H., Stavropoulos P., and Chryssolouris G. Modelling of additive manufacturing processes: a review and classification. *Int J Adv Manuf Technol.*, doi: 10.1007/s00170-015-7576-2:1–17, 2016.

[33] Castro A.P.G., Ruben R.B., Gonçalves S.B., Pinheiro J., Guedes J.M., and Fernandes P.R. Numerical and experimental evaluation of TPMS Gyroid scaffolds for bone tissue engineering. *Comput Methods Biomech Biomed Engin.*, **22**, No. 6:567–573, 2019.

[34] Fantini M., Curto M., and De Crescenzio F. *TPMS for interactive modelling of trabecular scaffolds for bone tissue engineering. In: Advances on Mechanics, Design Engineering and Manufacturing : Proceedings of the International Joint Conference on Mechanics, Design Engineering & Advanced Manufacturing (JCM 2016), 14-16 September, 2016, Catania, Italy, pg: 425-435.* Springer International Publishing. ISBN: 978-3-319-45781-9, 2017.

[35] Castro A.P.G., Santos J., Pires T., and Fernandes P.R. Micromechanical behavior of TPMS scaffolds for bone tissue engineering. *Macromol Mater Eng.*, **305**:2000487, 2020.

[36] Cowin S.C. *Bone mechanics hanbook.* Boca Ratón, Florida: CRC Press, ISBN: 9780849391170 - CAT# 9117, 2001.

[37] Landis W.J. The strength of a calcified tissue depends in part on the molecular structure and organization of its constituent mineal crystals in their organix matrix. *Bone*, **16** No.5:533–544, 1995.

[38] Weiner S. and Traub W. Bone structure: from angstroms to microns. *FASEB*, **6**:879–885, 1992.

[39] Currey J.D. The structure and mechanics of bone. *J Mater Sci.*, **47**:41–54, 2012.

[40] Prada D.M., Galvis A.F., Miller J., Foster J.M., and Zavaglia C. Multiscale sitffness characterisation of both healthy and osteoporotic

bone tissue using subject-specific data. *J Mech Behav Biomed Mater.*, **135**:105431, 2022.

[41] Martini and Timmons. Gross structure of a long bone (human femur). Prentince-Hall - Long Bones: https://www.daviddarling.info/encyclopedia/L/ - LongBones, 1997.

[42] Gray H. *Anatomy of the human body.* Philadelphia: Lea & Febiger, ISBN: 1-58734-102-6, 1918.

[43] Parfitt A. M. and Chir B. Bone remodeling and bone loss: understanding the pathophysiology of osteoporosis. *Clin Obste Gynecol.*, **30**:789–811, 1987.

[44] Martínez-Reina J., Domínguez J., and García-Aznar J.M. Effect of porosity and mineral content on the elastic constants of cortical bone: a multiscale approach. *Biomech Model Mechanobiol.*, **10**:309–322, 2011.

[45] Reisinger A.G., Pahr D.H., and Zysset P.K. Sensitivity analysis and parametric study of elastic properties of unidirectional mineralized bone fibril-array using mean field methods. *Biomech Model Mechanobiol.*, **9**:499–510, 2010.

[46] Vercher-Martínez A., Giner E., Belda R., Aigoun A., and Fuenmayor F.J. Explicit expressions for the estimation of the elastic constants of lamellar bone as a function of the volumetric mineral content using a multi-scale approach. *Biomech Model Mechanobiol.*, **17**:449–464, 2018.

[47] Currey J.D. Power law models for the mechanical properties of cancellous bone. *Eng Med.*, **15** (3):153–154, 1986.

[48] Currey J.D. The effect of porosity and mineral content on the Young's modulus of elasticity of compact bone. *J Biomech.*, **21**:131–139, 1988.

[49] Schaffler M.B. and Burr D.B. Stiffness of compact bone: effects of porosity and density. *J Biomech.*, **21**:13–16, 1988.

[50] Tommasini S.M., Nasser P., Hu B., and Jepsen K.J. Biological co-adaptation of morphological and composition traits contributes to mechanical functionality and skeletal fragility. *J Bone Miner Res.*, **23**:236–246, 2008.

[51] Manolagas S.C. and Parfitt A.M. For whom the bell tolls: distress signals from long-lived osteocytes and the pathogenesis of metabolic bone diseases. *Bone*, **54** (2):272–278, 2012.

[52] Parfitt A.M. Age-related structural changes in trabecular and cortical bone: cellular mechanisms and biomechanical consequences. *Calcif Tissue Int.*, **36**:S123–S128, 1984.

[53] Mosekilde L. Consequences of the remodelling process for vertebral trabecular bone structure: a scanning electron microscopy study (uncoupling of unloaded structures). *Bone Miner.*, **10**:13–35, 1990.

[54] Gentzsch C., Delling G., and Kaiser E. Microstructural classification of resorption lacunae and perforations in human proximal femora. *Calcif Tissue Int.*, **72**:698–709, 2003.

[55] Marotti G. Osteocyte orientation in human lamellar bone and its relevance to the morphometry of periosteocytic lacunae. *Biomech Model Mechanobiol.*, **10**:309–322, 1979.

[56] Cowin S.C. Bone poroelasticity. *Biomech Model Mechanobiol.*, **10**:309–322, 1999.

[57] Bassett J.H.D., O'shea P.J., Chassande O., Samarut J., Cheng S.Y., Vennstrom B., Howel P.G.T., Boyde A., and Williams G.R. Analysis of skeletal phenotypes in thyroid hormone receptor mutant in mouse. *Scanning*, Vol **28**, No.2:91–93, 2006.

[58] Chappard D., Baslé M.F., Legrand E., and Audran M. New laboratory tools in the assessment of bone quality. *Osteoporos Int.*, **22**:2225–2240, 2011.

[59] Oftadeh R., Pérez-Viloria M., Villa-Camacho J.C., Vaziri A., and Nazarian A. Biomechanics and mechanobiology of trabecular bone: a review. *J Biol Eng.*, **137**:010802–1–010802–15, 2015.

[60] Georgiadis M., Guizar-Sicairos M., Gschwend O., Hangartner P. abd Bunk O., Müller R., and Schneider P. Ultrastructure organization of human trabeculae assessed by 3D sSAXS and relation to bone microarchitecture. *PLoS ONE*, **11** (8):e0159838. doi:10.1371/journal.pone.0159838, 2016.

[61] Donnelly E., Williams R.M., Downs S.H., Dickinson M.E., Baker S.P., and van der Meulen M.C.H. Quasistatic and dynamic nanomechanical properties of cancellous bone tissue relate to collagen content and organization. *J Mater Res.*, **21** (8):2106–2117, 2006.

[62] Hosaki-Takamiya R., Hashimoto M., Imai Y., Nishida T., Yamada N., Mori H., Tanaka T., Kawanabe N., Yamashiro T., and Kamioka H. Collagen production of osteoblasts revealed by ultra-high voltage electron microscopy. *J Bone Miner Metab.*, **34**:491–499, 2016.

[63] Hammond M.A., Wallace J.M., Allen M.R., and Siegmund T. Incorporating tissue anisotropy and heterogeneity in finite element methods of trabecular bone altered predicted local stress distributions. *Biomech Model Mechanobiol.*, **17**:605–614, 2018.

[64] Haj-Ali R., Massarwa E., Aboudi J., Galbusera F., Wolfram U., and Wilke H.J. A new multiscale micromechanical model of vertebral trabecular bones. *Biomech Model. Mechanobiol.*, **16**:933–946, 2017.

[65] Fritsch A. and Hellmich C. Universal microstructural patterns in cortical and trabecular, extracellular and extravascular bone materials: Micromechanics-based prediction of anisotropic elasticity. *J Theor Biol.*, **244**:597–620, 2007.

[66] Colloca M., Blanchard R., Hellmich C., Ito K., and van Rietbergen B. A multiscale analytical approach for bone remodeling simulations: Linking scales from collagen to trabeculae. *Bone*, **64**:303–313, 2014.

[67] Hammond M.A., Wallace J.M., Allen M.R., and Siegmund T. Mechanics of linear microcracking in trabecular bone. *J Biomech.*, **83**:34–42, 2019.

[68] Torres A.M., Matheny J.B., Keaveny T.M., Taylor D., Rimnac C.M., and Hernandez C.J. Material heterogeneity in cancellous bone promotes deformation recovery after mechanical failure. *Proc Natl Acad Sci.*, **113**:2891–2897, 2016.

[69] Renders G.A.P., Mulder L., Langenbach G.E.L., van Ruijven L.J., and van Eijden T.M.G.J. Biomechanical effect of mineral heterogeneity in trabecular bone. *J Biomech.*, **41**:2793–2798, 2008.

[70] Turner C.H. and Burr D.B. Basic biomechanical measurements of bone: A tutorial. *Bone*, **14**:595–608, 1993.

[71] Hambli R. and Thurner P.J. Finite element prediction with experimental validation of damage distribution in single trabeculae during three-point bending tests. *J Mech Behav Biomed Mater.*, **27**:94–106, 2013.

[72] Keaveny T.M. Guo X.E., Wachtel E.F., McMahon A., and Hayes W. Trabecular bone exhibits fully linear elastic behavior and yields at low strains. *J Biomech.*, **27**(9):1127–1136, 1994.

[73] Gupta H.S. and Zioupos P. Fracture of bone tissue: The hows and the whys. *Med Eng Phys.*, **30**:1209–1226, 2008.

[74] Kopperdahl D.L. and Keaveny T.M. Yield strain behaviour of trabecular bone. *J Biomech.*, **31**:601–608, 1998.

[75] Prot M., Cloete T.J., Saletti D., and Laporte S. The behavior of cancellous bone from quasi-static to dynamic strain rates with emphasis on the intermediate regime. *J Biomech.*, **49**:1050–1057, 2016.

[76] Keaveny T.M., Morgan E.F., Niebur G.L., and Yeh O.C. Biomechanics of trabecular bone. *Annu Rev Biomed Eng.*, **3**:307–333, 2001.

[77] Novitskaya E., Zin C., Chang N., Cory E., Cheng P., D'Lima D., Sah R.L., and McKitrick J. Creep of trabecular bone from human proximal tibia. *Mater Sci Eng C.*, **40**:219–227, 2014.

[78] Bowman S.M., Guo X.E., Chen D.W., Keaveny T.M., Gibson L.J., Hayes W.C., and McMahon T.A. Creep contributes to the fatigue behavior of bovine trabecular bone. *J Biomech Eng-T ASME*, **120**:647–654, 1998.

[79] Szebényi G., Görög P., TöRök Á., and Kiss R.M. *Effect of different conservation methods on some mechanical properties of swine bone.*, volume **17**. WIT Press. ISSN 1743-3525 (on-line). Modelling in Medicine and Biology X., 2013.

[80] Belda R. *Mechanical and morphometric characterization of cancellous bone.* PhD thesis, Universitat Politècnica de València, 2020.

[81] Bérot M., Aurégan J.C., Imbert L., Magoariec H., Budyn E., Zadegan F., Hanouche D., Bensidhoum M., and Hoc T. Mechanics of osteoporotic trabecular bone. *Mechanics & Insdustry*, **13**:373–380, 2012.

[82] Morgan E.F. and Keaveny T.M. Dependence of yield strain of human trabecular bone on anatomic site. *J Biomech.*, **34**:569–577, 2001.

[83] Li B. and Aspden R.M. Composition and mechanical properties of cancellous bone from the femoral head of patients with osteoporosis or osteoarthritis. *J Bone Miner Res.*, **12**(4):641–651, 1997.

[84] Chevalier Y., Pahr D., Allmer H., Charlebois M., and Zysset P. Validation of a voxel-based FE method for prediction of the uniaxial apparent modulus of human trabecular bone using macroscopic mechanical tests and nanoindentation. *J Biomech.*, **40**:3333–3340, 2007.

[85] Lad A.J.C., Kinney J.H., Haupt D.L., and Goldstein S.A. Finite-element modeling of trabecular bone: comparison with mechanical testing and determination of tissue modulus. *J Orthop Res.*, **16**:622–628, 1998.

[86] Lambers F.M., Bouman A.R., Tkachenko E.V, Keaveny T.M., and Hernandez C.J. The effects of tensile-compressive loading mode and microarchitecture on microdamage in human vertebral cancellous bone. *J Biomech.*, **47**:3605–3612, 2014.

[87] Odgaard A., Hvid I., and Linde F. Compressive axial strain distribution in cancellous bone specimens. *J Biomec.*, **22**(8-9):829–835, 1989.

[88] Odgaard A. and Linde F. The underestimation of Young's modulus in compressive testing of cancellous bone specimens. *J Biomech.*, **24**(8):691–698, 1991.

[89] Wu D., Isaksson P., Ferguson S.J., and Persson C. Young's modulus of trabecular bone at the tissue level: A review. *Acta Biomater.*, **78**:1–12, 2018.

[90] Norman J., Shapter J.G., Short K., Smith L.J., and Fazzlari N.L. Micromechanical properties of human trabecular bone: A hierarchical investigation using nanoindentation. *J Biomed Mater Res A.*, **87**(1):196–202, 2008.

[91] Zysset P.K., Guo X.E., Hoffler C.E., Moore K.E, and Goldstein S.A. Elastic modulus and hardness of cortical and trabecular bone lamellae measured by nanoindentation in the human femur. *J Biomech.*, **32**:1005–1012, 1999.

[92] Rho J.Y., Tsui T.Y., and Pharr G.M. Elastic properties of human cortical and trabecular lamellar bone measured by nanoindentation. *Biomaterials*, **18**:1325–1330, 1997.

[93] Dendorfer S., Maier H.J., and Hammer H. Transverse isotropic elastic properties of vertebral trabecular bone matrix measured using microindentation under dry conditions (effects of age, gender, and vertebral level). *J Mech Med Biol.*, **10**(1):139–150, 2010.

[94] Gross T., Pahr D.H., Peyrin F., and Zysset P.K. Mineral heterogeneity has a minor influence on the apparent elastic properties of human cancellous bone: a SRμCT-based finite element study. *Comput Methods Biomech Biomed Eng.*, **15**(11):1137–1144, 2012.

[95] Bayraktar H.H., Morgan E.F., Niebur G.L., Morris G.L. Wong E.K., and Keaveny T.M. Comparison of the elastic and yield properties of human trabecular and cortical bone tissue. *J Biomech.*, **37**:27–35, 2004.

[96] Kabel J., van Rietbergen B., Odgaard A., and Huiskes R. Constitutive relationships of fabric, density and elastic properties in cancellous bone architecture. *Bone*, **25**:481–486, 1999.

[97] Hambli R. Micro-CT finite element model and experimental validation of trabecular bone damage and fracture. *Bone*, **56**:363–374, 2013.

[98] Niebur G.L., Feldstein M.J., Yuen J.C., Chen T.J., and Keaveny T.M. Highresolution finite element models with tissue strength asymmetry accurately predict failure of trabecular bone. *J Biomech.*, **33**:1575–1583, 2000.

[99] Carretta R., Stüssi E., Müller R., and Lorenzetti S. Within subject heterogeneity in tissue-level post-yield mechanical and material properties in human trabecular bone. *J Mech Behav Biomed.*, **24**:64–73, 2013.

[100] Rho J.Y., Ashman R.B., and Turner C.H. Young's modulus of trabecular and cortical bone material: ultrasonic and microtensile measurements. *J Biomech.*, **26**(2):111–119, 1993.

[101] Jungmann R., Szabo M.E., Schitter G., Tang R.Y.S. Vashishth D., Hansma P.K., and Thurner P.J. Local strain and damage mapping in single trabeculae during three-point bending tests. *J Mech Behav Biomed.*, **4**(4):523–534, 2011.

[102] Keaveny T.M., Borchers R.E., Gibson L.J., and Hayes W. Theoretical analysis of the experimental artifact in trabecular bone compressive modulus. *J Biomech.*, **26**(4-5):599–607, 1993.

[103] Linde F. and Hvid I. Stiffness behaviour of trabecular bone specimens. *J Biomech.*, **20**(1):83–89, 1987.

[104] Keaveny T.M., Pinilla T.P., Crawford R.P., Kopperdahl D.L., and Lou A. Systematic and random errors in compression testing of trabecular bone. *J Orthop Res.*, **15**:101–110, 1997.

[105] Nagaraja S., Couse T.L., and Guldberg R.E. Trabecular bone microdamage and microstructural stresses under uniaxial compression. *J Biomech.*, **38** 4:707–716, 2005.

[106] Bevill G., Eswaran S.K., Gupta A., Papadopoulos P., and Keaveny T.M. Influence of bone volume fraction and architecture on computed large-deformation failure mechanisms in human trabecular bone. *Bone*, **39**:1218–1225, 2006.

[107] Wolfram U., Wilke H.J., and Zysset P.K. Damage accumulation in vertebral trabecular bone depends on loading mode and direction. *J Biomech.*, **44** (6):1164–1169, 2011.

[108] Niebur G.L., Yuen J.C., Hsia A.C., and Keaveny T.M. Convergence behavior of high-resolution finite element models of trabecular bone. *J Biomech Eng.*, **121**:629–635, 1999.

[109] Hernandez C.J., Lambers F.M., Widjaja J., Chapa C., and rimnac C.M. Quantitative relationships between microdamage and cancellous bone strength and stiffness. *Bone*, **66**:205–213, 2014.

[110] Nazarian A. and Müller R. Time-lapsed microstructural imaging of bone failure behavior. *J Biomech.*, **37**:55–65, 2004.

[111] Gibson J.L. The mechanical behaviour of cancellous bone. *J Biomech.*, **18**(5):317–328, 1985.

[112] Zioupos P. Recent developments in the study of failure of solid biomaterials and bone: "fracture" and "pre-fracture" thoughness. *Mater Sci Eng C.*, **6**:33–40, 1998.

[113] Launey M.E., Buehler M.J., and Ritchie R.O. On the mechanistic origins of toughness in bone. *Annu Rev Mater Res.*, **40**:25–53, 2010.

[114] Thurner P.J., Erickson B., Jungmann R., Schriock Z., Weaver J.C., Fantner G.E., Schitter G., Morse D.E., and Hansma P.K. High-speed photography of compressed human trabecular bone correlates whitening to microscopic damage. *Eng Fract Mech.*, **74**:1928–1941, 2007.

[115] Wang X., Masse D.B., Leng H., Hess K.P., Ross R.D., Roeder R.K., and Niebur G.L. Detection of trabecular bone microdamage by microcomputed tomography. *J Biomech.*, **40**:3397–3403, 2007.

[116] Wachtel E.F. and Keaveny T.M. Dependence of trabecular damage on mechanical strain. *J Orthop Res.*, **15**(5):781–787, 1997.

[117] Panjabi M.M., Krag M., Summers D., and Videman T. Biomechanical time-tolerance of fresh cadaveris human spine specimens. *J Orthp Res.*, **3**:292–300, 1985.

[118] Linde F. and Soresen H.C.F. The effect of different storage methods on the mechanical properties of trabecular bone. *J Biomec.*, **26**(10):1249–1252, 1993.

[119] van Rietbergen B., Weinans H., Huiskes R., and Odergaard A. A new method to determine trabecular bone elastic properties and loading using micromechanical finite-element models. *J Biomech.*, **28**(1):69–85, 1995.

[120] van Rietbergen B., Odgaard A., Kabel J., and Huiskes R. Direct mechanics assessment of elastic symmetries and properties of trabecular bone architecture. *J Biomech.*, **29**(12):1653–1657, 1996.

[121] Bailey S. and Vashishth D. Mechanical characterization of bone: State of the art in experimental approaches - What types of experiments do people do and how does one interpret the results? *Curr Osteoporor Rep.*, **16**(4):423–433, 2018.

[122] YamadaS., Tadano S., and Fukuda S. Nanostructure and elastic modulus of single trabecula in bovine cancellous bone. *J Biomec.*, **47**:3482–3487, 2014.

[123] YamadaS., Tadano S., and Fukuda S. Micro-cantilever bending for elastic modulus measurements of a single trabecula in cancellous bone. *J Biomec.*, **49**(16):4124–4127, 2016.

[124] Ün K., Bevill G., and Keaveny T.M. The effects of side-artifacts on the elastic modulus of trabecular bone. *J Biomech.*, **39**:1955–1963, 2006.

[125] Bevill G., Easley S., and KeavenyT.M. Side-artifact errors in yield strength and elastic modulus for human trabecular bone and their dependence on bone volume fraction and anatomic site. *J Biomech.*, **40**(15):3381–3388, 2007.

[126] Zysset P.K. Indentation of bone tissue: a short review. *Osteoporos Int.*, **20**:1049–1055, 2009.

[127] Khoo S., Karuppanan S., and Tan C. A review of surface deformation and strain measurement using two-dimensional digital image correlation. *Metrol Meas Syst.*, **3**:461–480, 2016.

[128] Palanca M., Tozzi G., and Cristofolini L. The use of digital image correlation in the biomechanical area: A review. *Int Biomech.*, **3**:1–21, 2016.

[129] Grassi L. and Isaksson H. Extracting accurate strain measurements in bone mechanics: A critical review of current methods. *J Mech Behav Biomed Mater.*, **50**:43–54, 2015.

[130] Grassi L., Väänänen S.P., Ristinmaa M., Jurvelin J.S., and Isaksson H. How accurately can subject-specific finite element models predict strains and strength of human femora? Investigation using full-field measurements. *J Biomech.*, **65**:801–807, 2017.

[131] Bay B.K. Texture correlation: a method for the measurement of detailed strain distributions within trabecular bone. *J Orthop Res.*, **13**:256–267, 1995.

[132] Whitehouse W.J. The quantitative morphology of anisotropic trabecular bone. *J Microsc.*, **101**(2):153–168, 1974.

[133] Odgaard A. Three- dimensional methods for quantification of cancellous bone architecture. *Bone*, **20**(4):315–328, 1997.

[134] Ulrich D., van Rietbergn B., Laib A., and Rüegsegger P. The ability of three-dimensional structural indices to reflect mechanical aspects of trabecular bone. *Bone*, **25**(1):55–60, 1999.

[135] Alberic Bayarri A. *In vivo morphometric and mechanical caracterization of trabecular bone from high resolution magnetic resonance imaging.* PhD thesis, Universitat Politècnica de València, 2010.

[136] Soltani P. Principle of the micro-computed tomography system. ResearchGate, http://www.researchgate.net/figure/Principle-of-the-micro-computed-tomography-system-Fig1, January 2016.

[137] Feldkamp L.A., Goldstein, Parfitt A.M., Jesion G., and Kleerekoper M. The direct examination of three-dimensional bone architecture in vitro by computed tomography. *J Bone Miner.*, **4**:2–11, 1989.

[138] Boerckel J.D., Mason D.E., McDermott A.M., and Alsberg E. Micro-computed tomography: approaches and applications in bioengineering. *Stem Cell Res Ther.*, **5**:144, 2014.

[139] Danielsson M., Persson M., and Sjolin M. Photon-counting x-ray detectors for CT. *Phys Med Biol.*, **66**(3):03TR1, 2021.

[140] van der Bie J., van Straten M., Booj R., Bos D., Dijkshoorn M.L., Hirsch A., Sharma S.P., Oei E.H.G., and Budde R.P.J. Photon-counting CT: Review of initial clinical results. *Eur J Radiol.*, **163**:110829, 2023.

[141] Willemink M.J., Persson M., Puormorteza A., Pelc N.J., and Fleishmann D. Photon-counting CT: Technical principles and clinical prospects. *Radiology*, **289**:293–312, 2018.

[142] Martin R.B. and Ishida J. The relative effects of collagen fiber orientation, porosity, density, and mineralization on bone strength. *J Biomech.*, **22**:419–426, 1989.

[143] Granke M., Gourrier A., Rupin F., Raum K., Peyrin F., Burghammer M., Saïed A, and Laugier P. Microfibril orientation dominates the microelastic properties of human bone tissue at the lamellar length scale. *PLoS ONE*, **8**(3):e58043, 2013.

[144] Martin R.B. and Boardman D.L. The effects of collagen fiber orientation, porosity, density, and mineralization on bovine cortical bone bending properties. *J Biomech.*, **26**:1047–1054, 1993.

[145] Georgeadis M., Müller R., and Schneider P. Techniques to assess bone ultrastructure organization: orientation and arrangement of mineralized collagen fibrils. *J R Soc Interface.*, **13**:2016088, 2016.

[146] Boyde A. *Scanning electron microscopy of bone.* In Bone research protocols (eds MH Helfrich, SH Ralston), Methods in Molecular Biology 816. NJ: Humana Press., Totowa, 2012.

[147] Boyde A. and Jones S.J. Scanning electron microscopy of bone: instrument, specimen, and issues. *Micros Res Tech.*, **33**:92–120, 1996.

[148] Suda K., Abe K., and Kaneda K. Changes in the orientation of collagen fibers on the superficial layer of the mouse tibial bone after denervation: scanning electron microscopic observations. *Arch Histol Cytol.*, **62**:231–235, 1999.

[149] Shah F.A., Zanghellini E., Matic A., Thomsen P., and Palmquist A. The orientation of nanoscale apatite platelets in relation to osteoblastic-osteocyte lacunae on trabecular bone surface. *Calcif Tissue Int.*, **98**:193–205, 2016.

[150] Almer J.D. and Stock S.R. Internal strains and stresses measured in cortical bone via high-energy X-ray diffraction. *J Struct Biol.*, **152**:14–27, 2005.

[151] Almer J.D. and Stock S.R. Micromechanical response of mineral and collagen phases in bone. *J Struct Biol.*, **157**:365–370, 2007.

[152] Georgeadis M., Guizar-Sicairos M., Zwahlen A., Trüssel A.J., Bunk O., Müller R., and Schneider P. 3D scanning SAXS: a novel method for the assessment of bone ultrastructure orientation. *Bone*, **71**:42–52, 2015.

[153] Niems M.H. *Medical applications of lasers. Laser-tissue interactions.* Springer, Berlin, Germany, 2004.

[154] Lakes R.S., Katz J.L., and Sternstein S.S. Viscoelastic properties of wet cortical bone—I. Torsional and biaxial studies. *J Biomech.*, **12**:657, 1979.

[155] Wentzell S., Nesbitt R.S., Macione J., and Kotha S. Measuring strain using digital image correlation of second harmonic generation images. *J Biomech.*, **46**:2032–2038, 2013.

[156] Chen H., Slipchenko M.N., Liu Y., Zhao X.F., Cheng J.X., Lanir Y., and Kassab G.S. Biaxial deformation of collagen and elastin fibers in coronary adventitia. *J Appl Physiol.*, **115**:1683–1693, 2013.

[157] Kirk S.E., Skepper J.N., and Donald A.M. Application of environmental scanning electron microscopy to determine biological surface structure. *J Microsc.*, **233**:205–224, 2009.

[158] Xiao X., De Carlo F., and Stock S.R. X-ray zoom in tomography of calcified tissue. *Proc. SPIE*, **7078**:707810, 2008.

[159] Xiao X., De Carlo F., and Stock S.R. Practical error estimation in zoom-in and truncated tomography reconstructions. *Rev Sci Instrum.*, **78**:063705, 2007.

[160] Velroyen A., Yaroshenko A., Hahn D., Fehringer A., and Tapfer A. et a.l. Grating-based X-ray darkfield computed tomography of living mice. *EBioMedicine*, **2**:1500–1506, 2015.

[161] Mamose A., Yashiro W., KidoK., Kiyohara J., Makifuchi C., and Ito T. et al. X-ray phase imaging: from synchrotron to hospital. *Phil Trans R Soc A.*, **372**:20130023, 2014.

[162] Tapfer A., Bech M., Velroyen A., Meiser J., Mohr J., and Walter M. et al. Experimental results from a preclinical X-ray phase-contrast CT scanner. *Proc Natl Acad Sci USA.*, **109**:15691– 15696, 2012.

[163] Thuring T., Guggenberger R., Alkadhi H., Holder J., Vich M., Wang Z., David C., and Stampanoni M. Human hand radiography using X-ray differential phase contrast combined with dark-field imaging. *Skelet Radiol.*, **42**:827–835, 2013.

[164] Liebi M., Georgeadis M., Menzel A., Schneider P., Kohlbrecher J., Bunk O., and Guizar-Sicairos M. Nanostructure surveys of macroscopic specimens by small-angle scattering tensor tomography. *Nature*, **527**:349–352, 2015.

[165] Buckley K., Kerns J.G., Gikas P.D., Birch H.L., Vinton J., Keen R., Parker A.W., Matousek P., and Goodship A.E. Measurement of abnormal bone composition in vivo using noninvasive Raman spectroscopy. *IBMS BoneKEy*, **11**:602, 2014.

[166] Matousek P., Draper E.R.C., Goodship A.E., Clark I.P, Ronayne K.L., and Parker A.W. Noninvasive Raman spectroscopy of human tissue *in vivo*. *Appl Spectrosc.*, **60**:758–763, 2006.

[167] Gu M., Bao H., and Kang H. Fibre-optical microendoscopy. *J Microsc.*, **254**:13–18, 2014.

[168] Fu L. and Gu M. Polarization anisotropy in fiberoptic second harmonic generation microscopy. *Opt Express.*, **16**:5000–5006, 2008.

[169] An Y.H. and Martin K.L. *Handbook of histology methods for bone cartilage.* NJ: Humana Press Inc. 6th edn., Totowa, 2003.

[170] Meganck J.A., Kozloff K.M., Thornton M.M., Broski S.M., and Goldstein S.A. Beam hardening artifacts in micro-computed tomography scanning can be reduced by X-ray beam filtration and the resulting images can be used to accurately measure BMD. *Bone*, **45**(6):1104–1116, 2009.

[171] Sartori P., Rozowykniat M., Siviero L., Barba G., Peña A., Mayol N., Acosta D., Castro J., and Ortiz A. Artefactos y artificios frecuentes en tomografía computada y resonancia magnética. *Rev Argent Radiol.*, **79**(4):192–204, 2015.

[172] Barrett J.F. and Keat N. Artifacts in CT: Recognition and avoidance. *RadioGraphics*, **24**:1679–1691, 2004.

[173] Kuhn J.L., Goldstein S.A., Feldkamp L.A., Goulet R.W., and Jesion G. Evaluation of a microcomputed tomography system to study trabecular bone structure. *J Orthop Res.*, **8**:833–842, 1990.

[174] Zhang J., Yan C.H., Chui C.K., and Ong S.H. Fast segmentation of bone in CT images using 3D adaptive thresholding. *Comput Biol Med.*, **40**:231–236, 2010.

[175] Otsu N. A threshold selection method from gray-scale histogram. *IEEE Trans Sys Man Cybern.*, **9**(1):62–66, 1979.

[176] Gómez W., Sales E., Lopes R.T., and Pereira W.C.A. A comparative study of automatic thresholding approaches for 3D x-ray microtomography of trabecular bone. *Med Phys.*, **40**:091903, 2013.

[177] Tassani S., Korfiatis V., and Matsopoulos G.K. Influence of segmentation on micro-CT images of trabecular bone. *J Micros.*, **256**(2):75–81, 2014.

[178] Baish J.W. and Jain R.K. Fractals and cancer. *Cancer Res.*, **60**:3683–3688, 2000.

[179] Chen Q., Bao N., Yao Q., and Li Z.Y. Fractal dimension: A complementary diagnostic indicator of osteoporosis to bone mineral density. *Med Hypotheses.*, **116**:136–138, 2018.

[180] Pothuaud L., Lespessailles E., Harba R., Jennane R., Royant V., Eynard E., and Benhamou C.L. Fractal analysis of trabecular bone texture on radiographs: discriminant value in postmenopausal osteoporosis. *Osteoporos Int.*, **8**:618–625, 1998.

[181] Messent E.A., Buckland-Wright J.C., and Blake G.M. Fractal analysis of trabecular bone in knee osteoarthritis (OA) is a more sesitive marker of disease status than bone mineral density (BMD). *Calified Tissue Int.*, **76**(6):419–425, 2005.

[182] Wu J., Jin X., Mi S., and Tang J. An effective method to compute the box-counting dimension based on the amthematical definition and intervals. *Results Eng.*, **6**:100106, 2020.

[183] Odgaard A. and Gundersen H.J.G. Quantification of connectivity in cancellous bone, with spatial emphasis on 3-D reconstructions. *Bone*, **14**:173–182, 1993.

[184] Hidelbrand T. and Rüegsegger P. Quantification of bone microarchitecture with the structural model index. *Comput Method Biomec.*, **1**(1):15–23, 1997.

[185] Doube M., Klosowski M.M., Arganda-Carreras I., Cordelières F.P., Dougherty R.P., Jackson J.S., Schmid B., Hutchinson J.R., and Shefelbine S.J. BoneJ: Free and extensible bone image analysis in ImageJ. *Bone*, **47**:1076–1079, 2010.

[186] Pothuaud L., Laib A., Levitz P., and Benhamou C.L. nd Majumdar S. Three-dimensional-line skeleton graph analysis of high-resolution magnetic resonance images: a validation study from 34-microm-resolution microcomputed tomography. *J Bone Miner Res.*, **17**:1883–1895, 2002.

[187] Pothuaud L., Porion P., Lespessailles E., Benhamou C.L., and Levitz P. A new method for three-dimensional skeleton graph analysis of porous media: application to trabecular bone microarchitecture. *K Microsc.*, **199**:149–161, 2000.

[188] Pothuaud L., van Rietbergen B., Mosekilde L., Beuf O., Levitz P., and Benhamou C.L. Combination of topological parameters and bone volume fraction better predicts the mechanical properties of trabecular bone. *J Biomech.*, **3**:1091–1099, 2002.

[189] Blain H., Chavassieux P., Portero-Muzy N., Bonnel F., Canovas F., Chammas M., Maury P., and Delmas P.D. Cortical and trabecular bone distribution in the femoral nexk in osteoporosis and osteoarthritis. *Bone*, **43**:862–868, 2008.

[190] Montoya M.J., Giner M., Miranda C., Vázquez M.A., Caeiro J.R., Guede D., and Pérez-Cano R. Microstructural trabecular bone from patients with osteoporotic hip fracture or osteoarthritis: Its relationship with bone mineral density and bone remodelling markers. *Maturitas*, doi.org/10.1016/j.maturitas.2014.07.006, 2014.

[191] Kim H.S. and Al-Hassani STS. Amorphological model of vertebral trabecular bone. *J Biomech.*, **35**:1101–1114, 2002.

[192] Mosekilde L. Age-related changes in vertebral trabecular bone architecture - Assessed by a new method. *Bone*, **9**:247–250, 1988.

[193] Dagan D., Be'ery M., and Gefen A. Single-trabecula building block for largescale finite element models of cancellous bone. *Med BiolEng Comput.*, **42**:549–556, 2004.

[194] Diamant I., Shahar R., and Gefen A. How to select the elastic modulus for cancellous bone in patient-specific continuum models of the spine. *Med BiolEng Comput.*, **43**:465–472, 2005.

[195] Diamant I., Shahar R., Masharawi Y., and Gefen A. A method for patient-specific evaluation of vertebral cancellous bone strength: In vitro validation. *Clin Biomech.*, **22**:282–291, 2007.

[196] Ulrich D., van Rietbergen B., Weinans H., and Rüegsegger P. Finite element analysis of trabecular bone structure: a comparison of image-based meshing techniques. *J Biomech.*, **31**:1187–1192, 1998.

[197] Bauer J.S., Sidorenko I., Mueller D., Baum T., Issever A.S., Eckstein F., Rummeny E.J., Link T.M., and Raeth C.W. Prediction of bone strength by μCT and MDCT-based finite-element models: How much resolution is needed? *Eur J Radiol.*, **83**:e36–e42, 2014.

[198] Bevill G. and Keaveny T.M. Trabecular bone strength predictions using finite element analysis of micro-scale images at limited spatial resolution. *Bone*, **44**:579–584, 2009.

[199] Pistoia W., van Rietbergen B., Lochmüller E.M, Lill C.A., Eckstein F., and Rüegsegger P. Estimation of distal radius failure load with micro-finite element analysis models based on three-dimensional peripheral quantitative computed tomography images. *Bone*, **6**(30):842–848. PMID: 12052451, 2002.

[200] Wang J., Zhou B., Liu X.S., Fields A.J., Sanyal A., Shi X., Adams M., Keaveny T.M., and Guo X.E. Trabecular plates and rods determine elastic modulus and yield strength of human trabecular bone. *Bone*, **72**:71–80, 2015.

[201] Bourne B.C. and van der Meulen M.C.H. Finite element models predict cancellous apparent modulus when tissue modulus is scaled from specimen CT-attenuation. *J Biomech.*, **37**:613–621, 2004.

[202] Morgan E.F., Bayraktar H.H., and Keaveny T.M. Trabecular bone modulus-density relationships depend on anatomic site. *J Biomech.*, **36**:897–904, 2003.

[203] Helgason B., Perilli E., Schileo E., Taddei F., Brynjólfsson S., and Viceconti M. Mathematical relationships between bone density and mechanical properties: A literature review. *Clin Biomech.*, **23**:135–146, 2008.

[204] Pahr D.H. and Zysset P.K. A comparison of enhanced continuum FE with micro FE models of human vertebral bodies. *J Biomech.*, **42**:455–462, 2009.

[205] Hollister S.J. and Kikuchi N. A comparison of homogenization and standard mechanics analyses for periodic porous composites. *Comput Mech.*, **10**:73–95, 1992.

[206] Pahr D.H. and Zysset P.K. Influence of boundary conditions on computed apparent elastic properties of cancellous bone. *Biomech Model Mechanobiol.*, **7**:463–476, 2008.

[207] Daszkiewicz K., Maquer G., and Zysset P.K. The effective elastic properties of human trabecular bone may be approximated using microfinite element analyses of embedded volume elements. *Biomech Model Mechanobiol.*, **16**(3):731–742, 2016.

[208] van Rietbergen B., Odgaard A., Kabel J., and Huiskes R. Relationships between bone morphology and bone elastic properties can be accurately quantified using high-resolution computer reconstructions. *J Orthop Res.*, **16**:23–28, 1998.

[209] García D., Zysset P.K., Charlebois M., and Curnier A. A three-dimensional elastic plastic damage constitutive law for bone tissue. *Biomech Model Mechanobiol.*, **8**:149–165, 2009.

[210] Hambli R. A quasi-brittle continuum damage finite element model of the human proximal femur based on element deletion. *Med Biol Eng Comput.*, **51**:219–231, 2013.

[211] Schwiedrzik J., Gross T., Bina M., Pretterklieber M., Zysset P., and Pahr D. Experimental validation of a nonlinear μFE model based on cohesivefrictional plasticity for trabecular bone. *Int J Numer Meth Biomed Engng.*, **32**(4):e02739, 2015.

[212] Hambli R. Multiscale prediction of crack density and crack length accumulation in trabecular bone based on neural networks and finite element simulation. *Int J Numer Methods Biomed Eng.*, **27**:461–475, 2011.

[213] Hambli R. Apparent damage accumulation in cancellous bone using neuronal networks. *J Mech Behav Biomed Mater.*, **4**:868–878, 2011.

[214] Harrison N.M., McDonnell P., Mullins L., Wilson N., O'Mahoney D., and McHugh P.E. Failure modelling of trabecular bone using a non-linear combined damage and fracture voxel finite element approach. *Biomech Model Mechanobiol.*, **12**:225–241, 2013.

[215] Mount Elizabeth Hospitals. Arthritis-osteoarthritis, rheumatoid arthritis or gout - Symptoms and Causes. In: https://www.mountelizabeth.com.sg/conditions-diseases/arthritis/symptoms-causes.

[216] Mercuri L.G. Osteoarthritis, osteoarthrosis and idiopathic condylar resorption. *Oral Maxillofac Surg Clin North Am.*, **20**:169–183, 2008.

[217] Faustino A. Osteoarthritis in the 21st century - a new paradigm: Osteoarthritis and osteoarthrosis. *Acta Reumatol Port.*, **46**:205–207, 2021.

[218] Management of osteoporosis in postmenopausal women: the 2021 position statement of The North American Menopause Society. *Menopause*, **28** (9) doi: 10.1097/GME.0000000000001831:973–997, 2021.

[219] NIH Consensus Development Panel on Osteoporosis Prevention Diagnosis and Therapy. Osteoporosis prevention, diagnosis and therapy. *JAMA Feb. 14*, **285**(6):785–795. doi: 10.1001/jama.285.6.785. PMID: 11176917, 2001.

[220] Grupo de consultores sobre osteoporosis de la Unión Europea. Osteoporosis en la Comunidad Europea: Plan de acción. pages 1–41, 2004.

[221] Kanis J.A., Norton N., Harvey N.C., Jacobson T., Johansson H., Lorentzon M., McCloskey E.V., Willers C., and Borgström F. SCOPE 2021: a new scorecard for osteoporosis in Europe. *Arch Osteoporos.*, **16**:1–82, 2021.

[222] Bernstein J. Describe the process of bone remodeling. OrthopaedicsOne Clerkship. In: Orthopaedic Knowledge Network. https://www.orthopaedicsone.com/x/MAJCB, January 2014.

[223] Seeman E. Reduced bone formation and increased bone resorption: rational targets for the treatment of osteoporosis. *Osteoporos Int.*, **14** (Suppl 3):S2–S8, 2003.

[224] Motta P. Osteoporotic bone, SEM. Science Photo Library https://www.sciencephoto.com/media/260090/view.

[225] Marcucci G. and Brandi M.L. Rare causes of osteoporosis. *Clin Cases MIner Bone Metab.*, **12** (2):151–156, 2015.

[226] Hermoso de Mendoza M.T. Classification of osteoporosis. Risk factors. Clinical manifestations and differential diagnosis. *An Sist Sanit Navar.*, **26** (Supl.3):29–52, 2003.

[227] Ji M.-X. and Yu Q. Primary osteoporosis in postmenopausal women. *Chronic Dis Transl Med.*, **1**:9–13, 2015.

[228] Khosla S. and Riggs B.L. Pathophysiology of age-related bone loss and osteoporosis. *Endocrinol Metab Clin N Am.*, **34**:1015–1030, 2005.

[229] Korpi-Steiner   N.,   Milhorn   D.,   and   Hammett-
Stabler   C.   Osteoporosis   in   men.   *Clin   Biochem.*,
http://dx.doi.org/10.1016/j.clinbiochem.2014.03.026, 2014.

[230] Lorenc R.S. Idiopathic juvenile osteoporosis. *Calcif Tissue Int.*, **70**:395–397, 2002.

[231] Emkey G.R. and Epstein S. Secondary osteoporosis: Pathophys-iology and diagnosis. *Best Pract Res Clin Endocrinol Metab.*, http://dx.doi.org/10.1016/j.beem.2014.07.002:1–25, 2014.

[232] Canalis E., Mazziotti G., Giustina A., and Bilezikian J.P. Glucocorticoid-induced osteoporosis: pathophysiology and therapy. *Osteoporos Int.*, **18**:1319–1328, 2017.

[233] Bysse B., Hahn M., Soltau M., Zustin J., Püschel K., Duda G.N., and Amling M. Increased calcium content and inhomogeneity of mineraliza-tion render bone toughness in osteoporosis: Mineralization, morphology and biomechanics of human single trabeculae. *Bone*, **45**:1034–1043, 2009.

[234] Densitometría   osea   -   Resolana   Diagnóstico   por   imagen. https://resolana.net/., Sevilla.

[235] Fariña Acosta L. Osteoporosis: un reto para el manejo de las fracturas. In: Aotrauma en Cuba. https://www.granma.cu/todo-salud/2016-09-20/osteoporosis-un-reto-para-el-manejo-de-las-fracturas-20-09-2016-22-09-13., September 2016.

[236] Müller R., Henss A., Kampschulte M., Rohnke M., Langheinrich A.C., Heiss C., Janek J., Voigt A., Wilke H.J., Ignatius A., Herfurth J., El Khassawna T., and Deutsch A. Analysis of microscopic bone properties in an osteoporotic sheep model: a combined biomechan-ics, FE and ToF-SIMS study. *Journal of the Royal Society Interface*, **16**(151):20180793, 2019.

[237] Wazeer A., Das A., Sinha A., Inaba K., Ziyi S., and Karmakar A. Ad-ditive manufacturing in biomedical field: a critical review on fabrication method, materials used, applications, challenges, and future prospects. *Prog Addit Manuf.*, doi.org/10.1007/s40964-022-00362-y:1–33, 2022.

[238] Kumar M.B. and Sathiya P. Methods and materials for additive manu-facturing: A critical review on advancements and challenges. *Thin Wall Struct.*, doi.org/10.1016/j.tws.2020.107228:1–42, 2021.

[239] Stavropoulos P. and Foteinopoulos P. Modelling of additive manufacturing processes: a review and classification. *Manufacturing Rev.*, **5**,2:1–26, 2018.

[240] Rosen D.W. A review of synthesis methods for additive manufacturing. *Virtual and Physical Prototyping*, doi: 10.1080/17452759.2016.1240208:1–14, 2016.

[241] Bhagyashri K. Which additive manufacturing process is right for you? The Manufacturing Report. https://manufacturing.report/articles/which-additive-manufacturing-process-is-right-for-you., December 06, 2021.

[242] Gibson I., Rosen D., and Stucker B. Additive manufacturing technologies: 3D printing, rapid prototyping and direct digital manufacturing. *Johnson Matthey Technol Rev.*, **59**,(3):193–198, 2015.

[243] Gibson I., Rosen D., and Stucker B. *Additive manufacturing technologies. 3D printing, rapid prototyping and direct digital manufacturing.* Springer, ISBN 978-1-4939-2112-6, 2 edition, 2010.

[244] Medellin-Castillo H.I. and Zaragoza-Siqueiros J. Design and manufacturing strategies for fused deposition modelling in additive manufacturing: A review. *Chin J Mech Eng.*, **32**,53:1–16, 2019.

[245] Gawel T.G. Review of additive manufacturing methods. *Solid State Phenomena*, **308**:1–20, 2020.

[246] Praveena B.A., Lokesh N., Abdulrajak B., Santhosh N., Praveena B.L., and Vignesh R. A comprehensive review of emerging additive manufacturing (3D printing technology): Methods, materials, applications, challenges, trends and furutre potential. *Materials Today:Proceedings*, **52**:1309–1313, 2022.

[247] de Albuquerque T.L., Marques Júnior J.E., Pinnheiro de Queiroz L., Souza Ricardo A.D., and Ponto Rocha M.V. Polylactic acid production from biotechnological routes: A review. *Int J Biol Macrom.*, **186**:933–951, 2021.

[248] Ashothaman A., Sudha J., and Senthilkumar N. A comprehensive review on biodegradable polylactic acid polymer matrix composite material reinforced with synthetic and natural fibers. *Materials Today:Proceedings*, doi.org/10.1016/j.matpr.2021.07.047:1–11, 2021.

[249] Li X., Lin Y., Liu M., Meng L., and Li C. A review of research and application of polylactic acid composites. *J Appl Polym Sci.*, e53477, doi.org/10.1002/app.53477:1–22, 2022.

[250] Manoj Prabhakar M., Saravanan A.K., Haiter Lenin A., Jerin Ieno I., Mayandi K., and Sethu Ramalingam P. A short on 3D printing models, process parameters and materials. *Materials Today:Proceedings*, doi.org/10.1016/j.matpr.2020.10.225:1–8, 2021.

[251] Peng T. and Sun W. Energy modelling for FDM 3D printing from a life cycle perspective. *Int J Manufacturing Research.*, **12**, No 1:83–98, 2017.

[252] Kaseem M., Hamad K., and Ur Rehman Z. Review of recent advances in polylactic acid/TiO$_2$ composites. *Materials*, **12**, 3659, doi:10.3390/ma12223659:1–16, 2019.

[253] Ali M., Kumar Pr A., Yoo J.J., Zahran F., Atala A., and Lee S.J. A photo-crosslinkable kidney ECM - derived bioink accelerates renal tissue formation. *Adv Healthc Mater.*, **8**(7):e1800992:1–10, 2019.

[254] Kim J.H., Seol Y.J., Ko I.K., Kang H.W., Lee Y.K., Yoo J.J., Atala A., and Lee S.J. 3D bioprinted human skeletal muscle constructs for muscle function restoration. *Sci Rep.*, **8**:1–5, 2018.

[255] Kim Y., Kang K., Yoon S., Kim J.S., Park S.A, Kim W.D., Lee S.B., Ryu K.Y., and Jeong J. Choi D. Prolongation of liver-specific function for primary hepatocytes maintenance in 3D printed architectures. *Organogenesis*, **14** (1):1–12, 2018.

[256] Reid J.A., Mollica P.A, Bruno R.D., and Sachs P.C. Consistent and reproducible cultures of large-scale 3D mammary epithelial structures using an accessible bioprinting platform. *Brest Cancer Res.*, **20**(1):122:1–13, 2018.

[257] Lee W., Pinckney J., Lee V., Lee J.H., Fischer K., Polio S., Park J.K., and Yoo S.S. Three-dimensional bioprinting of rat embryonic neural cells. *Neuro Report.*, **20**:798–803, 2009.

[258] Zhang Y.S., Arneri A., Bersini S., Shin S.R., and Zhu K. et al. Bioprinting 3D microfibrous scaffolds for engineering endothelialized myocardium and heart-on-a-chip. *Biomaterials*, **110**:45–59, 2016.

[259] Osidak E.O., Karalkin P.A, Osidak M.S., Parfenov V.A., Sivogrivov D.E., and Pereira F. et al. Viscoll collagen solution as a novel bioink for direct 3D biorpinting. *J Mater Aci Mater Med.*, **30**:31:1–12, 2009.

[260] Belda R., Megías R., Marco M., Vercher-Martínez A., and Giner E. Numerical analysis of the influence of triply periodic minimal surface structures morphometry on the mechanical response. *Comput Methods Programs Biomed.*, **230**:107342, 2023.

[261] Li Z.G., Zhang X.G., Huang P., Hu L., and Zu G.Y. Preparation and properties of open-cell zinc foams as human bone substitute material. *China Foundry*, **16**:414–422, 2019.

[262] Anselme K. Osteoblast adhesion on biomaterials. *Biomaterials*, **21**(7):667–681, 2000.

[263] Park J.Y., Park S.H. Kim M.G., Park S.H., Yoo T.H., and Kim M.S. Biomimetic scaffolds for bone tissue engineering. *Adv Exp Med Biol.*, **1064**:109–121, 2018.

[264] Zhang Z., Jones D., Yue S. Lee P.D., Jones J.R., Sutcliffe C.J., and Jones E. Hierarchical tailoring of strut architecture to control permeability of additive manufacturing titanium implants. *Mater Sci Eng C Mater Biol Appl.*, **33**(7):4055–4062, doi:10.1016/j.msec.2013.05.050, 2013.

[265] Winarso R., Anggoro P.W., Ismail R., Jamari J., and Bayuseno A.P. Aplication of fused deposition modeling (FDM) on bone scaffold manufacturing process: A review. *Heliyon*, **8**:e11701, 2022.

[266] Donate R., Monzón M., and Alemán-Domínguez M.A. Additive manufacturing of PLA-based scaffolds intended for bone regeneration and strategies to improve their biological properties. *e-Polymers*, **20**:571–599, 2020.

[267] Grémare A., Guduric V., Bereille R., Heroguez V., Latour S., and L'heureux N. et al. Characterization of printed PLA scaffolds for bone tissue engineering. *J Biomed Mater Res A.*, **106**(4):887–894, doi:10.1002/jbm.a.36289, 2018.

[268] Reina S.A, Tito B.J.E., Malini M.H., Iqrimatien F.G., Sa'diyah E., and Aminatun. Porosity and compressive strength of PLA-based scaffolds coated with hydroxyapatite-gelatin to reconstruct mandibula: A literature review. *J Phys Conf Ser.*, **1816**:012085, doi:10.1088/1742–6596/1816/1/012085, 2021.

[269] Baptista R. and Guedes M. Morphological and mechanical characterization of 3D printed PLA scaffolds with controlled porosity for trabecular bone tissue replacement. *Mater Sci Eng C.*, **118**:111528, 2021.

[270] Mahmood M.A., Rehman A.U., Pitir F., Salamci M.U, and Mihailescu I. Laser melting deposition additive manufacturing of Ti6Tl4V biomedical alloy: Mesoscopic in-situ flow field mapping via computational. *Materials*, **14**:7749, 2021.

[271] Zhang B., Wang L., Song. P., Pei X., Sun H., Wu L., Zhou C., Wang K., Fan Y., and Zhang X. 3D printed bone tissue regenerative PLA-HA scaffolds with comprehensive performance optimizations. *Mater Des.*, **201**:109490, 2021.

[272] Zimina A., Senatov F., Choudhary R., Kolesnikov E., and Anisimova N et al. Biocompatibility and physico-chemical properties of highly porous PLA-HA scafflods for bone reconstruction. *Polymers*, **12**:2938, doi:10.3390/polym12122938, 2020.

[273] Wang N., Zang Y., Ren G., and Wu Q. Fabrication and properties of porous scaffolds of PLA-PEG biocomposite for bone tissue engineering. *Materials Science Forum*, **789**:130–135, doi:10.4028/www.scientific.net/MSF.789.130, 2014.

[274] Chen X., Gao C., Jiang J., Wu Y., Zhu P., and Chen G. 3D printed porous PLA/nHA composite scaffolds with enhanced osteogenesis and osteoconductivity in vivo for bone regeneration. *Biomed Mater.*, **14**(6):065003, doi: 10.1088/1748–605X/ab388d, 2019.

[275] Hassanajili S., Karami-Pour A., Oryan A., and Talaei-Khozani T. Preparations and characterization of PLA/PCL/HA composite scaffolds using indirect 3D printing for bone tissue engineering. *Mater Sci Eng C.*, **104**:109960, 2019.

[276] Getme A.S. and Patel B. A review: Bio-fiber's as reinforcement in composites of polylactic acid (PLA). *Materials Today: Proceedings*, **26** Part 2:2116–2122, 2020.

[277] Kondiah P., Choonara Y.E., Kondiah P.J., Marmuthu T., du Toit L.C., Kumar P., and Pillay V. Recent progress in 3D-printed polymeric scaffolds for bone tissue engineering. In Lisa C. du Toit, Pradeep Kumar, Yahya E. Choonara, and Viness Pillay, editors, *Advanced 3D-Printed Systems and Nanosystems for Drug Delivery and Tissue Engineering*, Woodhead Publishing Series in Biomaterials, pages 59–81, ISBN: 978–0–12–818471–4, doi:https://doi.org/10.1016/B978–0–12–818471–4.00003–0. Elsevier, 2020.

[278] Lämmermann M., Horak G., and Schwieger W. Freund H. Periodic open cellular structures (POCS) for intensification of multiphase reactors: Liquid holdup and two-phase pressure drop. *Chem Eng Process.: Process Intensif.*, **126**:178–189, 2018.

[279] de Aquino D.A., Maskery I., Longhitano G.A., Jardini A.L., and del Conte E.G. Investigation of load direction on the compressive strength of additively manufactured triply periodic minimal surface scaffolds. *J Adv Manuf Technol.*, **109**:771–779, 2020.

[280] Naghavi S.A., Tamaddon M., Marghoub A., Wang K., Babamiri B.B., Hazeli K., Xu W., and Lu X. et al. Mechanical characterisation and numerical modelling TPMS-based gyroid and diamond Ti6Al4V scaffolds for bone implants: An integrated approach for translational consideration. *Bioengineering*, **9**(10):504, https://doi.org/10.3390/bioengineering9100504, 2022.

[281] Viet N.V., Waheed W., Alazzam A., and Zaki W. Effective compressive behaviour of functionally graded TPMS titanium implants with ingrown cortical or trabecular bone. *Composite Structures*, **303**:116288, https://doi.org/10.1016/j.compstruct.2022.116288, 2023.

[282] Song K., Wang Z., Lan J., and Ma S. Porous structure design and mechanical behavior analysis based on TPMS for customizes root analogue implant. *J Mech Behav Biomed Mater.*, **115**:104222, https://doi.org/10.1016/j.jmbbm.2020.104222, 2021.

[283] Mahadevan V. Anatomy of the vertebral column. *Surgery*, **36**(7):327–332, 2018.

[284] Dath R., Ebinesan A.D., Porter K.M., and Miles A.W. Anatomical measurements of porcine lumbar vertebrae. *Clin Biomec.*, **22**:607–613, 2007.

[285] McLain R.F., Yerby S.A., and Moseley T.A. Comparative morphometry of L4 vertebrae: comparison of large animal models for human lumbar spine. *Spine*, **27**(8):E200–E206, 2002.

[286] Pope M.H. Biomechanics of the lumpar spine. *Annals of Medicine*, **21**:347–351, 1989.

[287] Mosekilde L. Age-related changes in bone mass, structure, and strength - effects of loading. *Z Rheumatol.*, **59**(1):1–9, 2000.

[288] Chang A., Breeland G., and Hubbard J.B. Anatomy, bony pelvis and lower limb, femur. Trasure Island (FL): StatPearls Publishing [Book] https://www.ncbi.nlm.nih.gov/books/NBK532982/, January 2022.

[289] Francis A., Shrivastava A., Masih C., Dwivedi N., Tiwari P., Nareliya R., and Kumar V. Biomechanical analysis of human femur: A review. *J Biomed Bioeng.*, **3**, Issue 1:67–70. ISSN: 0976–8084 & E–ISSN: 0976–8092, 2012.

[290] Fisher S.J. and Gray J.L. The areas of the femur (thighbone). Most hip fractures occur in the femoral neck or intertrochanteric area. [Image] https://orthoinfo.aaos.org/en/diseases–conditions/hip-fractures/, November 2020.

[291] Egol K.A. and Leucht P. *Proximal Femur Fractures. An evidence-based approach to evaluation and management.* Springer, ISBN: 978-3-319-64902-3, 2017.

[292] Büchler L., Tannast M., Siebenrock K.A., and Schwab J.M. Biomechanics of the hip. *Biomechanics of the Hip. In: Egol K. and Leucht P. (eds.) Proxima Femur Fractures. Springer*, pages 9–15, 2018.

[293] The First National Conference for Engineering Sciences FNCES'12. *Stress analysis for osteoporosis head of femur*, November 2012.

[294] Bombelli R. *Osteoarthritis of the hip.* Springer-Verlag, Berlin, 1983.

[295] Harris W.H. Etiology of osteoarthritis of the hip. *Clin Orthop Relat Res.*, **213**:20–33, 1986.

[296] Dalstra M., Huiskes R., and van Ernin L. Development and validation of a three-dimensional finite element model of the pelvic bone. *J Biomech Eng.*, **117**(3):272–278, 1995.

[297] Garden R.S. Age-related changes in bone mass, structure, and strength - effects of loading. *J Bone Joint Surg.*, **46 B**(3):576–589, 1961.

[298] Ward F.O. *Outlines of Human Osteology.* Henry Renshaw, London, 1838.

[299] Bouxsein M.L. Biomechanics of osteoporotic fractures. *Clin Rev Min Metab.*, **4**(3):143–154, 2006.

[300] Machado M.M., Fernandes P.R., Zymbal V., and Baptista F. Human proximal femur bone adaptation to variations in hip geometry. *Bone*, **67**:193–199, 2014.

324

[301] Gdoutos E.E., Raftopoulos D.D., and Baril J.D. A critical review of the biomechanical stress analysis of the human femur. *Biomaterials*, **3**(1):2–8, 1982.

[302] Sheehan S.E., Shyu J.Y., Weaver M.J., Sodickson A.D., and Khurana B. Proximal femoral fractures: what the orthopdic surgeon wants to know. *Radiographics*, **35**(5):1563–1584, 2015.

[303] Praxys Fisioterapia. Fracturas Intracapsulares y fracturas extracapsulares. [Image] https://praxys.es/especialidades-fisioterapia-a-domicilio/protesis-de-cadera/.

[304] Poilliot A., Gay-Dujak M.H.P., and Müller-Gerbl M. The quantification of 3D-trabecular architecture of the fourth cervical vertebra using CT osteoabsorptiometry and micro-CT. *J Orthop Surg J Orthop Surg Res.*, **18** (1):297, 2023.

[305] Liu X.S., Sajda P., Saha P.K., Wehrli F.W., Bevill G., Leaveny T.M., and Guo X.E. Complete volumetric decomposition of individual trabecular plates and rods and its morphological correlations with anisotropic elastic moduli in human trabecular bone. *J Bone Miner Res.*, **23** (2):223–235, 2008.

[306] Li Y., Liem Y., Dall'Ara E., Sullivan N., Ahmed H., Blom A., and Sharif M. Subchondral bone microarchitecture and mineral density in human osteoarthritis and osteoporosis: A regional and compartmental analysis. *J Orthop Res.*, **39**:2568–2580, 2021.

[307] He Z., Chu L., Liu X., Han X., Zhang K., Yan M., Li X., and Yu Z. Differences in subchondral trabecular bone microarchitecture and finite element analysis-based biomechanical properties between osteoporosis and osteoarthritis. *J Orthop Transl.*, **24**:39–45, 2020.

[308] Ries C., Boese C.K., Stürznickel J., Koehne T., Hubert J., Pasto M.F., Hahn M., Meier S.L., Beil F.T., Püschel K., Amling M., and Rolvien T. Age-related changes of micro-morphological subchondral bone properties in the healthy femoral head. *Osteoarthr Cartil.*, **28** (11):1437–1447, 2020.

[309] Belda R., Palomar M., Peris-Serra J.L., Vercher-Martínez A., and Giner E. Compression failure characterization of cancellous bone combining experimental testing. digital image correlation and finite element modelling. *Int J Mech Sci.*, **165**:105213, 2020.

[310] Schwiedrzik J.J. and Zysset P.K. An anisotropic elastic-viscoplastic damage model for bone tissue. *Biomech Model Mechanobiol.*, **12** (2):201–213, 2013.

[311] Lemaitre J. A continuous damage mechanics model for ductile fracture. *J Eng Mater Technol.*, **107**:83–89, 1985.

[312] Ascenzi A. and Bonucci E. The tensile properties of single osteons. *Anat Rec.*, **158**:375–386, 1967.

[313] Ascenzi A. and Bonucci E. The compressive properties of single osteons. *Anat Rec.*, **161**:377–392, 1968.

[314] Ascenzi A. and Bonucci E. The shearing properties of single osteons. *Anat Rec.*, **172**:499–510, 1972.

[315] Hashin Z. Failure criteria for unidirectional fiber composites. *J Appl Mech.*, **47**:329–334, 1980.

[316] Koller B. and Laib A. Calibration of micro-CT data for quantifying bone mineral and biomaterial density and microarchitecture. *Advanced Bioimagin Technologies in Assessment of the Quality of Bone and Scaffold Materials: Techniques and Applications*, doi:10.1007/978-3-540-45456-4-5, 2007.

[317] Yu W., Glüer C.C., Grampp S., Jergas M., Fuerst T., Wu C.Y., Lu Y., Fan B., and Genant H.K. Spinal bone mineral assessment in post-menopausal women: a comparison between dual X-ray absorptiometry and quantitative computed tomography. *Osteoporos Int.*, **5**:433–439, 1995.

[318] Hohe J. A direct homogenization approach for determination of the stiffness matrix for microheterogeneous plates with application to sandwich panels. *Compos Part B*, **34**:615–626, 2003.

[319] Giner E., Arango C., Vercher A., and Fuenmayor F.J. Numerical modelling of the machanical behaviour of an osteon with microcracks. *J Mech Behav Biomed Mater.*, **37**:109–124, 2014.

[320] Barbero E.J. and Cabrera J. Determination of material properties for progressive damage analysis of carbon/epoxy laminates. *Mech Adv Mater Struct.*, **0**:1–10, 2018.

[321] Matzenmiller A., Lubliner J., and Taylor R.L. A constitutive model for anisotropic damage in fiber-composites. *Mech Mater.*, **20**:125–152, 1995.

[322] Barbero E.J. and Cosso F.A. Determination of material parameters for discrete damage mechanics analysis of carbon-epoxy laminates. *Compos Part B*, **56**:638–646, 2014.

[323] Wili P., Maquer G., Panyasantisuk J., and Zysset P.K. Estimation of the effective yield properties of human trabecular bone using nonlinear micro-finite element analysis. *Biomech Model Mechanobiol.*, **16**:1925–1936, 2017.

[324] Turner C.H. Yield behaviour of bovine cancellous bone. *J Biomech Eng.*, **111**:256–260, 1989.

[325] Cowin S.C., Moss-Salentijn L., and Moss M.L. Candidates for the mechanosensory system in bone. *J Biomech Eng.*, **191**:191–197, 1991.

[326] Prendergast P.J. and Huiskes R. Microdamage and osteocyte-lacuna strain in bone: a microstructural finite element analysis. *J Biomech Eng.*, **118**:240–246, 1996.

[327] Reilly G.C. Observations of microdamage around osteocyte lacunae in bone. *J Biomech.*, **33**:1131–1134, 2000.

[328] Reilly G.C. and Currey J.D. Candidates for the mechanosensory system in bone. *J Exp Biol.*, **202**:543–552, 1999.

[329] Ebacher V., Guy P., Oxland T.R., and Wang R. Sub-lamellar microcracking and roles of canaliculi in human cortical bone. *Acta Biomater.*, **8**:1093–1100, 2012.

[330] Voide R., Schneider P., Stauber M., Wyss P., Stampanoni M., Sennhauser U., van Lenthe G.H., and Müller R. Time-lapsed assessment of microcrack initiation and propagation in murine cortical bone at submicrometer resolution. *Bone*, **45**:164–173, 2009.

[331] Megías R., Vercher-Martínez A., Belda R., Peris J.L., Larrainzar-Garijo R., Giner E, and Fuenmayor F.J. Numerical modelling of cancellous bone damage using an orthotropic failure criterion and tissue elastic properties as a function of the mineral content and microporosity. *Comput Methods Programs Biomed.*, **219**:106764, 2022.

[332] Casari D., Michler J., Zysset P., and Schwiedrzik J. Microtensile properties and failure mechanisms f cortical bone at the lamellar level. *Acta Biomater.*, **120**:135–145, 2021.

[333] Hernandez C.J., Beupré G.S., Keller T.S., and Carter D.R. Numerical modelling of cancellous bone damage using an orthotropic failure criterion and tissue elastic properties as a function of the mineral content and microporosity. *Bone*, **29**, (1):74–78, 2001.

[334] Abere D.V., Ojo S.A., Oyatogun G.M., Paredes-Espinosa M.B., Dharsika Niluxsshun M.C., and Hakami A. Mechanical and mophological characterization of nano-hydroxyapatite (nHA) for bone regeneration: A mini review. *Biomed Eng Adv.*, **4**:100056, 2022.

[335] Sang W. and Ural A. Quantifying how altered lacunar morphology and perilacunar tissue properties influence local mechanical environment of osteocyte lacunae using finite element modeling. *J Mech Behav Biomed Mater.*, **135**:105433, 2022.

[336] Collins C.J., Kozyrev M., Frank M., Andriotis O.G., Byrne R.A., Kiener H.P., Pretterklieber M.L., and Turner P.J. The impact of age, mineralization, and collagen orientation on the mechanics of individual osteons from human femurs. *Materialia*, **9**:100573, 2020.

[337] Dudaric L., Dumic-Cule I., Divjak E., Cengic T., Brkljacic B, and Ivanac G. Bone remodeling in osteoarthritis - Biological and radiological aspects. *Medicina*, **59**:1613, 2023.

[338] Fazzalari N.L. and ParkinsonI.H. Fractal properties of suchondral cancellous bone in severe osteoarthritis of the hip. *J Bone Miner Res.*, **12**, (4):632–640, 1997.

[339] Arden N.K., Griffiths G.O., Hart D.J., Doyle D.V., and Spector T.D. The association between osteoarthritis and osteoporotic fractures: the Chingford study. *Br J Rheumatol.*, **35**:1299–1304, 1996.

[340] Hannan M.T., Anderson J.J., Zhang Y., Levy D., and Felson D.T. Bone mineral density and knee osteoarthritis in elderly men and women. *Arthritis Rheum.*, **36**:1671–1680, 1993.

[341] Tanchev P. Osteoarthritis or osteoarthrosis: Commentary on misuse of terms. *Reconstructuve Review*, **7**(1):45–46, 2017.

[342] Jeremic D., Gluscevic B., Rajkovic S., Jovanovic Z., and Krivokapic B. Osteoarthritis, osteoarthrosis and osteoarthropathy - What is the diffeerence? *Serbian J Med Chamber.*, **2**(1):25–32, 2021.

[343] Atkinson M.H. Osteoarthrosis. *Can Fam Physician.*, **30**:1503–1507, 1984.

[344] Decquer J. and Luyten F.P. The history of osteoarthritis-osteoarthrosis. *J Orthop Translat.*, **12**:26–35, 2015.

[345] Kanis J.A., Borgström F., Compston J., Drenhöfer K., Nolte E., Jonsson L., Lems W.F., McCloskey E.V., Rozzoli R., and Stenmark J. SCOPE: a scorecard for osteoporosis in Europe. *Arch Osteoporos.*, **8**,144:1–63, 2013.

[346] Nazarian A., Snyder B.D., Zurakowski D., and Müller R. Quantitative micro-computed tomography: A non-invasive method to assess equivalent bone mineral density. *Bone*, **43**:302–311, 2008.

[347] Schileo E., Dall'Ara E., Taddei F., Malandrino A., Schotkamp T., Baleani M., and Viceconti M. An accurate estimation of bone density improves the accuracy of subject-specific finite element models. *J Biomech.*, **41**:2483–2491, 2008.

[348] Ranjanomennahary P., Ghalia S.S., Malouche D., Marchadier A., Rachidi M., Benhamou Cl., and Chappard C. Comparison of radiograph-based texture analysis and bone mineral density with three-dimensional microarchitecture of trabecular bone. *Med Phys.*, **38**(1):420–428, 2010.

[349] Gujar R.A. and Warhatkar H.N. Estimation of mass apparent density and Ypung's modulus of femoral neck-head region. *J Med Eng Technol.*, **44**(7):378–388, 2020.

[350] Abdullah A.H. and Todo M. Prediction of bone mineral density (BMD) adaptation pelvis-femur model with hip arthroplasties. *J Funct Biomater.*, **12**(3):49, 2021.

[351] Auger J.D., Naik A.J., Murakami A.M., and Gerstenfels L.C. Spatial assessment of femoral neck bone density and microstructure in hip osteoarthritis. *Bone Rep.*, **16**:101155, 2022.

[352] Pumarino H., González P., Oviedo S., and Lillo R. Density and bone mineral content and their relation to antropometric parameters in a normal Chilean population. A study with women. *Revista Medica de Chile*, **119**(3):279–286, 1991.

[353] Kröger H., Kotaniemi A., Vainio P., and Alhava E. Bone densitometry of the spine and femur in children by dual-energy x-ray absorptiometry. *Bone and Mineral*, **17**:75–85, 1992.

[354] Cossio-Bolanos M., Vidal-Espinoza R., Fuentes-López J., Castelli L.F., Andruske C.L., Urra-Albornoz C., Vasquez F., and Gomez-Campos R.

Reference values for bone densirt and bone mineral content from 5 to 80 years old in a province of Chile. *PeerJ*, 10:e13092:1–18, 2022.

[355] Zlamal P., Jrousek O., Doktor T., and Kytyr D. Modellingelasto-plastic behaviour of human single trabecula - comparison with bending test. *J Biomech.*, **45**:S494–S, 2012.

[356] Tjhia C.K., Odvina C.V., Rao D.S., Stover S.M., Wang X., and Fyhrie D.P. Mechanical property and tissue mineral density differences among severely suppressed bone turnover (SSBT) patients, osteoporotic patients, and normal subjects. *Bone*, **49**(6):1279–1289, 2011.

[357] Harrigan T.P. and Mann R.W. Characterization of microstructural anisotropy in orthotropic materials using a second rank tensor. *J Mater Sci.*, **19**:761–767, 1984.

[358] Kabel J., Odgaard A., van Rietbergen B., and Huiskes R. Connectivity and the elastic properties of cancellous bone. *Bone*, **24**(2):115–120, 1999.

[359] Toriwaki J. and Yonekura T. Euler number and connectivity indexes of a three dimensional digital picture. *Forma*, **17**:183–209, 2002.

[360] Fractal dimension of the Menger Sponge. (10 january 2024) Fractal Foundation Online Course - Chapter 1- Fractals in Nature: https://fractalfoundation.org/OFC/OFC-10-3.html.

[361] Sierpinski dreieck Fractal Pascal's dreieck Sierpinski carpet - Dreieck. (10 january 2024) CleanPNG: https://de.cleanpng.com/png-sitvz5/.

[362] Klinström E., Smedby O., Klinström B., Brismar T.B., and Moreno R. Trabecular bone histomorphometric measurements and contrast-to-noise ratio in CBCT. *Dentomaxillofac Radiol.*, **43**(8):20140196, 2014.

[363] Marín Ribas R. Trabecular Thickness (Tb.Th), Trabecular Spacing (Tb.Sp). Scientific Illustrator: https://graphictextile.blogspot.com/2018/06/trabecular-thickness-tbth-trabecular.html?spref=pi, 26 june 2018.

[364] Metzner F., Neupetsch C., Fischer J.P., Drossel W.G., Heyde C.E., and Schleifenbaum S. Influence of the osteporosis on the compressive properties of femoral cancellous bone and its dependence on various density parameters. *Sci Rep.*, **11**:13284, 2021.

[365] Homminga J., McCreadie B.R., Ciarelli T.E., Weinans H., Goldstein S.A., and Huiskes R. Cancellous bone mechanical properties from normals and patients with hip fractures differ on the structure level, not on the bone hard tissue level. *Bone*, **30**, 5:759–764, 2002.

[366] Sun S.S., Ma H.L., Liu C.L., Huang C.H., Cheng C.K., and Wei H.W. Differences in femoral head and neck material properties between osteoarthritis and osteoporosis. *Clin Biomech.*, **23**:S39–S47, 2007.

[367] Kabel J., van Rietbergen B., Dalstra M., Odgaard A, and Huiskes R. The role of an effective isotropic tissue modulus in the elastic properties of cancellous bone. *J Biomech.*, **32**:673–680, 1999.

[368] Keaveny T.M. and Heves W.C. A 20-year perspective on the mechanical properties of trabecular bone. *J Biomech Eng.*, **115**(4B):534–542, 1993.

[369] Jirásek M. Damage and smeared crack models. In: Hofstetter G. and Meschke G, editors. Numerical modeling of concrete cracking, CSIM courses and lectures. *Springer*, **532**:1–49, 2011.

[370] Nalla R.K., Kinney J.H., and Ritchie R.O. Mechanistic fracture criteria for failure of human cortical bone. *Nat Mater.*, **2**:164–168, 2003.

[371] Burr D.B. and Stafford T. Validity of the bulk-staining technique to separate artifactual from in vivo bone microdamage. *Clin Orthop Relat Res.*, **260**:305–308, 1990.

[372] Taylor D. and Lee T.C. A crack growth model for the simulation of fatigue in bone. *Int J Fatigue.*, **2**:287–295, 2003.

[373] Farlay D., Bala Y., Rizzo S., Bare S., Lappe J.M., Recker R., and Boivin G. Bone remodelling and bone matrix quality before and after menopause in helathy women. *Bone*, **128**:115030, 2019.

[374] Yang G., Kabel J., Van Rietbergen B., Adgaard A., Huiskes R., and Cowin S. The anisotropic hooke's law for cancellous bone and wood. *J Elast.*, **53**:125–146, 1999.

[375] Smith L.J., Schirer J.P, and Fazzalari N.L. The role of mineral content in determining the micromechanical properties of discrete trabecular bone remodeling packets. *J Bimoech.*, **43**:3144–3149, 2010.

[376] Jrousek O., Nemecek J., Kytyr D., Kunecy J., Zlamal P., and Doktor T. Nanoindentation of trabecular bone-comparison with uniaxial testing of single trabecula. *Chemicke listy*, **105**:668–671, 2011.

[377] Morgan E.F., Unnikrisnan G.U., and Huseein A.I. Bone mechanical properties in healthy and diseased states. *Annu Rev Biomed Eng.*, **20**:119–143, 2018.

[378] Bayraktar H.H. and Keaveny T.M. The uniformity of trabecular bone failure strains at the human femoral neck. Poster No: 0554. *48th Annual meeting of the orthopaedic research society*, 2002.

[379] Neves S.C., Mota C., Longoni A., Barrias C., Granja P.L., and Moroni L. Additive manufactured polymeric 3D scaffolds with tailored surface topography influence mesenchymal stromal cells activity. *Biofabrication*, **8**:025012, 2016.

[380] Bobbert F.S.L. and Zadpoor A.A. Effects of bone substitute architecture and surface properties on cell response, angiogenesis and structure of new bone. *J Mater Chem B.*, **5**:6175, 2017.

[381] Al-Ketan O. and Abu Al-Rub R.K. MSLattice: A free software for generating uniform and graded lattices based on triply periodic minimal surfaces. *Mat Design Process Comm.*, **3**(6):e205, 2020.

[382] Dimitriou R., Jones E., McGonagle D., and Giannoudis P. Bone regeneration: current concepts and future directions. *BMC Medicine*, **9**(66):1–10, 2011.

[383] Stevens M.M. Biomaterials for bone tissue engineering. *Materials Today*, **11**(5):18–25, 2008.

[384] Stevens B., Yang Y., Mohandas A., Stucker B., and Nguyen K.T. A review of amterials, fabrication methods, and strategies used to enhance bone regeneration in engineered bone tissues. *J Biomed Mater Res B Appl Biomater.*, **85**(2):573–582, 2007.

[385] Ficha técnica Smartfil PLA. Smart Materials 3D: https://www.smartmaterials3d.com/, 30 october 2020.